Exploring the climate variability of sea surface dynamics: extremes and climate change impact

Héctor Lobeto Alonso

Supervisors: Melisa Menéndez García
Raúl Medina Santamaría

Universidad de Cantabria

This dissertation is submitted for the degree of
Doctor en Ingeniería de Costas, Hidrobiología y Gestión de Sistemas Acuáticos (IH2O)

July 2022

Agradecimientos

Agradezco al Ministerio de Universidades del Gobierno de España la financiación del presente proyecto de tesis doctoral a través de la beca de Formación de Profesorado Universitario con referencia FPU2017/06203.

Quiero mostrar mi más sincero agradecimiento a mis directores, Melisa Menéndez Y Raúl Medina. A Melisa, porque junto a ella he comenzado mi camino en el bonito mundo de la investigación, por transmitirme su pasión por entender, conocer e innovar, por enseñarme, aconsejarme y ayudarme siempre que lo he necesitado. A Raúl, por ser un gran apoyo desde el primer día que llegué a IHCantabria, siempre dispuesto a darme consejo y ayuda.

Quiero también decir gracias a Iñigo J. Losada, por su ayuda y apoyo a lo largo de esta tesis, por estar siempre dispuesto a formar parte de los estudios que hemos desarrollado, aportando su inestimable conocimiento y experiencia. Me gustaría extender este agradecimiento a todos mis compañeros del grupo de Clima Marino y Cambio Climático de IHCantabria, tanto a los que a día de hoy forman parte de él, como a aquellos que ya no están, porque me hicieron sentir como en casa desde el primer día y siempre me han echado una mano cuando la he necesitado. Así mismo, quiero decir gracias a todas las personas que forman parte de IHCantabria y que, de una forma u otra, han facilitado el desarrollo de este proyecto.

Agradezco a Alvaro Semedo su ayuda durante la estancia predoctoral. Primero, desde el punto de vista personal, por hacer mi adaptación más sencilla y prestarme ayuda en todo momento. Segundo, desde el punto de vista profesional, por darme la posibilidad de vivir esta experiencia tan enriquecedora, permitiéndome colaborar con nuevos investigadores, aprendiendo de sus conocimientos y formas de trabajar. Del mismo modo, quiero dar las gracias a Rosh Ranasinghe por aceptarme dentro del departamento "*Department of Coastal and Urban Risk and Resilience*" de la institución UNESCO-IHE Delft, donde me sentí muy cómodo desde el primer día.

Gracias a Mark Hemer por su amable predisposición a participar en nuestros estudios, aportando su incuestionable conocimiento en la materia y enriqueciendo el resultado final. Así mismo, agradezco su ayuda y aporte de conocimiento a Gil Lemos, Ali Dastgheib y al resto de coautores que participan en los estudios realizados.

Finalmente, y no por ello menos importante, quiero dedicar unas líneas a agradecer el apoyo incondicional de mis padres, su paciencia y su comprensión. A mi pareja, Nuria, por acompañarme durante este camino, compartir conmigo los momentos buenos y, sobre todo, por ser comprensiva y paciente en los momentos difíciles. Y por supuesto, a mis amigos, a los que ya tenía al empezar la tesis y a los que he conseguido por ella, gracias.

Abstract

Sea level and ocean wind waves are two of the main drivers of the ocean sea surface behavior. These sea surface dynamics, independently or combined, can cause impacts over the open ocean (offshore) and in the coastal zone (nearshore). Furthermore, the impact severity increases during unusual extreme events. In this context, this dissertation proposes new methods and develops new climate products to increase understanding of the characteristics and climate variations of these sea surface dynamics, especially under extreme conditions. Research particularly focuses on the effect that climate change may have on the behavior of both dynamics. Accordingly, this thesis is based on three pivotal elements: (i) sea level and wind wave dynamics, (ii) extreme events and (iii) climate variability. The present dissertation is structured in three parts resultant from the interrelationships between these elements. Part 1 analyzes extreme events of sea level and wind waves. Part 2 assesses the extreme climate variability of both dynamics. Part 3 particularly assesses the effect of climate change on wind waves.

Regarding the first part of the document and the sea level dynamic, a novel method to analyze coastal sea level extremes from satellite altimetry data is proposed. An approach based on the application of a non-stationary extreme model to non-tidal residual monthly maxima is presented. With the aim of countering the lack of accuracy of altimetry data, a correction is proposed. This correction depends on the local morphology and its definition makes use of the information provided by tide gauges. The correction procedure results in low errors for extreme estimates associated to high return periods. On the other hand, the main characteristics of coastal wind wave storms along the global coastlines are also analyzed. The frequency of occurrence, duration and intensity, as well as other secondary characteristics such as the wind-sea vs. swell dominance during wave storms are assessed. Finally, a global coastal classification in terms of the degree of storminess is proposed.

The climate variability of sea surface dynamics, specially for extremes, as well as the divergences in the behavior between mean and extreme conditions is then explored. Here, the variability of coastal sea level extremes is assessed from altimetry data along the global coastlines at different time scales: within the year, interannual and long-term. The skill of altimetry data to reproduce sea level extreme climate variations is validated against tide gauge data. Additionally, the relative contribution of the non-tidal residual component and the astronomical tide to sea level extremes is explored. Regarding wind waves, the assessment of the extreme climate variability focuses on the long-term variations due to climate change. Projected changes in significant wave height for different return periods are estimated by the end of the century under different climate change concentration scenarios for all ocean basins. Additionally, regional differences between the projected behavior of mean and extreme wave climate conditions are analyzed.

Finally, this dissertation proposes a novel approach to assess the effect of climate change on wave climate based on the wave energy frequency-direction spectrum, in contrast to current studies based on integrated wave parameters (e.g., significant wave height). Results show that the standard approach based on integrated wave parameters could mask relevant information about the magnitude, sign and robustness of the projected changes. On this basis, a global assessment of the the effect of climate change on wave spectra by the end of the century under the business-as-usual concentration scenario is presented. Regional patterns of spectral change are identified and analyzed, allowing to individually assess the projected changes in the main swell systems propagating across the oceans.

Table of contents

List of figures

List of tables

List of Acronyms

AM	Annual Maxima
AMM	Annual Maxima Method
AO	Arctic Oscillation
AR5	Fifth Assessment Report from IPCC
AVISO	Archiving, Validation and Interpretation of Satellite Oceanographic Data
BC	Bias Correction
CCI	Climate Change Initiative
CDF	Cumulative Distribution Function
CMEMS	Copernicus Marine Environment Monitoring Service
COWCLIP	Coordinated Ocean Wave Climate Project
DAC	Dynamic Atmosphere Correction
DFJ	December February January
DS	Degree of Storminess
DSSH	Dynamics Sea Surface Height
DTRC	Dry Troposphere Refraction Correction
DUACS	Data Unification and Altimeter Combination System
EC	Energy Content
ECMWF	European Centre for Medium-Range Weather Forecasts
ESA	European Space Agency
ESF	Extreme Scale Factor
ESL	Extreme Sea Level
EVA	Extreme Value Analysis
EVD	Extreme Value Distribution

EVT	Extreme Value Theory
EQM	Empirical Quantile Mapping
GC	Geoid Correction
GCM	General Circulation Model
GEVD	Generalized Extreme Value Distribution
GWP	Global wave projections
GHG	Greenhouse-Gas
IOD	Indian Ocean Dipole
IPCC	Intergovernamental Panel on Climate Change
IRC	Ionosphere Refraction Correction
JONSWAP	Joint North Sea Wave Project
JJA	June July August
LWC	Long Wave Correction
MAM	March April May
MM	Monthly Maxima
MSL	Mean Sea Level
MSLR	Mean Sea Level Rise
MSS	Mean Sea Surface
NA	North Atlantic
NAO	North Atlantic Oscillation
NH	Northern Hemisphere
NTR	Non-tidal residual
NOAA	National Oceanic and Atmospheric Administration
PDF	Probability Density Function
RCM	Regional Circulation Model
RCP	Representative Concentration Pathway
RMSE	Root-Mean Square Error
SAM	Southern Annular Mode
SH	Southern Hemisphere
SLA	Sea Level Anomaly
SON	September October November

SP	Spectral Partition
SPP	Spectral Partition Parameters
SSBC	Sea-State Bias Correction
SSH	Sea Surface Height
SST	Sea Surface Temperature
SWL	Still Water Level
TC	Tropical Cyclone
TCC	Tidal Component Correction
TG	Tide Gauge
TWL	Total Water Level
UHSLC	University of Hawaii Sea Level Data Center
WMO	World Meteorological Organization
WTRC	Wet Troposphere Refraction Correction
WW3	WaveWatchIII

List of symbols

C_{CE}	Exposure of a coastal location to the open ocean
C_S	Minimum width of the continental shelf at the coastal location [km]
C_{RE}	Exposure of a coastal region to the open ocean
C_L	Absolute value of the latitude [°]
C_W	Correlation between extreme NTR events and contemporaneous E_f values
c_g	Wave group celerity [m/s]
CV^{20}	Coefficient of variation of the 20-year return period NTR within the year
D	Storm mean duration [$hours$].
DAC	Dynamic atmosphere correction [m]
DS	Degree of storminess
$DSSH$	Dynamic sea surface height [m]
$DTRC$	Dry troposphere refraction correction [m]
E	Wave Energy [$W\,m/s^2$]
EC	Energy content [m^2h]
ED	H_s vs. T_m contribution to the E_f [%]
E_f	Wave energy flux [W/m]
EF_w	Effective energy flux [$W/m/^\circ$]
ESF	Extreme scale factor
g	Gravity acceleration [m/s^2]
GC	Geoid correction [m]
H_0	Null hypothesis
H_1	Alternative hypothesis
H_s	Significant wave height [m]

H_s95	95th percentile significant wave height $[m]$
H_s99	99th percentile significant wave height $[m]$
H_s^m	Annual mean significant wave height $[m]$
H_s^5	5-year return period significant wave height $[m]$
H_s^{20}	20-year return period significant wave height $[m]$
H_s^{50}	50-year return period significant wave height $[m]$
H_s^{100}	100-year return period significant wave height $[m]$
$H_s^{q0.5}$	Median significant wave height $[m]$
H_s^{max}	Maximum significant wave height $[m]$
H_t	Total sea surface height $[m]$
IRC	Ionosphere refraction correction $[m]$
IT_s	Inter-arrival time between wave storms $[days]$
IWP	Mean integrated wave parameter of wave storms.
LWC	Long wave correction $[m]$
m_0	Zeroth-order moment $[m^2 s/rad]$
m_0^s	Swell partition zeroth-order moment $[m^2 s/rad]$
m_0^{ws}	Wind-sea partition zeroth-order moment $[m^2 s/rad]$
MSS	Mean sea surface height $[m]$
N	Storm mean frequency of occurrence $[events/year]$
NTR	Non-tidal residual $[m]$
NTR^5	5-year return period non-tidal residual $[m]$
NTR^{10}	10-year return period non-tidal residual $[m]$
NTR^{20}	20-year return period non-tidal residual $[m]$
PDF_{sc}	PDF-based skill score
r	Pearson correlation coefficient
R_{obs}	Observed altimeter range $[m]$
R_{corr}	Corrected altimer range $[m]$
R_m	Monthly frequency ratio
$RMSE$	Root-mean squared error
R^2	Coefficient of determination
SLA	Sea level anomaly $[m]$

Spr_Θ	Directional spread [°]
SSH	Sea surface height [m]
$SSBC$	Sea-state bias correction [m]
TCC	Tidal component correction [m]
TD	Tidal dominance
TD^5	Tidal dominance for 5-year return period non-tidal residual
TD^{20}	Tidal dominance for 20-year return period non-tidal residual
T_m	Mean wave period [s]
T_{max}	Mean annual maximum tide [m]
T_p	Peak wave period [s]
WD_s	Swell dominance during wave storms [%]
WD_{ws}	Wind-sea dominance during wave storms [%]
$WTRC$	Wet troposphere refraction correction [m]
$\overline{z_R}$	Quantile associated to a R-year return period
Θ_m	Mean wave direction [°]
γ	JONSWAP peak-enhancement parameter
$\sigma_{a,b}$	Peak-width parameters in the Goda's defintion of the JONSWAP spectrum
α	Significance level
μ	Location parameter of the GEVD
σ	Scale parameter of the GEVD
ξ	Shape parameter of the GEVD
ρ	Water density
κ_{R_i}	Ratio between tide gauge and altimetry non-tidal residual quantiles associated to a return period R_i
$\overline{\kappa}$	Mean ratio between non-tidal residual return period estimates from tide gauge and altimetry
κ_{CE}	Coastal exposure constituent
κ_S	Continental shelf width constituent
κ_{RE}	Regional exposure constituent
κ_L	Latitudinal gradient constituent
κ_W	Wave climate constituent

Resumen en castellano

De acuerdo con la normativa de estudios de doctorado de la Universidad de Cantabria en relación a los requerimientos exigidos para aquellas tesis redactadas en un idioma diferente al castellano, a continuación se presenta un resumen del documento original redactado en inglés. Dicho resumen condensa los principales resultados del presente trabajo de investigación y una discusión de los mismos, las conclusiones alcanzadas, así como los posibles desarrollos futuros derivados de los estudios realizados. Dado que el resumen no constituye una traducción literal del documento completo, para una información más detallada, se remite al lector a la versión extendida en inglés.

Introduction

Antecedentes y motivación

La superficie del mar toma a cada instante una forma distinta, moldeada por las dinámicas que coexisten en ella, como el oleaje, el nivel del mar y las corrientes. Entre todas ellas, el oleaje es, sin duda, el que otorga una forma más característica a la superficie. La dirección y la altura de las olas que se propagan, las distancias entre los frentes y, en definitiva, la combinación de todos estos elementos, crean una infinidad de patrones de la superficie del mar. Las olas se generan por el viento que sopla sobre la superficie oceánica. Tras su generación, éstas se propagan, clasificándose en grupos de características similares, pudiendo recorrer miles de kilómetros hasta alcanzar la costa.

El oleaje no se propaga sobre un nivel de mar constante, sino que éste también varía a lo largo del tiempo. El nivel del mar está, en parte, modulado por forzamientos astronómicos. La marea astronómica se genera por la atracción gravitatoria de la luna y el sol sobre masas de agua en la corteza terrestre. La contribución de la componente mareal varía según los océanos, así como su variabilidad. Otras componentes del nivel del mar son generadas por forzamientos atmosféricos. Los gradientes de presión atmosférica inducen cambios en el nivel del mar según el efecto barómetro inverso. Además, el viento sostenido soplando hacia la costa puede inducir variaciones del nivel del mar en la zona costera. La sobreelevación del oleaje por rotura (setup) es también una componente importante del nivel del mar. Así mismo, las corrientes marinas pueden generar alteraciones del nivel, aunque a menor escala que las componentes anteriormente descritas.

Los eventos extremos de las dinámicas superficiales marinas pueden causar impactos significativos tanto en mar abierto como en la zona costera. Las alturas de ola extremas pueden alterar las rutas marítimas y causar graves daños a infraestructuras en alta mar, como plataformas de gas o turbinas eólicas. En la zona costera, las alturas de ola extremas pueden alterar el equilibrio medio a lo largo de la línea de costa, induciendo importantes eventos de erosión del litoral. Las variaciones extremas del nivel del mar no sólo son más evidentes, sino también potencialmente más dañinas cerca de la costa. Los niveles del mar extremos pueden inducir episodios de inundación, especialmente en zonas someras. Además, la combinación de ambas dinámicas, sobre todo en condiciones de tormenta, puede acarrear consecuencias catastróficas.

Por todo ello, es importante caracterizar los eventos extremos de las dinámicas superficiales marinas. El estudio de los eventos extremos del nivel del mar se ha abordado tradicionalmente a través de la información que ofrecen los mareógrafos. La modelización numérica es la alternativa más precisa en la actualidad, aunque sigue estando limitada por la demanda computacional de los modelos numéricos. La altimetría satelital ofrece información global de nivel del mar desde los años 90, por lo que también supone una alternativa potencial a los datos numéricos e instrumentales in situ. A pesar de los puntos débiles de esta fuente de información, el periodo de tiempo cubierto de aproximadamente 30 años, desde 1992 hasta 2022, y la continua mejora de su precisión, especialmente en la zona costera, la hacen atractiva para ser utilizada en aplicaciones tradicionalmente desarrolladas con otro tipo de datos. Sin embargo, *¿pueden los datos altimétricos ser una fuente de información fiable para analizar los extremos del nivel del mar?*

En lo que respecta a los extremos de oleaje, su caracterización ha sido objeto de estudio durante mucho tiempo con el fin de evaluar correctamente sus impactos. Estos estudios se desarrollan normalmente a partir de hindcasts o reanálisis de oleaje. A diferencia del nivel del mar, los productos numéricos de oleaje han superado claramente el uso de datos instrumentales in situ (principalmente boyas). Así mismo, el uso de datos altimétricos para estudiar el clima de las olas es también una práctica común, sobre todo en aguas profundas y para caracterizar las condiciones medias del oleaje. En cuanto a los extremos de las olas, a pesar de que algunos estudios ya han estimado las alturas de ola asociadas a periodos de retorno utilizando estos datos, el aumento de la incertidumbre para alturas de ola extremas sigue frenando hoy en día su uso para este fin. Las condiciones extremas de oleaje se caracterizan de forma diferente según su aplicación posterior. El diseño de estructuras en alta mar (por ejemplo, turbinas eólicas flotantes, plataformas de gravedad) o de estructuras de protección de la costa (por ejemplo, diques rompeolas), requiere el conocimiento de las olas más extremas que llegan a una localización determinada. Para ello, se estiman las características de las olas con muy baja probabilidad de ocurrencia, es decir, eventos con altos periodos de retorno. Por otro lado, la evaluación de los impactos costeros, como la erosión costera y el retroceso de la línea de costa, se basan en el concepto de temporales costeros, en los cuales las olas juegan un papel importante. Los temporales de oleaje pueden definirse como eventos en los que la altura de ola excede significativamente las condiciones medias en la costa, pudiendo alterar el equilibrio a lo largo de la misma. El análisis de los temporales de oleaje costeros se ha abordado en base a diferentes criterios, aunque siempre a escalas locales o regionales. Pero, *¿es posible evaluar tormentosidad del oleaje a lo largo de la costa mundial en base a un único criterio?*

Más allá de la caracterización de las magnitudes de las dinámicas superficiales marinas, un entendimiento completo de su comportamiento requiere también el conocimiento de su variabilidad en diferentes escalas de tiempo. Estudios previos han demostrado que las características tanto del nivel del mar como del oleaje varían a lo largo del año. Además, también varían entre años, es decir, las magnitudes experimentan una variabilidad interanual. Especialmente interesantes son las tendencias a largo plazo, en particular aquellas atribuibles al efecto del cambio climático. El cambio climático está afectando al nivel del mar al inducir un aumento del nivel medio. Estos cambios son críticos en las zonas poco profundas, donde pequeños cambios en el nivel medio pueden originar graves impactos en la costa, a través de episodios de inundación más frecuentes y fuertes, y generando el retroceso de las líneas de costa. Además, se ha demostrado que el aumento del nivel medio del mar es el principal causante de la intensificación de los extremos de nivel del mar. Sin embargo, mientras que la variabilidad de los extremos del oleaje ha sido evaluada globalmente, concretamente en base a datos de altimetría, no se puede encontrar una referencia similar para el nivel del mar hasta la fecha. Por tanto, *¿sería posible evaluar la variabilidad global de los extremos de nivel del mar a partir de datos altimétricos como se ha hecho con el oleaje?*

El comportamiento futuro del clima del oleaje ha sido ampliamente estudiado durante las dos últimas décadas. Estos estudios se llevan a cabo principalmente a través de proyecciones climáticas de oleaje desarrollas a partir de modelos numéricos o métodos estadísticos alimentados con forzamientos atmosféricos producidos por modelos de circulación general o regional. Esto ha permitido alcanzar un consenso sobre los cambios esperados a largo plazo en las condiciones medias del oleaje en algunas regiones oceánicas, como un descenso en el Atlántico Norte, un aumento en el Océano Austral y un aumento en el Pacífico Sureste tropical. La incertidumbre aumenta al evaluar los cambios en las condiciones extremas del oleaje, existiendo un número muy escaso de estudios sobre este tema, la mayoría de ellos sólo proporcionando cambios relativos. Por lo tanto, todavía surgen algunas preguntas a este respecto, *¿cuáles son las magnitudes de cambio proyectadas en los extremos del oleaje con* *alto periodo de retorno? ¿Son las variaciones a largo plazo inducidas por el cambio climático en las condiciones medias del oleaje consistentes con las propias de las condiciones extremas?.*

A pesar de que la información completa sobre el oleaje sólo se representa a través del espectro de energía, la mayoría de los estudios sobre este tema se han llevado a cabo en base a parámetros integrados del estado de mar. El parámetro más comúnmente utilizado para representar las condiciones climáticas del oleaje y, consecuentemente, para evaluar el efecto del cambio climático sobre ellas, es la altura de ola significante (H_s). Sólo unos pocos estudios han ido más allá del enfoque estándar y han intentado considerar la coexistencia de olas con diferentes orígenes dentro de un estado del mar, explicando el comportamiento futuro del oleaje mediante la evaluación de los cambios en los sistemas de oleaje individuales, aunque siempre basándose en parámetros integrados y no en información espectral. En este contexto, surgen inevitablemente las siguientes preguntas *¿Están los parámetros integrados del estado de mar enmascarando información relevante sobre los futuros cambios en el clima del oleaje? ¿Es posible profundizar en el efecto del cambio climático sobre el clima del oleaje utilizando el espectro de energía?*

Objetivos

La presente tesis se enmarca en el contexto anteriormente descrito. Los principales objetivos se describen a continuación:

- Desarrollar nuevas metodologías y productos climáticos para mejorar la caracterización de los eventos extremos de las dinámicas superficiales marinas.
- Mejorar la comprensión de la variabilidad global de los fenómenos extremos de las dinámicas superficiales marinas en diferentes escalas de tiempo.
- Mejorar la comprensión de la variabilidad a largo plazo del oleaje por efecto del cambio climático a través del espectro frecuencia-dirección.

A continuación se resumen los objetivos específicos de esta tesis, que tratan de dar respuesta a todas las preguntas *plateadas* en la motivación:

1. Explorar el uso de datos de altimetría satelital para caracterizar eventos extremos costeros de nivel del mar.
2. Analizar las principales características de los temporales de oleaje que impactan en la costa mundial en base a un criterio único.
3. Clasificar la costa mundial en función de su tormentosidad de oleaje.

4. Evaluar la variabilidad de los extremos del nivel del mar a lo largo de la costa mundial en diferentes escalas de tiempo a partir de datos de altimetría satelital.
5. Evaluar la variabilidad a largo plazo de los eventos extremos de oleaje con muy baja probabilidad de ocurrencia a escala global bajo diferentes escenarios de concentración de gases de efecto invernadero.
6. Comparar el comportamiento futuro de las condiciones medias y extremas del oleaje por efecto del cambio climático.
7. Explorar el valor añadido de los espectros frecuencia-dirección para evaluar los cambios proyectados en el clima del oleaje debidos al cambio climático con respecto al uso estándar de los parámetros integrados del estado de mar, destacando la información que estos últimas podrían esconder.
8. Evaluar los cambios proyectados en el clima del oleaje a partir de los espectros frecuencia-dirección a escala global.
9. Evaluar el cambio proyectado en los principales sistemas de oleaje que se propagan por los océanos.

Estructura del documento

Esta tesis está estructurada en base a los objetivos descritos anteriormente. El marco de la investigación gira en torno a los tres elementos y sus interrelaciones representados en la Fig. 1. El nivel del mar y el oleaje son las principales variables que intervienen en los análisis realizados y constituyen el primer elemento central de análisis. Como se mencionó anteriormente, estas variables, solas y combinadas, juegan un papel clave en los impactos marinos tanto en mar abierto, como en la zona costera. Estos impactos son causados principalmente por eventos extremos, por lo que el análisis extremal del nivel del mar y del oleaje es el segundo elemento central de análisis. Por último, el tercer elemento central de análisis es la evaluación de la variabilidad de estas dinámicas y, especialmente, de sus extremos, con especial interés en la variabilidad a largo plazo inducida por el cambio climático.

Las interrelaciones entre los elementos centrales de análisis (Fig. 1) llevan a estructurar el documento en tres partes. Cada una de estas partes se divide internamente en dos capítulos.

La parte 1 caracteriza los eventos extremos costeros de las dos dinámicas superficiales marinas analizadas en esta tesis: el nivel del mar y el oleaje. En el capítulo 2 se propone una metodología novedosa basada en datos de altimetría satelital para estudiar los extremos costeros de nivel del mar. En el capítulo 3 se evalúa la tormentosidad de oleaje a lo largo de la costa mundial.

La parte 2 aborda la variabilidad de los eventos extremos de las dinámicas superficiales marinas. El capítulo 4 evalúa la variabilidad de los eventos extremos del nivel del mar en diferentes escalas de tiempo a lo largo de la costa mundial a partir de datos de altimetría. El capítulo 5 evalúa la variabilidad a largo plazo de los extremos de oleaje debido al efecto del cambio climático a escala global. Además, evalúa la diferencia en el comportamiento futuro de las condiciones de oleaje extremo con respecto al proyectado para las condiciones medias.

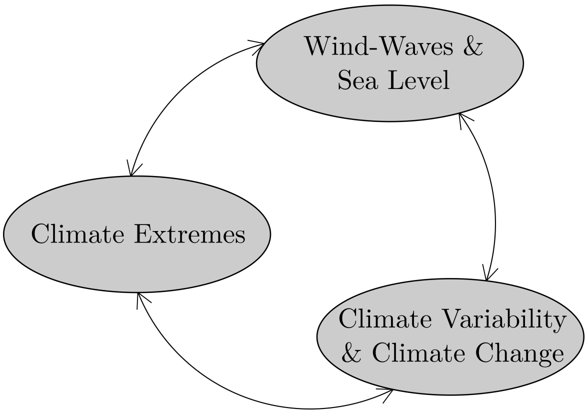

Fig. 1 Esquema general de la tesis.

En la parte 3 se evalúa el futuro clima del oleaje mediante un enfoque novedoso basado en espectros frecuencia-dirección. El capítulo 6 evalúa el valor añadido de los espectros de oleaje para estudiar el efecto del cambio climático en el clima del oleaje con respecto al uso estándar de parámetros integrados del estado de mar. El capítulo 7 evalúa los cambios globales en el clima del oleaje basándose en los espectros frecuencia-dirección.

Para finalizar, el capítulo 8 resume las principales conclusiones a las que se ha llegado a lo largo de esta tesis y recoge las futuras líneas de investigación a las que podría dar lugar esta tesis.

Análisis de eventos extremos de nivel del mar a partir de datos de altimetría satelital

Introducción

La altimetría satelital proporciona información global de nivel del mar desde la década de los 90. Su cobertura global y la cantidad de datos disponibles, aproximadamente 30 años, hacen de la altimetría satelital una alternativa potencial a los datos de mareógrafo y de modelización numérica para desarrollar estudios climáticos. En primer lugar, para el océano profundo, donde esta fuente global de información ha sido ampliamente utilizada durante décadas como proveedor de datos del nivel medio del mar, permitiendo la estimación de tendencias. En segundo lugar, para las zonas costeras, donde las mediciones altimétricas pueden complementar la información proporcionada por los mareógrafos o incluso sustituirla cuando no se dispone de ella. A pesar de que todavía hay margen de mejora, estudios previos ya han encontrado una buena concordancia entre los datos in situ y los remotos en la costa del Reino Unido, lo que ofrece perspectivas optimistas con respecto al uso de los datos altimétricos a lo largo de la costa. Además, la Iniciativa sobre el Cambio Climático creada por la Agencia Espacial Europea en 2010, ha fomentado la mejora de las correcciones altimétricas para maximizar la precisión de estos datos.

A pesar de todas estas mejoras, la información altimétrica aún no se ha utilizado para analizar los extremos de nivel del mar costeros. Aquí presentamos un método novedoso para analizar las condiciones extremas de la componente del nivel del mar no causada por forzamientos astronómicos (residuo meteorológico) a lo largo de la costa con datos altimétricos, basado en la aplicación de un modelo estadístico de extremos no estacionario a partir de los máximos mensuales y considerando también la morfología costera local. El estudio se ha abordado en dos etapas. En primer lugar, se define y valida la metodología a lo largo de la costa este de América del Norte. A continuación, el análisis se extiende a escala global.

Datos climáticos

En este trabajo se han utilizado datos de altimetría satelital de nivel del mar proporcionados por el Servicio de Vigilancia del Medio Marino de Copernicus (CMEMS). La primera etapa de este trabajo desarrollada a lo largo de la costa este de América del Norte utiliza el producto de altimetría *SEALEVEL-GLO-PHY-L3-REP-OBSERVATIONS-008-045* para el periodo 1992-2015. El estudio global utiliza una versión actualizada de este último producto, *SEALEVEL-GLO-PHY-L3-REP-OBSERVATIONS-008-062*, que cubre el periodo 1992-2018. Estos productos han sido procesados mediante el sistema de procesamiento de datos altimétricos multimisión DUACS, que integra las mediciones de varias misiones de satélite que operan desde 1992 en adelante para proporcionar una base de datos global intercalibrada de la anomalía del nivel del mar (SLA, del inglés Sea Level Anomaly). SLA representa las variaciones del nivel del mar con respecto al nivel medio producidas por procesos oceánicos.

Como se ha explicado anteriormente, este trabajo evalúa especialmente el comportamiento extremo del residuo meteorológico del nivel del mar (NTR, del inglés non-tidal residual). Por lo tanto, es necesario construir una base de datos de NTR a partir de datos de altimetría (NTR_{SAT}). NTR_{SAT} se calcula deshaciendo la corrección de la atmósfera dinámica aplicada sobre la medición del altímetro (DAC, del inglés Dynamic Atmosphere Correction). Para ello, añadimos el mismo producto DAC aplicado para procesar el producto SLA proporcionado por CMEMS. La corrección DAC integra dos componentes: la respuesta oceánica de baja frecuencia al forzamiento de la presión atmosférica (periodos superiores a 20 días), calculada mediante el barómetro inverso clásico, y la respuesta oceánica de alta frecuencia a los forzamientos meteorológicos de presión y viento (periodos inferiores a 20 días), obtenida a partir del modelo numérico barotrópico MOG2D.

Este estudio hace uso de de 22 registros de mareógrafo a lo largo de la costa este de América del Norte (Fig. 2) gestionados y distribuidos por la NOAA (National Oceanic and Atmospheric Administration). La componente NTR de mareógrafo (NTR_{TG}) se calcula restando la marea astronómica (análisis armónico de la NOAA) del registro bruto de nivel del mar. El criterio para seleccionar los 22 mareógrafos en la región de estudio se basa en la existencia de un proceso de control de calidad, la cobertura temporal (concordancia con el periodo de tiempo en que se dispone de información altimétrica) y la disponibilidad de series temporales continuas.

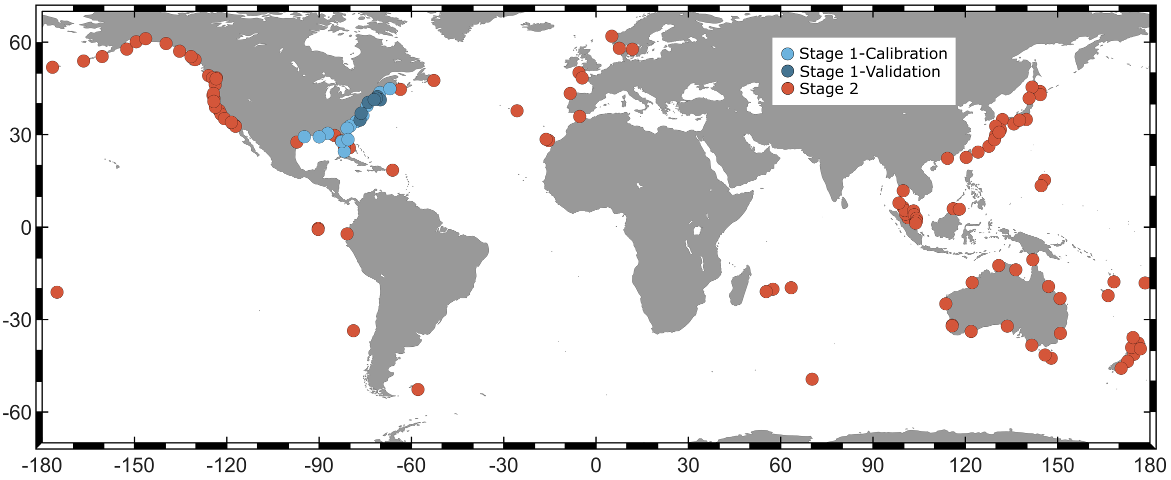

Fig. 2 Ubicación de los mareógrafos utilizados para realizar el análisis. Los círculos azul claro representan las estaciones utilizadas para calibrar la metodología a lo largo de la costa este de América del Norte. Ídem para los círculos azul oscuro pero para la validación de la metodología. Los círculos rojos representan las estaciones utilizadas en el estudio a escala global.

El estudio global utiliza un total de 400 registros de mareógrafo distribuidos a lo largo de la costa mundial. Estos registros se han descargado del portal de datos de UHSLC (University of Hawaii Sea Level Data Center). Se dispone de valores horarios de nivel del mar en cada mareógrafo. De este número inicial de registros, se rechazan 150 en base a dos criterios. Primero, se rechazan los registros con menos del 75% de datos horarios dentro del periodo de análisis (es decir, 1992-2018). Segundo, no se consideran las estaciones instaladas en lugares complejos ya que se espera que estén muy afectados por los procesos locales. A continuación, se aplica a las estaciones seleccionadas un control de calidad que consiste en buscar valores atípicos, cambios en el nivel de referencia y valores extraños.

Posteriormente, se aplica un análisis de descomposición armónica para la extracción de la marea astronómica utilizando la herramienta de análisis de mareas U-tide. Los años con menos del 60% de datos horarios no se consideran en el análisis. Tras el análisis, se calcula el registro de NTR_{TG} como se indicó anteriormente para la primera fase del estudio y se re-evalúa el número de datos disponibles, dejando un total de 170 mareógrafos.

Métodos

Muestra extremal costera

NTR_{SAT} se caracteriza por una discretización espacial y temporal heterogénea. Por lo tanto, se requiere un método para seleccionar una muestra de datos altimétricos que pueda ser comparada con cada registro de mareógrafo. El método plateado para tal fin se basa en la correlación existente entre NTR_{TG} y NTR_{SAT} en las proximidades de la estación in situ.

El primer paso consiste en seleccionar pares utilizando cada medición NTR_{SAT} y el valor NTR_{TG} más cercano en el tiempo. A continuación, se define para cada mareógrafo un área circundante delimitada por un círculo de 7,5° de radio cuyo centro se encuentra en la ubicación de la estación. Esta zona circular se cuadricula con una malla regular de 0,25°. En cada nodo de la malla calculamos el coeficiente de correlación de Pierson entre todos los pares NTR_{TG}-NTR_{SAT} dentro de un círculo de 0,25° de radio con centro en el nodo. La muestra de altimetría que se va a comparar con los datos in situ se compone de todas las mediciones cuyos nodos tienen correlaciones superiores a un determinado límite. Mientras que para el análisis a lo largo de la costa este de América del Norte establecimos un límite de correlación fijo de 0,5, para el estudio global se mejoró el método para seleccionar dicho valor. Así, el límite evoluciona hasta tener una muestra de NTR_{SAT} de aproximadamente una medición/día después de realizar un remuestreo horario en cada iteración.

Tras seleccionar la muestra de NTR_{SAT} para cada estación, evaluamos de nuevo la calidad y el número de datos de altimetría y mareógrafo disponibles. Finalmente, se consideran un total de 22 estaciones para el estudio a lo largo de la costa este de América del Norte y 123 para el estudio a lo largo de la costa global (Fig. 2).

Modelo estadístico de extremos

En este estudio se utiliza un modelo estadístico de extremos GEVD (Generalized Extreme Value Distribution). El modelo GEVD utiliza normalmente valores máximos anuales para ajustar los parámetros de la distribución y estimar los cuantiles asociados a periodos de retorno elevados (por ejemplo, periodos de retorno de 20, 50 y 100 años). Dado que la información altimétrica sólo está disponible a partir de los años 90, se seleccionan valores mensuales como input del modelo para aumentar el tamaño de la muestra de máximos. La variabilidad de los máximos mensuales se modela a través del parámetro de localización. La estacionalidad se introduce a través de tres funciones sinusoidales que modelan uno, dos y cuatro ciclos completos por año, respectivamente. Además, las tendencias a largo plazo se modelan mediante una función exponencial.

Estimación de periodos de retorno

Tras el análisis extremal en todos los mareógrafos, comparamos los valores para diferentes periodos de retorno (valores de retorno) a partir de NTR_{TG} y NTR_{SAT}. Las diferencias encontradas pueden estar relacionadas con las características morfológicas, geográficas y climáticas del lugar de estudio. Por lo tanto, para tener en cuenta estas diferencias y corregir las estimaciones extremas de NTR_{SAT}, se define un factor de corrección denominado Factor de Escala Extremal (ESF, del inglés extreme scale factor).

El ESF se calcula como una combinación ponderada de varios componentes, cada uno de los cuales representa una posible fuente de discrepancias entre los extremos de mareógrafo y de altimetría. La exploración de estos componentes se ha actualizado entre las dos etapas de este estudio, por lo que en cada una de ellas se propone una definición diferente de ESF.

Resultados

Costa este de América del Norte

Después de realizar el análisis extremal en los 14 mareógrafos utilizadas para la calibración, dos componentes resultan significativos en la definición de ESF:

- Componente de exposición costera: Tiene en cuenta la exposición de un lugar específico al océano abierto. Trata de reflejar, en primer lugar, el hecho de que más cerca de la costa se dispone de un menor número de mediciones altimétricas, especialmente en costas escarpadas y estuarios protegidos. En segundo lugar, la amplificación que experimenta la onda larga a medida que se acerca al mareógrafo, en particular en aquellos lugares en los que el camino desde el océano abierto hasta la estación de medida es poco profundo, estrecho y sinuoso debido a la morfología local.
- Componente de anchura de la plataforma continental: Representa la pérdida de precisión de la altimetría de radar en la plataforma y los cambios en la onda larga a medida que se reduce la profundidad.

Se calcula la contribución de cada componente, resultando una mayor contribución de la exposición costera con respecto a la anchura de la plataforma (65% frente a 35%).

La validación de la metodología se lleva a cabo con la información proporcionada por 8 registros de mareógrafo no utilizados previamente en la definición de ESF y situados igualmente a lo largo de la costa este de América del Norte. El ESF se calcula para todos los lugares de validación. La corrección permite reducir significativamente las diferencias entre valores de retorno estimados a partir de datos de mareógrafo y altimetría (Fig. 3). Antes de la corrección, el error relativo medio es 43%, mientras que después de la corrección el error relativo medio es 2%.

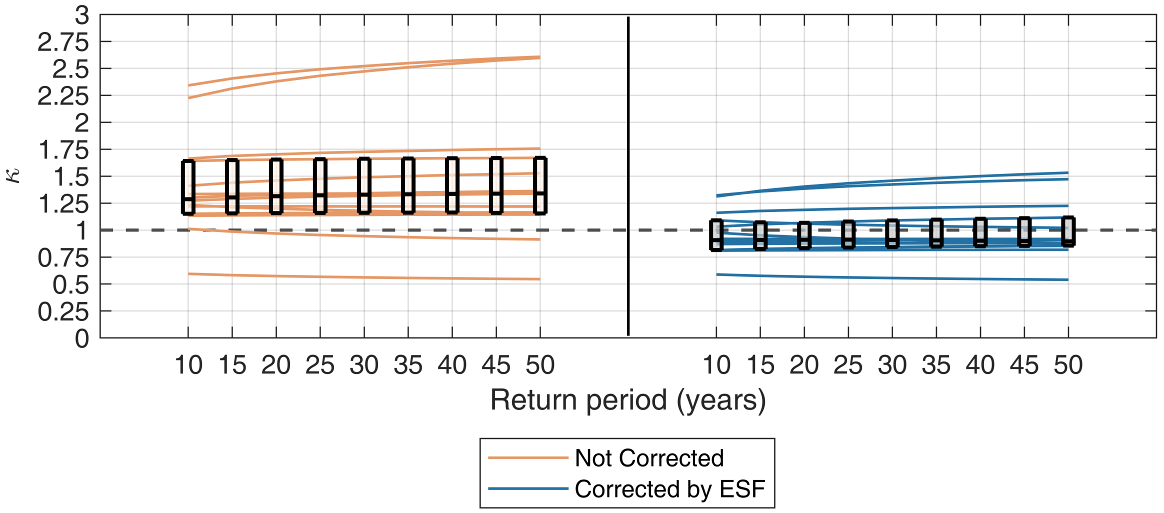

Fig. 3 Ratio entre los valores de NTR con periodos de retorno de 10 a 50 años obtenidos a partir de datos de mareógrafo y de altimetría para los ocho registros utilizados para validación en la costa este de América del Norte. Las líneas naranjas representan las ratios antes de corregir con ESF. Las líneas azules representan las ratios después de corregir con ESF. Las cajas representan los cuantiles de 0,25, 0,50 y 0,75 de las ratios para cada periodo de retorno analizado.

Costa global

El elevado número de mareógrafos disponibles permite una parametrización más precisa del ESF. Para ello, las estaciones se agrupan geográficamente en seis submuestras, lo que da lugar a seis definiciones diferentes de ESF. En primer lugar, los mareógrafos se dividen entre los situados en las costas continentales y las insulares. A continuación, las estaciones se agrupan por cuencas oceánicas: Atlántico, Pacífico e Índico. No se dispone de datos suficientes para realizar un ajuste robusto para las costas insulares del Océano Índico, por lo que no se propone ninguna corrección para ellas. Tras analizar varias posibles fuentes de discrepancias, cuatro componentes resultan significativos para definir el ESF.

- Componente de exposición regional: Refleja la exposición de una región específica al océano abierto. Pretende representar la diferencia entre los eventos registrados por los mareógrafos y los altímetros en función de la ubicación costera desde una perspectiva regional, es decir, si dicha ubicación pertenece a una isla abierta al océano, al margen continental, a una isla cercana a tierra firme, etc.
- Componente de anchura de la plataforma continental.

- Componente del gradiente latitudinal: El hecho de que los ciclones tropicales no sean captados en su totalidad en la muestra extremal de altimetría es probablemente la causa principal de estas diferencias meridionales.
- Componente del clima del oleaje: Representa el efecto del clima del oleaje en las diferencias encontradas entre los eventos extremos medidos por los altímetros y los mareógrafos. Refleja la contribución de las olas en los eventos extremos registrados en los mareógrafos.

Se propone una combinación ponderada de los componentes para calcular el ESF de cada grupo de mareógrafos, tal y como se mostró anteriormente para la costa este de América del Norte. En la Tabla 1 se resumen las ponderaciones obtenidas para cada componente.

Table 1 Peso de componente de ESF para los distintos grupos de mareógrafos

	Mainland margins				**Ocean islands**			
Basin	Regional Exposure	Shelf width	Latitude	Wave climate	Regional Exposure	Shelf width	Latitude	Wave climate
Pacific	-	-	33%	67%	-	-	86%	14%
Atlantic	-	33%	67%	-	39%	20%	-	41%
Indian	32%	-	64%	4%	Not enough data			

La corrección con ESF da lugar a una reducción del error medio y de su desviación (Fig. 4). El error relativo medio se reduce de un 18% antes de la corrección, a un 1% tras corregir.

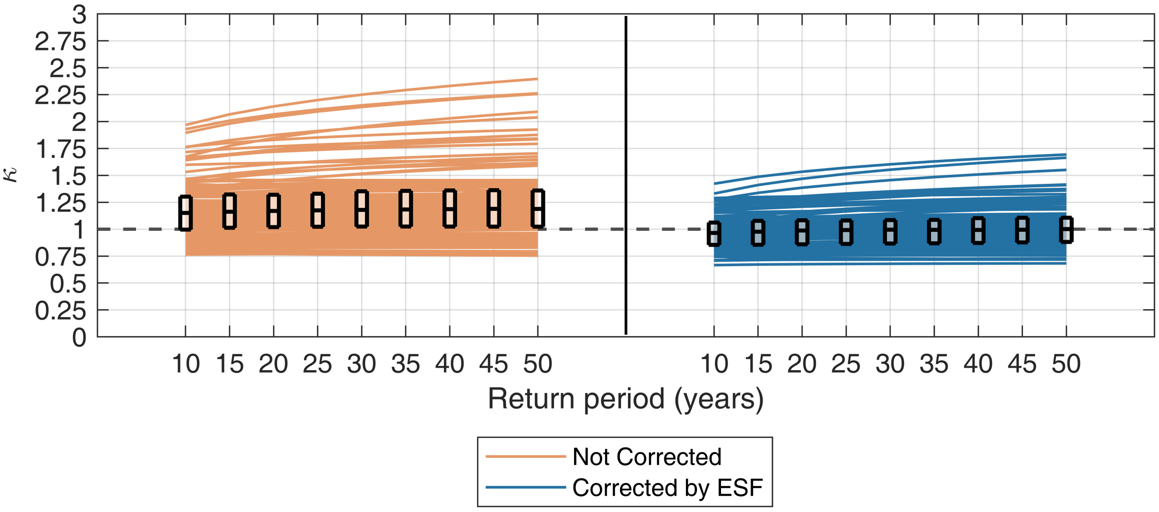

Fig. 4 Ratio entre los valores de NTR con periodos de retorno de 10 a 50 años obtenidos a partir de datos de mareógrafo y de altimetría para todos los registros utilizados en el estudio global. Las líneas naranjas representan las ratios antes de corregir con ESF. Las líneas azules representan las ratios después de corregir con ESF. Las cajas representan los cuantiles de 0,25, 0,50 y 0,75 de las ratios para cada periodo de retorno analizado.

Conclusiones

Este estudio representa el primer intento de caracterizar el comportamiento de los eventos extremos de nivel del mar en la costa a partir de datos de altimetría satelital. Se presenta un enfoque novedoso basado en la aplicación de un modelo de extremos no estacionario a partir de máximos mensuales de residuo meteorológico. La metodología se calibra y valida utilizando datos de mareógrafos. Los extremos procedentes de altimetría muestran una subestimación generalizada con respecto a los de las observaciones in situ. Para contrarrestar estas diferencias, se define un factor de corrección para los datos altimétricos llamado factor de escala extremal. El factor de escala extremal depende de las características geográficas y físicas del lugar de análisis. Su aplicación permite mejorar significativamente la precisión de las estimaciones del valor de retorno de la altimetría, reduciendo el error relativo medio en más de 50%. El estudio se aborda primero a lo largo de la costa este de América del Norte y luego se extiende a escala mundial.

Este trabajo demuestra la capacidad de los datos altimétricos para captar los extremos de nivel del mar en la costa. Por lo tanto, la altimetría por satélite podría ser considerada como una fuente de información válida sobre estos eventos, especialmente cuando no existe un proveedor de observaciones in situ como mareógrafos. Este hecho puede tener un gran impacto para una amplia gama de aplicaciones costeras. No obstante, a pesar de los prometedores resultados, las estimaciones extremas a partir de datos altimétricos deben interpretarse con cautela cuando los procesos muy locales controlados por interacciones no lineales son importantes. Por ello, se recomienda captar estos procesos con medios más precisos, como el modelado numérico. No obstante, los resultados presentados aquí pueden aportar una buena aproximación del régimen extremal de residuo meteorológico en la costa.

Tormentosidad del oleaje a escala global

Introducción

Los temporales de oleaje costeros son eventos en los que la energía de las olas supera claramente los valores climatológicos medios. Estos eventos desempeñan un papel fundamental en los impactos costeros. En este sentido, el setup de las olas, combinado con la marea meteorológica y la marea astronómica, puede aumentar significativamente la cota de inundación en la costa. Además, los temporales de oleaje se consideran un importante factor de erosión costera.

Los temporales de oleaje se estudian tradicionalmente a través de series temporales de H_s. El enfoque estándar se basa en las excedencias de un determinado umbral de H_s, de modo que los eventos individuales que lo superan se clasifican como temporales. El umbral de temporal se ha definido según diferentes criterios, tales como el impacto en la costa, la concordancia con la distribución Generalizada de Pareto o, más recientemente, mediante métodos estadísticos más complejos que analizan la distribución conjunta de las variables que intervienen en la definición del temporal. Sin embargo, todos estos criterios comparten la limitación de estar restringidos a un ámbito regional. Una opción más pragmática y adecuada para estudios a mayor escala consiste en definir el umbral en base a estadísticos H_s. El uso del percentil 95% de H_s o la suma de la media de H_s y dos desviaciones estándar de H_s son ejemplos de enfoques flexibles que se adaptan al clima local.

Todos los estudios mencionados anteriormente han evaluado las condiciones de los temporales de oleaje a escala local o, a lo sumo, regional. Algunos de ellos han dado lugar a estudios climáticos en los que se clasifican los eventos o se analizan las tendencias en la intensidad de los temporales de oleaje y la frecuencia de ocurrencia. Sin embargo, el propósito más común de los estudios de temporales de oleaje disponibles en la literatura es la evaluación de impactos costeros.

En este contexto, el presente estudio tiene como objetivo principal proporcionar una evaluación cuantitativa y cualitativa global de los temporales de oleaje costeros utilizando un hindcast de alta resolución.

Datos climáticos

El presente estudio utiliza un hindcast global de oleaje de alta resolución desarrollado por el Centro Europeo de Previsiones Meteorológicas a Medio Plazo (ECMWF), que cubre el periodo comprendido entre 1979 y 2020.

ERA-5 es el último reanálisis del ECMWF. Tiene una resolución horizontal de 40 km (0,36°) y una resolución temporal de 1 hora. Junto con el reanálisis ERA-5, se ha generado un hindcast de oleaje de alta resolución (resolución horizontal de 0,2 y salida horaria) forzado con los vientos superficiales y la cobertura de hielo marino de ERA-5: el ERA-5H.

El presente estudio utiliza campos de oleaje horarios de los parámetros H_s, T_m y Θ_m del ERA-5H a lo largo de la costa global. Además, se ha realizado un análisis detallado en doce ubicaciones específicas distribuidas a lo largo de la costa mundial.

Métodos

Definición de temporal de oleaje

El criterio de selección de los temporales de oleaje costeros se basa en las superaciones de un umbral de la serie temporal de H_s. En aras de la coherencia en la interpretación de los resultados, se ha definido un único umbral global. El umbral por encima del cual un evento se clasifica como temporal de oleaje es el percentil 95% de H_s. La clasificación de los temporales de oleaje requiere dos criterios adicionales además del propio umbral de H_s: el periodo de calma entre temporales consecutivos y la duración mínima de los eventos para ser clasificados como temporales. Dos temporales de oleaje se clasifican de forma independiente cuando el tiempo entre dos picos de eventos consecutivos H_s sobre el umbral es superior a 48 horas. En lo que respecta a la duración, ésta debe ser como mínimo de 12 horas.

Además, en el estudio se analiza individualmente una submuestra de temporales de oleaje denominados temporales de oleaje severos. El percentil 99% de H_s es el umbral a partir del cual un evento de H_s se clasificará como temporal de oleaje severo. Por lo tanto, un temporal de oleaje severo se produce cuando el tiempo de superación del percentil 95% de H_s es superior a 12 horas y, además, supera el percentil 99% de H_s durante 6 horas o más.

Evaluación de las características principales de los temporales

Se calculan varios estadísticos e índices para ofrecer un análisis completo y detallado de las características de los temporales de oleaje que llegan a las costas de todo el mundo. Se analizan cuestiones como: la frecuencia de ocurrencia, la duración, la intensidad, los parámetros integrados medios del estado de mar durante los temporales o la dominancia entre mares de viento o de fondo durante los eventos.

Resultados

La H_s media anual a lo largo de la costa mundial muestra, en general, un gradiente meridional. Los valores más altos se observan en las latitudes medias, sobre todo en latitudes superiores a 35° en ambos hemisferios. Además, se observan diferencias significativas entre las costas orientales y occidentales de los continentes, siendo estas últimas las que alcanzan mayores valores de H_s media anual. Los valores más bajos de la H_s media anual se encuentran a lo largo de las costas ecuatoriales y, como es lógico, en las cuencas semicerradas y en los mares marginales. Además, existe un predominio del mar de fondo a lo largo de la costa mundial, de forma que una gran parte de ella (aprox. el 50%) muestra una dominancia del mar de fondo frente al mar de viento por encima del 70%.

El número medio anual de temporales de oleaje y de temporales severos de oleaje muestra una heterogeneidad notable a lo largo de la costa mundial, observándose diferencias de más de 10 eventos de temporal y 5 eventos de temporal severo por año entre costas de diferentes regiones. Las costas extratropicales muestran, en general, un número anual de eventos superior al de latitudes más bajas. El patrón global del número medio anual de temporales severos es similar al de los eventos de tormentas normales, aunque mostrando, como era de esperar, frecuencias más bajas. Además, los resultados muestran que la frecuencia de ocurrencia de los temporales de oleaje es altamente estacional, es decir, existe una fuerte variabilidad en el número de temporales dentro del año en casi todas las costas globales. Prácticamente todos los temporales en las latitudes extratropicales del hemisferio norte se producen durante el invierno boreal. En cambio, las costas en la región extratropical del hemisferio sur pueden sufrir el impacto de 1 o 2 tormentas en algunas zonas durante su verano. La estacionalidad se acentúa en las costas intertropicales y subtropicales afectadas por los temporales de oleaje que se propagan desde las zonas extratropicales.

La mayoría de las costas (casi cuatro quintas partes) experimentan una sola estación de temporales, es decir, los temporales de oleaje se producen mayoritariamente en un único periodo continuo. Algunas localidades costeras tienen más de una estación de temporales, principalmente en latitudes intertropicales y subtropicales. Además, hay costas en las que, a pesar de existir cierta estacionalidad (débil), el número de temporales se mantiene bastante estable durante todo el año. El tiempo medio entre temporales durante las estaciones de temporales varía de menos de 10 días a más de 25, dependiendo del número de eventos y de la duración de la estación.

El patrón espacial de la duración media de los temporales es, en términos generales, opuesto al número medio de eventos por año. La duración media de los temporales de oleaje que impactan en las costas de las regiones extratropicales de ambos hemisferios oscila entre 12 y 36 horas, siendo la costa occidental europea la que muestra los valores mayores. En las regiones intertropicales y subtropicales la duración media de los temporales de oleaje es mayor, mostrando una duración media de 45 horas entre 30°S y 30°N.

Como era de esperar, los temporales de oleaje severos son incluso más duraderos, por lo que aumenta su capacidad de daño. Los temporales más energéticos generados en las regiones extratropicales pueden durar, por término medio, más de 36 horas. En consonancia, la duración media en las regiones intertropical y subtropical también aumenta, mostrando duraciones medias mínimas de temporales de oleaje severos de 60 horas a lo largo de costas abiertas y, particularmente, superiores a 100 horas en la costa del Mar Arábigo.

La H_s media de los temporales de oleaje muestra un patrón meridional con valores más altos en latitudes extratropicales, especialmente a lo largo de las costas occidentales de los continentes. Los temporales de oleaje severos muestran un patrón de H_s media similar pero, como era de esperar, con magnitudes más altas. Además, el aumento de la H_s media para los temporales severos no es homogéneo a lo largo de la costa mundial, oscilando entre menos del 2% y más del 25%.

Dado que el clima de temporales de oleaje en las costas occidentales de los continentes está impulsado en gran medida por las olas generadas por los ciclones extratropicales, la Θ_m media a lo largo de estas costas está determinada principalmente por la trayectoria media seguida por estas olas a medida que se propagan desde la zona de generación hacia las costas.

Por otro lado, el clima de temporales de oleaje en las costas orientales de los continentes es más complejo y, en consecuencia, también lo es el patrón de Θ_m media. Esto se debe a la coexistencia de temporales con diferentes orígenes a lo largo del año. La ciclogénesis marina extratropical, los vientos alisios y los ciclones tropicales son los principales sistemas generadores de temporales de oleaje que impactan en estas costas, aparte de sistemas locales, tales como son los Nortes en el Golfo de México, o el Monzón en el Mar Arábigo. Los resultados para los temporales de oleaje severos son muy similares a los de los temporales de oleaje.

El patrón de E_f medio de los temporales de oleaje a lo largo de la costa mundial muestra valores más altos en costas afectadas por temporales con mayor H_s media, las cuales se caracterizan también por un T_m bastante elevado. En cambio, las costas alcanzadas por los temporales de oleaje con los T_m más grandes y H_s relativamente bajos, como en el Golfo de Guinea y el sur de Sumatra, no muestran flujos de energía tan elevados como las primeras. El aumento del E_f medio entre los temporales regulares y los temporales severos muestra un amplio rango de variación que va desde menos del 10% hasta más del 90%.

Los temporales de oleaje están dominados en su mayoría por olas de mar de viento. La proporción de las costas globales dominadas por mar de fondo es del 40% cuando se consideran los temporales de oleaje y del 35% si sólo se consideran los temporales severos. Se observan notables diferencias entre las costas orientales y occidentales abiertas al océano. Las costas occidentales están dominadas principalmente por mar de fondo en las regiones intertropicales y subtropicales. En las latitudes medias y altas, los temporales de olas empiezan a estar controlados principalmente por las olas de mar de viento. Las costas de estas latitudes sufren el impacto de olas muy grandes, todavía en su fase de desarrollo, debido a la proximidad entre la zona de generación y la costa. Por otro lado, la dominancia a lo largo de las costas orientales de los continentes no es tan clara, mostrando un patrón heterogéneo. El patrón de dominancia de los temporales de oleaje severos es muy similar al de los temporales de olas regulares.

La intensidad de los temporales de oleaje se evalúa en el presente estudio mediante el índice de contenido energético. Los resultados muestran un gradiente muy fuerte entre las altas intensidades de los temporales en las costas extratropicales y las bajas intensidades encontradas en latitudes intertropicales y subtropicales, tanto para los temporales de oleaje como para los temporales de oleaje severos. A pesar del mencionado gradiente meridional, algunas costas intertropicales y subtropicales específicas pueden seguir sufriendo el impacto de temporales muy intensos como, por ejemplo, aquellos generados por ciclones tropicales.

Las principales características de los temporales de oleaje se muestran en la Fig. 5.

Por último, se lleva a cabo una clasificación de la costa mundial en función de su grado de tormentosidad (DS; Fig. 6), el cual proporciona una visión cualitativa integrada de lo

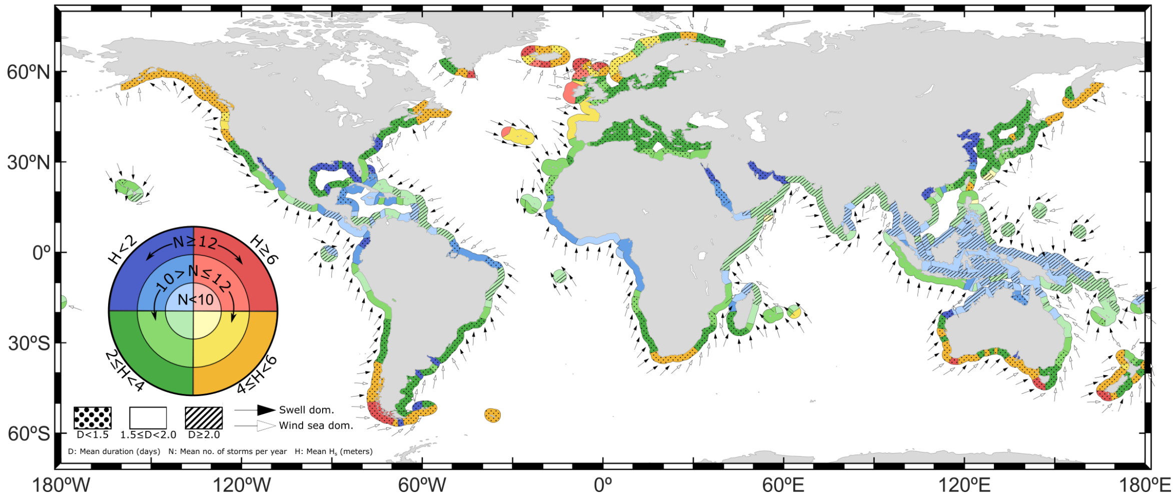

Fig. 5 Clasificación climática de los temporales de oleaje a lo largo de la costa mundial según sus principales características: H_s media (color), número medio de eventos (escala de colores), duración media de los temporales de oleaje (sombreado), Θ_m (dirección de la flecha) y predominio del mar de fondo frente al mar de viento (color de la punta de la flecha).

tormentosa que puede ser una costa. Este índice integra el número de eventos y el índice de intensidad, el cual as su vez ofrece información sobre la duración y la altura de ola de los eventos. Los resultados muestran, a pesar de algunas excepciones, un claro gradiente meridional. Cabe señalar que este gradiente meridional es el patrón esperado, ya que cada índice individual analizado muestra notables diferencias entre el comportamiento de los temporales en las regiones tropicales y extratropicales. Las regiones extratropicales muestran un grado de tormentosidad más alto. Por otro lado, en las regiones intertropicales y subtropicales las costas se caracterizan por una tormentosidad baja o muy baja. No obstante, se observan algunas excepciones como, por ejemplo, las costas afectadas por ciclones tropicales.

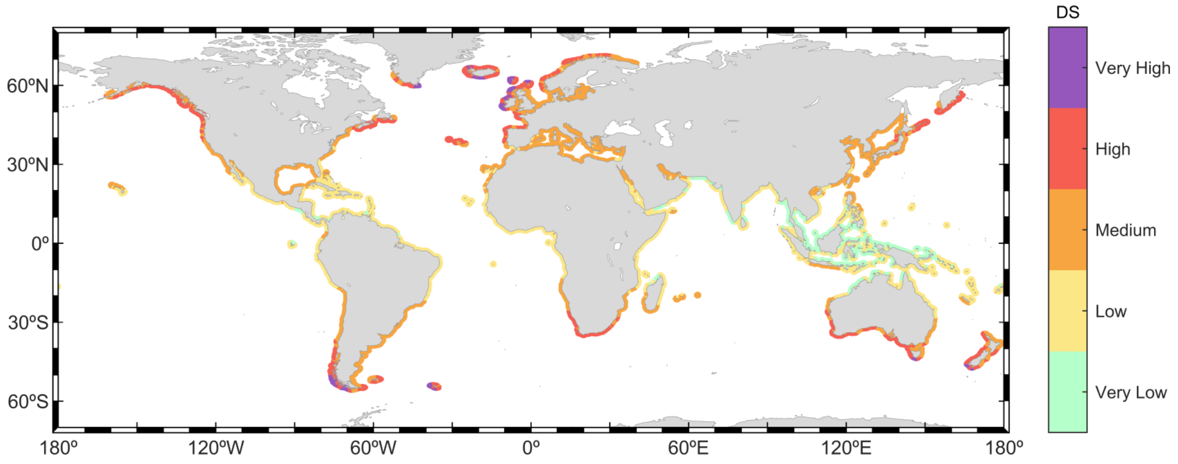

Fig. 6 Grado de tormentosidad de oleaje a lo largo d ela costa mundial.

Conclusiones

En este capítulo se presenta una evaluación de los temporales de oleaje a lo largo de la costa mundial. Este trabajo se basa en un hindcast de alta resolución de 42 años, forzado por el reanálisis ERA5 del ECMWF. Los temporales de oleaje se clasifican evaluando las excedencias del percentil 95% de H_s. Además, los temporales de oleaje más severos que afectan a la costa se aíslan analizando las excedencias sobre el percentil 99% de H_s. Se estudian las principales características de los temporales de olas: frecuencia de ocurrencia, duración e intensidad, así como los parámetros integrados del estado de mar medios de la tormenta H_s, Θ_m, T_m y E_f. También se analizan otras características secundarias como el predominio del mar de fondo frente al mar de viento durante los temporales.

Los resultados muestran un patrón general meridional de tormentosidad. Las costas más tormentosas son las situadas en latitudes extratropicales, consecuencia del impacto de los temporales de oleaje caracterizados por una gran altura de ola y alta frecuencia de ocurrencia. El grado de tormentosidad disminuye hacia el ecuador, con la principal excepción de las costas afectadas por ciclones tropicales, alcanzando su mínimo a lo largo de las costas protegidas de Indonesia. Las duraciones medias máximas de los temporales de oleaje se encuentran a lo largo de la costa oriental de la India, superando los 3,5 días. Los temporales de mares de fondo dominan las costas occidentales de los continentes hasta latitudes en las que los ciclones extratropicales tocan tierra, generando un dominio de los mares de viento sobre los mares de fondo.

Análisis de la variabilidad global de eventos extremos del nivel del mar en la costa a partir de datos altimétricos

Introducción

La altimetría satelital es una nueva fuente de datos sobre el nivel del mar que proporciona información desde los años 90 con cobertura global. Los altímetros muestrean a lo largo de sus trayectorias con una tasa de muestreo característica (por ejemplo, el Altika muestrea a 1 Hz), de manera que cada medición altimétrica se caracteriza por unas coordenadas y un tiempo de muestreo específicos, provocando una cobertura espacial y temporal irregular en productos de satélite con niveles de procesamiento inferiores a L4. No obstante, la duración actual de esta base de datos, aproximadamente 30 años, permite superar, en parte, las principales limitaciones intrínsecas de este tipo de información en cuanto a la resolución espacial y temporal irregular. La combinación de registros largos con la mejora continua de la precisión, especialmente en la zona costera, favorece el uso de la altimetría para desarrollar estudios climáticos. En este sentido, el principal resultado climático basado en datos altimétricos a lo largo de las últimas tres décadas es la estimación de las tendencias históricas del nivel medio del mar. A pesar de que estas tendencias se proporcionan en el océano profundo, la creciente precisión cerca de la costa ofrece actualmente la posibilidad de estimar las tendencias del nivel medio del mar en la zona costera con notable precisión. Además, se han estudiado otras características climáticas del nivel del mar, como la relación entre la SLA y los patrones de teleconexión climática y la variabilidad estacional y de mesoescala del nivel del mar.

En este contexto, este capítulo pretende demostrar la capacidad de los datos altimétricos para reproducir la variabilidad climática global de los extremos de nivel del mar en la costa. La investigación se centra en el residuo meteorológico del nivel del mar definido anteriormente. Sobre esta base, este estudio pretende proporcionar no sólo valores asociados a diferentes periodos de retorno, sino también evaluar la variabilidad en diferentes escalas temporales. Además, se analiza la importancia relativa del residuo meteorológico con respecto a la marea astronómica en los eventos extremos de nivel del mar.

Datos climáticos

En este estudio se utilizan datos de altimetría satelital procedentes una base de datos global de SLA distribuida por CMEMS que integra las mediciones inter-calibradas de más de veinte misiones desde 1992 en adelante y procesadas a través del sistema de procesamiento multimisión DUACS. En concreto, este estudio se centra en el periodo que va desde enero (1993) hasta diciembre (2021), es decir, 29 años de datos. Además de SLA, este producto proporciona también algunas de las correcciones geofísicas aplicadas a las mediciones altimétricas brutas como, por ejemplo, la corrección DAC.

Para evaluar la variabilidad de los eventos extremos de NTR costeros a escala global, se definen un total de 445 unidades costeras con una longitud de 500 km y una anchura de 100 km que cubren la totalidad de la costa mundial (Fig. 7).

La validación de la habilidad de los datos de altimetría para reproducir la variabilidad climática de los extremos de NTR se lleva a cabo a partir de la información aportada por 400 mareógrafos. El registro de NTR de los mareógrafos (NTR_{TG}) se obtiene de acuerdo a lo descrito en secciones previas.

Se consideran cuatro índices de teleconexión para evaluar la variabilidad interanual de los extremos de NTR: Arctic Oscillation index (índice AO), the Niño 3.4 index (índice Niño 3.4), Dipole Mode index (índice DMI) and Southern Annular Mode index (índice SAM).

La marea astronómica se reconstruye a partir de las componentes de marea proporcionadas por la base de datos TPXO9. La marea astronómica se reconstruye en el punto del océano más cercano al punto medio del tramo costero cubierto por cada unidad costera (Fig. 7).

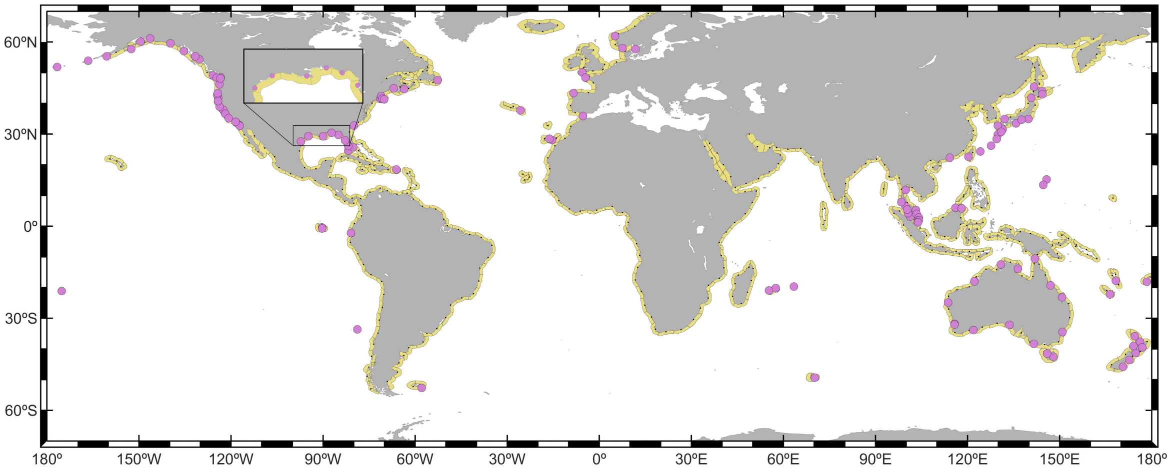

Fig. 7 Unidades costeras definidas para realizar el análisis (en amarillo). Los círculos rosas representan la ubicación de los mareógrafos seleccionados para la validación. Los puntos negros representan la ubicación donde se extraen las componentes de marea del modelo TPXO9.

Métodos

Modelo estadístico de extremos

Este estudio utiliza un modelo estadístico no estacionario GEVD a partir de máximos mensuales de NTR. Las variaciones climáticas se incluyen en el parámetro de localización del modelo. Se modelan variaciones climáticas en tres escalas temporales: variaciones dentro del año, variaciones interanuales y tendencias a largo plazo.

Selección de la muestra de residuo meteorológico

Como se ha mencionado anteriormente, este estudio se centra en la evaluación de la variabilidad climática de eventos extremos de la componente NTR del nivel del mar. Por tanto, el análisis requiere la generación de una base de datos NTR a partir de datos de altimetría. Como se indicó en secciones anteriores, el NTR_{SAT} se calcula deshaciendo la corrección DAC del producto SLA. Posteriormente, se seleccionan datos de NTR_{SAT} para cada unidad costera definida a lo largo de la costa mundial. Por último, se seleccionan los máximos mensuales en cada unidad costera para alimentar el análisis extremal.

Selección de muestras extremales de validación

La capacidad de los datos altimétricos para reproducir la variabilidad climática de los extremos de nivel del mar se valida con datos de mareógrafos. Para ello, primero se realiza un filtrado de los registros con el fin de no incluir aquellos afectados por procesos muy locales o que contienen valores anómalos. El proceso de selección, explicado en secciones anteriores, da lugar a un conjunto de 123 mareógrafos distribuidos globalmente (Fig. 7). Tras el filtrado, se seleccionan los máximos mensuales de NTR_{TG} y NTR_{SAT} para cada estación para utilizarlos como input del análisis extremal.

Evaluación de la variabilidad extremal

Se plantean diferentes métricas para analizar la variabilidad de los valores de extremos de NTR con muy baja frecuencia de ocurrencia. La variabilidad extremal dentro del año se representa a través de dos métricas. En primer lugar, el coeficiente de variación de NTR con periodo de retorno de 20 años dentro del año. Segundo, se identifican los meses con mayor probabilidad de presentar mayores extremos de NTR durante el año. La variabilidad interanual se analiza a partir de la contribución de los índices climáticos a las magnitudes extremas de NTR. Las tendencias a largo plazo se evalúan a través del cambio relativo en el NTR con periodo de retorno de 20 años entre 1995 y 2020. Por último, se analiza la dominancia relativa de la marea astronómica con respecto a la componente NTR a través del parámetro TD, calculado como la proporción entre la marea máxima media anual y valores de NTR con diferentes periodos de retorno.

Resultados

Validación frente a datos de mareógrafo

Los resultados muestran valores de correlación superiores a 0,7 entre los máximos mensuales de altimetría y de mareógrafo para la mayoría de las estaciones (más del 80%). Además, más del 50% de las estaciones muestran correlaciones superiores a 0,8. Se puede apreciar una subestimación general en los valores de NTR con periodo de retorno de 10 años estimados a partir de datos altimétricos (sesgo de -0,10 m), una buena correlación (0,74) y errores moderados (RMSE de 0,19 m). Cabe destacar que los errores aumentan en las latitudes tropicales, principalmente debido a la representación incompleta en la muestra extremal de altimetría de los eventos extremos de NTR generados por ciclones tropicales.

La variabilidad climática dentro del año se valida a través del coeficiente de variación del NTR con periodo de retorno de 20 años dentro del año. Los resultados muestran una buena concordancia, con un sesgo casi nulo, una alta correlación (0,89) y bajos errores (RMSE de 0,04). Las mayores diferencias en la tendencia a largo plazo se encuentran, como era de esperar, en los mareógrafos situados en la costa del Golfo de Alaska, principalmente debido al levantamiento de la plataforma continental en esta región. En general, existe un acuerdo aceptable entre ambas fuentes de información. La validación de la variabilidad interanual muestra excelentes resultados. Tres de los cuatro índices climáticos considerados muestran correlaciones superiores a 0,9, sesgos casi nulos y errores muy bajos (RMSE $<$ 0,025 m/IU).

En lo sucesivo, IU se refiere a las unidades del índice climático. El índice restante (SAM), muestra una correlación de 0,75.

Por tanto, los resultados de validación proporcionan confianza al análisis de variabilidad climática desarrollado a lo largo de la costa mundial con datos de altimetría.

Valores de periodo de retorno

Los resultados muestran que la costa del Mar del Norte y las costas de Argentina y Uruguay son las que sufren los eventos de NTR más intensos, superando la primera 1,8 m y la segunda 1,4 m para eventos con 20 años de periodo de retorno. A pesar de que los ciclones tropicales no son captados en su totalidad por los datos de altimetría en las unidades costeras, las costas impactadas por este tipo de tormentas, como las costas del Golfo de México, las costas de China y del Sur de Japón y la costa del Golfo de Carpentaria, muestran extremos de NTR notablemente elevados, superando todos ellos 1 m para 20 años de periodo de retorno.

Análisis de la variabilidad climática

La evaluación de la variabilidad extremal dentro del año muestra que las costas en latitudes extratropicales se caracterizan por un claro patrón de variabilidad invierno-verano, de forma que los mayores eventos de NTR ocurren durante los correspondientes meses de invierno de cada hemisferio. Además, los resultados muestran que esta estacionalidad es más prominente en el hemisferio norte que en el sur. Por otro lado, existe una gran heterogeneidad en el mes con mayor probabilidad de mostrar los extremos más altos en las costas subtropicales e intertropicales. Muchas de estas costas no muestran un patrón de variabilidad simple dentro del año con una periodicidad anual (por ejemplo, la variabilidad invierno-verano), sino que muestran dos estaciones de temporales, principalmente debido a que sufren extremos con diferentes orígenes. Por ejemplo, la costa del Golfo de México sufre el impacto de los extremos de NTR más intensos durante la temporada de ciclones tropicales, especialmente en septiembre y octubre, y muestra otro máximo entre mayo y abril.

El principal resultado de la evaluación de la variabilidad a largo plazo es un claro incremento general a lo largo de la costa mundial. Se han encontrado tendencias significativas con un nivel de confianza superior al 95% en más del 95% de las unidades costeras analizadas. Pueden observarse cambios relativos superiores al 50% en eventos de NTR con periodo de retorno de 20 años a lo largo de algunas partes de la costa suroccidental africana y del canal de Mozambique. Por otro lado, las tendencias más débiles se observan en la costa noroeste de América, mostrando incrementos casi nulos y valores de significancia bajos.

El índice AO muestra correlaciones significativas en las costas extratropicales del hemisferio norte, y especialmente en la cuenca atlántica. Existe una fuerte correlación negativa a lo

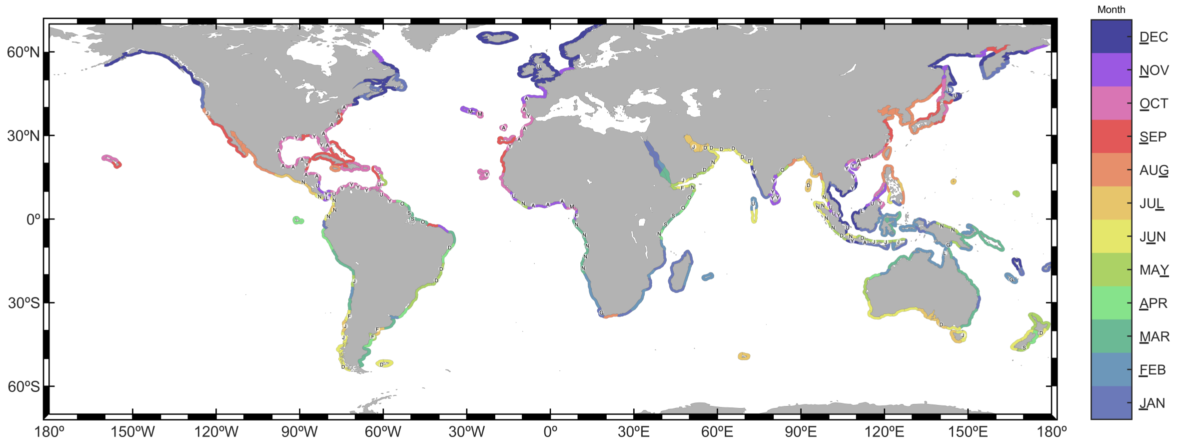

Fig. 8 Mes con mayor probabilidad de presentar mayores extremos. Los círculos blancos identifican unidades costeras con más de un máximo dentro del año para el NTR con periodo de retorno de 20 años. La letra dentro de los círculos indica el segundo mes con mayor probabilidad de presentar mayores extremos de NTR.

largo de la costa noreste americana y la costa atlántica del sur de Europa, mientras que existe una fuerte correlación positiva en la costa atlántica del norte de Europa. El índice SAM muestra correlaciones significativas en dos regiones costeras: una correlación negativa en la costa sur de Australia y una correlación positiva en las costas meridionales de Sumatra y Java. El fenómeno ENSO muestra una fuerte correlación con los eventos extremos de NTR en las costas intertropicales del Océano Pacífico. Esta influencia se extiende también a las costas extratropicales occidentales del continente americano y a algunas costas intertropicales y subtropicales del océano Índico y del Atlántico Oeste. En general, se observa una correlación positiva (fase El Niño) a lo largo de las costas del Pacífico Este tropical, y lo contrario (fase La Niña) en el Pacífico Oeste tropical. El patrón de influencia encontrado para el índice DMI muestra correlaciones negativas significativas en las costas orientales del Océano Índico y lo opuesto en las occidentales. Además, se observa que el patrón del DMI está fuertemente correlacionado con el fenómeno ENSO.

Importancia relativa del residuo meteorológico

La marea astronómica modula los eventos extremos de nivel del mar en aproximadamente el 80% de la costa mundial con respecto a eventos extremos NTR con periodos de retorno de entre 5 y 20 años. Las principales regiones costeras dominadas por los extremos de NTR son las costas del Golfo de México, las costas sur y este del Mar del Norte, las costas de Argentina y Uruguay y las costas en mares semicerrados, tales como el Mar Rojo y el Mar de Japón. Como era de esperar, la magnitud de los extremos de nivel del mar en las costas macromareales está controlada principalmente por la marea astronómica, como en las costas

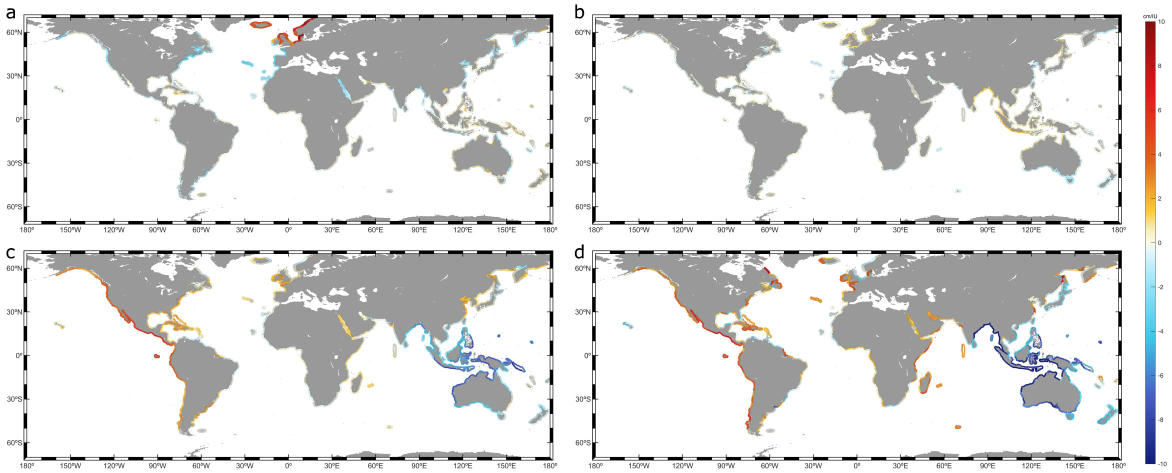

Fig. 9 Contribición costera global de (a) índice AO, (b) índice SAM, (c) índice Niño 3.4 y (d) índice DMI.

del Canal de Mozambique, la costa noroeste de Australia o las costas atlánticas del norte de España y el suroeste de Francia.

Conclusiones

Este capítulo evalúa la variabilidad climática de los fenómenos extremos del nivel del mar a lo largo de la costa mundial a partir de datos de altimetría satelital. En concreto, la componente NTR del nivel del mar es la principal variable analizada. Para ello, se genera una base de datos de esta variable a partir de datos altimétricos cubriendo el periodo 1993-2021. La variabilidad climática de los valores extremos de nivel del mar se modela mediante un modelo estadístico de extremos paramétrico no estacionario. Dicho modelo considera variaciones en tres escalas temporales: dentro del año, interanual y tendencias a largo plazo.

Antes de la evaluación climática, se valida la habilidad de los datos altimétricos para reproducir la variabilidad climática de los eventos extremos de nivel del mar frente a datos de mareógrafo. Las costas en latitudes extratropicales muestran un claro patrón de estacionalidad invierno-verano. Los patrones de variabilidad dentro del año son, sin embargo, más complejos en las latitudes tropicales, mostrando normalmente múltiples estaciones de temporales. Los resultados muestran un patrón general de incremento en las magnitudes con periodo de retorno de 20 años. En lo que respecta a la variabilidad interanual, en el norte de Europa se observa una clara relación entre el patrón climático AO y los extremos de NTR. El fenómeno de El Niño-ENSO modula claramente la aparición de extremos a lo largo de toda la costa americana del Pacífico durante la fase de El Niño, mientras que la fase de La Niña lo hace para las costas tropicales del Pacífico Oeste. También se evalúa la importancia relativa de la marea astronómica con respecto al componente residual no mareal del nivel del mar. Los resultados muestran un predominio de la marea astronómica en más del 80% de las costas mundiales.

Cambios en eventos extremos de oleaje bajo distintos escenarios de cambio climático

Introducción

Numerosos estudios han abordado el análisis de los cambios futuros en el clima del oleaje, generalmente a través de proyecciones climáticas. Dos son los principales enfoques utilizados para generar proyecciones climáticas de oleaje tanto a escala regional como global: dinámico y estadístico. La comunidad del COWCLIP está realizando notables esfuerzos para integrar los estudios existentes acerca de los futuros cambios en el clima del oleaje y evaluar su robustez e incertidumbres. Los resultados obtenidos en estos estudios evidencian un consenso sobre el futuro aumento de la H_s media anual en el Océano Austral y el Pacífico Este tropical, y un descenso en el Atlántico Norte y el Pacífico Noroeste.

A pesar de su relevancia, el análisis de los cambios proyectados en las condiciones extremas del oleaje bajo escenarios de cambio climático no ha sido ampliamente estudiado. Hasta el momento, la evaluación de las variaciones futuras de los extremos de oleaje se ha realizado principalmente a través del análisis de percentiles altos de series temporales de H_s o máximos anuales. Un análisis preciso de los eventos extremos con una probabilidad de ocurrencia muy baja debe basarse en la teoría de valores extremos, la cual proporciona distribuciones asintóticas a largo plazo para los extremos y los enfoques para estimar los valores asociados a periodos de retorno. El número limitado de estudios sobre este tema, comúnmente abordado a través de la evaluación de los cambios en los periodos de retorno de H_s, junto con la complejidad intrínseca de los extremos del oleaje, hace que sea difícil llegar a un consenso acerca de los cambios regionales proyectados para el final del siglo. Con el fin de comprender mejor el comportamiento futuro de los extremos de oleaje poco frecuentes, este estudio propone la evaluación de los cambios proyectados en H_s para diferentes periodos de retorno bajo escenarios de cambio climático, analizando su magnitud, incertidumbre, distribución geográfica y su comportamiento con respecto a las condiciones medias de oleaje.

Datos climáticos

Este estudio utiliza un conjunto de siete modelos de circulación general del CMIP5 (GCMs; Tabla 2) para desarrollar proyecciones climáticas de oleaje. El criterio para seleccionar los GCMs está condicionado por la necesidad de producir series temporales horarias de H_s para capturar mejor los valores extremos.

Table 2 Características principales de los modelos de circulación general seleccionados.

GCM	Institution	Country	Atmospheric resolution (latxlon)
MIROC5	MIROC	Japan	1.40°x1.40°
IPSL-CM5A-MR	Institut Pierre-Simon Laplace	France	1.25°x1.25°
GFDL-ESM2G	NOAA Geophysical Fluid Dynamics Laboratory	USA	2.00°x2.50°
CNRM-CM5	Centre National de Recherches Météorologique	France	1.40°x1.40°
CMCC-CM	Centro Euro-Mediterraneo per I Cambiamenti Climatici	Italy	0.75°x0.75°
ACCESS1.0	CSIRO-BOM	Australia	1.25°x1.90°
HadGEM2-ES	Met Office Hadley Centre	UK	1.25°x1.90°

Las proyecciones son generadas dinámicamente utilizando como forzamiento los campos de hielo y viento output de los GCMs. Las simulaciones se realizan en una malla regular que cubre las latitudes entre 88°N y 85°S con una resolución espacial de un grado, mediante el modelo de propagación de tercera generación WaveWatchIII (WW3) versión 4.18. Las proyecciones de oleaje globales resultantes simulan el clima del oleaje para el periodo histórico de referencia climática 1986-2005 y el periodo temporal futuro 2081-2100 bajo los escenarios de concentración de gases de efecto invernadero RCP4.5 y RCP8.5.

Métodos

Corrección del sesgo

Aunque los GCMs tienen la capacidad de reproducir el sistema climático y las interconexiones entre sus componentes, ciertas cuestiones como la resolución espacial y las simplificaciones introducidas por las parametrizaciones numéricas de algunos procesos físicos provocan un sesgo sistemático inherente a cada modelo. Estos sesgos se transmiten al oleaje principalmente a través de los sesgos en los campos de viento superficiales. Esto, junto con el hecho de que los eventos extremos presentan mayores sesgos, hacen que la corrección del sesgo sea esencial en este estudio. Por ello, se aplica una técnica de corrección para reducir los sesgos en cada miembro del conjunto de proyecciones climáticas, utilizando como referencia el hindcast de oleaje global GOW2.

La técnica de mapeo de cuantiles empíricos (EQM, del inglés empirical quantile mapping), ligeramente modificada para corregir mejor la cola superior de la distribución, es el método seleccionado para corregir el sesgo de las proyecciones climáticas de oleaje. El rendimiento de la corrección del sesgo se evalúa mediante la métrica PDF-based skill score (PDF_{sc}), la cual se basa en la comparación entre la función de densidad de probabilidad (PDF) del clima presente para el hindcast de referencia y para las proyecciones climáticas.

Modelo estadístico de extremos

El análisis de valores extremos se realiza siguiendo el método de máximos anuales, el cual se basa en el ajuste de los máximos anuales a un modelo estadístico tipo GEVD. En particular, aplicamos la familia de distribución de valores extremos simplificada de la GEVD: distribución de valores extremos tipo I (EVD tipo I) o distribución de Gumbel.

La bondad del ajuste de la distribución de Gumbel se evalúa con la prueba de Anderson-Darling (AD). Este estadístico mide la distancia entre la distribución propuesta con los parámetros estimados y la distribución empírica, introduciendo además una función de peso que otorga ponderaciones más pesadas en ambas colas para mejorar el rendimiento.

Validación con datos instrumentales

Los valores de H_s asociados a periodos de retorno se validan con los datos medidos por boyas. Todas las boyas seleccionadas cumplen una serie de requisitos de calidad para garantizar una correcta aplicación del análisis de valores extremos y una adecuada comparación con los resultados de las proyecciones numéricas, dando como resultado un conjunto final de cincuenta y dos boyas.

Robustez del cambio proyectado

La evaluación de la incertidumbre de los cambios proyectados se basa en considerar, en primer lugar, la significancia del cambio y, en segundo lugar, la concordancia en el signo del cambio entre los miembros del conjunto. El cambio se considera robusto si es estadísticamente significativo a un nivel de confianza del 95% en más del 50% de los miembros del conjunto y al menos el 80% de ellos coinciden en el signo del cambio.

Resultados

Análisis de valores extremos

Se estudia el comportamiento de los extremos de oleaje mediante una evaluación de valores extremos de la serie temporal de H_s una vez corregido el sesgo. Tras el análisis, se observa una baja proporción del océano global donde el ajuste del parámetro de forma sea estadísticamente significativo y el cambio proyectado en el mismo sea robusto (14% y 16%, respectivamente). Esto indica una inestabilidad subyacente al añadir este grado de libertad en el modelo de extremos para estimar los valores de retorno, lo que nos lleva a ajustar los máximos anuales a una función de distribución tipo Gumbel. El uso de un modelo extremal biparamétrico más sencillo ofrece una mayor robustez general, aunque puede llevar a una subestimación de las distribuciones de cola pesada en las zonas de actividad de ciclones tropicales. El análisis de bondad del ajuste muestra, en general, un buen ajuste del modelo. La zonas donde la idoneidad de la distribución de Gumbel se ve comprometida coinciden en su mayoría, como cabría esperar, con aquellas en las que el ajuste del parámetro de forma resulta significativo.

Validación de valores extremos

Con el fin de proporcionar confianza en los valores de H_s asociados a periodos retorno estimados a partir de datos de simulaciones numéricas, se lleva a cabo una validación con valores de periodo de retorno estimados a partir de registros de boyas. La comparativa resulta en errores relativos medios de 13%, 18% y 20% y un errores cuadráticos medios de 2 m^2, 7 m^2 y 12 m^2 después de aplicar la corrección del sesgo para H_s^5, H_s^{20} y H_s^{50}, respectivamente.

Cambios futuros en extremos de oleaje

Evaluamos los cambios proyectados en los eventos extremos de H_s para periodos de retorno de 5, 20, 50 y 100 años (H_s^5, H_s^{20}, H_s^{50} and H_s^{100}, respectivamente). Para facilitar la compresión de los cambios, se propone una regionalización del oceano global (Fig. 10a). Los cambios proyectados y su robustez quedan recogidos en la Tabla 3 para los escenarios RCP4.5 y RCP8.5. Además, a modo de ejemplo, la Fig. 10b muestra los cambios proyectados en H_s^{20} para el escenario RCP8.5. Más allá del aumento de la incertidumbre encontrado para los cambios en los extremos menos frecuentes (por ejemplo, la robustez de los cambios a escala global se reduce del 32% para H_s^5 al 24% para H_s^{100} en el escenario RCP8.5), se pueden extraer dos conclusiones generales a medida que los periodos de retorno son mayores. En primer lugar, la proporción de cambios positivos aumenta, lo que conduce a un incremento del cambio medio global (de -0,5% para H_s^5 a +0,3% para H_s^{100} y de -0,0% a +0,6% para RCP8.5 y RCP4.5, respectivamente). En segundo lugar, la magnitud de los cambios observados es mayor en las regiones con cambios positivos.

Así mismo, se comparan los cambios proyectados en las condiciones extremas de H_s para el periodo de retorno de 20 años y las condiciones medias (H_s^m; Fig. 11). Los resultados muestran una concordancia espacial general en el signo del cambio (aproximadamente dos tercios del océano global). No obstante, también surgen discrepancias robustas en algunas zonas para finales de siglo en relación no sólo con esta característica, sino también con la magnitud y la incertidumbre.

El Océano Austral presenta un aumento de los valores de H_s para distintos periodos de retorno caracterizado por un cambio medio de hasta +0,5 m para los escenarios RCP4.5 y +0,9 m para los escenarios RCP8.5, mostrando para este último aumentos locales superiores

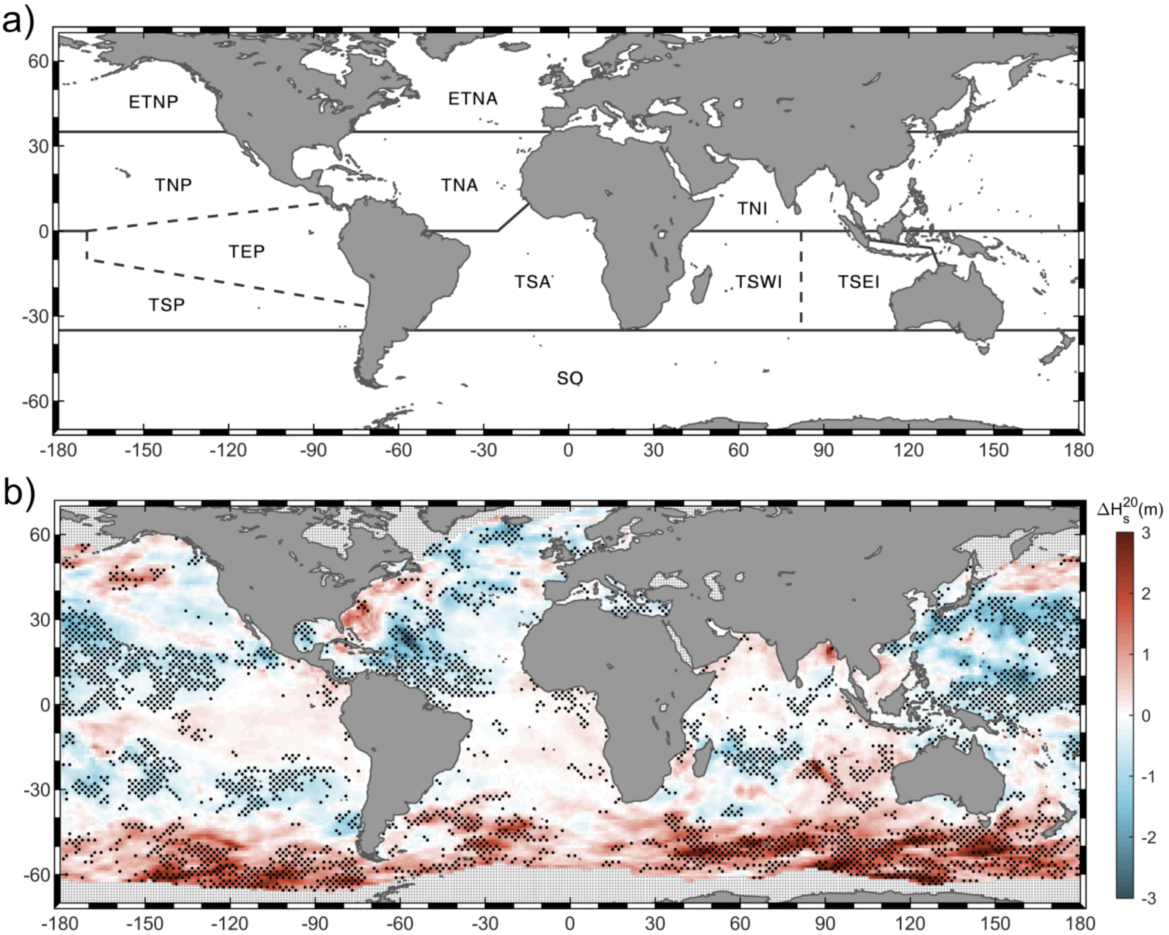

Fig. 10 Propuesta de regionalización oceánica global. ETNP (Pacífico Norte Extratropical), ETNA (Atlántico Norte Extratropical), TNP (Pacífico Norte Tropical), TNA (Atlántico Norte Tropical), TNI (Índico Norte Tropical), TEP (Pacífico Este Tropical), TSP (Pacífico Sur tropical), TSA (Atlántico Sur Tropical), TSWI (Índico Suroeste Tropical), TSEI (Índico Sureste Tropical), SO (Océano Austral). (b) Cambio medio del conjunto multimodelo en H_s^{20} bajo RCP8.5 a finales de siglo (2081-2100 con respecto a 1986-2005). El punteado denota cambios estadísticamente significativos con un nivel de confianza del 95% en al menos el 50% de los miembros y un acuerdo en el signo del cambio en más del 80% de los miembros.

a 3,5 m para un periodo de retorno de 20 años y superior. En el Atlántico Norte, aunque se observa un descenso robusto y homogéneo para H_s^m, los cambios para los extremos se caracterizan por una gran incertidumbre, con la única excepción del descenso encontrado en el Atlántico Noroeste tropical. Además, se observa un aumento poco robusto en la parte más occidental de la cuenca (costas de Estados Unidos y Canadá) y en algunas otras zonas europeas. El Océano Pacífico muestra un descenso robusto general de los fenómenos extremos en la región tropical. Esta señal de descenso, sin embargo, no se encuentra en el Pacífico Este tropical (la zona de génesis del fenómeno ENSO), donde las proyecciones proporcionan un aumento robusto de las condiciones medias y un aumento incierto de los extremos. El Océano

Table 3 Para cada región oceánica analizada, fila superior: proporción de la región que muestra cambios robustos y (entre paréntesis) proporción de la región que muestra un aumento robusto. Fila inferior: magnitud media de los cambios proyectados y (entre paréntesis) percentiles 5% y 95% de los cambios proyectados con el mismo signo que la media estimada en la región. Los resultados se muestran para periodos de retorno de 5, 20, 50 y 100 años bajo los escenarios RCP4.5 y RCP8.5. Todos los resultados están redondeados a un decimal.

	RCP4.5				**RCP8.5**			
	$\mathrm{H}_\mathrm{s}^{5}$	$\mathrm{H}_\mathrm{s}^{20}$	$\mathrm{H}_\mathrm{s}^{50}$	$\mathrm{H}_\mathrm{s}^{100}$	$\mathrm{H}_\mathrm{s}^{5}$	$\mathrm{H}_\mathrm{s}^{20}$	$\mathrm{H}_\mathrm{s}^{50}$	$\mathrm{H}_\mathrm{s}^{100}$
Global								
Robustness(%)	$22.4_{(10.5)}$	$18.2_{(8.7)}$	$16.8_{(8.1)}$	$16.2_{(7.7)}$	$31.6_{(14.2)}$	$27.6_{(12.3)}$	$25.4_{(11.3)}$	$24.3_{(10.8)}$
Avg. change (m)	$+0.0_{(+0.0;+0.8)}$	$+0.1_{(+0.0;+1.1)}$	$+0.1_{(+0.0;+1.3)}$	$+0.1_{(+0.0;+1.5)}$	$+0.1_{(+0.0;+1.5)}$	$+0.1_{(+0.0;+1.8)}$	$+0.1_{(+0.0;+2.0)}$	$+0.1_{(+0.0;+2.2)}$
ETNP								
Robustness(%)	$16.3_{(8.5)}$	$12.4_{(4.8)}$	$12.2_{(4.9)}$	$11.9_{(4.5)}$	$15.6_{(5.9)}$	$12.6_{(5.5)}$	$11.4_{(5.2)}$	$11.6_{(5.1)}$
Avg. change (m)	$+0.1_{(+0.0;+0.7)}$	$+0.1_{(+0.0;+1.1)}$	$+0.1_{(+0.0;+1.3)}$	$+0.2_{(+0.0;+1.5)}$	$+0.0_{(+0.0;+0.8)}$	$+0.0_{(+0.0;+1.2)}$	$+0.0_{(+0.0;+1.5)}$	$+0.0_{(+0.0;+1.7)}$
TNP								
Robustness(%)	$31.1_{(0.7)}$	$22.2_{(1.1)}$	$19.9_{(1.5)}$	$18.6_{(1.9)}$	$44.6_{(0.1)}$	$42.4_{(0.3)}$	$39.6_{(0.3)}$	$38.1_{(0.4)}$
Avg. change (m)	$-0.2_{(-0.0;-0.9)}$	$-0.2_{(-0.0;-1.3)}$	$-0.2_{(-0.0;-1.5)}$	$-0.2_{(-0.0;-1.7)}$	$-0.5_{(-0.1;-1.2)}$	$-0.5_{(-0.1;-1.5)}$	$-0.6_{(-0.1;-1.7)}$	$-0.6_{(-0.1;-1.9)}$
TEP								
Robustness(%)	$11.1_{(9.2)}$	$8.3_{(6.8)}$	$7.3_{(5.7)}$	$7.1_{(5.3)}$	$9.4_{(8.1)}$	$9.1_{(6.1)}$	$8.7_{(5.3)}$	$8.6_{(5.2)}$
Avg. change (m)	$+0.0_{(+0.0;+0.1)}$	$+0.0_{(+0.0;+0.2)}$	$+0.0_{(+0.0;+0.3)}$	$+0.0_{(+0.0;+0.3)}$	$+0.1_{(+0.0;+0.3)}$	$+0.1_{(+0.0;+0.4)}$	$+0.1_{(+0.0;+0.4)}$	$+0.1_{(+0.0;+0.5)}$
TSP								
Robustness(%)	$24.0_{(1.0)}$	$20.7_{(1.0)}$	$19.8_{(1.3)}$	$19.5_{(1.6)}$	$30.6_{(0.2)}$	$27.2_{(0.5)}$	$25.9_{(0.8)}$	$25.5_{(0.7)}$
Avg. change (m)	$-0.2_{(-0.0;-0.6)}$	$-0.2_{(-0.0;-0.9)}$	$-0.2_{(-0.0;-1.1)}$	$-0.2_{(-0.0;-1.2)}$	$-0.2_{(-0.0;-0.6)}$	$-0.3_{(-0.0;-0.9)}$	$-0.3_{(-0.0;-1.1)}$	$-0.4_{(-0.1;-1.2)}$
ETNA								
Robustness(%)	$18.4_{(1.7)}$	$13.4_{(2.2)}$	$11.7_{(2.1)}$	$10.7_{(1.9)}$	$25.3_{(1.6)}$	$17.6_{(2.1)}$	$14.7_{(2.4)}$	$12.8_{(2.2)}$
Avg. change (m)	$-0.3_{(-0.0;-0.9)}$	$-0.2_{(-0.0;-1.1)}$	$-0.2_{(-0.0;-1.2)}$	$-0.2_{(-0.1;-1.4)}$	$-0.3_{(-0.1;-1.0)}$	$-0.3_{(-0.0;-1.2)}$	$-0.3_{(-0.1;-1.4)}$	$-0.2_{(-0.0;-1.5)}$
TNA								
Robustness(%)	$25.0_{(2.5)}$	$22.2_{(2.9)}$	$20.7_{(3.0)}$	$21.0_{(2.9)}$	$37.7_{(0.6)}$	$31.4_{(1.0)}$	$29.3_{(0.9)}$	$28.5_{(0.8)}$
Avg. change (m)	$-0.1_{(-0.0;-0.4)}$	$-0.0_{(-0.0;-0.6)}$	$-0.0_{(-0.0;-0.8)}$	$-0.0_{(-0.0;-0.8)}$	$-0.3_{(-0.0;-1.0)}$	$-0.4_{(-0.0;-1.4)}$	$-0.4_{(-0.0;-1.7)}$	$-0.4_{(-0.0;-2.0)}$
TSA								
Robustness(%)	$15.4_{(13.2)}$	$15.5_{(12.4)}$	$15.2_{(11.7)}$	$14.6_{(11.2)}$	$10.2_{(8.3)}$	$10.4_{(8.1)}$	$10.2_{(8.1)}$	$10.1_{(8.1)}$
Avg. change (m)	$+0.0_{(+0.0;+0.2)}$	$+0.1_{(+0.0;+0.4)}$	$+0.1_{(+0.0;+0.5)}$	$+0.1_{(+0.0;+0.5)}$	$+0.0_{(+0.0;+0.2)}$	$+0.1_{(+0.0;+0.3)}$	$+0.1_{(+0.0;+0.4)}$	$+0.1_{(+0.0;+0.4)}$
TNI								
Robustness(%)	$12.5_{(3.4)}$	$11.3_{(5.8)}$	$10.6_{(5.9)}$	$11.3_{(6.9)}$	$15.8_{(3.4)}$	$10.7_{(4.2)}$	$8.8_{(4.1)}$	$8.5_{(4.6)}$
Avg. change (m)	$+0.0_{(+0.0;+0.3)}$	$+0.0_{(+0.0;+0.4)}$	$+0.1_{(+0.0;+0.5)}$	$+0.1_{(+0.0;+0.6)}$	$+0.0_{(+0.0;+0.5)}$	$+0.1_{(+0.0;+0.7)}$	$+0.2_{(+0.0;+0.8)}$	$+0.2_{(+0.0;+0.9)}$
TSWI								
Robustness(%)	$15.1_{(4.8)}$	$16.3_{(7.2)}$	$15.8_{(6.8)}$	$15.9_{(6.9)}$	$24.3_{(2.0)}$	$21.9_{(2.5)}$	$20.5_{(2.7)}$	$20.1_{(3.2)}$
Avg. change (m)	$-0.0_{(-0.0;-0.5)}$	$-0.0_{(-0.0;-0.8)}$	$-0.0_{(-0.0;-0.9)}$	$-0.1_{(-0.0;-1.1)}$	$-0.1_{(-0.0;-0.6)}$	$-0.1_{(-0.0;-1.0)}$	$-0.2_{(-0.0;-1.2)}$	$-0.2_{(-0.0;-1.3)}$
TSEI								
Robustness(%)	$19.7_{(15.4)}$	$18.8_{(14.0)}$	$19.2_{(14.3)}$	$19.1_{(14.0)}$	$20.6_{(14.6)}$	$27.3_{(21.0)}$	$27.6_{(22.0)}$	$28.4_{(22.9)}$
Avg. change (m)	$+0.1_{(+0.0;+0.6)}$	$+0.2_{(+0.0;+0.9)}$	$+0.3_{(+0.0;+1.2)}$	$+0.3_{(+0.0;+1.3)}$	$+0.1_{(+0.0;+0.5)}$	$+0.2_{(+0.0;+0.9)}$	$+0.3_{(+0.1;+1.1)}$	$+0.4_{(+0.1;+1.3)}$
SO								
Robustness(%)	$25.3_{(23.6)}$	$20.2_{(18.2)}$	$18.2_{(16.2)}$	$17.1_{(15.0)}$	$41.4_{(39.7)}$	$34.3_{(32.5)}$	$30.9_{(29.2)}$	$28.8_{(27.0)}$
Avg. change (m)	$+0.3_{(+0.0;+1.0)}$	$+0.4_{(+0.1;+1.3)}$	$+0.5_{(+0.1;+1.5)}$	$+0.5_{(+0.1;+1.7)}$	$+0.6_{(+0.1;+1.7)}$	$+0.8_{(+0.1;+2.2)}$	$+0.9_{(+0.1;+2.5)}$	$+0.9_{(+0.1;+2.8)}$

Índico muestra notables diferencias entre los cambios proyectados en las condiciones medias y las extremas de H_s. Estas discrepancias son especialmente relevantes en la región sureste tropical, a lo largo de las costas del oeste de Australia e Indonesia, donde los resultados indican un aumento robusto de los valores de periodo de retorno de H_s y un descenso de H_s^m.

Los cambios en los fenómenos extremos son menores y menos robustos para los escenarios de menor concentración. La solidez de los cambios proyectados se reduce de RCP8.5 a RCP4.5 globalmente en torno al 10% para cualquiera de los periodos de retorno estimados (por ejemplo, del 25% al 17% para el periodo de retorno de 50 años).

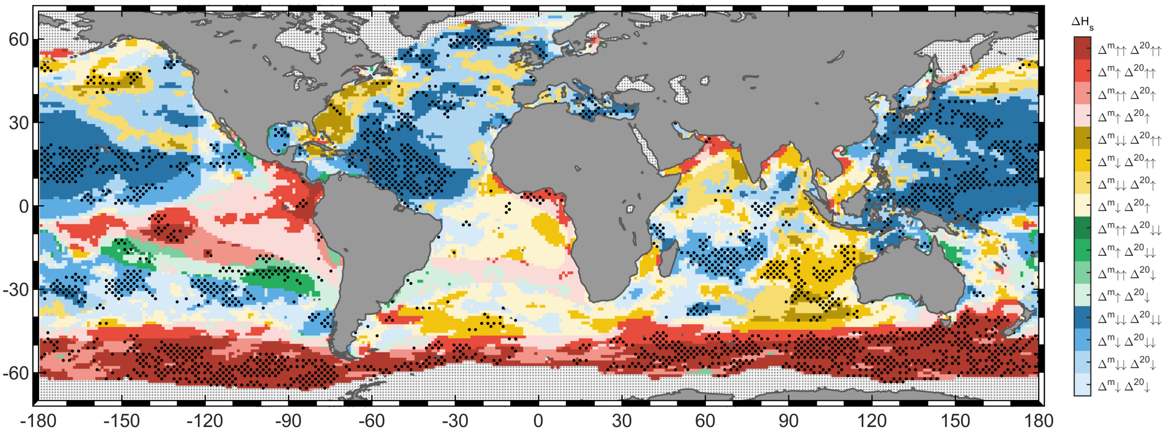

Fig. 11 Comparación entre los cambios proyectados en las condiciones medias (Δ^m) y extremas (Δ^{20}) de H_s bajo el escenario RCP8.5 para finales de siglo (2081-2100 con respecto a 1986-2005). Los colores representan las combinaciones del signo del cambio entre las condiciones medias y extremas del oleaje: el rojo indica un aumento de ambas condiciones, el azul representa un descenso de ambas condiciones, el amarillo representa un descenso de la media y un aumento de las condiciones extremas y el verde representa un aumento de la media y un descenso de las condiciones extremas. Para cada combinación, una flecha indica un cambio relativo inferior a la mediana global y dos flechas indican cambios relativos superiores a la mediana global. La mediana global se obtiene como la mediana de los cambios relativos con el mismo signo que la variación analizada. El punteado denota cambios estadísticamente significativos con un nivel de confianza del 95% en al menos el 50% de los miembros y una coincidencia en el signo del cambio en más del 80% de los miembros tanto para la media como para los extremos de H_s.

Conclusiones

Las olas extremas sufrirán cambios en el futuro al estar expuestas a diferentes escenarios de cambio climático. Estos cambios se evalúan mediante el análisis de los valores de H_s asociados a periodos de retorno. Además, estos cambios se comparan con los proyectados para la H_s media anual. Se analizan series temporales horarias mediante un conjunto de siete miembros de proyecciones climáticas de olas y se estiman los cambios en H_s para periodos de retorno de 5 a 100 años a fin de siglo bajo los escenarios RCP4.5 y RCP8.5.

A pesar de la incertidumbre subyacente que caracteriza a los extremos, se obtienen cambios robustos en eventos extremos de H_s en más de aproximadamente el 25% de la superficie del océano. Los resultados obtenidos concluyen que los aumentos cubren áreas más amplias y son de mayor magnitud que los descensos para mayores periodos de retorno. El Océano Austral es la región en la que se proyecta el aumento más robusto de los extremos de H_s, mostrando incrementos locales de más de 2 m independientemente del periodo de retorno analizado bajo el escenario RCP8.5. Por el contrario, el Pacífico Norte tropical muestra el descenso más acusado en H_s extrema, con descensos locales de más de 1,5 m.

En varias regiones oceánicas se encuentran divergencias relevantes entre el comportamiento proyectado de las condiciones de oleaje medias y extremas. Por ejemplo, se observa un aumento de los valores de H_s extremos y un descenso de la H_s media anual en el Índico Sureste, el Atlántico Noroeste y el Pacífico Noreste. Por lo tanto, la extrapolación del cambio previsto en las condiciones medias del oleaje a las extremas en las regiones que presentan tales divergencias debe realizarse con suma precaución, ya que puede llevar a una interpretación errónea cuando se utiliza para el diseño de estructuras o en la evaluación de impactos costeros.

Valor añadido de los espectros direccionales para evaluar el comportamiento futuro del clima del oleaje

Introducción

El espectro de elevación de la superficie libre constituye la forma más completa de describir el oleaje como un proceso estocástico. Este espectro representa la distribución de energía resultante de la contribución de varios trenes de ondas superpuestos con diferentes periodos y direcciones que llegan a una determinada localización, y es esencial para evaluar los procesos costeros y los diseños en ingeniería. La distribución y la magnitud de la energía dentro del espectro proporcionan información sobre el número de sistemas de olas que contiene, así como su grado de desarrollo.

A pesar de que el espectro de olas describe completamente el clima del oleaje, casi todos los estudios sobre los cambios en éste debidos al cambio climático evalúan los cambios proyectados en los parámetros integrados del estado de mar. Las razones de esta simplificación residen en la enorme cantidad de almacenamiento que exigen los espectros frecuencia-dirección (espectro direccional) y en el uso extendido de los parámetros integrados en múltiples formulaciones relacionadas con el diseño de estructuras y procesos costeros. En particular, el enfoque habitual relaciona los cambios esperados en el clima del oleaje con los cambios futuros en H_s, permitiendo alcanzar un consenso sobre los cambios esperados en la media anual y estacional de H_s en algunas regiones a lo largo del océano global. No obstante, un entendimiento más detallado de estas variaciones futuras requiere el estudio de un mayor número de variables, como el periodo y la dirección, especialmente teniendo en cuenta el notable papel que sus cambios pueden tener en los impactos costeros. La evaluación de los cambios en el periodo y la dirección a través de parámetros como T_m y Θ_m, es ahora una práctica habitual en este tipo de estudios, lo que ofrece una visión más cercana al cambio esperado en el espectro completo del oleaje. En la misma línea, existe un creciente interés por evaluar el efecto del cambio climático en variables que integran diferentes parámetros y que proporcionan una información más completa sobre el clima del oleaje. Por ejemplo, E_f integra la altura y el periodo, y ha demostrado ser un indicador válido del calentamiento global y ha proporcionado cambios robustos en zonas donde los cambios de H_s por sí solos tienen una gran incertidumbre.

Sobre esta base y con el fin de obtener una comprensión más amplia de cómo el clima del oleaje global se verá afectado por el cambio climático, así como sus consecuencias para las evaluaciones de impacto, este estudio intenta explorar los futuros cambios en los espectros direccionales bajo un escenario de alta emisión en todas las regiones oceánicas. Pretendemos mostrar el valor añadido que ofrece un enfoque novedoso que explora simultáneamente el efecto del cambio climático sobre la energía, el periodo y la dirección de las olas, explorando además las diferencias con respecto al uso estándar de los parámetros integrados del oleaje.

Datos climáticos

Este estudio utiliza las mismas proyecciones climáticas de oleaje descritas anteriormente y formadas por un conjunto de siete miembros. Las condiciones actuales y futuras de las olas se caracterizan mediante periodos temporales de 20 años (1986-2005 y 2081-2100, respectivamente). Los cambios se evalúan para el escenario de concentración RCP8.5. Además, se utiliza el hindcast de oleaje GOW2 como referencia para el clima del oleaje actual, tanto para analizar la climatología media de oleaje como para evaluar la magnitud de los sesgos sistemáticos en las proyecciones mediante la comparación del espectro direccional medio anual.

Como resultado de las simulaciones, se almacenan series temporales horarias de espectros direccionales en 14 localizaciones de análisis (Fig. 12). Así mismo, se almacenan series temporales horarias de los parámetros integrados H_s, T_m y Θ_m.

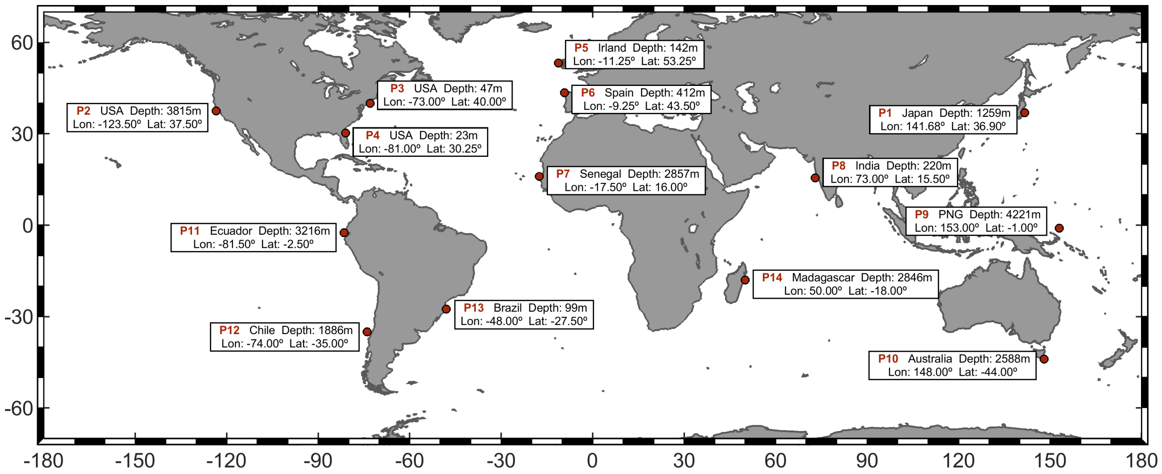

Fig. 12 Catorce puntos objetivo seleccionados para desarrollar el análisis. Para cada ubicación, se muestra el país más cercano, las coordenadas y la profundidad.

Métodos

Estimación de los cambios proyectados

El enfoque espectral permite el estudio detallado de los futuros cambios en la energía del oleaje, proporcionando las variaciones en cada celda espectral. Así mismo, es posible evaluar cómo se desplaza el grueso de la energía a lo largo del eje de frecuencias. Teniendo en cuenta el objetivo principal de este trabajo, nos centramos únicamente en los principales sistemas de olas que llegan a los puntos objetivo, despreciando los pequeños cambios relacionados con los mares de viento locales que representan un porcentaje muy pequeño de la energía total del espectro.

El cambio proyectado para cada miembro del conjunto se obtiene como la diferencia entre el espectro medio anual del clima del oleaje futuro y el actual. A continuación, el cambio medio del conjunto se calcula como la media de los cambios individuales de cada miembro, es decir, suponemos que la contribución de todos los miembros del conjunto es la misma.

Para calcular el desplazamiento de la energía media del oleaje a lo largo del eje de frecuencias (es decir, hacia periodos más bajos o más altos) para cada dirección, calculamos el rango de periodos en el que se concentra el rango intercuartílico de la energía en el presente y en el futuro, y luego determinamos su desplazamiento.

Análisis de incertidumbre

La incertidumbre del cambio proyectado se evalúa en base a analizar primero su significancia y luego considerar el acuerdo en el signo del cambio entre los miembros del conjunto de proyecciones climáticas de oleaje. Más del 80% de los modelos (6) deben presentar un cambio estadísticamente significativo, y al menos el 80% de ellos deben estar de acuerdo en el signo del cambio. La significancia estadística se calcula aplicando un test-t heterocedástico a la media de los periodos de referencia y futuro con un nivel de confianza del 95%.

Resultados

El análisis de sesgo muestra que éste aumenta con la latitud, lo cual es coherente con la mayor energía de las olas en la región extratropical. Además, se observa que en los espectros coexisten sesgos positivos y negativos. Las razones pueden ser, en primer lugar, sesgos con diferente signo asociados a diferentes sistemas de oleaje. En segundo lugar, sesgos en la localización de las zonas de generación.

A continuación, ofrecemos una breve descripción del clima del oleaje en cada punto de análisis y los principales cambios previstos para finales de siglo bajo el escenario RCP8.5

(Fig. 13). Además, se explora el desplazamiento de la energía a lo largo del eje de frecuencias (Fig. 14).

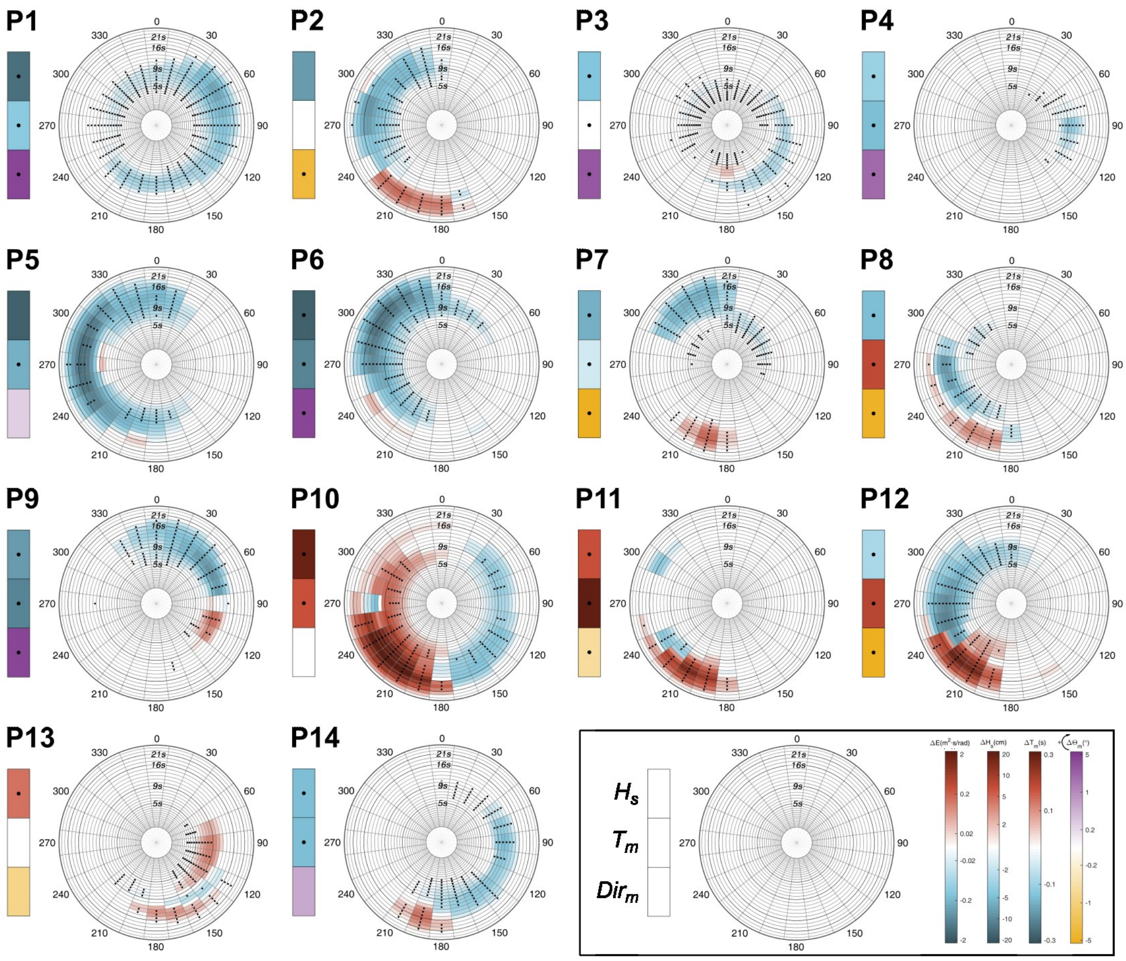

Fig. 13 Cambios proyectados en las localizaciones analizadas para finales de siglo (2081-2100) bajo el escenario RCP8.5 con respecto al clima del oleaje actual (1986-2005). Gráficos polares: cambio medio del conjunto multimodelo en la energía espectral media anual. Cuadros de la izquierda (de arriba a abajo): cambios medios del conjunto multimodelo en la media anual de H_s, T_m y Θ_m. El punteado denota un cambio estadísticamente significativo y un acuerdo en el signo del cambio en al menos el 80% de los modelos. Las barras de color utilizadas para representar el cambio de cada variable se muestran en la parte inferior derecha de la figura. De izquierda a derecha: energía (m^2 s/rad), H_s (cm), T_m (s) and Θ_m (°).

P5 y P6 se encuentran en el Atlántico Noreste. La mayor parte de la energía de las olas en estos puntos es transportada por el oleaje que se propaga desde el oeste en P5 y el noroeste en P6 generados por tormentas extratropicales en el Atlántico Norte. Estos puntos muestran un descenso de energía, así como un desplazamiento hacia periodos más bajos. P7 está afectado tanto por el oleaje generado en el hemisferio norte como por el oleaje que viaja desde el hemisferio sur. Este punto también es alcanzado por mares de viento procedentes del noreste y noroeste. Por lo tanto, los robustos descensos de H_s y T_m integran las variaciones de estos cuatro sistemas de ondas.

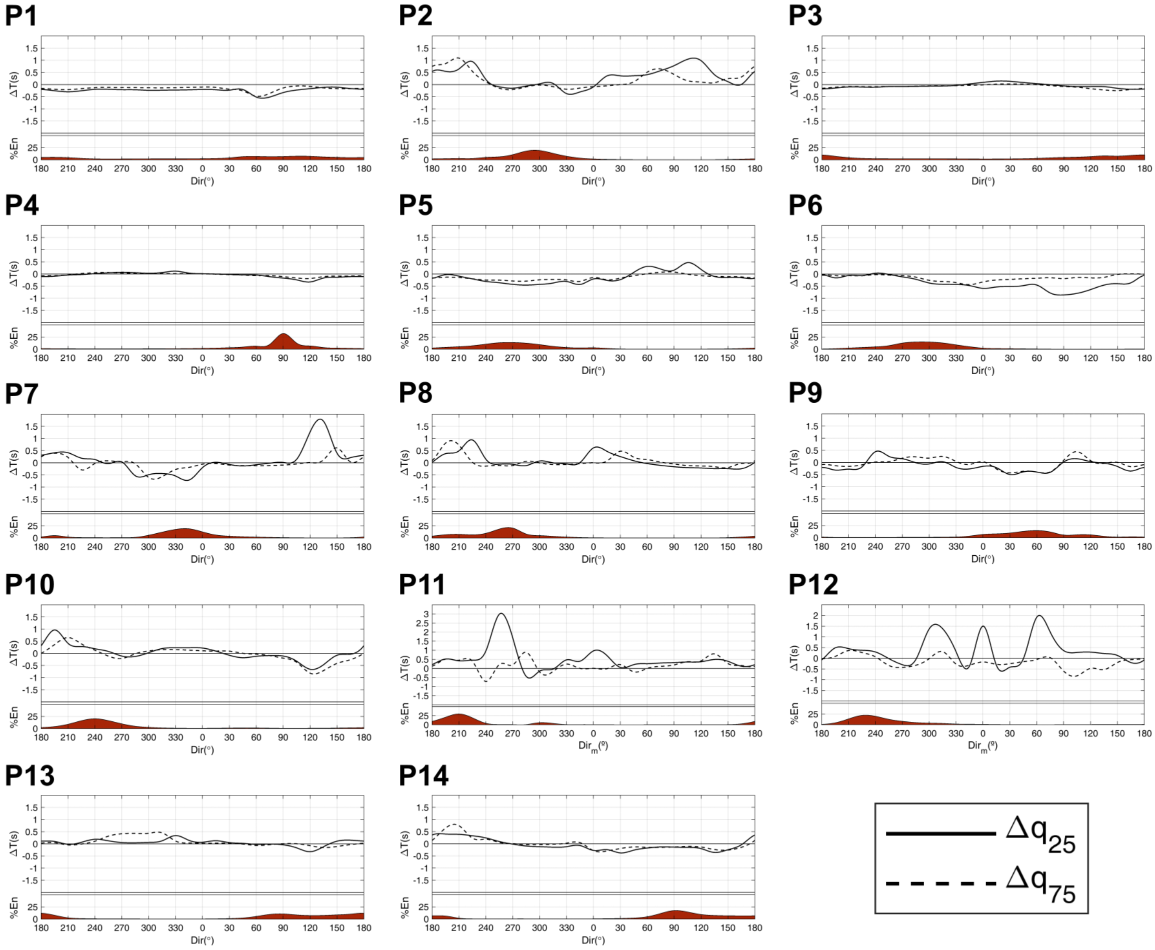

Fig. 14 Desplazamiento del rango intercuartílico de la energía entre el presente (1986-2005) y el final de siglo (2086-2100) bajo el escenario RCP8.5. Para cada panel: desplazamiento en segundos del cuantil 0,25 (línea continua) y del cuantil 0,75 (línea discontinua) de la energía para cada dirección. Porcentaje de energía procedente de cada dirección (en rojo).

La mayor parte de la energía que llega a P4 procede de oleajes generados por los vientos alisios del Atlántico Norte. Los resultados muestran un fuerte descenso de esta energía y un desplazamiento hacia periodos más bajos, lo que concuerda con los descensos previstas en H_s y T_m. P3 está afectado principalmente por mares de fondo generados por vientos alisios procedentes del sureste y por dos sistemas locales de mares de viento que se propagan desde el sur y el este. Los resultados muestran un descenso generalizado y un desplazamiento despreciable de la energía, lo cual es coherente con el descenso en H_s y el descenso casi nulo en T_m. P13 está afectado principalmente por mares de fondo generados en el Océano Austral, mares de fondo generados en el Atlántico Sur tropical que provienen del este y mares de viento que se propagan desde 200°. El aumento previsto en H_s coincide con el cambio esperado para la energía transportada por los mares de fondo del sur y del este. Sin embargo, mientras que se espera un desplazamiento de la energía hacia periodos más altos para los mares de fondo procedentes del Océano Austral, se obtiene lo contrario para las olas del este, lo que probablemente provoca el pequeño cambio proyectado en T_m.

El punto P2 está afectado principalmente por oleajes generados por tormentas extratropicales en el Pacífico Norte, además de por mares de viento procedentes del noroeste y por mares de fondo del Océano Austral. Los resultados muestran un aumento robusto proyectado en los mares de fondo del sur. Sin embargo, no se encuentra un cambio robusto para los mares de fondo generados en el Pacífico Norte. Se aprecia un cambio notable en la energía del sur hacia periodos más altos y un cambio casi nulo en la energía del Pacífico norte. La integración de todos estos cambios espectrales conduce a un descenso poco robusto de H_s y a un aumento muy pequeño de T_m.

El clima del oleaje del Pacífico Sureste se estudia en las localizaciones P11 y P12. Los principales contribuyentes a la energía total en estos puntos son los oleajes generados en el Océano Austral. Ambos puntos reciben también una baja cantidad de energía del hemisferio norte. P11 muestra un patrón de cambio bipolar con un aumento robusto en los mares de fondo generadas por debajo de aproximadamente 40°S y un descenso robusto de las olas provenientes de latitudes más altas. El desplazamiento hacia periodos más altos y los grandes cambios esperados para la energía transportada por los mares de fondo más meridionales inducen un aumento en H_s y T_m. Los resultados en P12 muestran el mismo patrón bipolar robusto que en P11. El balance entre variaciones espectrales de distinto signo es la causa del cambio negativo pequeño proyectado en H_s.

P1 está afectado por mares de fondo generados en el Pacífico más septentrional, mares de fondo procedentes del este y mares de fondo procedentes del sur. Los cambios espectrales proyectados ponen de manifiesto un fuerte descenso de la energía y un notable desplazamiento hacia periodos más bajos coherente con los cambios negativos proyectados en H_s y T_m. La mayor parte de la energía que llega a P9 es transportada por oleajes que se originan en el hemisferio norte. Se observa un fuerte descenso con un desplazamiento hacia periodos más bajos, lo cual induce cambios negativos proyectados en H_s y T_m. P10 está afectado por oleajes muy energéticos generados por los vientos del oeste del Océano Austral. Además, también lo alcanzan mares de fondo procedentes del sureste y del noreste y mares de viento procedentes del oeste. Los cambios espectrales proyectados muestran un robusto patrón bipolar caracterizado por un aumento de los sistemas de oleaje con componente occidental y un descenso de los sistemas de oleaje procedentes de los sectores direccionales del este. Además, existe un desplazamiento de la energía hacia periodos más altos para los mares de fondo que se propagan desde el suroeste y lo contrario para las olas procedentes del este, lo que da lugar a un aumento robusto en T_m.

Los cambios en las condiciones del oleaje en el Océano Índico se estudian en P14 y P8. P14 es alcanzado principalmente por tres sistemas de olas: mares de fondo del Océano Austral procedentes del sur y del sureste y mares de fondo procedentes del noreste. Mientras que se obtiene un fuerte aumento en los mares de fondo del sur, se observa un descenso robusto para los otros dos sistemas de olas. Además, se observa un desplazamiento hacia periodos más bajos para las olas procedentes del este y un desplazamiento hacia periodos más altos para la energía del Océano Austral. Esto se traduce en descensos robustos en H_s y T_m. P8 es alcanzado por mares de fondo generadas en el Océano Austral, por olas generadas en el Índico tropical que se propagan desde el oeste y mares de viento del noroeste. Se observa un descenso poco robusto para los mares de fondo tropicales. Por el contrario, se encuentra un aumento robusto de la energía transportada por los mares de fondo generadas en el Océano Austral con un cambio a periodos más altos. Los parámetros de oleaje integrados indican un descenso robusto de H_s.

Conclusiones

A partir de un enfoque novedoso, se comparan las condiciones espectrales actuales y futuras del oleaje en un escenario de altas emisiones a partir de un conjunto de proyecciones climáticas de oleaje de siete miembros. El análisis espectral en catorce puntos distribuidos globalmente ayuda a comprender la propagación de los cambios proyectados del oleaje desde las zonas de generación a través de las cuencas oceánicas. Por ejemplo, se observa un aumento proyectado de la energía de los mares de fondo del Océano Austral en todas las cuencas oceánicas y en ambos hemisferios, lo que es especialmente relevante en la costa oeste de América del Norte debido a la penetración de estos oleajes más allá de los 30°N. Del mismo modo, se observa un descenso robusto de la energía de los grandes mares de fondo del Atlántico Norte cerca del ecuador.

Este trabajo demuestra que el análisis de los cambios proyectados en el clima del oleaje basados únicamente en los parámetros de oleaje integrados (por ejemplo, H_s y T_m) pueden enmascarar la información relevante sobre el signo, la magnitud y la robustez de los cambios reales del oleaje debido a la compensación entre variaciones positivas y negativas dentro del espectro, lo que conduce a una subestimación significativa del cambio asociado a determinados sistemas de oleaje.

Análisis del efecto del cambio climático en el clima del oleaje a partir de espectros direccionales

Introducción

El enfoque estándar para evaluar el comportamiento futuro de las condiciones del oleaje consiste en analizar los cambios previstos en los parámetros integrados del estado de mar (por ejemplo, H_s, T_m o Θ_m). En particular, el parámetro H_s ha sido el más estudiado ya que sus cambios se consideran una representación válida de las variaciones esperadas en la energía capturada en el espectro completo. La evaluación de los cambios en T_m o en variables que integran tanto la altura de ola como el periodo, como es E_f, está ganando popularidad. Este hecho demuestra los avances de la comunidad climática para alcanzar un conocimiento más amplio del efecto del cambio climático sobre las olas del viento, no estando constreñidos a las limitaciones que ofrece el análisis de sólo H_s. Además, la probada influencia del periodo y la dirección de las olas en los cambios en procesos costeros como, por ejemplo, la evolución de la línea de costa, proporciona una razón de peso para ampliar el análisis a otros parámetros integrados menos analizados. Más recientemente, se han desarrollado nuevos estudios basados en el análisis de sistemas de oleaje individuales a través de su H_s asociado. Aunque estos análisis no se basan en los datos espectrales, sino que se derivan de los parámetros integrados mediante una formulación de seguimiento de oleaje, han demostrado la existencia de diferentes señales de cambio climático para distintos sistemas y la importancia de la direccionalidad.

Este estudio pretende ir más allá, contribuyendo a la comprensión del comportamiento futuro del oleaje a nivel global mediante la evaluación de los cambios proyectados en la energía de las olas a partir de espectros direccionales. El alcance no sólo se limita a proporcionar una visión global de los cambios proyectados, sino también a identificar patrones regionales de cambio que permitan describir el comportamiento futuro de los principales sistemas de oleaje que se propagan por los océanos.

Datos climáticos

Este estudio utiliza las mismas proyecciones climáticas de oleaje descritas anteriormente formadas por un conjunto de siete miembros. Las condiciones actuales y futuras de las olas se caracterizan mediante periodos temporales de 20 años (1986-2005 y 2081-2100, respectivamente). Los cambios se evalúan para el escenario de concentración RCP8.5. Además, se desarrolla una simulación para el periodo histórico con forzamientos del ERA5 y la misma configuración del modelo numérico utilizada para generar las proyecciones dinámicas para ser utilizada como referencia.

En este estudio se utilizan series temporales horarias de H_s y datos espectrales. Los espectros direccionales son reconstruidos a partir de particiones espectrales. El número de particiones espectrales almacenadas es un compromiso entre una reconstrucción precisa de los espectros completos y una cantidad razonable de datos a almacenar. En este caso, se utilizan tres particiones espectrales, dos de ellas correspondientes a mares de fondo y la restante relacionada con el mar de viento. Para cada partición se almacenan los parámetros H_s, T_p, Θ_m y Spr_Θ.

Métodos

Resumen de la metodología

La Fig. 15 muestra un diagrama de flujo que resume el esquema seguido en este estudio. La metodología se basa en un conjunto de proyecciones climáticas de oleaje de siete miembros. Como resultado de las simulaciones, se genera un conjunto de datos espectrales globales compuesto por tres particiones espectrales. A continuación, se reconstruyen los espectros a partir de la información particional globalmente con una resolución espacial de 8 grados. Los cambios proyectados en el clima del oleaje se estiman comparando las climatologías medias presentes y futuras. Los cambios medios anuales resultantes se clasifican geográficamente en dieciséis regiones oceánicas con un patrón similar de cambio espectral mediante el algoritmo k-medias. Finalmente, se exploran los mecanismos subyacentes a los cambios encontrados en los sistemas de oleaje mediante el método ESTELA.

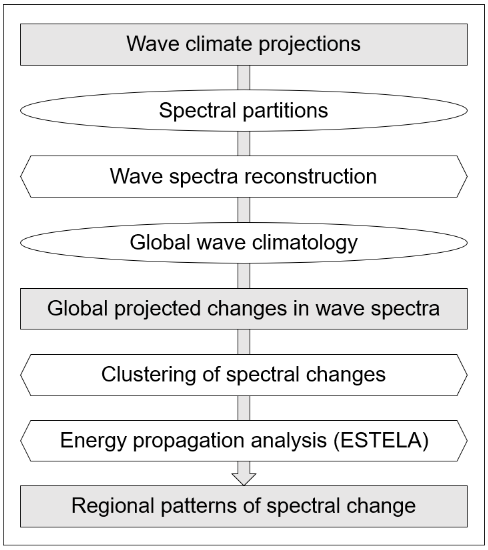

Fig. 15 Esquema general de la metodología. Los rectángulos representan resultados principales, las elipses resultados intermedios y los hexágonos métodos.

Reconstrucción espectral

La reconstrucción de espectros direccionales se realiza considerando que cada partición espectral tiene la forma del espectro JONSWAP con $\gamma = 3{,}3$, $\sigma_a = 0{,}07$ y $\sigma_b = 0{,}09$. Entre las diferentes funciones de dispersión direccional propuestas en la literatura, se selecciona la formulación de Mitsuyasu. En este estudio, la energía espectral se discretiza en 32 celdas de frecuencia y 24 sectores direccionales.

La reconstrucción se valida por comparación con espectros direccionales completos igualmente discretizados en tres localizaciones de diferentes cuencas. Como resultado se observa una ligera sobreestimación de la energía total en los espectros reconstruidos del 4%, 7% y 3% para espectros localizados Pacífico Sureste, Atlántico Noroeste e Índico Suroeste, respectivamente.

Método ESTELA

El método ESTELA permite estudiar la propagación de la energía del oleaje desde la zona de generación hasta cualquier localización oceánica suponiendo que viaja siguiendo los grandes círculos. El flujo de energía efectivo que se propaga hacia un lugar objetivo desde cualquier punto del océano se calcula a partir de criterios geográficos y físicos. El flujo de energía efectivo medio anual se calcula para los periodos de tiempo actuales y futuros en los puntos de interés para todos los miembros del conjunto. A continuación, se estima el cambio medio proyectado del conjunto en el flujo de energía efectivo medio anual y se evalúa la incertidumbre asociada.

Cambios proyectados y evaluación de incertidumbre

Evaluamos las diferencias entre el clima del oleaje actual y el proyectado para finales de siglo bajo el escenario de alta concentración RCP8.5. El cambio proyectado se estima como el cambio medio del conjunto no ponderado, es decir, se calcula como la media de los cambios individuales de cada miembro asumiendo una contribución homogénea de todos ellos.

El método propuesto para evaluar la incertidumbre de los cambios proyectados considera cambios robustos cuando más del 80% de los miembros presentan un cambio estadísticamente significativo con un nivel de confianza del 95% y al menos el 80% de ellos coinciden en el signo del cambio. La significancia estadística se calcula aplicando un test-t heterocedástico a la media de los periodos histórico y futuro con un nivel de confianza del 95%. Los cambios proyectados en H_s se evalúan de acuerdo al mismo método. Los cambios proyectados en el flujo de energía efectivo se consideran robustos cuando el valor absoluto del cambio es superior a la desviación estándar entre modelos.

Clustering

Los cambios proyectados en la energía espectral media anual se agrupan para identificar las regiones oceánicas con un patrón de cambio similar. Tras probar varias técnicas de clustering, seleccionamos k-medias. Se aplica k-medias a los cambios espectrales considerando las celdas espectrales como variables y los espectros como observaciones.

Resultados

Los cambios espectrales (Fig. 16) evidencian la propagación de la señal de cambio asociada a cada sistema de olas desde la zona de generación. Los resultados muestran un aumento robusto en los mares de fondo del oeste generadas en el Océano Austral. La señal de aumento se propaga hacia el norte en todas las cuencas oceánicas, alcanzando latitudes más allá de los 30°N en los océanos Pacífico y Atlántico. Además, este aumento contribuye significativamente al cambio proyectado en las zonas tropicales como, por ejemplo, en el Pacífico Sureste tropical.

Se observa un descenso robusto en la energía de los mares de fondo generados en el Atlántico Norte extratropical. La señal de descenso se propaga hacia el sur, combinándose en la región tropical con los descensos previstas en las olas generadas por los vientos alisios. Más al sur, la señal de descenso del Atlántico Norte extratropical converge alrededor del ecuador con los cambios proyectados en los mares de fondo provenientes del Atlantico Sur extratropical y los cambios proyectados en las olas tropicales.

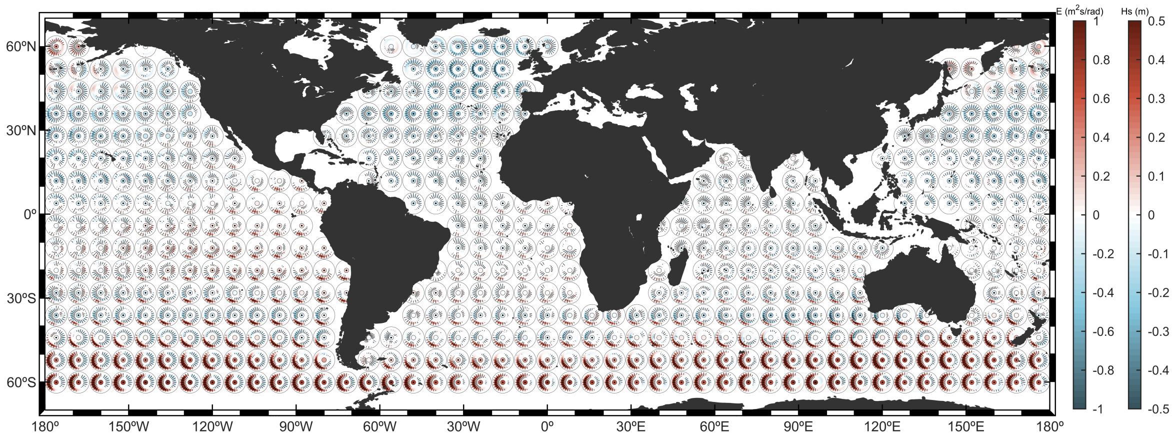

Fig. 16 Cambios medios proyectados del conjunto en la energía espectral media anual del oleaje (gráficos polares) y H_s (puntos en el centro de los gráficos polares) bajo el escenario RCP.8.5 para finales de siglo. El punteado indica cambios robustos.

Los cambios en el Pacífico Norte extratropical no presentan un patrón homogéneo como en el Atlántico Norte. En primer lugar, los espectros en las latitudes más altas muestran un aumento general de la energía. A medida que nos desplazamos hacia el sur, se puede identificar fácilmente un aumento de energía asociado a los mares de fondo del oeste. Esta señal de cambio positivo evoluciona hacia un cambio negativo a medida que nos alejamos del polo. La propagación de estos mares de fondo hacia la región tropical hace que su señal de cambio se combine con el descenso de las olas tropicales inducida por los alisios y con el aumento previsto de los mares de fondo del Océano Austral. El patrón de cambio espectral en el Océano Índico se caracteriza principalmente por la combinación de los aumentos previstos en los mares de fondo del Océano Austral y los cambios asociados a las ondas tropicales inducidas por los vientos alisios. En cuanto a la región noroeste, la zona del Océano Índico fuertemente afectada por el Monzón, se espera un fuerte descenso de la energía de los sistemas de oleaje generados por los vientos inducidos por este fenómeno.

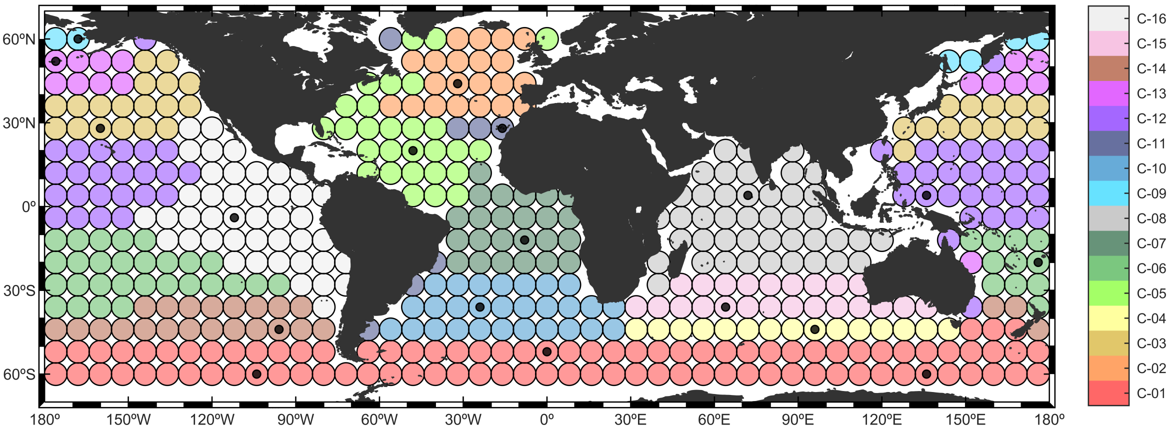

Fig. 17 Dieciséis patrones regionales de cambio espectral. Los puntos negros indican la ubicación de referencia utilizada para analizar cada grupo.

Para completar el análisis espectral, agrupamos los cambios espectrales medios anuales. Se encuentran dieciséis grupos distribuidos por las cuencas oceánicas con un patrón de cambio espectral similar (Fig. 17). Los resultados permiten apreciar un aumento robusto de la energía transportada por los mares de fondo del oeste generados al sur de 45°S, así como una clara transición hacia una señal de cambio decreciente al norte de dicha latitud. Esto es causado probablemente por un desplazamiento hacia el polo de la trayectoria de los ciclones extratropicales del hemisferio sur, lo que induce un descenso en H_s al norte de la latitud mencionada.

El comportamiento proyectado en la región extratropical del hemisferio norte es significativamente diferente entre el Atlántico y el Pacífico. Mientras que el océano Atlántico muestra un descenso homogéneo independientemente de la zona de generación, el océano Pacífico muestra tres patrones de cambio espectral diferentes. En el Pacífico, el efecto combinado del deshielo en latitudes altas y el cambio previsto en la trayectoria de los ciclones extratropicales provoca una transición aumento-descenso en dirección norte-sur en la energía de los oleajes del oeste, de forma similar a lo que ocurre en el Océano Austral. Además, este análisis permite observar más claramente el efecto del desplazamiento hacia el polo que se espera en los vientos alisios debido a la expansión de la célula de Hadley. Esta expansión domina los sistemas de oleaje generados por los alisios en las cuencas del Atlántico Sur y del Índico Sur, induciendo un patrón de cambio bipolar e impidiendo determinar una señal de cambio clara asociada a la energía del oleaje.

Conclusiones

Este estudio proporciona una explicación detallada sobre los cambios proyectados a finales del siglo XXI en la climatología global del oleaje bajo un escenario de altas emisiones de gases de efecto invernadero mediante la evaluación de los cambios en espectros direccionales de oleaje. Estimamos los cambios en el oleaje comparando las climatologías actuales y las proyectadas a partir de un conjunto de proyecciones climáticas de oleaje formado por siete miembros. Con base en los cambios espectrales, se aplican técnicas de agrupación para definir patrones regionales de cambio con un comportamiento homogéneo. Posteriormente, se exploran los mecanismos subyacentes a los cambios analizando la relación entre el área de generación de olas y el flujo de energía efectivo que se propaga hacia un lugar objetivo.

Se ha encontrado una transición de cambio positivo a negativo alrededor de los 45°S en los mares de fondo del oeste que se propagan en el Océano Austral. El incremento asociado a los mares de fondo más meridionales se propaga hacia el norte más allá de los 30°N, contribuyendo significativamente a los cambios proyectados en regiones tropicales como el Atlántico Sur tropical y el Pacífico Sureste tropical. Los resultados ponen de manifiesto la gran complejidad del Océano Pacífico como consecuencia de la convergencia de múltiples sistemas de oleaje con diferentes orígenes. En el Pacífico Norte extratropical, el efecto combinado del deshielo y del desplazamiento hacia el polo de la trayectoria de los ciclones extratropicales induce un incremento en la energía del oleaje del oeste más septentrional. Por el contrario, en el Atlántico Norte se aprecia un descenso generalizado en los principales sistemas de oleaje. Así mismo, se observa un desplazamiento generalizado hacia el polo de las olas generadas por los vientos alisios debido a la expansión de la célula de Hadley, lo que provoca un claro patrón de cambio de bipolar en el Atlántico Sur tropical e Índico Sur tropical.

Conclusiones y futuras líneas de investigación

Conclusiones

En este apartado se resumen las principales aportaciones realizadas y las conclusiones alcanzadas a lo largo de esta tesis.

- Tras finalizar la investigación de la tesis y recapitular los estudios desarrollados en base a los tres elementos centrales de análisis descritos al principio de este documento, se puede concluir que se ha avanzado en el estado del arte y que se han cumplido todos los objetivos generales planteados. Se proponen métodos específicos para una mejor caracterización de las condiciones climáticas del nivel del mar y del oleaje, permitiendo comprender mejor el comportamiento de las condiciones extremas de ambas dinámicas a escala global.

- Esta tesis demuestra que los datos de altimetría satelital pueden utilizarse para caracterizar los eventos costeros extremos de nivel del mar con una precisión significativa. Por lo tanto, este tipo de datos podría ser una alternativa válida a los datos de los mareógrafos y de modelos numéricos, especialmente en las zonas costeras cuando estas fuentes de datos no están disponibles.

- Se ha propuesto una metodología novedosa para estudiar el comportamiento de los extremos de nivel del mar a partir de datos altimétricos. La metodología está basada en datos inter-calibrados de múltiples misiones satelitales. El estudio se centra en el análisis de la componente residuo meteorológico del nivel de mar. El método se ha calibrado y validado utilizando la información proporcionada por mareógrafos. El análisis se ha realizado a nivel regional a lo largo de la costa este de América del Norte y a escala global.

- Esta tesis proporciona una evaluación global de la tormentosidad del oleaje a lo largo de la costa mundial. El análisis se ha realizado utilizando un criterio global único, lo cual ha permitido la comparación entre diferentes regiones costeras.

- Se han analizado las características más relevantes de los temporales de oleaje, tales como la frecuencia de ocurrencia, la duración y la intensidad. Además, se han evaluado los parámetros integrados del estado de mar medios durante los temporales: altura de ola significante, dirección media, periodo medio y flujo de energía. Para completar el análisis, se han examinado otras características secundarias de los temporales de oleaje, tales como el predominio de la energía del mar de viento frente a la del mar de fondo o el predominio en el flujo de energía del periodo de las olas frente a la altura de las mismas.

- La costa mundial se ha clasificado en función de la tormentosidad del oleaje en base a una nueva métrica que integra la frecuencia de ocurrencia de los temporales y su intensidad.

- Se ha evaluado la variabilidad de los extremos de residuo meteorológico a partir de datos de altimetría lo largo de la costa mundial considerando tres escalos temporales: dentro del año, tendencias a largo plazo e interanual.

- La altimetría satelital ha demostrado una buena habilidad para reproducir la variabilidad de los extremos del nivel del mar mediante la validación con un conjunto global de 123 registros de mareógrafos. Los resultados han mostrado buenas correlaciones y bajos errores para las variaciones climáticas dentro del año y entre años (interanuales). Además, se han encontrado resultados aceptables en la estimación de las tendencias a largo plazo.

- Se han obtenido cambios proyectados robustos en más del 25% de la superficie oceánica en H_s para periodos de retorno de 5 a 100 años para finales de siglo bajo los escenarios de concentración RCP4.5 y RCP8.5. El Océano Austral es la región en la que se proyecta el aumento más acusado de los extremos de H_s, mientras que el Pacífico Norte tropical muestra el descenso más significativo en los extremos de H_s.

- Los cambios en los fenómenos extremos de H_s son menores y menos robustos para el RCP4.5 que para el RCP8.5. La robustez de los cambios proyectados se reduce de la segunda a la primera globalmente en torno al 10% para todos los periodos de retorno estimados.

- Se han encontrado fuertes discrepancias tras comparar el comportamiento futuro de las condiciones medias y extremas del oleaje. Las principales regiones oceánicas que muestran comportamientos divergentes son el Índico Sudeste, Atlántico Noroeste y Pacífico Noreste, proyectando todas ellas un aumento de los valores de retorno de H_s y un descenso de la H_s media.

- El análisis de los futuros cambios en el clima del oleaje a partir de los espectros de frecuencia-dirección en catorce lugares del océano ha demostrado que el enfoque estándar basado en parámetros integrados del estado de mar puede enmascarar información relevante sobre los cambios proyectados acerca de su magnitud, signo y robustez.

- El uso de parámetros integrados del estado de mar puede llevar a resultados engañosos en los estudios de evaluación de impacto, ya que podrían enmascarar aumentos importantes de la altura y/o el periodo de las olas.

- La evaluación del comportamiento futuro del oleaje basada en los espectros dirección-frecuencia de las olas a escala global aumenta significativamente la comprensión de los cambios proyectados debido al cambio climático.

- La señal de cambio individual de cada sistema de olas se propaga a través de los océanos, de modo que el cambio proyectado en cada lugar del océano puede integrar los cambios individuales de sistemas generados localmente o en áreas remotas.

- El análisis global del comportamiento futuro del oleaje a partir de espectros de oleaje ha permitido identificar 16 patrones regionales de cambio espectral.

Futuras líneas de investigación

Esta sección resume los trabajos en curso y las posibles líneas de investigación futuras derivadas de los análisis realizados a lo largo de esta tesis.

- Los nuevos retrackers de altimetría costera están mejorando continuamente la precisión de las mediciones altimétricas cerca de la costa y reduciendo las distancias a la costa en las que los datos altimétricos son fiables. La incorporación de estos nuevos productos de altimetría con mayor precisión a la metodología propuesta podría mejorar la caracterización de los eventos extremos del nivel del mar y reducir las diferencias encontradas con respecto a los datos de los mareógrafos.
- Se proponen varios componentes de corrección para reducir las diferencias entre los valores de retorno de altimetría y mareógrafos. Es necesario explorar nuevos componentes de corrección, así como posibles mejoras de los aquí propuestos.
- Es necesario definir un método para definir en una localización costera aleatoria la forma y la extensión del área dentro de la cual deberían seleccionarse los datos satelitales para poder aplicar la metodología de análisis extremal.
- La metodología propuesta para el análisis extremal de nivel del mar a partir de datos altimétricos podría aplicarse a eventos extremos de otras dinámicas superficiales marinas, como las olas del viento, utilizando boyas como referencia de calibración en lugar de mareógrafos.
- Se ha planteado un análisis del oleaje costero a lo largo de la costa mundial basado en un criterio único. Este enfoque es muy útil, ya que permite comparar los resultados de diferentes regiones geográficas. Sin embargo, dado que los temporales de oleaje pueden tener diferentes orígenes, la metodología podría mejorarse seleccionando individualmente los umbrales y/o los tiempos de independencia necesarios para clasificar los eventos de temporal para cada ubicación costera.
- En este documento se ha clasificado la costa mundial en función de su grado de tormentosidad de oleaje. Sin embargo, los temporales costeros implican otras dinámicas superficiales marinas más allá del oleaje, como el nivel del mar. Por ello, podría seguirse un enfoque similar al propuesto en esta tesis para evaluar el temporal costero teniendo en cuenta diferentes componentes del nivel del mar en la definición de los temporales.
- El capítulo 4 ha analizado la variabilidad a largo plazo de los fenómenos extremos de residuo meteorológico. Los resultados han mostrado un aumento generalizado, probablemente inducido por el aumento del nivel medio del mar. No obstante, se

necesitan estudios más detallados para dilucidar las causas de estos cambios a largo plazo.

- El capítulo 5 ha evaluado los cambios proyectados en las alturas de ola con muy baja probabilidad de ocurrencia y ha discutido sobre las posibles causas de los cambios encontrados. Sin embargo, se requieren estudios más profundos para identificar las causas reales de los cambios proyectados encontrados, así como las razones para la gran incertidumbre encontrada en algunas regiones oceánicas.
- La evaluación de los cambios proyectados en las condiciones extremas de oleaje debido al cambio climático se caracteriza por una gran incertidumbre. Es necesario seguir investigando sobre las causas de esta incertidumbre.
- El capítulo 5 ha demostrado que el comportamiento futuro de las condiciones climáticas medias y extremas del oleaje es divergente en algunas regiones oceánicas. Es necesario seguir investigando para identificar las causas de estas divergencias.
- Las técnicas estándar de corrección del sesgo aplicadas a las variables meteorológicas son una práctica común para estimar los cambios proyectados en el clima del oleaje. No obstante, es necesario el desarrollo de nuevas estrategias enfocadas a la corrección del sesgo en eventos extremos de oleaje.
- A pesar de que existen varios métodos para corregir el sesgo de los parámetros integrados del estado de mar, estos no pueden ser aplicados de forma directa para corregir el sesgo de espectros direccionales. Por lo tanto, se requiere el desarrollo de nuevas metodologías para la corrección del sesgo en espectros.
- El capítulo 7 ha mostrado un claro límite de cambio en 45°S en la energía del oeste que se propaga en el Océano Austral. Mientras que al sur de esa latitud se proyecta un aumento, al norte se proyecta un descenso. Es necesario un análisis detallado para desentrañar las causas e implicaciones de este comportamiento bipolar.
- La disponibilidad de particiones espectrales a partir de hindcasts o reanálisis de oleaje es cada vez mayor. Se necesitan nuevas metodologías para clasificar particiones espectrales desde un punto de vista climático.
- A pesar de que la información proporcionada por los espectros de oleaje es muy útil para entender el comportamiento futuro de las olas del viento, su aplicabilidad en la evaluación del impacto costero es muy compleja. El aislamiento de los sistemas de olas y el posterior análisis de los cambios proyectados en sus características y en la variabilidad climática podrían permitir identificar más fácilmente qué sistemas inducirán impactos más severos en el futuro.

- Esta tesis ha investigado sobre las componentes del nivel del mar y el oleaje. Dado que la cota de inundación resulta de la combinación de ambas dinámicas superficiales marinas, estudios futuros pueden centrarse en estudiar la contribución combinada de ambas en eventos extremos de esta variable. La caracterización de la peligrosidad de los eventos extremos de cota de inundación con otros componentes del riesgo, como la exposición, puede ser útil para identificar zonas de alta vulnerabilidad.

Chapter 1

Introduction

1.1 Background and motivation

The ocean sea surface is a living element. Every instant it takes a shape never seen before, molded by the dynamics coexisting in it, such as wind waves, sea level and currents. Among all of them, ocean wind waves (or simply wind waves or waves) are undoubtedly those more characteristically shaping the surface for someone beholding the sea. Waves may propagate in an orderly manner, showing parallel and regularly sequenced fronts, drawing a regular sea surface pattern, which sometimes seems artificially created, that depicts a peaceful picture of the sea. On the other hand, the chaos under stormy climate conditions, characterized by waves propagating without an evident order, depicts a wild and fierce sea surface picture. Therefore, the direction and height of the propagating waves, the distances between fronts and, ultimately, the combination of all these elements, create an infinite number of sea surface patterns. Wind waves are generated by the sustained wind blowing over the sea surface. After generation, waves propagate away from the generation areas, classifying in groups of similar characteristics, sometimes traveling thousands of kilometers until reaching the coast.

Wind waves do not propagate over a constant sea level. This surface dynamic also varies through time as a result of the intrinsic variability of components with different origins. The sea level is, in part, modulated by astronomical forcings. The astronomical tide is generated by the gravitational attraction of the moon and the sun over massive water bodies on the earth crust (Pugh, 1987). The contribution of the tidal component varies across the oceans, as well as its variability pattern. Regarding the former, the tidal range varies from zero at specific ocean locations (i.e. amphidromic points) to more than 10 meters in coastal areas such as the Bay of Fundy (Canada) and the English Channel. The intrinsic tidal variability resulting from the combined influence of the moon and the sun lead to diurnal, semidiurnal and mixed tides, depending on whether the tide shows one or two cycles per day, or a combination of both, respectively (Gerkema, 2019; Short, 1991). Other sea level components are driven by atmospheric forcings. Atmospheric pressure gradients induce changes in sea level according to the inverse barometer effect. Additionally, the sustained wind blowing toward the coast may induce sea level variations in the coastal zone. The wind waves setup is also an important sea level component nearshore, especially for extreme waves (Melet et al., 2018). Marine currents may also generate sea level disruptions, although at minor scale than the previously described components. As expected, the interaction between wind waves and the sea level plays a more important role in the coastal zone as water depth reduces. At low depths, sea level variations may significantly change the height of the water column through which wind waves propagate. This issue mainly affects the degree of interaction between waves and the sea floor, which alters the wave characteristics (mainly wave height and direction) and, ultimately, the wave breaking zone and properties.

Extreme events of sea surface dynamics may cause significant impacts both in the deep ocean and the coastal zone. Extreme wave heights may prevent the normal operation of seagoing shipping routes, causing unexpected waiting times in ports, on route mechanical problems or route deviations to avoid extreme wave conditions (Notteboom, 2006; Rawson et al., 2021). Also, extreme waves might cause severe damage to offshore infrastructures, such as gas platforms or wind turbines (Haritos, 2007). In the coastal zone, extreme wave heights can alter the mean equilibrium along the coastline, inducing major shoreline erosion events, sometimes naturally irreversible. Extreme sea level (ESL) variations are not only more evident, but also more potentially damaging nearshore as the water depth reduces. Extreme sea levels can induce flooding episodes, especially in low lying areas, that penetrate inland, likely causing important damage (Kates et al., 2006). Moreover, the combination of both, mostly under storm conditions, could lead to catastrophic consequences. High sea levels delay the breaking of high waves, thus allowing them to penetrate further inland with two main results: higher eroding capacity and higher wave setup, which combined with ESLs, likely lead to more damaging flooding episodes.

In this context, a deep understanding of the characteristics of extreme events of sea surface dynamics is strongly required. The study of ESLs has been traditionally addressed through the information offered by tide gauge (TG) stations. Nevertheless, the information they provide is restricted to very small areas due to the strong dependency between TG records and the station location, precluding fair extrapolations to adjacent zones. In addition, the global coverage is heterogeneous, which also limit their use at large scales. The development of new databases that can overcome the intrinsic weaknesses of TG records is therefore necessary. Numerical modelling is the most accurate alternative today, although still limited by the computational demand of numerical models. Satellite altimetry offers global information of sea level since the 90's, thus also being a potential alternative to numerical and TG data. These type of data present a number of limitations that prevent a more widespread use:

an irregular spatial and time sampling, and a significant decrease off accuracy nearshore. Despite these weaknesses, the time period covered of approximately 30 years from 1992 to 2022 and the continuous improvement of accuracy, especially in the coastal zone, make them attractive today to be used in applications traditionally developed using other data sources. However, *can altimetry data be a reliable source of information to analyze ESLs?* This approach would be especially noteworthy for coastal areas where no in situ information is available, nor numerical high-resolution simulations.

With regard to wind wave extremes, their characterization has been subject of study for a long time, mainly seeking to correctly assess their induced impacts. These studies are normally developed based on wave hindcast or reanalysis products. In contrast to sea level studies, wave climate numerical products have clearly surpassed the use of instrumental in situ data (mainly buoys). The reasons are, first, the fact that wave propagation models demand lower computational effort than sea level models. Second, all the drawbacks experienced by buoys, some of which are similar to those of TG stations, such as providing very local information, irregular coverage of the ocean and being prone to suffer sudden shut downs under extreme climates. The use of altimetry data to study wave climate is also common practice, especially across the deep ocean and to characterize mean wave conditions. Regarding wave extremes, despite some studies have already estimated return period wave heights using these data, the abrupt increase of uncertainty for extreme wave heights (Dodet et al., 2020) still holds back their use to characterize extreme wave magnitudes today. Note that wave extremes are characterized differently depending on their further application. The design of offshore structures (e.g., floating wind turbines, gravity based founded platforms) or coastal protection structures (e.g., rubble mound breakwaters), require knowledge of the most extreme waves reaching a target location. For that matter, extreme sea states are represented through wave heights with very low probability of occurrence, namely events with high return periods. This analysis is normally conducted based on the extreme value theory (EVT; Coles 2001), which models the behavior of the tail of the distribution of a variable. On the other hand, the assessment of coastal impacts, such as coastal erosion and shoreline retreat, are based on the concept of coastal storms (Harley et al., 2017). By definition, coastal storms must comprise at least extreme magnitudes of one sea surface dynamic. However, they usually combine intense events of more than one dynamic with strong winds and/or heavy rains. Wind waves play a key role within coastal storms. In this regard, wave storms can be defined as wave height events significantly exceeding the mean coastal wave conditions, thus potentially altering the mean equilibrium along the coastlines. The analysis of the coastal wave storminess has been addressed based on different criteria, although always at local or regional scales. Then, *is it possible to assess the wave storminess along the global coastlines based on a unique criterion?*

Beyond the characterization of the magnitudes of sea surface dynamics, a deep understanding of their behavior also requires knowledge of their variability at different time scales.

In this regard, previous studies have demonstrated that the magnitudes of both sea level and wind waves vary within the year. This variability modulates the behavior of mean conditions (Young, 1999) and enhances for extremes (Cid et al., 2016). Sea level and wave climate conditions also vary between years, i.e. magnitudes experience an interannual variability. In particular, the interannual variability of extreme events has been demonstrated to be intimately correlated with climate teleconnection patterns (Menéndez and Woodworth, 2010). Particularly interesting are the long term trends expected in magnitudes of these sea surface dynamics, especially those attributable to the effect of climate change. Climate change is affecting the sea level by inducing a global mean sea level rise (MSLR; Cazenave et al. 2014; Nicholls and Cazenave 2010). Global mean sea level (MSL) is projected to increase 0.84 m (0.61-1.10 m) by 2100 under the current emission conditions (IPCC, 2019). These changes are critical in low lying areas, where small changes in MSL may originate severe impacts on the coast, causing more frequent and strong flooding episodes (Vousdoukas et al., 2020b), and generating shorelines retreat (Marsooli et al., 2019). Additionally, MSLR has been proven to be the main driver of the effect of climate change on sea level extremes (Menéndez and Woodworth, 2010; Vousdoukas et al., 2020b). Nevertheless, while the variability of wave climate extremes has been assessed globally, particularly based on altimetry data (Izaguirre et al., 2011), a similar reference cannot be found for sea level to date. Therefore, *would it be possible to assess the global variability of ESLs from altimetry data as it has been done for wind waves?*

The future behavior of wind wave climate has been widely studied during the last two decades. These studies are mainly carried out through development of wave climate projections. These projections include wave climate information for different future time slices and green-house gas (GHG) concentration scenarios. They are developed through numerical models or statistical methods fed with atmospheric and physical forcings output of general (GCM) or regional (RCM) circulation models (statistical and dynamical projections, respectively). The Coordinated Ocean Wave Climate Project community (COWCLIP) collects the studies on the matter and analyzes the uncertainty in the projected changes (e.g., Morim et al. 2019, 2020). Consensus has been reached on the expected long term changes in mean wave conditions in some ocean regions, such as a decrease in the North Atlantic Ocean, an increase in the Southern Ocean and an increase in the tropical eastern Pacific Ocean. Uncertainty increases when assessing changes in extreme wave conditions. In fact, the number of studies analyzing the future behavior of return period wave extremes is still very low (e.g., Meucci et al. 2020), besides most of them only providing relative changes. Thus, some questions still arise on this matter, *what are the change magnitudes projected in return period wave extremes? Are long term variations induced by climate change in wind wave mean conditions consistent with projected changes in extreme conditions?* Regarding the latter, a different projected behavior would lead to severe misinterpretations for derived impact studies if an extrapolation from the consensus expected in mean wave conditions is assumed.

Most studies on this matter have been conducted based on wave parameters that integrate the information about all the waves converging in a sea state (i.e., period of time in which wave conditions are assumed to be stationary) in certain ocean location. Despite complete information about the sea state being only represented through the wave energy frequency-direction spectrum (hereinafter directional spectrum), these parameters are traditionally used instead mainly for the shake of simplicity and lower storage demand. The most common integrated wave parameter used to represent the wave climate conditions and, consistently, to assess the effect of climate change on wave climate, is the significant wave height (H_s; Mori et al. 2013). Others, such as the mean wave period (T_m), the peak wave period (T_p), the mean wave direction (Θ_m) and the wave energy flux (E_f) are also commonly assessed (e.g., Hemer et al. 2013a). Only a few studies have gone beyond the standard approach and tried to consider the coexistence of waves with different origins within a sea state, explaining the future behavior of waves by assessing the changes in individual wave systems, although always building upon integrated parameters and not on spectral information (e.g., Lemos et al. 2021a). In this context, the following questions inevitably arise: *Are integrated wave parameters masking relevant information about the future changes in wave climate? Is it possible to deep on the effect of climate change on wave climate using the wave spectrum?*

1.2 Objectives

The present dissertation is framed in the context previously depicted. The main objectives are described below:

- Develop new methodologies and climate products to improve the characterization of extreme events of sea surface dynamics.
- Improve understanding of the global variability of extreme events of sea surface dynamics at different time scales.
- Improve understanding of the long term variability of wind waves due to the effect of climate change through the directional spectrum.

The specific objectives of this dissertation (henceforth *S.Obj.*), which try to give an answer to all the questions *highlighted* throughout the motivation section, are summarized below:

1. Explore the use of satellite altimetry data to characterize coastal ESLs.
2. Analyze the main characteristics of wave storms impacting the global coastlines based on a unique criterion.

3. Classify the global coastlines in terms of their wave storminess.
4. Assess the variability of ESLs along the global coastlines at different time scales from satellite altimetry data .
5. Assess the long term variability of wind wave extremes with very low probability of occurrence under different GHG concentration scenarios globally.
6. Compare the future behavior of mean and extreme wind wave conditions due to the effect of climate change.
7. Explore the added value of the directional spectrum to assess the projected changes in wave climate due to climate change with respect to the standard use of integrated wave parameters, highlighting the information the latter could mask.
8. Assess the projected changes in wave climate from directional spectra globally.
9. Assess the individual change of the main swell systems propagating across the oceans.

1.3 Dissertation structure

This dissertation is structured based on the objectives described above. The research framework hinges on the three elements depicted in Fig. 1.1 and their interrelationships. Sea level and wind waves sea surface dynamics are the main variables involved in the analyses conducted and constitute the first pivotal element. As it was mentioned above, these variables, alone and combined, play a key role on the marine impacts in both the deep ocean and the coastal zone. These impacts are mainly caused by dynamics' extreme events, thus being the extreme analysis of sea level and wind waves the second pivotal element of the dissertation. Finally, the third pivotal element is the assessment of the variability of these dynamics and, especially, of their extremes, with particular interest in the long term variability induced by climate change.

Cross relations between the pivotal elements (Fig. 1.1) lead to structure the document in three parts. Each of these parts is internally divided into two chapters.

Part I characterizes coastal extreme events of sea level and wind waves. Chapter 2 proposes a novel methodology based on satellite altimetry data to study coastal ESLs. Chapter 3 assesses the wind wave storminess along the global coastlines based on a high resolution hindcast.

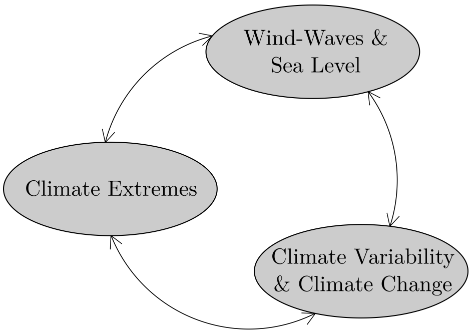

Fig. 1.1 Overall scheme of the dissertation.

Part II addresses the variability of extreme events of sea level and wind waves. Chapter 4 assesses the variability of ESLs at different time scales along the global coastlines based on satellite altimetry data. Chapter 5 assesses the long-term variability of wind wave extremes due to the effect of climate change globally. Additionally, it assesses the differences in the future behavior of extreme wave conditions and mean wave conditions.

Part III assesses the future long-term wave climate through a novel approach based on directional spectra. Chapter 6 assesses the added value of the wave spectrum to study the effect of climate change on wave climate with respect to the standard use of integrated wave parameters. Chapter 7 assesses the global changes in wave climate based on directional spectra.

To conclude, Chapter 8 summarizes the main conclusions reached throughout this dissertation and the main scientific contributions this thesis has led to. Additionally, it comprises the future research lines this dissertation may lead to.

Part I

Analysis of extreme events of sea surface dynamics

Chapter 2

Analysis of coastal sea level extremes from satellite altimetry

Abstract

This study represents the first attempt to characterize the behavior of coastal sea level extreme events from satellite altimetry data. A novel approach based on the application of a non-stationary extreme model to non-tidal residual monthly maxima is presented. The methodology is calibrated and validated using tide gauge data. Altimetry extremes show a general underestimation with respect to those from in situ observations. To counter these differences, a correction factor for altimetry data is defined, namely the extreme scale factor. The extreme scale factor depends on geographical and physical features at the location of analysis. It allows to significantly improve the accuracy of altimetry return values by reducing the mean relative error in more than 50%. The study is addressed first along the East coast of North America, and then extended to global scale.

2.1 Introduction

The rising population together with the change in natural defenses make the coastal areas particularly vulnerable to the impact of ESLs. These events have a vast destructive power in the coastal area, mainly through damaging flooding episodes that penetrate inland causing important losses. Extreme sea levels are projected to be more intense in the coming years due to the effect of climate change (Vousdoukas et al., 2018). In this regard, the MSLR has been proven to be the main driver of this projected increase (Menéndez and Woodworth, 2010). Hence, a correct characterization of ESLs variability is essential to understand not only the historical behavior of these damaging events, but also their projected behavior under the ineluctable effect of climate change.

Tide gauge stations have been considered as the main providers of coastal sea level information for centuries. For example, San Francisco TG (USA) provides data since 1854, Fort Denison TG (USA) since 1897 and Alicante TG (Spain) since 1874. Nevertheless, TGs have a series of limitations that restrict their use, such as only providing information on land margins. Therefore, their records may be affected by the local morphology, especially due to the common installation of these instruments in protected basins such as estuaries or ports. Additionally, TG stations measure sea level relative to a local godetic benchmark, causing measurements to be conditioned by vertical land signals and the stability of the surface they are built on (Denys et al., 2020; Peltier, 2001; Wöppelmann and Marcos, 2016). Furthermore, not only they provide an irregular time sampling between stations (e.g., 5-minute, hourly products) and suffer sudden operational shutdowns, but also the spatial coverage is unbalanced between continents and, on top of that, hemispheres, being most of the stations located in Northern Hemisphere (NH). Despite all these issues, the information provided by TGs is still considered as the most reliable source to analyze the sea level behavior and is widely used to develop climate studies at local (Liu et al., 2020), regional (Wahl and Chambers, 2015; Woolf et al., 2003) and global scales (Kopp et al., 2014), or also to conduct validation analyses (Kirezci et al., 2020).

The use of numerical models is a reliable alternative to in situ information to study sea level. Sea level numerical products are more accessible each day due to computational development, allowing to model sea level processes at very small scale (few meters along the coast) or to develop simulations that provide results at very large scale, even global. Despite local studies addressed through numerical modelling being common practice (e.g. Pandey et al. 2021; Silva-Araya et al. 2018), the number of large-scale sea level hindcasts is still scarce (e.g. Cid et al. 2014; Muis et al. 2020), remaining as a field open for further research within the climate community.

Satellite altimetry provides global information of sea level since the 90's (Fig. 2.1). Its global coverage and the amount of available data, approximately 30 years, make satellite altimetry a potential alternative to TG and numerical modelling data to develop climate studies on sea level and improve understanding of the ocean. First, the open ocean, where this global source of information has been extensively used for decades as a provider of MSL data, allowing the estimation of historical MSLR trends (Cazenave et al., 2014; Church et al., 2013). Second, coastal regions, where altimetry measurements may complement the information provided by TGs (Madsen et al., 2015) or even replace it where no in situ information is available (Vinogradov and Ponte, 2011). Furthermore, the coastal altimetry community is making remarkable advances in this field to increase the accuracy of these data nearshore. To achieve this goal, efforts are focused on the improvement of the corrections applied to the radar pulse (Vignudelli et al., 2011), the development of coastal re-trackers to reduce the contamination caused by land on the measurements (Passaro et al., 2014) and the combination of both (Birol et al., 2021). Despite there is still room for improvement, previous studies have already found good agreement between in situ and remote data in the coast of the United Kingdom, giving optimistic prospects with regard to the use of altimetry data along the coast (Cipollini et al., 2017). Moreover, the Climate Change Initiative (CCI) set up by the European Space Agency (ESA) in 2010 (Quartly et al., 2017), which includes the definition of a consistent sea level dataset from satellite altimetry measurements, among others essential climate variables, has encouraged the improvement of altimetry corrections to maximize the accuracy of these data (Legeais et al., 2017). As a major result of this project, MSLR trends have been recently provided with high accuracy in a set of virtual stations along the global coast (Cazenave et al., 2019), thus overcoming one of the major weaknesses of in situ information, namely the loss of accuracy nearshore.

Notwithstanding all these improvements, the information provided by satellite altimeters has not been used to analyze coastal ESLs yet. Here, we present a novel method to analyze the extreme conditions of the non-tidal residual sea level component (NTR) along the coast. The non-tidal residual component represents the variations with respect to he mean sea level not caused by astronomic forcings. The method is based on the application of a non-stationary extreme model to monthly maxima (MM) from altimetry measurements, also considering the local coastal morphology. The study has been addressed in two stages. The methodology is first defined and validated along the East coast of North America. Next, the analysis is extended to global scale. Consistently, the sections of this chapter difference between the outcomes obtained for the two spatial scales.

2.2 Climate data

Satellite altimetry data

The operating principle of satellite altimetry consists in calculating the distance between the altimeter and a reference surface, recording the traveling time of the pulse from the antenna to the ocean and back again after being reflected. The magnitude and shape of the received waves inform about the reflecting surface, thereby allowing to measure not only the sea level, but also other sea surface dynamics such as wind waves through the parameter H_s.

The range recorded by the altimeter (R_{obs}) requires a series of corrections (Fig. 2.2) that fall into two different groups: range correction and geophysical corrections (Vignudelli et al., 2011). Range corrections consider the alteration of the radar speed and the actual scattering surface of the radar pulse. Geophysical corrections essentially identify different components of the sea level to further isolate the oceanic contribution to sea surface height (SSH)

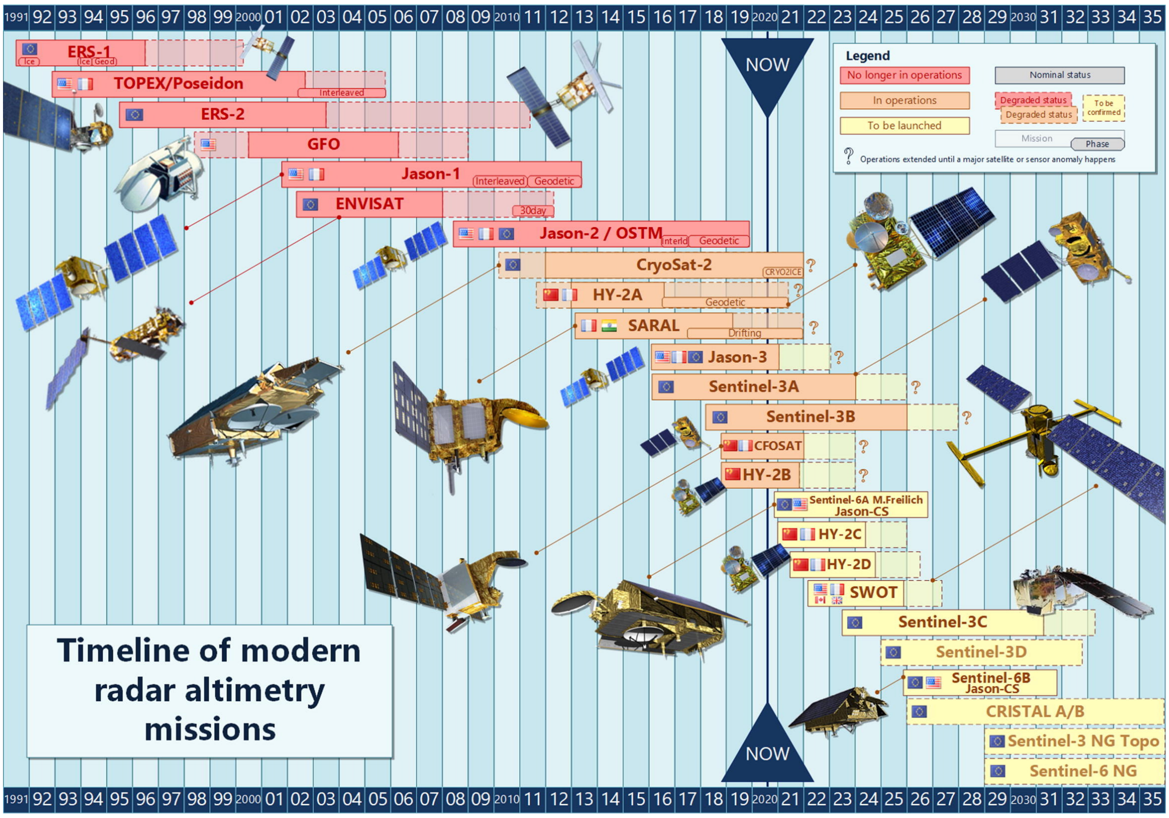

Fig. 2.1 Altimetry missions timeline (extracted from Abdalla et al. 2021).

variations (Vignudelli et al., 2011). Range corrections include the dry troposphere refraction correction (DTRC), the effect of dry gases on the radar pulse; the wet troposphere refraction correction (WTRC), refraction due to the presence of water vapor in the troposphere; the ionosphere refraction correction (IRC), wave refraction in the ionosphere; and the sea-state bias correction (SSBC), the bias of the range measurement due to the ocean wave troughs. On the other hand, geophysical corrections include the dynamic atmosphere correction (DAC), the effect of pressure and wind; the tidal component correction (TCC), the tide component of sea level; and the geoid correction (GC), the difference between the reference surface and the geoid.

Thus, the corrected range (R_{corr}) can be computed as:

$$R_{corr} = R_{obs} + DTRC + WTRC + IRC + SSBC \tag{2.1}$$

The SSH referenced to the ellipsoid is related to the total height (H_t) through the following expression:

$$SSH = H_t - R_{corr} = H_t - (R_{obs} + DTRC + WTRC + IRC + SSBC) \tag{2.2}$$

SSH can also be expressed as the sum of the geophysical corrections and the dynamic sea surface height (DSSH):

$$SSH = DSSH + GC + TCC + DAC \tag{2.3}$$

$$DSSH = SSH - GC - TCC - DAC \tag{2.4}$$

Therefore, it is possible to relate DSSH with all the corrections described as:

$$DSSH = H_t - R_{obs} - DTRC - WTRC - IRC - SSBC - GC - TCC - DAC \tag{2.5}$$

Finally, the reference level is changed by subtracting the mean sea surface (MSS). As a result, the variations of SSH due to oceanic processes (e.g., ocean currents) referenced to the MSL are obtained, namely the sea level anomaly (SLA):

$$SLA = DSSH - MSS \tag{2.6}$$

In this work, satellite altimetry sea level data provided by the Copernicus Marine Environment Monitoring Service (CMEMS) are used. The first stage of this work developed along the East coast of North America uses the altimetry product *SEALEVEL-GLO-PHY-L3-REP-OBSERVATIONS-008-045* for the period 1992-2015. The global study uses an updated version of the latter product, *SEALEVEL-GLO-PHY-L3-REP-OBSERVATIONS-008-062*, covering the time period 1992-2018. These products are processed with the multi-mission altimeter data processing system DUACS (Data Unification and Altimeter Combination System), integrating the along-track measurements of several satellite missions operating from 1992 onward (Fig. 2.1) to provide an inter-calibrated global dataset of SLA. Further information about the processing system and the corrections applied can be found in Pujol et al. (2016).

As previously explained, this work particularly assesses the extreme behavior of the the NTR component of sea level. Therefore, an equivalent altimetry-based NTR dataset (NTR_{SAT}) needs to be built. NTR_{SAT} is computed by undoing the DAC from the SLA product. To that end, we add the very same DAC product applied to compute the SLA dataset provided by CMEMS (Eq. 2.7). This product is managed by AVISO (Archiving, Validation and Interpretation of Satellite Oceanographic data) and integrates two constituents: the low-frequency oceanic response to atmospheric pressure forcing (periods longer than 20 days), calculated through the classical inverse barometer, and the high-frequency oceanic response to pressure and wind meteorological forcings (periods shorter than 20 days), obtained from

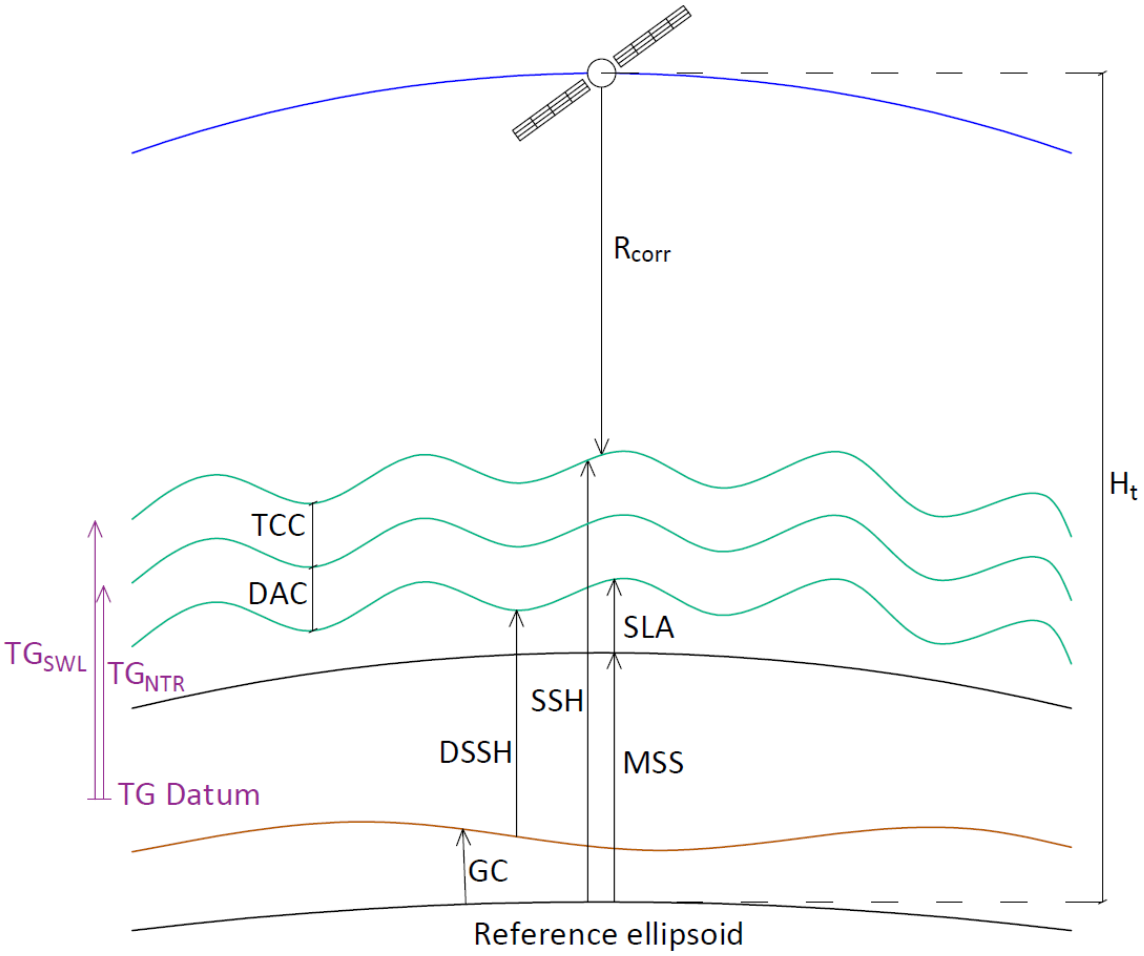

Fig. 2.2 Corrections applied to SSH altimeter observations. TG record components are also included. TCC = Tide Component Correction; DAC = Dynamic Atmosphere Correction; TG = Tide Gauge; NTR = Non-tidal Residual; SSH = Sea Surface Height; DSSH = Dynamic SSH; SLA = Sea Level Anomaly; MSS = Mean Sea Surface; GC = Geoid Correction; SWL = Still Water Level.

MOG2D numerical barotropic model (Carrère and Lyard, 2003).

$$NTR_{SAT} = SLA + DAC \tag{2.7}$$

In situ data

This work makes use of a set of 22 TG records along the East coast of North America (Fig. 2.3) managed and distributed by the National Oceanic and Atmospheric Administration (NOAA). Information about both the observed sea level and predicted tide for each station is available at NOAA COOPS website (URL, last time accessed on June 2022). The NTR component (NTR_{TG}) is computed by subtracting the predicted astronomical tide (NOAA harmonic analysis) from the still water level (SWL) record. Consequently, the remaining NTR variable is mainly driven by meteorological and oceanographic processes and can be considered as a random variable of the climate system. The criterion to select the 22 TGs in the study region is based on the existence of a quality control process, the temporal coverage (agreement with the time span in which altimetry information is available) and the availability of continuous time series.

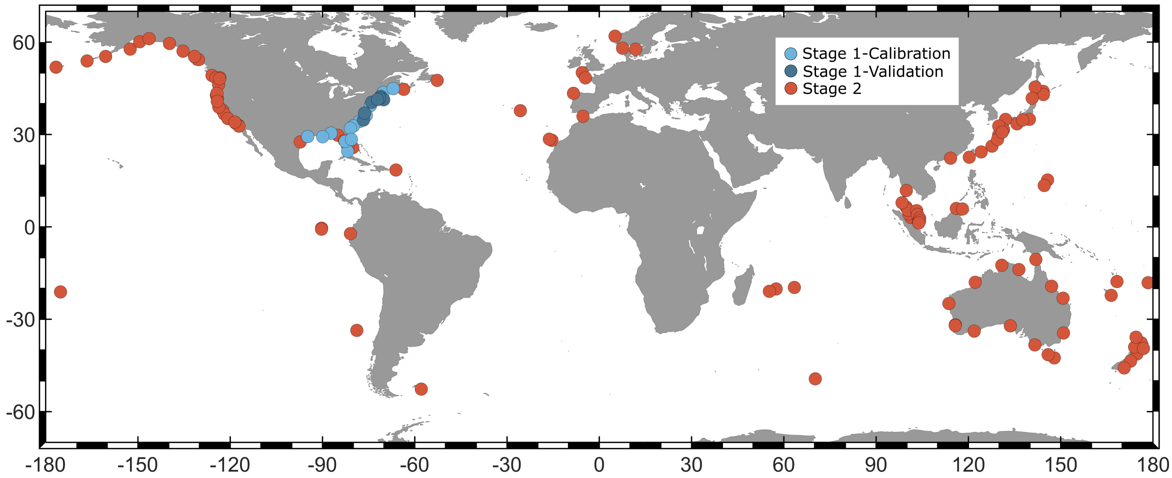

Fig. 2.3 Location of the TG stations used to conduct the analysis. Light blue circles represent the stations used to calibrate the methodology along the East coast of North America. Idem for dark blue circles but for the validation of the methodology. Red circles represent the stations used for the study at global scale.

The global study uses a set of 400 TG records distributed along the global coastlines. These records have been downloaded from the legacy data portal at the University of Hawaii Sea Level Data Center (UHSLC) webpage (URL, last time accessed on June 2022). Hourly values of SWL are available for each TG station. Among the initial amount of records, 150 stations are rejected. Two criteria are considered to conduct this preliminary selection. We rejected records with less than 75% of hourly data within the period of analysis (i.e., 1992-2018). Also, stations installed in complex locations expected to be highly affected by local processes (e.g., innermost part of ports, within atolls) are not considered. Next, a quality control that consists in looking for the presence of outliers, changes in the reference level and odd values is applied to the selected stations.

Prior to the tidal harmonic analysis, the SWL record is de-trended by subtracting the annual median. Since the nodal cycle (18.61-year cycle due to lunar precession) can have great influence on high tidal levels in some locations (Haigh et al., 2011), we assess whether or not the nodal cycle correction is needed to be applied within the harmonic analysis for each TG record. We address this issue by fitting the annual standard deviation of the SWL time series to a 18.6-year period sine function. Thus, we assume that the nodal correction is needed at stations in which the parameters' fit is significant at 95% confidence level.

The harmonic analysis is developed using the tidal analysis tool U-tide (Codiga, 2011). Although this model uses by default a total of 68 components to reconstruct the tide, here components SA and SSA are not considered. The harmonic analysis is conducted through a moving two-year time window (Fig. 2.4). Years with less than 60% of hourly data are not considered. At each step, the two-year window has two overlap periods of half year at the beginning and at the end of it, so that we only store the central one-year period of the simulated block. Finally, the astronomical tide time series is built by concatenating one-year length effective periods produced at each calculation step.

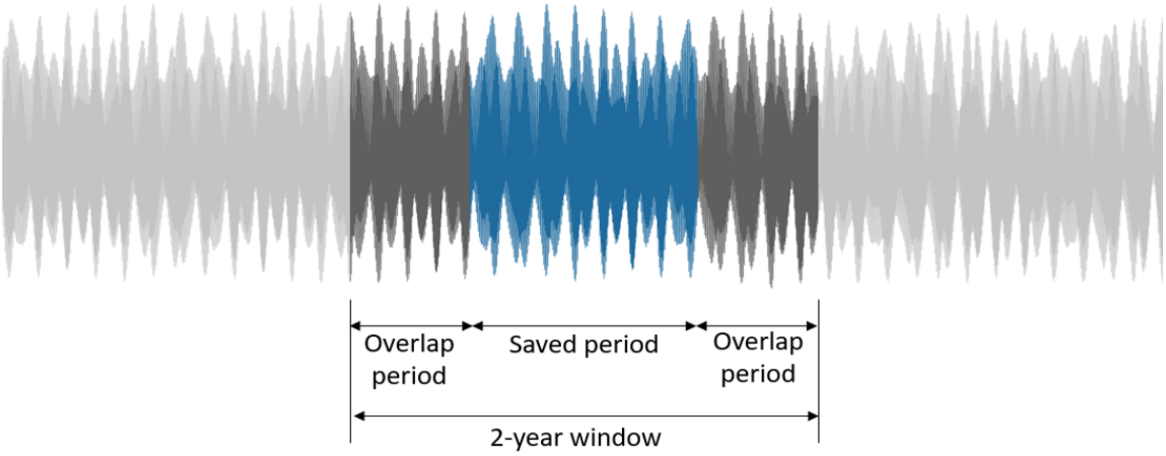

Fig. 2.4 Harmonic analysis scheme. The effective 1-year period stored at each simulation step is represented in blue. The half-year overlapped periods are displayed in dark gray. SWL time series is represented in light gray.

In order to evaluate the continuity of the resulting astronomical tide time series, the differences between the values twelve hours after and before the beginning of each effective period are compared. A warning flag is set on those cases in which these differences are higher than 1% of the tidal range. Warning cases have been carefully checked, ensuring that there are not discontinuities in the time series.

After the tidal harmonic decomposition, the previously removed trend is re-added. The non-tidal residual record (NTR_{TG}) is finally computed as the difference between the SWL and the astronomical tide time series. The number of available data is reassessed, rejecting TG records with less than 75% of hourly data within the period of analysis, leaving a total of 170 TG stations.

2.3 Methods

2.3.1 The coastal extreme sample

The NTR_{SAT} dataset is characterized by a heterogeneous space and time sampling. Therefore, a method to select an altimetry data sample to be compared against each in situ record is required. For a particular TG, the selection is based on the existing correlation between NTR_{TG} and NTR_{SAT} in the vicinity of the station.

First step consists in building pairs using each NTR_{SAT} measurement and the closest in time NTR_{TG} value. Next, a surrounding area delimited by a 7.5° radius circle whose center is at the station location is defined for each TG. This circular area is gridded with a 0.25° regular mesh. At each grid node, we compute the Pierson correlation coefficient (r) between all the NTR_{TG}-NTR_{SAT} pairs within a 0.25° radius circle centered in the node. As an example, Fig. 2.5 shows the correlation values obtained after applying this method to Corpus Cristi (Texas, USA) and Lumut (Malasya) TG stations. Results show that correlation values are roughly inversely proportional to the distance to the TG, as well as the existence of different correlation patterns depending on the target location.

The altimetry sample to be compared against in situ data is made of all measurements whose grid nodes have correlations higher than a selected cut-off. While for the analysis along the East coast of North America we set a fixed correlation cut-off of 0.5, for the global study the method to select the cut-off was improved. Thus, the cut-off evolves from an initial value of 0.50, increasing 0.01 at each time step, continuously reducing the amount of data but improving the accuracy. The final cut-off is a compromise between both features. At each step, altimetry data are re-sampled to hourly data by selecting the maximum hourly value. The final correlation cut-off is the one that produces a NTR_{SAT} sample of around one measurement per day after the hourly re-sampling. This criterion is defined based on a sensitivity analysis of r and the root mean square error (RMSE) between MM from NTR_{TG} and NTR_{SAT}.

After selecting the NTR_{SAT} sample for each station, we assess again the quality and number of altimetry and TG data available. Some of the stations had to be rejected due to the lack of altimetry data and odd values after the harmonic analysis. Finally, a total of 22 stations are considered for the study along the East coast of North America and 123 are considered for the study along the global coastlines (Fig. 2.3).

Next, the extreme samples to be used as input in the following extreme value analysis (EVA) are defined. For a given dataset, we define the extreme sample as the MM. Regarding NTR_{TG}, only months including more than 60% of the recorded hourly values are considered. Concerning satellite altimetry data, MM from NTR_{SAT} are selected for months with at least 10 measurements after hourly re-sampling.

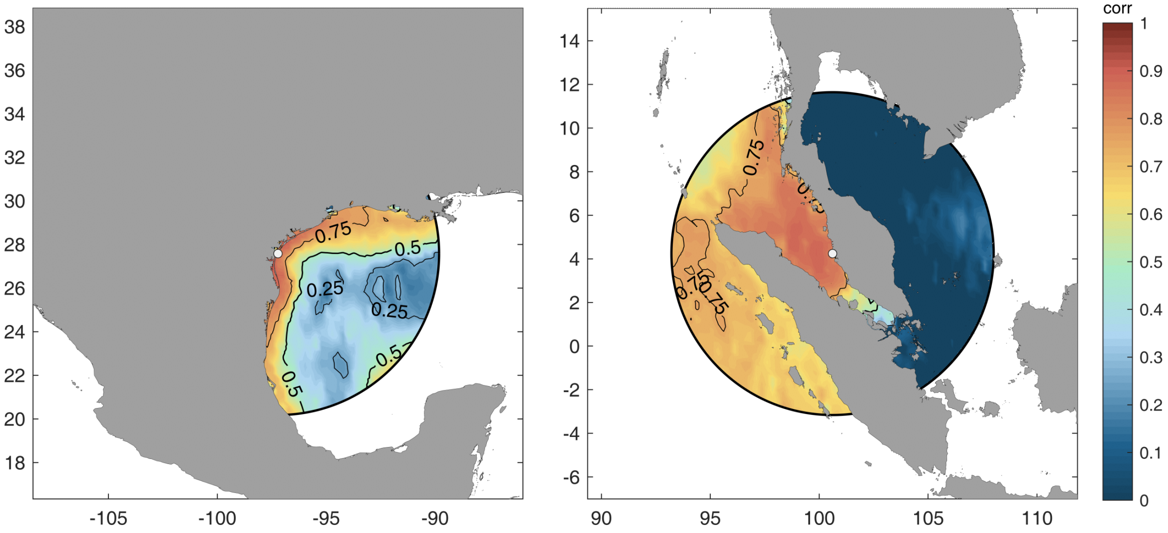

Fig. 2.5 Pierson correlation between NTR_{TG} and NTR_{SAT} around the TG station location for (a) Corpus Cristi TG station (Texas, USA) and (b) Lumut TG station (Malaysia). The 0.25, 0.50, and 0.75 correlation contours are displayed. The location of the station is represented with a white circle.

Tsunamis may contaminate the extreme sample. These events can appear within TG records as events of significant magnitude, even exceeding for some stations the greatest events with an atmospheric origin. Thus, some MM values recorded by TGs may be originated by tsunamis. In order to avoid these spurious events, MM with a tsunami origin are removed. To do that, the list of recent tsunamis from NOAA webpage URL (last time accessed on June 2022) is crossed with MM from TG data with a time lag of 36 hours since generation. All events matching a tsunami are removed and not taken into account for the ESL characterization.

In order to make a fair comparison between altimetry and TG data, only MM available for both datasets are considered in the EVA.

2.3.2 Statistical extreme model

The classical theorem in the EVT (Fisher and Tippett, 1928) states that the limiting distributions of sequences of maxima of independent and identically distributed random variables must belong to one of three possible families of the probability distribution functions, usually named as Weibull, Gumbel and Fréchet. The generalized extreme value (GEVD) is a reformulation of these three limiting families. The GEVD cumulative distribution function (CDF) is given by:

$$F(z) = \begin{cases} exp - \left[1 + \xi\left(\frac{z-\mu}{\sigma}\right)\right]^{\frac{-1}{\xi}} & \xi \neq 0 \\ exp\left[-exp\left(-\frac{z-\mu}{\sigma}\right)\right] & \xi = 0 \end{cases} \tag{2.8}$$

where μ is the location parameter, σ is the scale parameter and ξ is the shape parameter. The Weibull, Gumbel and Fréchet families correspond to $\xi < 0$, $\xi = 0$ and $\xi > 0$, respectively.

GEVD model uses time block maxima values (usually annual maxima, AM) to fit the GEVD parameters and estimate quantiles associated to high return periods (e.g. 20, 50, 100-year return period). Since altimetry information is only available from the 90's, monthly values are selected as block maxima to increase the size of the maxima sample. This approach has already been successfully applied to characterize ESLs in previous studies (e.g., Méndez et al. 2007; Menéndez and Woodworth 2010). Monthly maxima dependence is modelled by introducing a non-stationary monthly behavior through μ. The seasonality is introduced through three sine functions that model one, two and four complete cycles per year, respectively. In addition, long-term trends are modelled through an exponential function.

The calculation of NTR quantiles associated to a R-year return period for a certain year t_i in a non-stationary GEVD ($\overline{z_R}$) can be done using the following expression:

$$1 - \frac{1}{R} = \begin{cases} exp\left\{ - \int_{t_i}^{t_i+T} \left[1 + \xi \left(\frac{\overline{z_R} - \mu(t)}{\sigma} \right) \right]^{\frac{-1}{\xi}} dt \right\} & \xi \neq 0 \\ exp\left\{ - \int_{t_i}^{t_i+T} \left[-exp\left(- \frac{\overline{z_R} - \mu(t)}{\sigma} \right) \right] dt \right\} & \xi = 0 \end{cases} \tag{2.9}$$

where T is the time variable with a year unit scale.

This study uses year 2015 as reference to estimate quantiles associated to return periods.

2.3.3 Inferences for return levels

Following the EVA at all TG station locations, we compare extreme estimates for different return periods from NTR_{TG} and NTR_{SAT}. Thus, κ_{R_i} is defined as the ratio between in situ and remote NTR quantiles associated to a return period R_i (in years) at a certain station (Eq. 2.11).

$$\kappa_{R_i} = \frac{z_{R_i}^{tg}}{z_{R_i}^{sat}} \tag{2.10}$$

where $z_{R_i}^{tg}$ is the NTR quantile associated to return period R_i from NTR_{TG} and $z_{R_i}^{sat}$ is the NTR quantile associated to return period R_i from NTR_{SAT}.

The mean ratio ($\overline{\kappa}$) between return period estimates from NTR_{TG} and NTR_{SAT} can be computed as:

$$\overline{\kappa} = \frac{1}{N_R} \sum_{R_i=10}^{R_i=50} \frac{z_{R_i}^{tg}}{z_{R_i}^{sat}} \tag{2.11}$$

where N_R is the number of return periods considered to compute $\overline{\kappa}$.

Perfect agreement between both datasets would result in $\overline{\kappa}$ equal to the unit. Consistently, $\overline{\kappa} > 1$ means underestimation by altimetry data and $\overline{\kappa} < 1$ means the opposite.

The differences between $z_{R_i}^{tg}$ and $z_{R_i}^{sat}$ can be related to morphological, geographical and climate characteristics at the location of study. The NTR signal over coastal areas against open ocean areas can be sensitive to amplifications/decreases due to depth-limitations and nonlinear interactions between individual sea level components. Consequently, in order to account for these differences and to correct NTR_{SAT} extreme estimates, a correction factor, henceforth named as Extreme Scale Factor (ESF), is defined.

ESF is computed as a weighted combination of several constituents, each of them accounting for a possible source of discrepancies between TG and altimetry extreme estimates (Eq. 2.12). The exploration of these constituents has been upgraded between the two stages of this study, hence resulting in a different definition of ESF for each of them.

$$ESF = \sum_{i=1}^{N_c} w_i \, \kappa_i \tag{2.12}$$

where N_c is the number of constituents considered, w_i is the weight associated to constituent i and κ_i is the value of constituent i.

The correction of $z_{R_i}^{sat}$ with ESF results in a corrected NTR_{SAT} quantile associated to a return period R_i ($z_{R_i}^{SAT^*}$; Eq. 2.13). Following Eq. 2.12, a corrected ratio $\kappa_{R_i}^*$ is obtained (Eq. 2.14).

$$z_{R_i}^{sat^*} = ESF \, z_{R_i}^{sat} \tag{2.13}$$

$$\kappa_{R_i}^* = \frac{z_{R_i}^{tg}}{z_{R_i}^{sat^*}} \tag{2.14}$$

The mean corrected ratio can be computed as:

$$\overline{\kappa^*} = \frac{1}{N_R} \sum_{R_i=10}^{R_i=50} \frac{z_{R_i}^{tg}}{z_{R_i}^{sat^*}} \tag{2.15}$$

Weights for all constituents are calculated by minimizing the RMSE between $\overline{\kappa^*}$ and the unit (i.e., case in which return values from TG are equal to those from altimetry).

2.4 Results

2.4.1 East Coast of North America

After conducting the EVA at the 14 TG stations used for calibration (Fig. 2.3), two constituents are found to be significant in the definition of ESF:

- Coastal exposure constituent (κ_{CE}): This constituent takes into consideration the exposure of a specific location to the open ocean (c_{CE}). It seeks to reflect, first, the fact that closer to the coast a lower number of altimeter measurements are available, especially in rugged coastlines and sheltered estuaries. Second, the amplification experienced by storm surge as it approaches the TG, in particular at those locations where the pathway from the open ocean to the TG location is shallow, narrow and winding due to local morphology (e.g., presence of islands) or human intervention (e.g., port infrastructures).

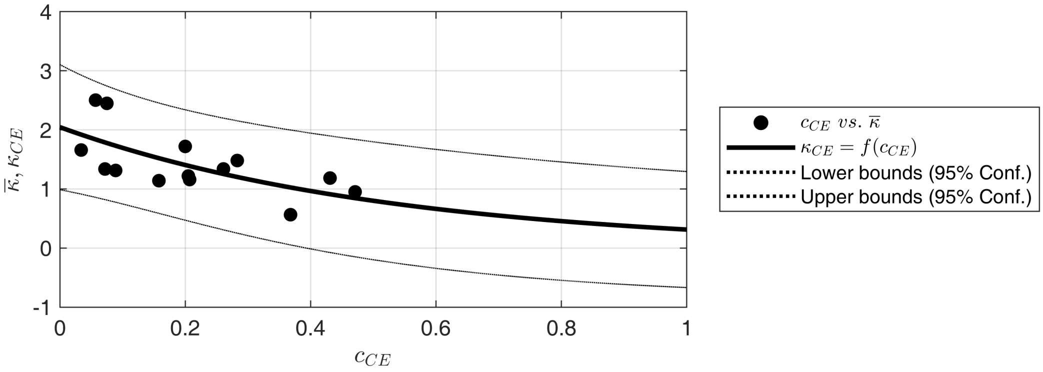

Fig. 2.6 Exponential relationship between κ_{CE} and c_{CE}.

c_{CE} is calculated as the mean relative ray length between the location of study and the first obstacle encountered considering more than 1,000 rays with a maximum length of 0.1 degrees. Since small obstacles (e.g., islands) have no significant effect on the propagation of long waves, those with an area smaller than 1 km^2 are not considered in the calculation algorithm.

c_{CE} is exponentially related with $\overline{\kappa}$ through the expression shown in Eq. 2.16 and represented in Fig. 2.6. Results show that TG stations less exposed to the open ocean show greater underestimation of altimetry data.

$$\kappa_{CE} = 2.046\, exp(-1.876 c_{CE}) \tag{2.16}$$

- Continental shelf width constituent (κ_S): It relates to the width of the continental shelf at the coastal location (c_S). This constituent represents the loss of precision of radar altimetry in the shelf (Volkov et al., 2007) and the changes in the storm surge long wave as the depth reduces. Here the shelf limit is defined as the 200-meter offshore isobath, where slope begins. c_S is obtained as the minimum width of the shelf at the coastal location.

c_s is linearly related with $\overline{\kappa}$ through the expression shown in Eq. 2.17 and represented in Fig. 2.7. Longer shelf widths induce stronger underestimations of altimetry data.

$$\kappa_S = 0.004954\, c_S + 0.8776 \tag{2.17}$$

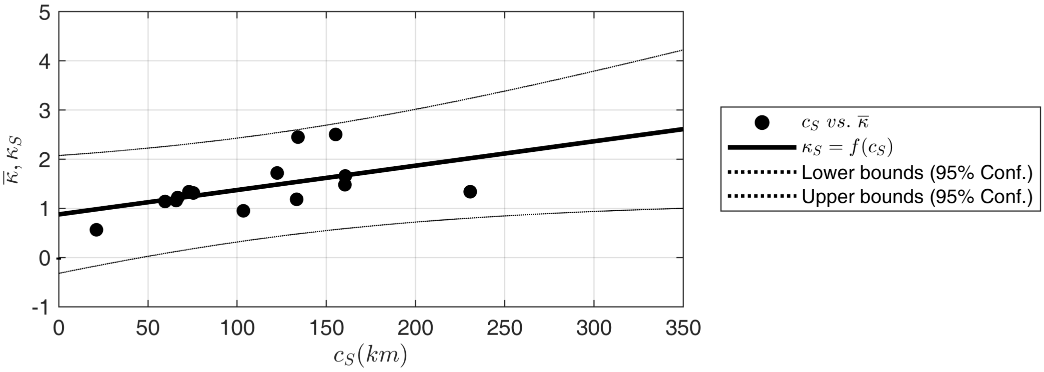

Fig. 2.7 Linear relationship between κ_S and c_S.

The contribution of each constituent to ESF is computed (Eq. 2.18). Results show a higher contribution of the coastal exposure with respect to the shelf width (65% vs. 35%).

$$ESF = 0.65\, \kappa_{CE} + 0.35\, \kappa_S \tag{2.18}$$

The validation of the methodology is carried out with the information provided by 8 TG records not previously used in the definition of ESF and located as well along the East coast of North America. After the quality control and following the methodology described above to obtain NTR extreme samples, an EVA is conducted for NTR_{SAT} and NTR_{TG} at these locations.

ESF is calculated for all validation sites according to Eq. 2.18. The correction of $z_{R_i}^{sat}$ allows to significantly reduce the differences with $z_{R_i}^{tg}$. Consistently, $\overline{\kappa^*}$ approaches to unit in all stations analyzed (Fig. 2.8). Before correction, the mean $\overline{\kappa}$ value is 1.43 with a standard deviation with respect to the unit of 0.53, whereas after correction the mean $\overline{\kappa^*}$ is 0.98 with a standard deviation of 0.24.

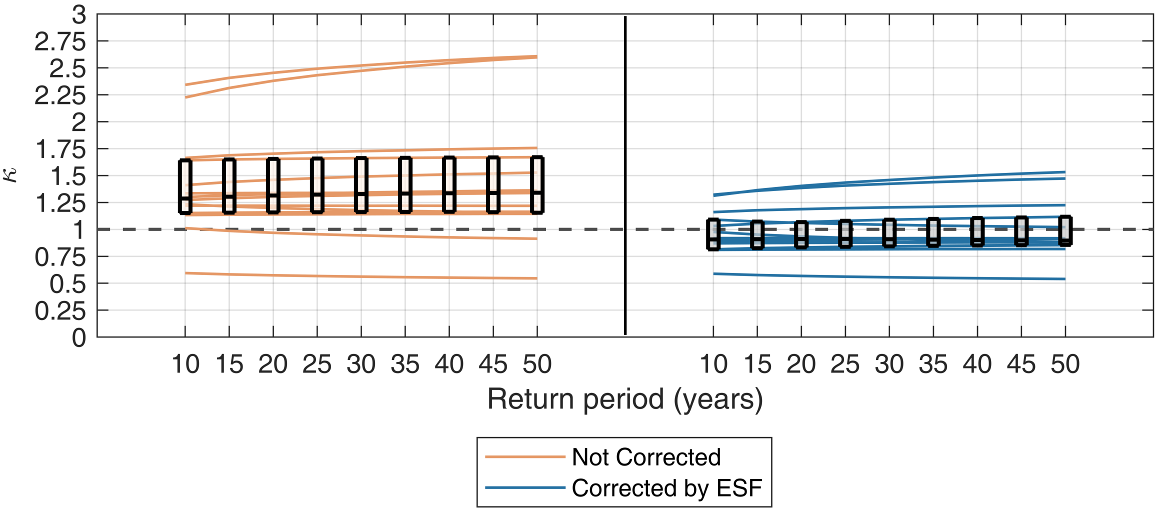

Fig. 2.8 Ratio between 10- to 50-year return values from NTR_{TG} and NTR_{SAT} for the eight TG records used for validation in the East coast of North America. Orange lines represent the ratios before correcting with ESF. Blue lines represent the ratios after correcting with ESF. Boxes represent 0.25, 0.50, and 0.75 quantiles ratios for each return period analyzed.

2.4.2 Global coast

The high number of TG stations available in the analysis along the global coastlines allows a more detailed parameterization of ESF. For that matter, TG stations are geographically grouped in six sub-samples, hence resulting in six different ESF definitions. First, TG stations are divided between those located on mainland and island coasts. Next, TG stations are grouped between ocean basins: Atlantic, Pacific and Indian. Not enough data is available to make a robust adjustment for islands coasts in the Indian basin, so no correction is proposed for them.

After exploring several issues affecting the differences found between TG and altimetry data, four constituents are found to be significant to define the ESF.

- Regional exposure constituent (κ_{RE}): It reflects the exposure of a specific region to the open ocean (c_{RE}). It seeks to represent the difference between the events recorded by TGs and altimeters depending on the coastal location from a regional perspective, i.e. if such location belongs to an open island, mainland margin, an island close to mainland, etc. c_{RE} is calculated as the proportion of water area in a 7.5° radius circle centered in the station location.

  c_{RE} is found to be exponentially related with $\overline{\kappa}$ (Eq. 2.19 and Table 2.1). Higher values of regional exposure show lower $\overline{\kappa}$. Results indicate that higher regional exposure values ($c_{RE} \approx 1$) are associated, in general, with open islands, whereas lower values are related with sheltered mainland coastlines.

$$\kappa_{RE} = a_1\, e^{a_2\, c_{RE}} \tag{2.19}$$

Table 2.1 Exponential fit parameters for κ_{RE}. Only model fits showing $R^2 > 0.1$ are shown. n.d. indicates not enough available data for model fitting.

	Mainland margins		Ocean islands	
Basin	a$_1$	a$_2$	a$_1$	a$_2$
Pacific	-	-	-	-
Atlantic	-	-	6.03	-1.96
Indian	2.00	-0.85	n.d.	n.d.

- Continental shelf width constituent (κ_S). Consistently with the results for the East coast of North America, c_S is found to be linearly related (positive slope) with $\overline{\kappa}$ (Eq. 2.20 and Table 2.2).

$$\kappa_S = a_1\, c_S + a_2 \tag{2.20}$$

Table 2.2 Linear fit parameters for κ_S. Only model fits showing $R^2 > 0.1$ are shown. n.d. indicates not enough available data for model fitting.

	Mainland margins		Ocean islands	
Basin	a$_1$	a$_2$	a$_1$	a$_2$
Pacific	-	-	-	-
Atlantic	0.00164	1.28	-	-
Indian	0.00015	1.20	n.d.	n.d.

- Latitudinal gradient constituent (κ_L): A quadratic relationship between $\overline{\kappa}$ and the absolute value of the latitude of a coastal location (c_L) is found (Eq. 2.21 and Table 2.3). The fact that tropical cyclones are not fully captured by the altimetry extreme sample is likely the main cause of these meridional differences.

$$\kappa_L = a_1\, c_L^2 + a_2\, c_L + a_3 \tag{2.21}$$

- Wave climate constituent (κ_W): It represents the effect of wave climate on the differences found between the extreme events measured by altimeters and the TGs (c_W). Waves have already been proven to be the main origin of SLAs in certain TGs such as in

Table 2.3 Quadratic fit parameters for κ_L. Only model fits showing $R^2 > 0.1$ are shown. n.d. indicates not enough available data for model fitting.

	Mainland margins			Ocean islands		
Basin	a_1	a_2	a_3	a_1	a_2	a_3
Pacific	-0.00041	0.025	0.96	-0.00051	0.036	0.75
Atlantic	-0.00050	0.029	1.10	-0.0013	0.093	-0.31
Indian	-0.0011	0.045	0.96	n.d.	n.d.	n.d.

Midway (Aucan et al., 2012). To evaluate this, we compute the correlation between the E_f of the waves propagating to the coast and the highest NTR events recorded by the altimeter. Thus, NTR values higher than the 90% percentile of NTR_{SAT} are first selected. Then, its contemporaneous E_f from GOW2 hidncast (Perez et al., 2017) values are identified and r coefficient is computed.

There is a strong exponential relation between $\overline{\kappa}$ and c_W (Eq. 2.22 and Table 2.4), namely higher correlations with waves result in a stronger underestimation by altimetry data.

$$\kappa_W = a_1\, e^{a_2\, c_W} \tag{2.22}$$

Table 2.4 Exponential fit parameters for κ_W. Only model fits showing $R^2 > 0.1$ are shown. n.d. indicates not enough available data for model fitting.

	Mainland margins		Ocean islands	
Basin	a_1	a_2	a_1	a_2
Pacific	0.96	0.94	1.04	0.52
Atlantic	-	-	0.61	3.25
Indian	2.00	-0.85	n.d.	n.d.

A weighted combination of the constituents to define ESF is proposed for each TG group as it was previously shown for the East coast of North America. Table 2.5 summarizes the weights obtained for each constituent after optimization.

Table 2.5 Weights of ESF constituents for the different global TG groups

	Mainland margins				**Ocean islands**			
Basin	Regional Exposure	Shelf width	Latitude	Wave climate	Regional Exposure	Shelf width	Latitude	Wave climate
Pacific	-	-	33%	67%	-	-	86%	14%
Atlantic	-	33%	67%	-	39%	20%	-	41%
Indian	32%	-	64%	4%	Not enough data			

Fig. 2.9 shows the effect of the correction at 4 TG stations: Burnie (Australia), Santa Monica (California, EEUU), Apalachicola (Florida, EEUU) and Wakkanai (Japan). All cases show an effective correction, so that corrected return values lie within the 95% confidence interval from TG data. The correction with ESF results in a reduction of the mean error and its deviation. Median $\overline{\kappa}$ and the 5th and 95th percentiles of $\overline{\kappa}$ before the correction are 1.18 [0.80, 1.82] and, after correcting with ESF, the values are 0.99 [0.76, 1.32]. Moreover, the mean absolute difference between $\overline{\kappa}$ and the unit is 0.26 and between $\overline{\kappa^*}$ and the unit is 0.13. The deviation of the absolute differences between $\overline{\kappa}$ and the unit is 0.29 and between $\overline{\kappa^*}$ and the unit is 0.17. Fig. 2.10 depicts the results of the correction for the 123 stations of analysis.

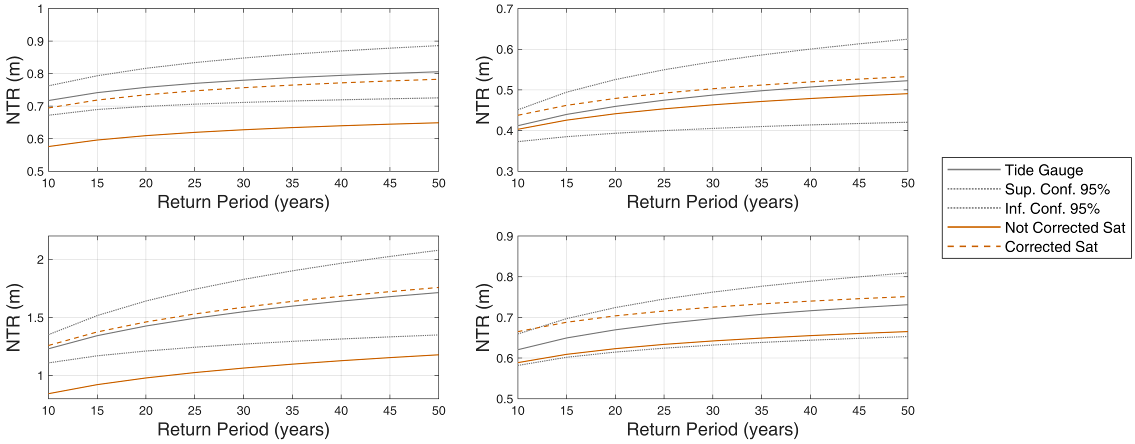

Fig. 2.9 Return level plots (m) of NTR_{TG}, NTR_{SAT} and NTR_{SAT} corrected by ESF for (a) Burnie TG in Australia, (b) Santa Monica TG in California, EEUU, (c) Apalachicola TG in Florida, EEUU and (d) Wakkanai TG in Japan. Panels include the 95% confidence bounds from TG data.

2.5 Conclusions

This study presents a novel approach to analyze ESLs from satellite altimetry data. In particular, we focus on the NTR component of sea level. A NTR dataset from altimetry data is built from a along-track inter-calibrated SLA product provided by CMEMS by undoing the DAC (Fig. 2.2). The calibration and validation of the methodology is conducted against TG records (Fig. 2.3). The study is developed through two different stages. First, the method is calibrated and validated along the East coast of North America. Next, given the promising results obtained, the analysis is extended to global scale.

A method to select an altimetry-based NTR sample to be compared with in situ data around each TG station of analysis is proposed. The selection is based on the correlation between altimetry and in situ data around the TG station. Despite altimeter measurements losing accuracy nearshore, correlation values higher than 0.75 are obtained around most of the stations analyzed (Fig. 2.5), reflecting consistency in the behavior of both datasets. A

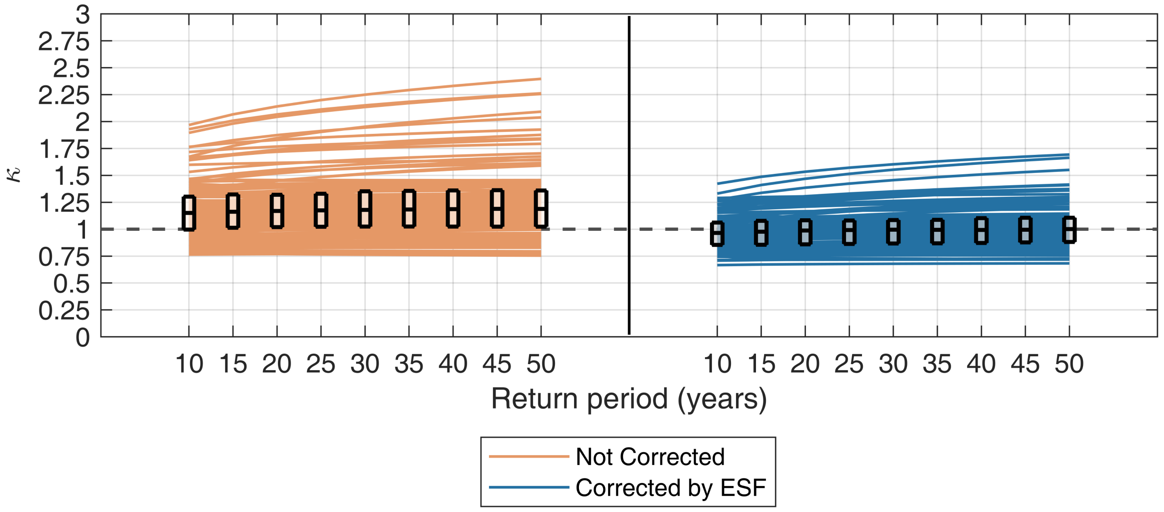

Fig. 2.10 Ratio between 10- to 50-year return values from NTR_{TG} and NTR_{SAT} for all TG records used in the global analysis. Orange lines represent the ratios before correcting with ESF. Blue lines represent the ratios after correcting with ESF. Boxes represent 0.25, 0.50, and 0.75 quantiles ratios for each return period analyzed.

minimum correlation cut-off to select the altimetry sample around each TG station is set to ensure a good agreement between MM from altimetry and in situ data. For each TG station, altimetry and TG MM are selected to be used as input in the EVA. A non-stationary GEVD model is used, modelling the variability at two time scales through the parameter μ: seasonal variations and long-term trends.

Extreme estimates from both data sources are compared. Results show a general underestimation of NTR return values from altimetry with respect to those computed from in situ data. Systematic biases are nevertheless found for different return periods (Fig. 2.9), which facilitates the correction. The differences are found to be highly correlated with geographical and physical coastal features. These features are quantified (named constituents) and combined to compute a correction factor, the ESF. This correction factor modifies the NTR return values from altimetry data to be more similar to those from TG data.

The influence of the coastal location of the TG station on the differences found between extreme estimates from altimetry and in situ data is quantified through different constituents. First, the local and regional exposure of the stations to the open ocean (coastal exposure constituent and regional exposure constituent, respectively), which measures the alteration of the NTR signal in protected basins with respect to open coasts. Secondly, the width of the continental shelf at the target coastal location (shelf width constituent), which accounts for the changes in the NTR as the depth reduces. The latitude of the station is also found to be strongly correlated with the underestimation of altimetry extremes very likely due to the incomplete TC representation within the remote extreme sample (latitudinal gradient constituent). In addition, the influence of extreme wind waves on the differences found is also measured (wave climate constituent).

The first stage of the study uses 14 stations to define ESF. Two constituents are found to be significant: the coastal exposure and shelf width. Results indicate a higher influence of the former on the discrepancies found (65% vs. 35%, respectively). The resulting ESF is validated at eight additional TG stations, significantly reducing the mean relative difference in return values from more than 40% to less than 2% (Fig. 2.8).

The global analysis considers four constituents to define ESF: regional exposure, shelf width, latitudinal gradient and wave climate. The higher number of TG stations used at this stage of the study (123) allows a more accurate definition of ESF. Specific ESFs for each basin, differentiating between mainland and island coasts, are defined (i.e., six different ESFs). Table 2.5 summarizes the relative importance of each constituent within each basin and coastal type to correct the differences found between altimetry and in situ return values. Again, ESF efficiently reduce the mean relative differences in return values from 18% to less than 1%.

This work demonstrates the skill of altimetry data to capture coastal ESLs. Therefore, satellite altimetry could be considered as a valid source of information about ESL, especially where there is no provider of in situ observations such as TGs, which may have a huge impact for a wide range of coastal applications. The methodology presented here provides an approach to model the behavior of NTR extremes and offers a validated correction method to account for the weaknesses inherent to the spatial and time sampling of altimetry data. This correction could be applied to a coastal altimetry sample to improve the accuracy of the extreme estimates. Further research is however needed to define the shape of the altimetry selection area. Despite the promising results, extreme estimates from altimetry data should be interpreted cautiously where very local processes controlled by non-linear interactions are important. These processes are recommended to be captured by more accurate means such as numerical modeling. Nevertheless, the results presented could be used as a good prospect of the NTR extreme regime on the coast. Furthermore, the high correlations found between both data sources open the possibility of future coastal climate studies on ESLs based on altimetry data.

Chapter 3

Global coastal wave storminess

Abstract

In this chapter an assessment of the wind wave storminess along the global coastlines is presented. This work is based on a 42-year high-resolution hindcast, forced by the ECMWF ERA5 reanalysis. Wave storm events are classified by assessing the exceedances over the significant wave height 95th percentile. Additionally, the most severe wave storms impacting the coast are isolated by analyzing the exceedances over the significant wave height 99th percentile. The main characteristics of wave storms: frequency of occurrence, duration and intensity, as well as the mean storm integrated parameters significant wave height, mean direction, mean period and energy flux, are assessed. Other secondary characteristics as the swell vs. wind sea dominance during storms, and the wave period vs. wave height dominance of the storm wave energy flux are also analyzed. Results show a general meridional storminess pattern. The stormiest coastlines are those located in extratropical latitudes, consequence of the impact of wave storms characterized by high wave heights and high frequency of occurrence. The degree of storminess decreases equatorward, reaching its minimum along the protected coasts of Indonesia. Maximum mean wave storm durations are found along the east coast of India, exceeding 3.5 days on average. Swell wave storms dominate the western open coastlines of the continents until latitudes where the landfall of storms induces a wind sea dominance on the storm wave climate.

3.1 Introduction

Coastal storms represent nature at its most energetic and violent states, with a considerable destructive power, impacting the coastal areas and coastlines. Coastal storms are easily related to strong winds, extreme wave heights and water levels, often together with intense precipitation, causing coastal flooding and devastating destruction. For that matter, coastal storms are often the cause of dramatic human (Hossain, 2015; Woodruff et al., 2013) and economic (Toimil et al., 2018; Vousdoukas et al., 2020a) losses, as well as ecological disturbance and damaging (Paprotny et al., 2021; Roebeling et al., 2013). Coastal storms are however part of the global weather and essential to the equilibrium of the climate system, redistributing coastal sediment, bringing fresh water and nutrients to coastal ecosystems, contributing to their rejuvenation, realigning barrier islands and recharging coastal river catchments, underground aquifers and water reservoirs with extreme precipitation (Sutton-Grier et al., 2015).

Efforts have been made to assess the impact of coastal storms, mainly in erosion and flooding processes. These studies can be developed from long historical climate data records, such as those provided by TGs, buoys, regional hindcasts and global reanalyses (Athanasiou et al., 2021; Christie et al., 2018; Jiménez et al., 2012), but also focusing on very relevant and powerful events such as the storms that hit western Europe during the 2013-2014 winter (Castelle et al., 2015; Masselink et al., 2016) or Hurricane Sandy in North America in 2012 (Hatzikyriakou and Lin, 2018). More recently, the coastal community has also been looking to the future and the potential effect that climate change can have on the coasts due to changes in the coastal climatic-impact drivers associated to coastal storms (e.g., sea level, waves). Many of these studies have been based on historical data, introducing the climate change effect only through the MSLR (e.g., Kirezci et al. 2020; Tebaldi et al. 2021). Therefore, assessing the coastal impacts of recent past coastal storms, as well as those of future events, requires deep knowledge of the characteristics of present coastal storms.

This study deals with a particular aspect of coastal storms: waves; henceforth designated as coastal wave storms, or simply wave storms (or just storms), always meaning the former. The waves studied here are ocean gravity waves, sometimes also referred to as wind waves, hereinafter only called waves. Waves are probably the most ubiquitous element of the ocean surface. Due to their propagating characteristic across entire ocean bases with minor attenuation (Ardhuin et al., 2009; Jiang et al., 2016), waves are usually separated into two categories: wind sea waves and swell waves. Wind seas are waves at their generation stage, under the effect of the overlaying winds. Swells are waves that have outrun the overlaying wind, propagating away from the generation area. Swell waves can be designated as young or old swells, depending on the distance to the generation area (Holthuijsen, 2007).

Wave storms play a key role in coastal impacts. The waves setup, combined with the storm surges and the astronomical tide, can significantly increase the total water level (TWL) at the coast (Melet et al., 2018), which may induce destructive coastal flooding events. In this regard, the wave contribution to coastal flooding can either be caused by wind sea waves generated under low-pressure systems passing close to the coast such as hurricane Katrina in 2005 in the Gulf of Mexico (Dietrich et al., 2010; Link, 2010), or by swell waves generated by remote storms, as in December 2008 in the tropical western Pacific islands (Hoeke et al., 2013; Smithers and Hoeke, 2014). Additionally, wave storms are considered a major coastal erosion driver (Ranasinghe, 2016; Toimil et al., 2020a). Coastal wave storms are indeed powerful events in which the energy of the waves clearly exceeds the climatological mean values. Usually, when referring to extreme sea states, the most relevant parameter is the wave height, which rises significantly above mean conditions. Nevertheless, it is important to note that wave height is not the only factor determining the impact of waves on the coast during wave storms. The wave setup, for example, is more dependent on the wave period than on wave heights (Stockdon et al., 2006). Also, the wave energy flux, determining the power of waves to actually perform work on the coast, is a function of both the wave heights and periods, to the second and first orders, respectively (Holthuijsen, 2007). Additionally, deviations of the predominant incoming wave direction during wave storm events, play an outmost role in coastal erosion rates (Harley et al., 2017; Splinter et al., 2017).

Wave storms are traditionally studied through H_s time series. The standard approach is based on exceedances over a certain H_s threshold, so that individual exceeding events are classified as wave storms. Nevertheless, there is no standard or unique criterion in the literature to define this threshold. Its dependence to the local wave climate conditions, the scope of the study, the available data and, to some extent, the intrinsic subjectivity (or empirical) of the author's understanding of what a wave storm is, ends up determining the choice. The storm threshold has been defined according to different criteria such as the impact on the coast (Armaroli et al., 2012; Del Río et al., 2012; Trifonova et al., 2012), the agreement to the Generalized Pareto distribution (e.g., Bernardara et al. 2014; Li et al. 2014; Martzikos et al. 2018; Ortego et al. 2012) or, more recently, through more complex statistically methods accounting for the joint distribution of the variables involved in the storm definition (Lira-Loarca et al., 2020). However, all these criteria share the limitation of being restricted to a regional area. A more pragmatic and suitable option for larger scales assessments consists in defining the threshold based on H_s statistics. It is worth to mention that the geneses of the wave storms arriving at the coast are significantly different across different ocean basins, and from one ocean region to another (Semedo et al., 2011; Young, 1999), thus increasing the inherent complexity of working close to the coast. The use of the H_s 95th percentile (H_s95; Castelle et al. 2015; Davies et al. 2017; Martzikos et al. 2021b; Masselink et al. 2014) or the sum of the mean H_s and two H_s standard deviations (Amarouche et al., 2020, 2022; Mendoza et al., 2013; Ojeda et al., 2017) are examples of flexible approaches that adapt to the local climate.

All the studies mentioned above have assessed wave storm conditions at local or, at the most, regional scales. Some of them have led to climate studies in which the events are classified (Anfuso et al., 2016; Dolan and Davis, 1994, 1992; Martzikos et al., 2018; Mendoza et al., 2011; Molina et al., 2019) or the trends in the wave storms intensity and frequency of occurrence are analyzed (Ojeda et al., 2017). However, the most common purpose of wave storm studies available in the literature are coastal impact studies (e.g., Castelle et al. 2015; Corbella and Stretch 2012; Masselink et al. 2016; Vousdoukas et al. 2012; Wahl et al. 2016), which also explains the limited spatial scales.

To the extent of our knowledge, a thorough analysis of the coastal wave storms at a global scale has not been conducted yet. Therefore, the present study aims to provide a global quantitative and qualitative assessment of the global coastal wave storminess using a high-resolution wave hindcast, produced with the latest European Centre for Medium-Range Weather Forecasts (ECMWF) wave model version (Hersbach et al., 2020), forced with ERA-5 reanalysis winds and sea ice cover. It is intended to provide a view of the coastal wave storms characteristics, assessing regional storm patterns across the global ocean.

3.2 Climate data

The present study uses a global high-resolution wave hindcast, produced by the ECMWF, covering the period from 1979 to 2020.

The ERA-5 is the latest ECMWF reanalysis. It has a horizontal resolution of 40 km (0.36°) and the time resolution is 1 hour. More details, including the data assimilation scheme, can be found in Hersbach et al. (2020).

Along with the ERA-5 reanalysis, a high-resolution (0.2 horizontal resolution and hourly output) wave hindcast, forced with hourly ERA-5 close-to-surface winds and sea ice, has been produced: the ERA-5H. It was produced using a more recent version of the ECMWF IFS (Cy46r1), updated wave physics for wind input and swell dissipation based on Ardhuin et al. (2010) and a more recent global bathymetry (ETOPO1).

The current study uses hourly wave fields of H_s, T_m and Θ_m parameters from ERA-5H. Grid nodes covering the global coastal areas along the coastline were selected to conduct the analysis. To ensure enough amount of data during stormy seasons, grid nodes covered by ice for more than 15% of the time within winter months are rejected, following Tuomi et al. (2011).

Additionally, a detailed analysis at twelve specific locations (key points) distributed across the global coastlines has been conducted. Five of these points are in the Pacific Ocean coasts, three of them in the NH and two in the SH. Four points are in the Atlantic Ocean coasts, three in the NH and one in the SH. The remaining three points are in the Indian Ocean coast, two in the NH and one in the SH.

3.3 Methods

3.3.1 Wave storm definition

The coastal wave storms selection criterion used here is based on the exceedances over a threshold of the H_s time series. For the sake of consistency in the interpretation of the results, a unique threshold has been defined globally. The threshold over which a high H_s sea state event is classified as a wave storm was set as the H_s95 at a specific place, an approach that has been widely used to this purpose (e.g., Castelle et al. 2015; Davies et al. 2017; Martzikos et al. 2018, 2021b; Masselink et al. 2014). This method has been chosen since it is more flexible than an absolute magnitude threshold, as it is truly dependent on the local wave conditions, an essential requirement to develop studies at large scales (global in this case), accounting for the differences between different coastal wave climates across the global ocean.

The wave storm classification also requires two additional criteria, apart from the H_s threshold itself: the calm period between consecutive storms and the minimum duration of the events to be classified as storms (Martzikos et al., 2021a). The time between storms must ensure the independency between consecutive events to avoid biasing in the results by considering incomplete and correlated storms. Two wave storms are classified independently when the time between two consecutive H_s event peaks over H_s95 threshold is higher than 48 hours, following Meucci et al. (2020).

Imposing a minimum coherent duration of the storms avoids short sparse exceedances that would not have a significant impact on the coast. In fact, besides the energy impairing the coast, i.e., the intensity of the wave storm, the duration of that extreme event is in fact what causes more impact on the coast (van Gent and Wolters, 2018). The wave storm duration criterion has been chosen in previous studies available in the literature according to different criteria, such as the number of available data (Martzikos et al., 2018), the tidal cycle duration (Rangel-Buitrago and Anfuso, 2011) or the minimum duration assumed to cause erosion damage in the coastline (Mendoza et al., 2006), ranging in most cases between 6 and 12 hours. A minimum duration of 12 hours has been chosen here for two main reasons. On the one hand, this value has been used in regions with very different wave climates such as the Mediterranean Sea (Lin-Ye et al., 2016; Molina et al., 2019), the Gulf of Mexico and the Caribbean Sea (Ojeda et al., 2017) and the Northeast Atlantic Ocean (Del Río et al., 2012; Rangel-Buitrago and Anfuso, 2011; Senechal et al., 2015), and, on the other hand, it represents the duration of the tidal cycle in semi-diurnal and mixed tidal regimes, which, together, cover the largest portion of the global coastal areas (Gerkema, 2019).

Following the criteria described above, a wave storm event starts at the up-crossing time and it ends at the down-crossing time of the H_s95 threshold, when the time between these two moments is greater than or equal to 12 hours. Two wave storm events are considered independent of each other, and classified as two separate storms, when the time between event peaks is higher than 48 hours. If the time gap between two consecutive events is, on the other hand, lower than 48 hours, the two events are merged into one wave storm.

Nevertheless, H_s95 can be seen as too low in some coastal areas, therefore smoothing out relevant information about extreme sea sate events. For that matter, a subsample of wave storms, henceforth designated as severe wave storms, is individually analyzed in the study. The 99th percentile H_s (H_s99) is the threshold over which a high H_s event will be classified as a severe wave storm. Therefore, a severe wave storm occurs when the time exceeding H_s95 is higher than at least 12 hours, and further exceeds H_s99 for 6 hours or more.

3.3.2 Wave storm analysis

In order to provide a complete and detailed analysis of the characteristics of wave storms reaching coastal areas globally, several statistics and indices have been computed.

The wave storm frequency is computed as the mean number of events reaching the coast in a reference period. This statistic has been computed annually, seasonally and monthly, hence resulting in the mean number of storms (N) per year, season or month at each location, respectively, as:

$$N = \frac{N_{tr}}{N_y} \tag{3.1}$$

where N_{tr} is the total number of storms during the reference period (i.e., year, season or month) and N_y is the number of available hindcast years.

The number of storm seasons, i.e. the continuous period of time recurrently affected by the impact of wave storms, is also assessed. This number is computed by first estimating the minimum number of months aggregating at least 75% of the storms and, then, the number of independent periods in which they group (i.e., periods separated by at least one month). In some coasts the monthly number of storms remains more or less constant throughout the year. Since these cases cannot be directly inferred through the latter method, a new metric measuring the variability of the monthly mean number of storms is proposed, the monthly frequency ratio (R_m), computed as:

$$R_m = \frac{N_{m,min}}{N_{m,max}} \tag{3.2}$$

where $N_{m,min}$ is the minimum monthly mean number of storms and $N_{m,max}$ is the maximum monthly mean number of storms.

A value of $R_m < 1/3$ has been estimated as the optimum to identify coastal locations with no storm seasons.

Because the time between storms is of critical importance for beach recovery after storms, the mean inter-arrival time between storm events within storm seasons is also computed (IT_s) at each coastal location, as:

$$IT_s = \frac{\sum_{k=1}^{k=NS} \sum_{i=1}^{i=N_{s,k}-1} it_{s,i,k}}{N_{st} - NS} \tag{3.3}$$

where $it_{s,i,k}$ is the time between the pair i of consecutive storm peaks in storm season k, $N_{s,k}$ is the total number of storms in the storm season k, N_{st} is the total number of storms in all storm seasons and NS is the number of storm seasons.

The mean wave storm duration (D) is computed as:

$$D = \frac{\sum_{i=1}^{i=N_t} d_i}{N_t} \tag{3.4}$$

where d_i is the duration of each individual storm and N_t is the total number of storm events.

The mean integrated wave parameters of wave storms (IWP) are computed as:

$$IWP = \frac{\sum_{i=1}^{i=N_t} \overline{IWP_i}}{N_t} \tag{3.5}$$

where IWP_i is the mean integrated wave parameter (e.g., H_s,T_m) during the storm i.

The wave field (or sea state) during coastal wave storms can be dominated by wind sea or swell waves, depending on the respective (wind sea and swell) energy proportion within the wave spectrum (Semedo et al., 2011). The wind sea and swell parts of the wave energy spectrum follow the WAM wave model spectral partition (further explained in Semedo et al. 2011), based on the wave age principle (Bidlot, 2001; Semedo et al., 2012). The wind sea and swell dominance (WD_{ws} and WD_s, respectively) is calculated based on the ratio between the swell zeroth-order moment (m_0^s) and the total m_0, as:

$$WD_s = \frac{\sum_{i=1}^{i=N_t} \overline{\left(\frac{m_0^s}{m_0}\right)_i}}{N_t} x100 \tag{3.6}$$

$$WD_{ws} = 100 - WD_s \tag{3.7}$$

where m_0^s is the swell zeroth order moment and m_0 is the total zeroth order moment.

Extreme E_f during coastal wave storm events can either be caused by long periods and/or high wave heights, considering that it is a function of both: $E_f = c_g E = (\rho g^2)/64\pi T_m H_s^2$; where c_g is the group celerity, E is the wave energy, ρ is the water density and g is the gravity acceleration. In order to assess the contribution of both wave parameters in the E_f of storm events, an index (ED) based on the ratio between the H_s^2 and the T_m is computed as:

$$ED = \frac{\sum_{i=1}^{i=N_t} \overline{\left(\frac{H_s^2}{T_m}\right)_i}}{N_t} x100 \tag{3.8}$$

The intensity of the wave storms is assessed in the present study through the energy content index (EC; Mendoza Jiménez, 2006), calculated as the integral of H_s^2 during storm events. Therefore, this index considers not only the energy of the storms, but implicitly also the durations as it is calculated by integration in time. This index is computed at each chosen location (node point) across the global coastal areas, as:

$$EC = \frac{\sum_{i=1}^{i=N_t} \int_{t_{0,i}}^{t_{f,i}} H_s^2 \, dt}{N_t} x100 \tag{3.9}$$

where $t_{0,i}$ is the starting time of the storm i and $t_{f,i}$ is the ending time of the storm i.

A new index, named as degree of storminess (DS), is defined to assess how stormy a coastal location is. It integrates the information about the frequency of occurrence through metric N, and about the duration and the H_s of the storms through EC. This index is computed by attributing the same weight to both N and EC components.

N and EC are first re-scaled (I_n and I_{ec}, respectively) by applying the transformation $Y(x)$, as:

$$I_n = Y(N) \tag{3.10}$$

$$I_{ec} = Y(EC) \tag{3.11}$$

where $Y(x) = \frac{x_i - min(x)}{max(x) - min(x)}$

DS is then defined as:

$$DS = I_n + I_{ec} \tag{3.12}$$

Finally, DS is re-scaled by applying $Y(x)$ and qualitative labels are attributed as:

$$\begin{cases} if\ DS \leq 0.2 \rightarrow Very\ low \\ if\ 0.2 < DS \leq 0.4 \rightarrow Low \\ if\ 0.4 < DS \leq 0.6 \rightarrow Medium \\ if\ 0.6 < DS \leq 0.8 \rightarrow High \\ if\ DS > 0.8 \rightarrow Very\ High \end{cases} \tag{3.13}$$

The analysis of wave storms is pursued yearly, seasonally and monthly. Since the present study is done at a global scale, no distinction is made between (boreal or austral) winter or summer seasons, unless that is specifically needed. For that matter, seasons are defined following the WMO (World Meteorological Organization) standards, as: December to February (DJF), March to May (MAM), June to August (JJA), and September to November (SON).

3.4 Results

3.4.1 Coastal mean wave climate

Prior to the global coastal wave storm detailed assessment, a brief description of the annual mean wave climate from the complete H_s time series from 1979 to 2020 along the global coastlines is presented (Fig. 3.1). This will then be used as a basis for further analyses and classification of the coastal wave storminess. The annual mean H_s along the global coastlines shows a general meridional gradient (Fig. 3.1a). The highest values of annual mean H_s are observed in the mid latitudes, mostly poleward of 35° in both hemispheres. Significant differences between eastern and western coastlines of the continents can be observed, being the latter reached by higher annual mean H_s due to the prominent eastward direction of extratropical waves (Semedo et al., 2011; Young, 1999).

The lowest values of annual mean H_s are found along the equatorial coastlines and, not surprisingly, in semi-enclosed basins, such as the Mediterranean Sea and Red Sea, and in marginal seas, such as the Yellow Sea and South China Sea. The highest values of annual mean H_s are found in extratropical coastlines of the SH, a consequence of the extended fetch

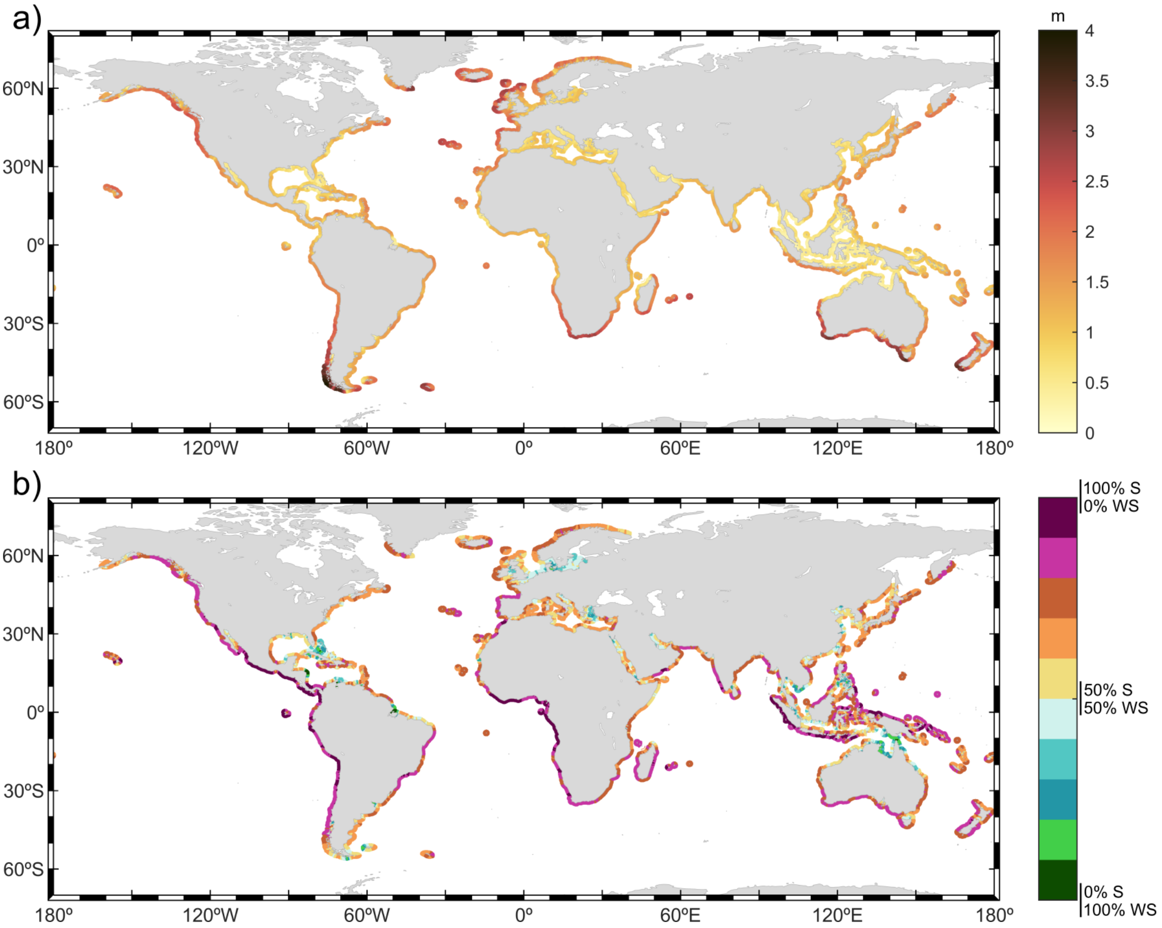

Fig. 3.1 Global coastal (a) mean H_s (m) and (b) swell vs. wind sea dominance (%).

and the sustained generation of waves caused by the prevailing westerly winds that blow all year round (Young, 1999). In particular, the southernmost part of the Chilean coast and the coast of East Tasmania show the highest annual mean H_s within SH extratropical coastlines, almost reaching 4 m. The annual mean H_s in the coastal mid latitudes of the NH are, on the other hand, lower than those in the SH. The highest values of annual mean H_s, of around 3 m, are observed in the west coasts of Ireland and Scotland, in the North Atlantic sub-basin. The lowest values of annual mean H_s along the global coastlines are found in the Java and Banda Seas in Indonesia, with values ranging between 1 and 2 m. These seas are, on the one hand, sheltered from the open Indian Ocean swell waves, compared, for example, with the south coast of Sumatra, and, on the other hand, the local mean wind speeds are rather low. Fig. 3.1b shows the annual mean swell and wind sea dominance along the global coastlines. A large proportion of it (aprox. 50%) shows a swell dominance above 70%, which is consistent with previous studies on the matter but for the deep ocean (Semedo et al., 2011). The coasts more clearly dominated by wind sea are those surrounding the Gulf of Carpentaria, South Vietnam, South Cambodia, Northeast Germany, West Turkey, Bahamas, the Caribbean coasts of Honduras and Nicaragua and the northernmost part of the coast of Brazil.

3.4.2 Assessment of wave storm characteristics

Frequency of occurrence

The annual mean number of wave storms and severe wave storms (Eq. 3.1; Fig. 3.2) show significant heterogeneity along the global coastlines. In this regard, differences of more than 10 storm events and 5 severe storms events per year can be observed between coastlines of different regions. Extratropical coastlines show an overall higher annual number of events than lower latitudes. The number of storm events poleward of 30° roughly exceeds 11 events per year in both hemispheres (Fig. 3.2a). Within these regions, the highest values are found in the northeastern coasts of North America, the coasts of South Africa, South Namibia, South Australia, South New Zealand, Northeast Japan and the southernmost part of the Argentinean coast, where more than 13 wave storms per year occur on average. On the other hand, the lowest values within these regions are observed along the Atlantic coasts of the Iberian Peninsula, the southeast coast of Australia, the north coast of New Zealand and the coastline of Oregon (USA), with around 11 events per year. Semi-enclosed seas, such as the Gulf of Mexico, the Persian Gulf, the Mediterranean Sea and the Red Sea, and marginal seas, such as the Yellow Sea, also show high storm frequencies with more than 10 storm events per year. The mean annual number of storm events decreases along open coastlines closer to the equator, ranging between 5 and 11. Among them, the highest annual number of storm events is found along coastlines reached by swells generated in the extratropical regions, such as the coasts of South Sumatra, South Java, Angola and the north coasts of the Canary Islands, where more than 10 events per year occur on average. The lowest annual number of storm events are found in the coasts of the Arabian Sea, showing an annual mean number of storms lower than 5.

The global pattern of the annual mean number of severe storms is similar to the one for simple storm events, although showing, as expected, lower frequencies (Fig. 3.2b). The mean number of severe storms per year poleward of 30°, in both hemispheres, roughly exceeds 4. The highest frequency of occurrence, more than 6 per year, can be observed at the mid to high latitudes along the coast of the Gulf of Alaska, the eastern coast of North America, the southernmost part of the coasts of Chile and Argentina, the southeast coast of South Africa, the north coast of Tasmania and the northeast coast of Japan. These high frequencies of occurrence can also be seen in the innermost coasts of semi-enclosed basins, such as the Red Sea, the Gulf of Mexico, the Persian Gulf and the north coasts of the Mediterranean Sea, and in marginal seas such as the Yellow Sea. On the other hand, the lowest severe storm frequencies can be observed along the coasts of West India, Pakistan, Oman, Northwest

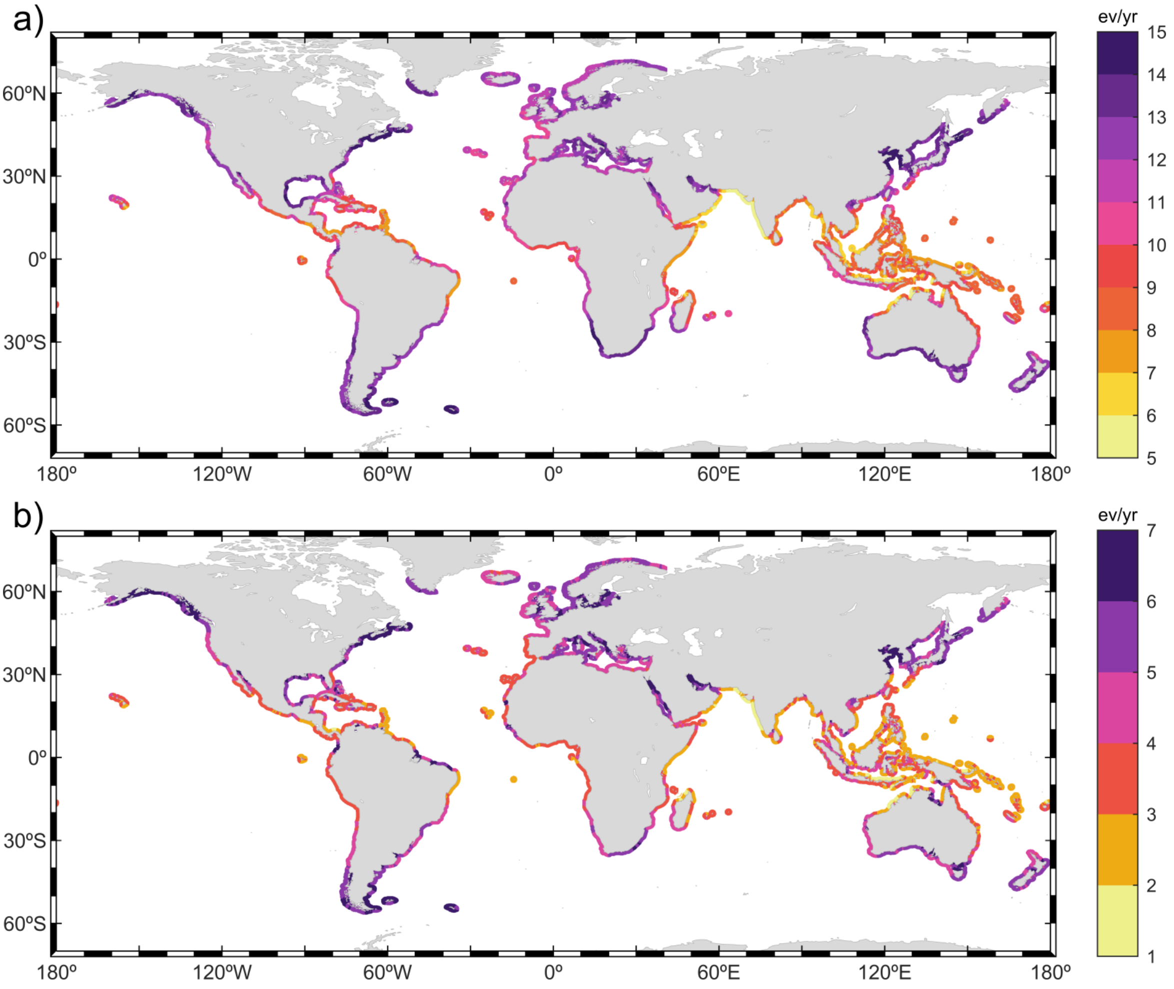

Fig. 3.2 Global coastal annual mean number (events/year – ev/yr) of (a) wave storms and (b) severe wave storms. The color scales vary between the panels.

Australia, North Sumatra, North Papua, South Somalia, Northwest Madagascar and North Panama, showing around 2 events per year, or less.

Fig. 3.3 shows the mean number of wave storms and severe wave storms in DJF and JJA. Results evidence that the frequency of occurrence of wave storms is highly seasonal, i.e. there is a strong variability in the number of storms within the year in almost all the global coastlines. Most of the storm events in NH extratropical latitudes occur during the boreal winter in DJF (Fig. 3.3a) and almost none in JJA (Fig. 3.3b). On the other hand, coasts in the extratropical SH can still suffer the impact of 1 or 2 storms in some areas in DJF, denoting a more pronounced seasonality in the NH. The seasonality is enhanced in the intertropical and subtropical coasts affected by swell storms propagating from extratropical areas, as no swells reaching these coasts during the austral winter are strong enough to meet the local criteria and be classified as wave storms during the summer. During MAM and SON, between 2 and 3 wave storm events, on average, take place along midlatitude coastlines.

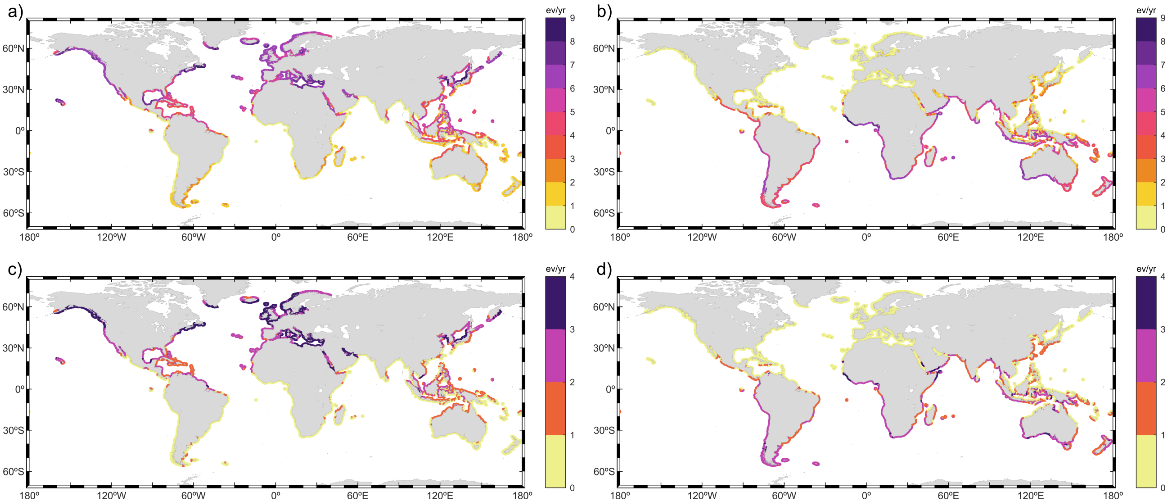

Fig. 3.3 Seasonal global coastal annual mean number (events/year - ev/yr) of (a) DJF wave storms, (b) JJA wave storms, (c) DJF severe wave storms and (d) JJA severe wave storms. The color scales vary between the panels.

The coasts affected by TCs and, especially, those in the NH tropical western Pacific, the region with the highest frequency of TCs (Emanuel, 2010), show a remarkable number of storm events during MAM and SOM as these months overlap with the TC seasons (i.e., roughly from June to November in the NH and from November to April the SH).

The occurrence variability of wave storms within the year is fully addressed in Fig. 3.4 and Fig. 3.5. Fig. 3.4 depicts the mean yearly clustering of storm events; Fig. 3.5 shows for several key points the variability of the monthly frequency of occurrence throughout the year. Most coastlines (almost four-fifths) experience only one storm season - in other words, wave storms mostly occur in a unique continuous period of consecutive months (Fig. 3.4a). Some coastal locations have more than one storm season. These are mainly located in intertropical and subtropical latitudes, with the main exceptions of the southernmost part of the Chilean coast and the northernmost Japanese coast. Additionally, there are coasts where despite existing some (weak) seasonality, the number of storms remains quite stable all year round, thus not showing any storm season. The coasts of Mozambique, East Tasmania and the southernmost part of the Argentinian coast are the main regions showing this behavior.

The length of storm seasons varies along the global coastlines. This issue is depicted in Fig. 3.4b through the number of months aggregating at least 75% of the storms. In general, NH extratropical coasts show shorter storm seasons than those in the SH. Thus, while in the former most of the events occur within 4-5 months, the latter may suffer wave storms for more than 7 months. Points P1 and P2, both located above 50°N in the North Pacific and Atlantic sub-basins, show that storms in NH extratropical latitudes mostly concentrate in the winter months, whereas points P10 and P11, both in SH extratropical latitudes, show a more even distribution of the storm occurrence across the year. Tropical coasts show great heterogeneity in the length of the storm season. Among them, the coasts of the Arabian sea show the shortest storm season as most of the storms occur in only two months, as can be seen in point P6 from Fig. 3.5. Wave storms are driven by the summer monsoon and its strong southwesterly winds, from June to August (Goswami et al., 2006).

The mean inter-arrival time between storms during the storm seasons (Eq. 3.3; Fig. 3.4c) vary from less than 10 days to more than 25, depending on the number of events and the length of the storm season. Note, nevertheless, the low storm inter-arrival times along the northwestern coastlines of the continents (from 10 to 14 days), despite being affected by a notable number of events (Fig. 3.2) and high annual mean H_s (Fig. 3.1). On the other hand, the coasts of Mozambique, North Argentina, East Australia, East New Caledonia and the southern islands of Vanuatu (among others), show high time gaps of more than 18 days. The mean time gap between wave storm events shows notable differences across the intertropical and subtropical regions and even within a specific ocean basin. For example, the mean time gap between storms in the Arabian Sea varies from more than 15 days along the west coast of India to barely more than 10 days in the coast of Oman. Further, the inter-arrival time along the south coastline of the Gulf of Mexico is around 12 days, whereas in the north it is around 15 days.

Storm duration

The mean duration of wave storms and severe wave storms (Eq. 3.4) is shown in Fig. 3.6. The spatial pattern of the mean storm duration (Fig. 3.6a) is, in general terms, opposite to the mean number of events per year (Fig. 3.2a). The mean duration of wave storms impacting coasts in the extratropical regions of both hemispheres ranges between 12 and 36 hours (Fig. 3.6a), being the western European coast the one showing the longest durations. Fig. 3.7 shows the histogram of storm durations for the same points analyzed in Fig. 3.5. The extratropical region of both hemispheres shows similar histograms of storm durations, as can be observed at points P1 and P2 (NH) and P10-P12 (SH). The most probable storm duration ranges between 12 and 24 hours for the five above mentioned extratropical key points, then the probability smoothly decreasing for longer wave storm durations.

In the intertropical and subtropical regions, the mean wave storm duration is higher (average mean storm duration of 45 hours between 30°S and 30°N). There are considerable differences between coasts, with minimum mean durations of around 36 hours in the innermost coasts of the Gulf of Mexico, Red Sea and Persian Gulf, and maximum values along the west coast of India of more than 120 hours (5 days). The shape of the mean duration histogram in the tropical key points varies depending on the origin of the wave storms. P5 and P7, both mainly affected by extratropical swell storms, show a histogram with a similar shape to points located poleward of 30° (e.g., P11 and P12). On the other hand, P8 and P9, affected

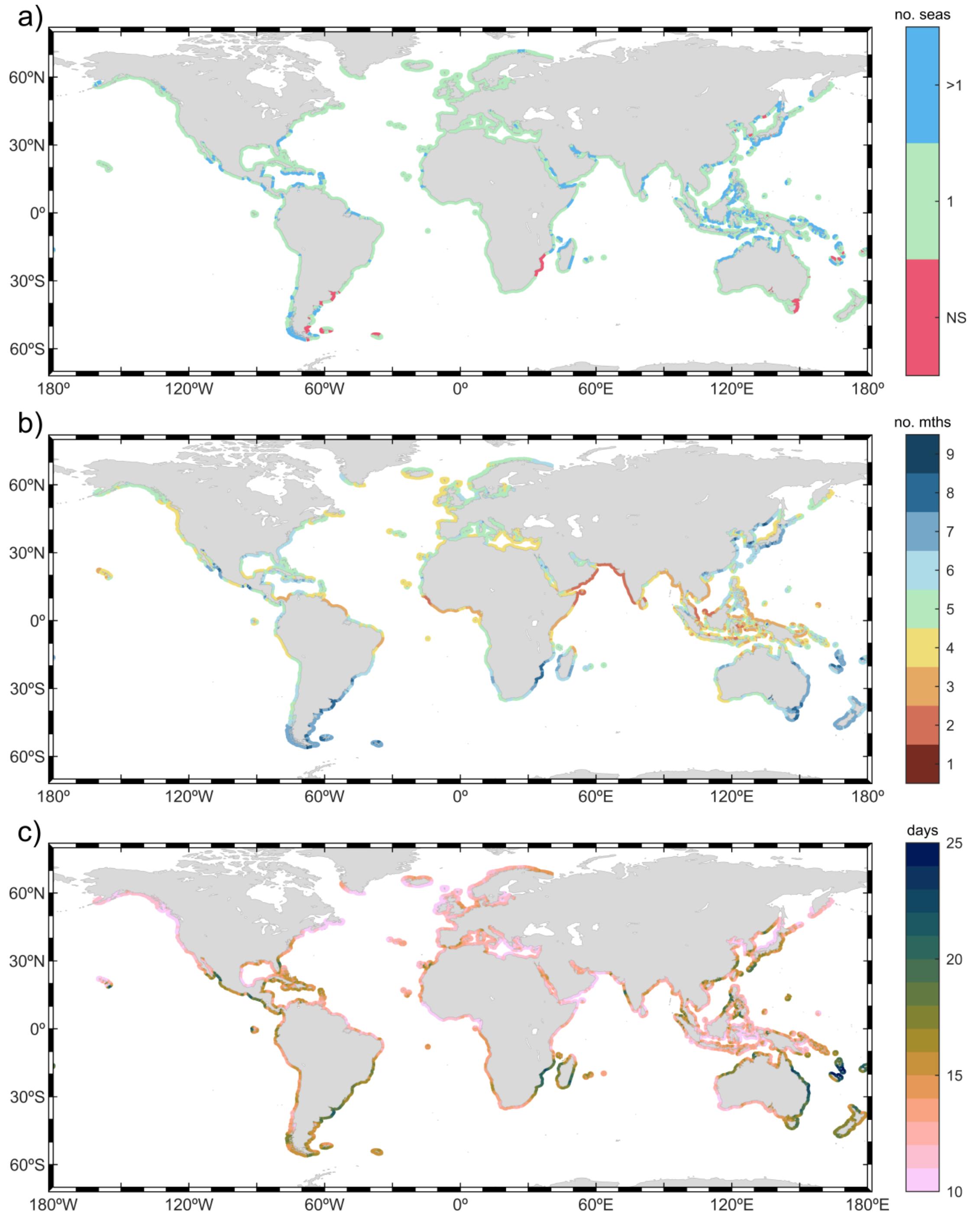

Fig. 3.4 Global coastal clustering of wave storms: (a) number of storm seasons (NS: No seasons), (b) number of months with 75% or more wave storms and (c) mean time (days) between wave storms during the storm seasons.

at the same time by wave storms with different geneses: tropical storms, extratropical storms and trade winds, show a more complex shape. The coast of the Arabian Sea has the longest wave storms in the global coastlines, which may last for more than 90 hours (i.e., more than

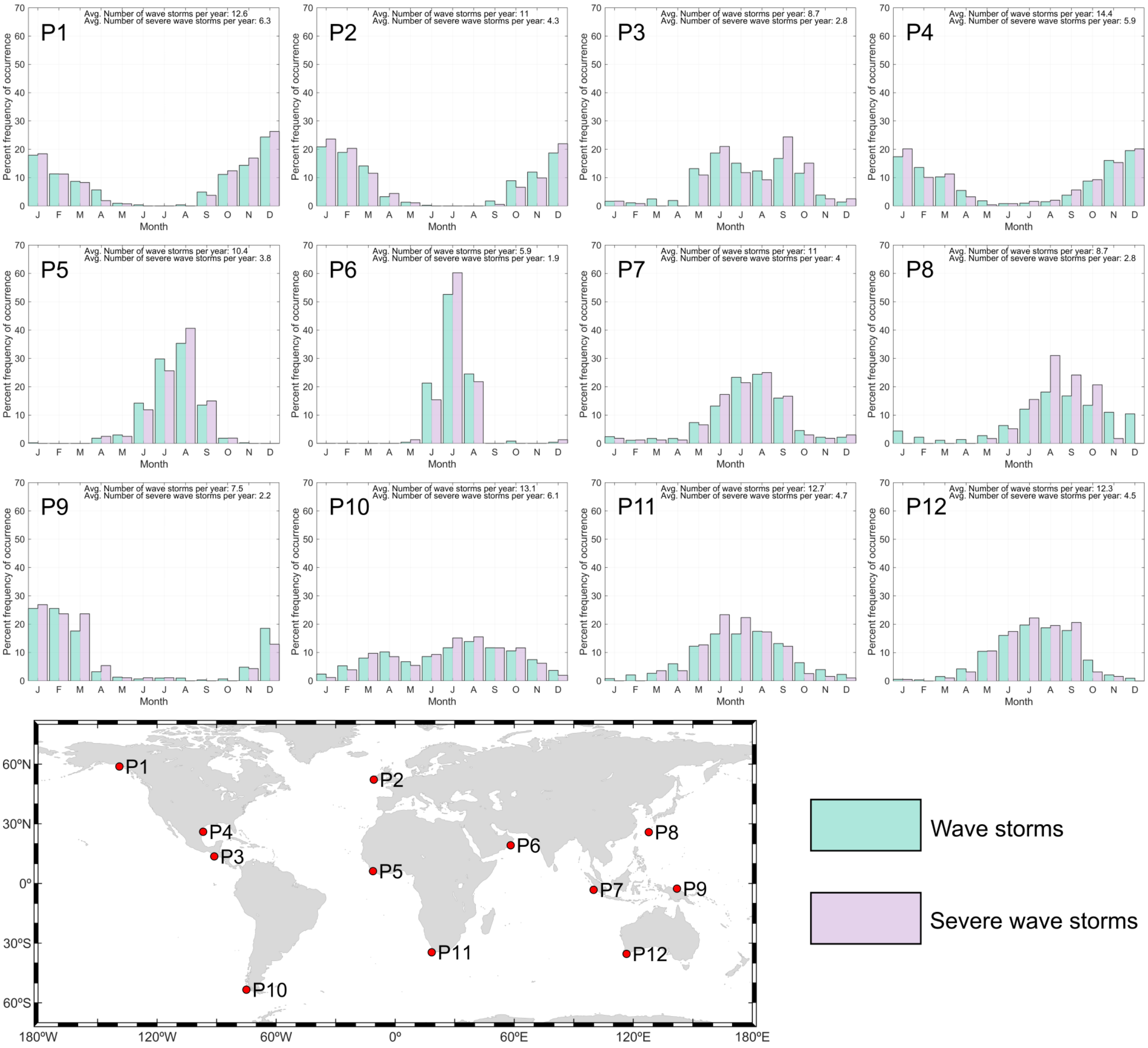

Fig. 3.5 Monthly percent frequency of occurrence of wave storm events at twelve key locations (P1 to P12: see map). Bars represent the monthly percent frequency of occurrence of wave storms (green) and severe wave storms (purple).

3.5 days). The sustained southwesterly winds during the summer monsoon (Goswami et al., 2006) most likely explain these extremely long events.

As expected, severe wave storms are even longer than wave storms (Fig. 3.6b), hence, increasing their damaging power. The most energetic storms generated in the extratropical regions can last, on average, longer than 36 hours. These extreme events are especially long along western European coasts, clearly exceeding 48 hours in the Atlantic coast of the Iberian Peninsula, the southwest coast of France and the west coasts of Ireland and Scotland. The most probable mean duration of severe storms in the extratropical region is higher than for regular storms, namely between 24 and 48 hours (key points P1-P2 and P10-P12 in Fig. 3.7). Consistently, the mean duration in the intertropical and subtropical regions also increases,

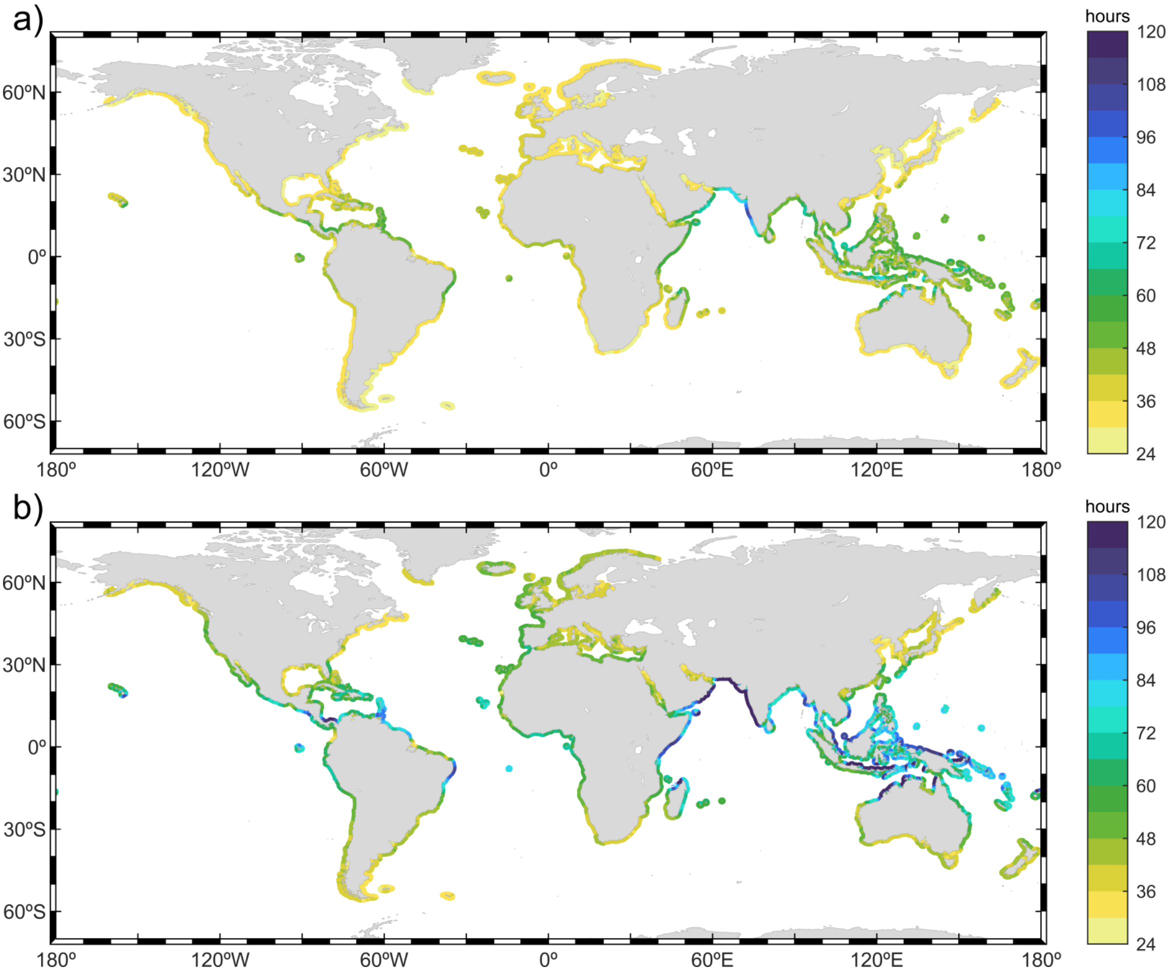

Fig. 3.6 Global coastal mean duration (hours) of (a) wave storms and (b) severe wave storms.

showing minimum mean severe wave storm durations of 60 hours along open coastlines and, particularly, higher than 100 hours in the Arabian Sea coast.

Significant wave height

The mean H_s of wave storms and severe wave storms (Eq. 3.5) are shown in Fig. 3.8. The mean H_s of wave storms, depicted in Fig. 3.8a, show a meridional pattern with higher values at extratropical latitudes, especially along the western coastlines of the continents. Severe wave storms show a similar mean H_s pattern but, as expected, with higher magnitudes (Fig. 3.8b). In addition, the increase in mean H_s for severe storms is not homogeneous along the global coastlines, ranging between less than 2% to more than 20%.

Storms impacting the northwestern European coasts are characterized by very high mean H_s, exceeding 6.5 m in the west coasts of Ireland, Scotland and Faroe Islands, and in the south coast of Iceland. The most severe storms reaching these coasts show mean H_s values

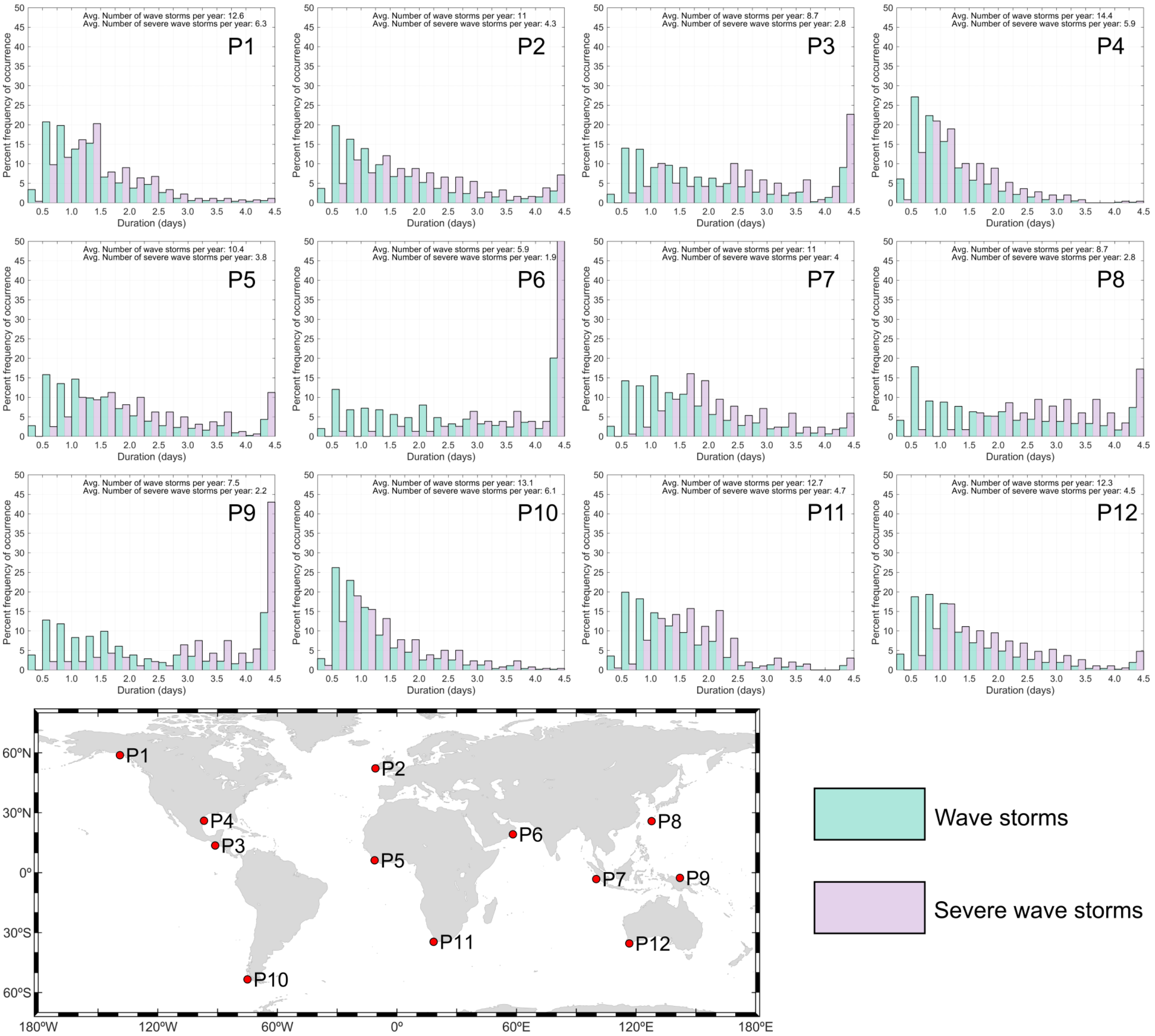

Fig. 3.7 Monthly percent frequency of occurrence of wave storm durations at twelve key locations (P1 to P12: see map). Bars represent the monthly percent frequency of occurrence of wave storms durations (green) and severe wave storms durations (purple).

between 6%-10% higher (above 7 m). Coastlines in the SH extratropical region show mean wave heights during storms of the same order of magnitude as the European coasts previously mentioned. These storms affect the southernmost part of the coasts of Chile, Australia and New Zealand. Other coasts poleward of 30° are also reached by storms of notably high mean H_s, such as the coasts of Alaska, West Canada and South Chile, among others, affected by wave storms (severe wave storms) of mean H_s higher than 5 m (6 m). The remainder of the coastlines in these latitudes show mean H_s values that range, approximately, between 2 to 4 m.

There are notable differences between the mean H_s of wave storms across the intertropical and subtropical coasts. The coasts affected by TCs show mean H_s always higher than 2

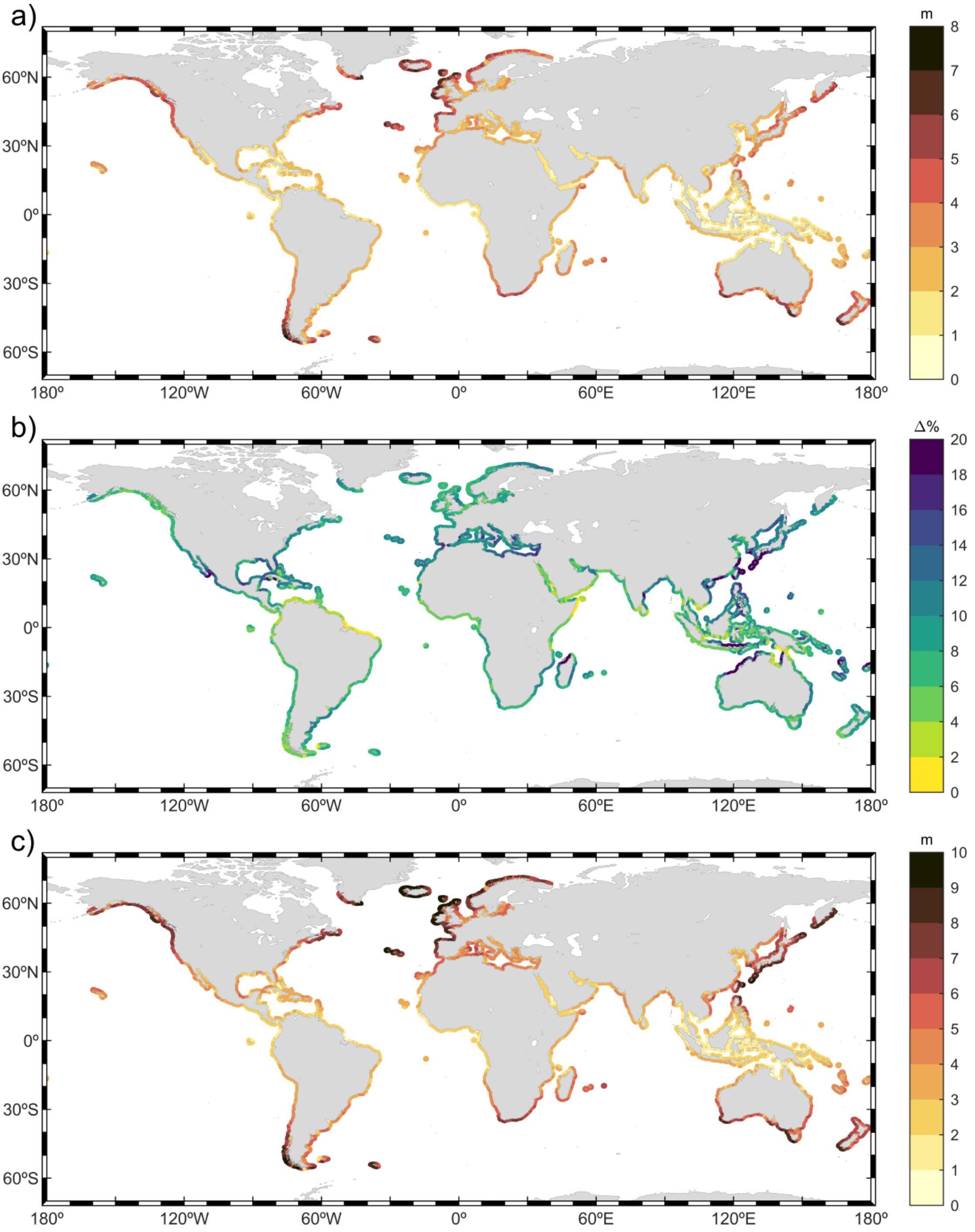

Fig. 3.8 (a) Global coastal mean H_s (m) of wave storms. (b) Global coastal increase in mean H_s (%) in severe wave storms. (c) Global coastal mean annual maxima H_s (m) registered in a wave storm. The color scales vary between the panels (a) and (c).

m. That is the case of the NH tropical western Pacific coastlines, where the wave storms mean H_s exceeds 4 m. Furthermore, this coast shows a remarkable increase in mean H_s for severe storms, exceeding 25%. Other coasts affected by TCs, such as the northwest coasts of Australia and Madagascar, and the southernmost coast of Baja California (Mexico), also show increases in mean H_s of severe storms above 25%. It is noteworthy to mention the high mean H_s of the storms at the coasts in the Arabian Sea. The intense storm activity during the summer monsoon season generates wave storms (severe wave storms) with mean H_s close to 3.5 m. Open coastlines directly affected by the propagation of energetic swells from the extratropical regions, such as the coasts of South Sumatra, South Java, Namibia and North Chile in the SH, for example, as well as the north coasts of the Canary Islands and the Atlantic coast of Morocco in the NH, also suffer quite intense wave storms of 3 m or more. Among these coasts, those located in the NH suffer higher increases in mean H_s during severe storms (between 8% and 12%), whereas the increase in SH coasts is mostly lower than 7.5%. It is also noteworthy the low increase in mean H_s for severe storms found in the northeastern coasts of Brazil and Somalia, reflecting a low variability in the storm wave climate intensity.

The lowest wave storm mean H_s values can be observed in marginal seas in low latitudes such as in the Persian Gulf, the Red Sea, the Gulf of California and all the coastlines facing the interior seas in Indonesia (Java Sea or Banda Seas). The mean H_s of storms in these regions range only between 0.5 to 2 m. Although in general these coasts show moderate increases of between 2.5% and 10% in mean H_s for severe storms, the north coast of Java stands out due to significant increases of above 20%.

The most extreme wave heights reaching the coast during severe wave storms cannot be assessed in Fig. 3.8a,b, since extreme values are smoothed in the H_s averaging process, also limited by the imposed storm duration. However, wave heights can be considerably higher at the storm peaks. Therefore, in order to assess the maximum wave heights arriving to the coast during wave storms, Fig. 3.8c shows the mean of the maximum H_s reached in a storm in each of the 42 years (i.e., the mean annual maxima H_s). Results show values higher than 10 m in the northwestern European coasts and the southernmost part of the Chilean coast. In addition, the TC activity is more clearly reflected by this parameter, with H_s values exceeding 9 m in the NH tropical western Pacific Ocean, 6 m in the SH tropical west Indian Ocean and 4 m in the Gulf of Mexico and Caribbean Sea.

Mean wave direction

The mean Θ_m of wave storms (Eq. 3.5) are shown in Fig. 3.9. Since the storm wave climate in the western coasts of the continents is mostly driven by waves generated by extratropical storms, the mean Θ_m along these coasts is mainly determined by the mean path followed by these waves while propagating away from the generation area toward the coasts. Starting at the north of the North Atlantic sub-basin, the mean Θ_m of incoming wave storms in the west coast of Ireland and Scotland is from the west. The incoming Θ_m of storms veers in coasts more to the south, with mean Θ_m from the west-northwest in the Atlantic coast of the Iberian Peninsula and from the north-northwest in the coast of Senegal. The wave storm climate along the African coastline that extends from Guinea-Bissau to Cape of Good Hope (in South Africa) is dominated by waves generated in the SH extratropical storm track. Accordingly, the incoming mean Θ_m in the Gulf of Guinea is approximately south-southwest, veering southward, reaching mean Θ_m from the west-southwest in the coastlines along and in the vicinity of Cape of Good Hope.

Analogous incoming wave storm directions can be observed along the western coast of America. The mean Θ_m of wave storms in the east part of the Gulf of Alaska is south-southwest, veering eastward, reaching southwest in the southernmost part of the Pacific coast of Canada. The incoming mean Θ_m of wave storms along the Pacific coastline of the USA is west. Southward of South California, the mean Θ_m is mainly driven by the propagation of long swells from the SH extratropical region. Thus, the coastline that extends from Mexico to Panama shows mean Θ_m from the south-southwest. The orientation of the Pacific coast of Colombia shelters it from swells with south-southwest direction, hence causing the mean storm Θ_m to be southwest. Southward, the mean Θ_m of wave storms in the coasts of Ecuador and Peru is south-southwest. The mean Θ_m of incoming wave storms in the coast of Chile, which extends from 18°S to 65°S, veers eastward from south-southwest at the frontier with Peru to almost west at its southernmost part.

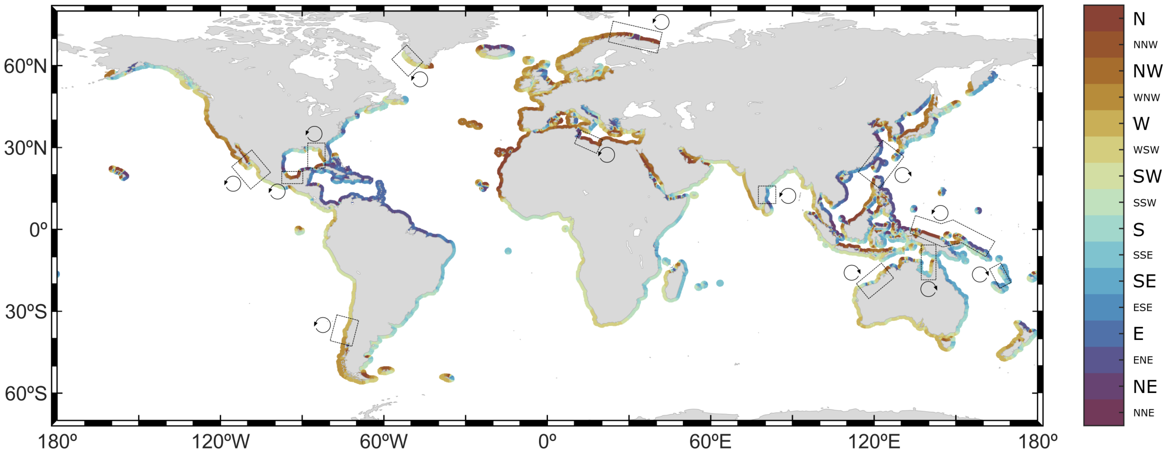

Fig. 3.9 Global coastal mean Θ_m (°) of wave storms. Boxes highlight coastal regions where the difference between Θ_m for wave storms and severe wave storms is higher than 15°.

The south and west coasts of Australia show mean storm Θ_m from the southwest. Wave storms at the south coastlines of Sumatra and Java are mainly generated at SH extratropical latitudes, hence showing north-northeastward directions. Mean storm Θ_m veer eastward along the south coast of Sumatra, being southwest in the westernmost part of the south coast of Sumatra and in the coast of Myanmar.

To a very good extent, wave storm climate in the eastern coastlines of the continents is more complex than in the western ones and, accordingly, so is the mean Θ_m pattern. That is due to the coexistence of wave storms with different geneses throughout the year. Extratropical storm systems are responsible for the wave storms in the eastern mid to high latitudes, mostly at the maritime cyclogenesis areas. On the other hand, results reveal trade winds to be the main forcing driver of the wave storm climate of eastern intertropical and subtropical open coastlines, inducing mean storm Θ_m with a prominent westward component. Additionally, most of the eastern tropical coastal areas are affected by TCs. Therefore, extra-topical marine cyclogenesis, trade winds, and TCs are the main wave storm generating systems impacting the eastern continental coasts, apart from local systems such as the Nortes-induced wave storms in the Gulf of Mexico, or the Monsoon-induced wave storms in the Arabian Sea.

There are, additionally, specific coasts affected by a strong wave climate seasonality that are worth to be highlighted. The wave storms reaching the coasts of Somalia, Kenya and Tanzania are mainly generated by winds associated to the Indian summer monsoon phenomenon. The wind systems associated to this phenomenon rotates 180° between summer and winter monsoons (Goswami et al., 2006; Ranjha et al., 2015), inducing differences in the incoming mean wave storm Θ_m between DJF and JJA of around 130°.

Results for severe wave storms are very similar to those for wave storms, only existing some exceptions highlighted in Fig. 3.9. These highlighted coastal regions show a veer in mean wave storm Θ_m higher than 15°. Most of them show an anticlockwise rotation, such the south coast of Chile, the east coast of India or the northwest coast of Libya. Others, such as the northwest coast of Australia or the east coast of Taiwan, show a notable clockwise veer.

Wave energy flux

The storms mean E_f has been computed (Eq. 3.5) and is shown in Fig. 3.10. The wave storm mean E_f pattern along the global coastlines (Fig. 3.10a) evidences that the highest values are seen along the coastlines affected by storms with the highest mean H_s (Fig. 3.8a), which are at the same time characterized by quite long T_m (Fig. 3.11). On the other hand, the coasts reached by swell storms with the longest T_m and relatively low H_s, such as in the Gulf of Guinea and South Sumatra, do not show energy fluxes as high as those in areas where the highest mean wave storm H_s occur. Additionally, Fig. 3.10b depicts the mean E_f increase between regular storms and severe storms, showing a wide range of variation, from less than 10% to more than 90%. The highest E_f are observed in extratropical coasts and, particularly, in those along the western coastlines of the continents. Storm mean E_f values of around 300 kW/m are observed for wave storms impacting the west coast of Ireland and the southernmost coast of Chile, almost reaching 400 kW/m for severe storms. The coasts of Alaska, West Canada, South Chile, South Africa, South Australia, New Zealand and the northwestern coasts of Europe show mean E_f exceeding 100 kW/m and values 5%-10% higher for severe storms (150 kW/m). In the tropical latitudes, the highest values are seen in the NH tropical western Pacific, the region affected by typhons, with mean E_f of around 90 kW/m for wave storms. For severe storms the mean E_f can increase almost a 100%, i.e. the energy transported by severe storms almost double the energy transported by wave storms. The storms along the rest of the global coastlines show mean E_f that range between 20 and 60 kW/m.

By decomposing E_f, the magnitude of H_s^2 and T_m will determine if the energy transport is dominated by the wave period or the wave height of the storm, i.e., high wave energy fluxes can be induced by high wave heights and/or high wave periods. The dominant parameter in the mean energy flux of wave storms is depicted in Fig. 3.8c through metric ED (Eq. 3.8). Results show an heterogeneous dominance pattern, in which wave periods control the wave energy impacting more than half of the global coastlines (68%).

In general, along open coastlines closer to the extratropical wave generation areas, mostly poleward of 30° in both hemispheres, wave heights clearly dominate the energy transport. On the other hand, open coastlines in low and low-to-mid latitudes are instead dominated by T_m. The wave height attenuation during propagation away from the generation areas and the frequency filtering of the waves, sending the energy to lower frequencies (higher periods), make these wave storms to be characterized by very long wave periods (Fig. 3.11), and relatively low wave heights (Fig. 3.8a), thus causing the energy flux to be dominated by the former. In semi-enclosed basins as the Red Sea or the Persian Gulf, the mean storm H_s is so low that low T_m values still control the energy flux. Finally, there are also coastal areas that can be seen as intermediate ones, in which the ratio is close to the unit, i.e., the dominance of H_s and T_m is almost even, such as the coasts of Argentina, Uruguay, East Madagascar, West India and the northern coasts of Africa.

Wind sea vs. swell dominance

Wave storms are mostly dominated by wind sea waves. The proportion of the global coastlines dominated by swells (i.e., $WD_s > 50\%$; Eq. 3.6) is 40% when wave storms are considered and 35% if only considering severe storms, as shown in Fig. 3.12.

Notable differences between the eastern and western open ocean coastlines can be observed. The western coastlines are mainly dominated by swells, especially in the intertropical and subtropical regions. For example, the coasts of the Gulf of Guinea, the western coasts of Central America and the coast of South Sumatra show a mean swell dominance above 75%. These coasts suffer the impact of eastward or north-eastward propagating swells generated in the SH extratropical region. In mid to high latitudes, wave storms start to be mostly

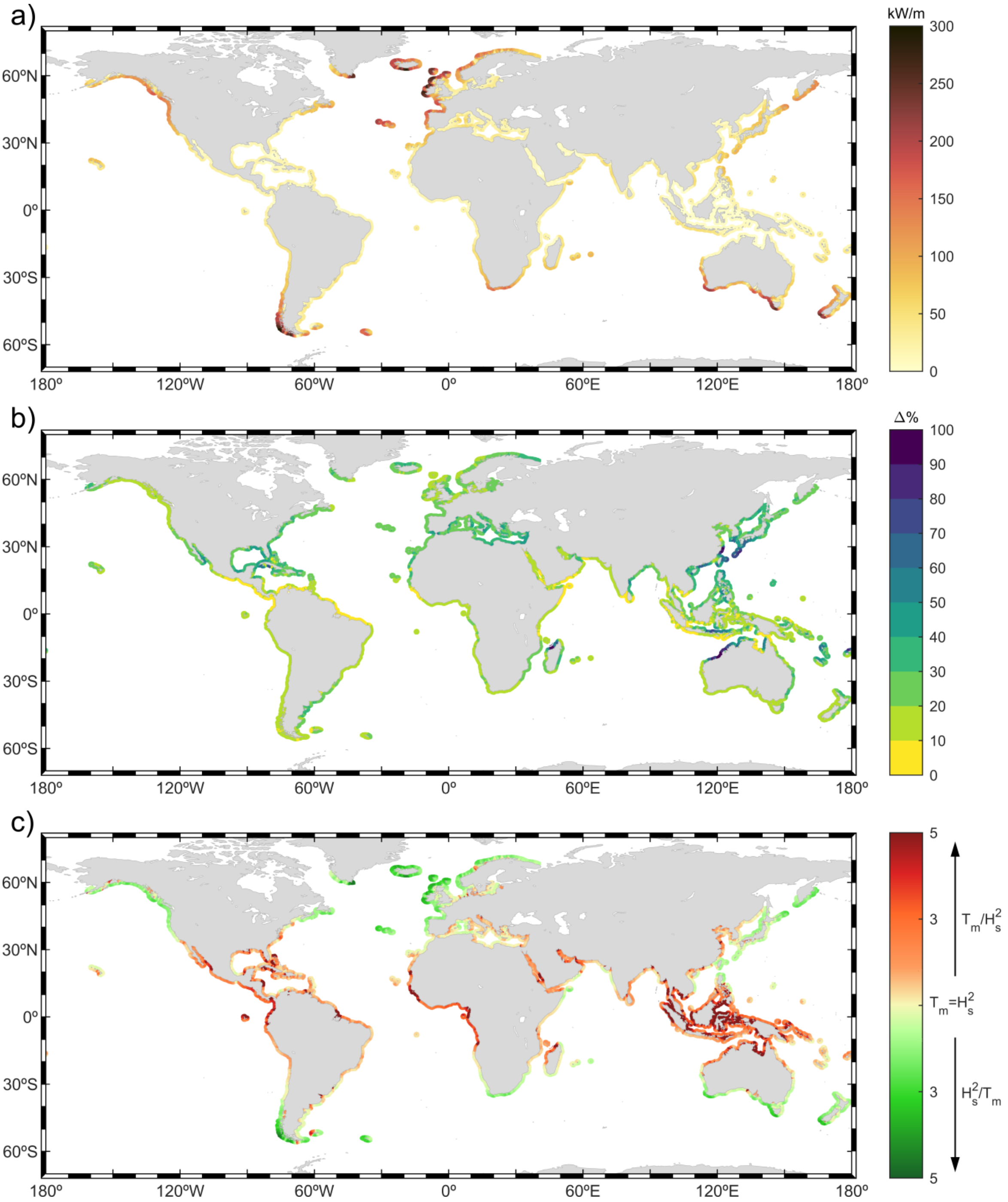

Fig. 3.10 (a) Global coastal mean E_f (kW/m) of wave storms. (b) Global coastal mean H_s and T_m contribution (%) to the E_f of wave storms. (c) Global coastal increase in mean E_f (%) for severe wave storms.

controlled by wind sea waves. The western European coast, the southernmost part of the coast of Chile and the west coast of Alaska show a strong wind sea dominance of the storm wave climate, reaching values of above 70%. The coasts in these latitudes are impacted by

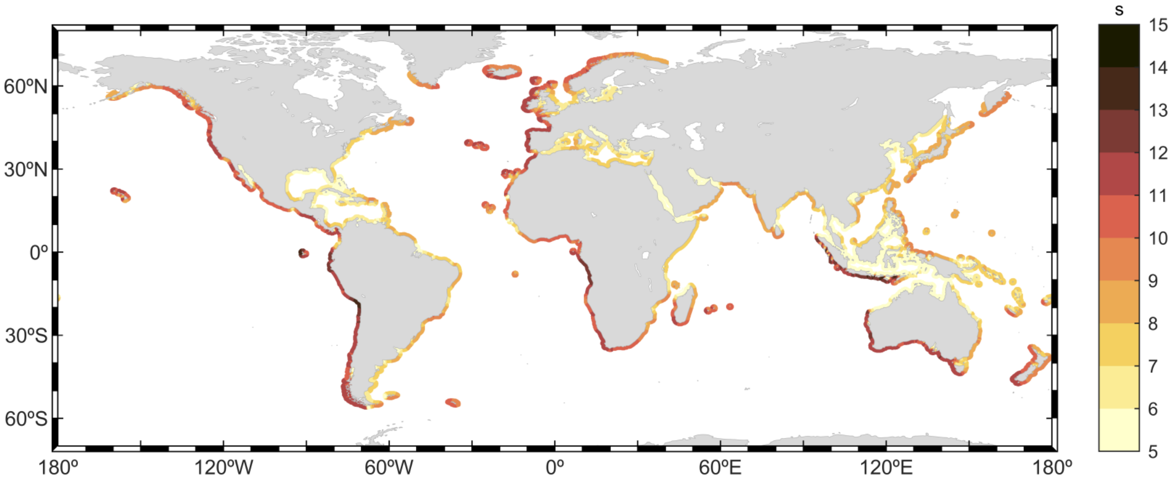

Fig. 3.11 Global coastal mean T_m (s) of wave storms.

very high waves (Fig. 3.8), still on their developing stage (wind seas), due to the proximity of the storm track to the coast, even occasionally landfalling on it.

The northwestern European coasts show the most intense wind sea dominance pattern, especially in the North Sea, due to the protection against swell storms generated remotely. The storm wave climate in this region is driven by the intensity and position of the extratropical North Atlantic storm track, being the latter highly correlated with the North Atlantic Oscillation teleconnection pattern (NAO; Bader et al. 2011; Bradbury 1958). The wave storms generated by extratropical storms on the storm track land in the Northwestern European coasts, especially during the positive NAO phase (Semedo et al., 2015), inducing a strong wind sea dominance. Similar conclusions can be extracted for the northernmost Pacific coast. The extratropical North Pacific storm track shows its highest cyclone track density close to the west coast of Alaska and a decrease to the east (Shaw et al., 2016; Ulbrich et al., 2009), which is consistent with the wind sea dominance pattern found in the westernmost part of the coast of Alaska. The fact that Pacific Ocean coasts are, mostly, fully opened to the ocean, makes them susceptible of being impacted by energetic swells generated remotely, thus countering the wind sea wave storms dominance, most likely explaining the swell dominance in the eastern Gulf of Alaska. Finally, regarding the coast of Chile, it is worth mentioning that it is in the southernmost part of any continent in the SH (except for Antarctica), extending poleward of 50°S. The extratropical southern storm track reaches this region, in latitudes characterized by a high-cyclone track density (Hoskins and Hodges, 2005; Ulbrich et al., 2009), inducing very high wind sea waves that dominate the wave storm climate. The strong wind sea dominance in the southernmost part of coast of the Argentinean coast, a coast protected against the high westerly swells generated in the South Indian Ocean, reflects the strong wind sea wave storm activity in these latitudes.

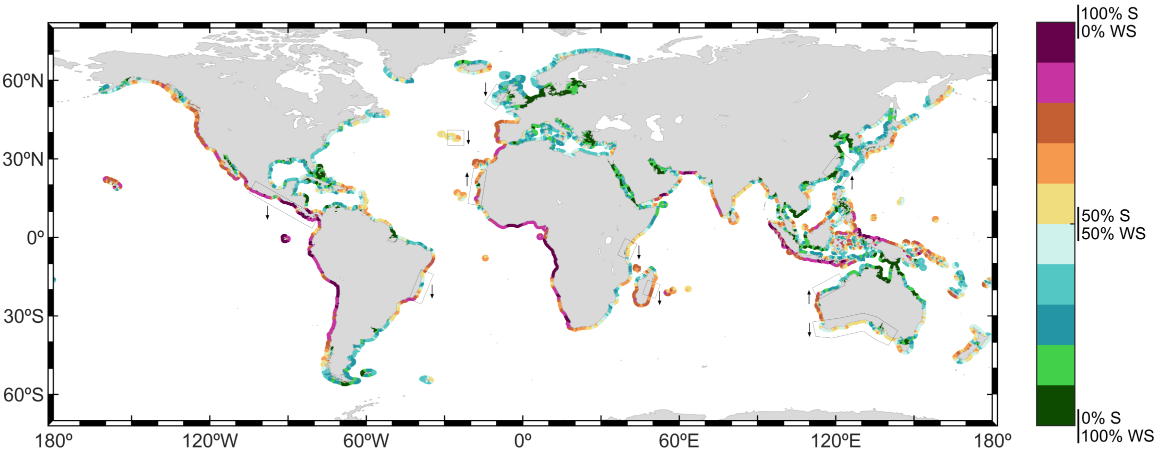

Fig. 3.12 Global coastal mean swell vs. wind sea dominance (%) during wave storms. Boxes highlight coastal regions where the difference between the swell dominance for wave storms and severe wave storms is higher than 10%.

On the other hand, the dominance along the eastern coastlines of the continents is not so clear, showing an heterogenous pattern, characterized by a split dominance in several areas, such as in the north coast of Brazil and the northeast coast of North America. The clearest eastern coast wind sea vs. swell dominance pattern can be found along the north coast of Papua and the east coast of Madagascar, where a swell-dominant storm climate is observed; and along the eastern coast of North America, the coasts of Argentina and Uruguay, the northeast coast of Australia and the east coast of Somalia, all dominated by wind sea wave storms. Marginal and semi-enclosed seas protected to the open ocean, show, in general, a clear wind sea dominance. The Gulf of Mexico, the Mediterranean Sea, the Red Sea, the Persian Gulf, the Yellow Sea, the Gulf of Carpentaria and the North Sea, are clear examples of this dominance pattern.

The dominance pattern for severe wave storms is very similar to the one for regular wave storms. The most relevant exceptions, namely coasts showing differences of above 10% in the swell dominance (Eq. 3.6), are highlighted in Fig. 3.12. The south coast of Australia, the west coast of Ireland, the east coast of Azores, the east coast of Madagascar, the coast of Tanzania, the south coast of Brazil the and western coasts of Central America show an increase of wind sea dominance. On the other hand, the coast of Taiwan, the northwest coast of Australia and the coasts of Mauritania and South Morocco, show a notable increase of the swell dominance for severe storms.

Storm intensity

The intensity of wave storms is assessed in the present chapter through the EC index (Eq. 3.9) and depicted in Fig. 3.13. Results show a very strong gradient between the high storm intensities at extratropical coasts and the low intensities found at intertropical and subtropical latitudes both for wave storms and severe wave storms (Fig. 3.13a and Fig. 3.13b, respectively). The highly intense wave storms generated in the NH extratropical storm track carry most of their energy to the northwestern coasts of the continents, i.e., the western European coast in the North Atlantic sub-basin, and the coasts of Canada and Alaska in the North Pacific sub-basin. The western European coast shows the most intense storms, reaching EC values of 2000 m^2h and, for severe storms, intensities can exceed ECs of 3400 m^2h. In addition, results show that the intensity of storms arriving at the northeastern coasts of North America and the coasts of East Japan and Kamchatka Peninsula is also relevant, showing EC values of 1200 m^2h. Wave storms reaching the coasts in the SH extratropical region are also characterized by high intensities: the southernmost coasts of Chile, South Africa and Australia can suffer the impact of storms with mean intensities of 1500 m^2h. Focusing on severe waves storms, these values increase until reaching 2000 m^2h.

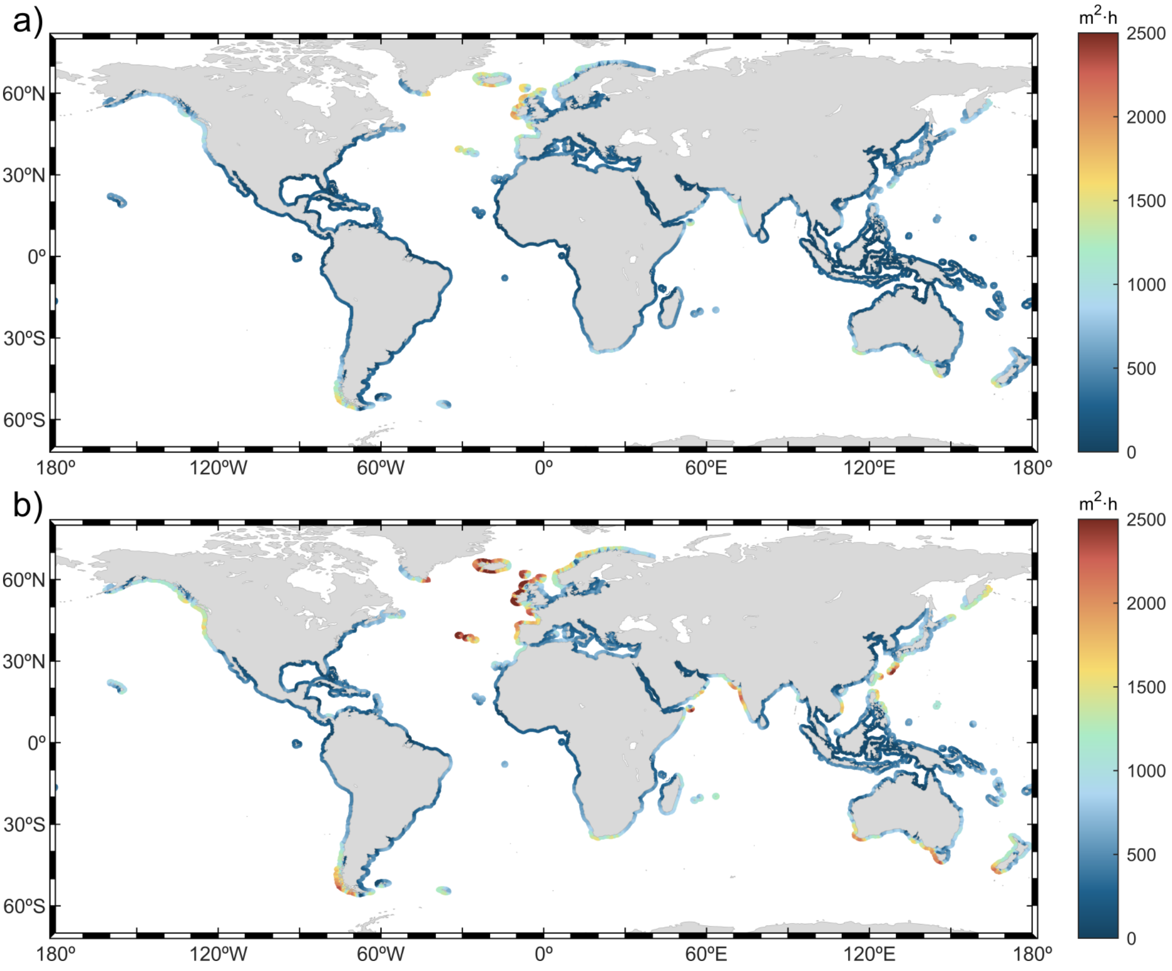

Fig. 3.13 Global coastal mean energy content (m^2h) of (a) wave storms and (c) severe wave storms.

Despite the mentioned storm intensity meridional gradient, some specific intertropical and subtropical coasts may still suffer the impact of very intense wave storms, such as the coastlines along the Arabian Sea during the Indian summer monsoon. These storms show relatively high mean H_s, between 3 and 4 m (Fig. 3.8) and, above all, extremely long durations (Fig. 3.6). As a result, the intensity of the storms arriving at these coasts reach EC values of 1300 $\mathrm{m}^2\mathrm{h}$. The intensity of TCs, which are extremely energetic events, also induces high storm intensities. This issue is most evident in the NH tropical western Pacific, showing EC values of 1000 $\mathrm{m}^2\mathrm{h}$. The intensity of the storms in the rest of the global coastlines is much lower, with EC values of around 500 $\mathrm{m}^2\mathrm{h}$ or less.

3.4.3 Coastal degree of storminess classification

After individually assessing the most important characteristics of coastal wave storms, the DS (Eq. 3.13) provides an integrated qualitative view of how stormy a coast can be (Fig. 3.14). The integration of the number of events blended with the intensity index (EC, Eq. 3.9) offers information about the duration and the wave height of the events. Results show, despite a few exceptions, a clear meridional gradient. It should be noted that this meridional gradient is the expected pattern as every individual index analyzed shows notable differences between the storm behavior in the tropical and extratropical regions.

Only a few coasts are classified with a very high DS. These coasts are the southernmost coast of Chile, the oceanward west coasts of Ireland and Scotland, the westernmost coast of the Azores Islands and the south coasts of Iceland, Greenland and Tasmania (Australia). The coasts classified with a high degree of storminess extend equatorward with respect to those showing a very high degree of storminess, although always poleward of 30°. The western coasts of Europe, the coasts of Alaska, East Canada, South Chile, Newfoundland, Azores Islands, Kamchatka Peninsula, northernmost Islands of Japan, south shores of South Africa, South Australia and South New Zealand, are the main coasts within this class. The rest of the open coasts poleward of 30° can be roughly classified as medium stormy, with the exception of the ocean coasts of Virginia and North Carolina (USA), and the coast of the Gulf of Cadiz, which shows a low degree of storminess. Semi-enclosed basins poleward of 30°, such as the Mediterranean Sea and the Sea of Japan, and marginal seas, such as the Yellow Sea, show an overall medium storminess.

In the intertropical and subtropical regions, results show that coasts are characterized by low or very low DS. Some exceptions can be observed, for example, in the western low latitudinal coasts of the South Pacific sub-basin, affected by typhons, such as the south coasts of Japan, the coast of Taiwan and the north shores of the Philippines. The coast of the Gulf of Mexico is also an exception. A very low storminess can be found in the low latitude coasts, close to the equator, in all oceans. The main coasts under this classification are the protected coasts of Indonesia, North Papua, North Australia, East India and the southernmost coasts of Myanmar.

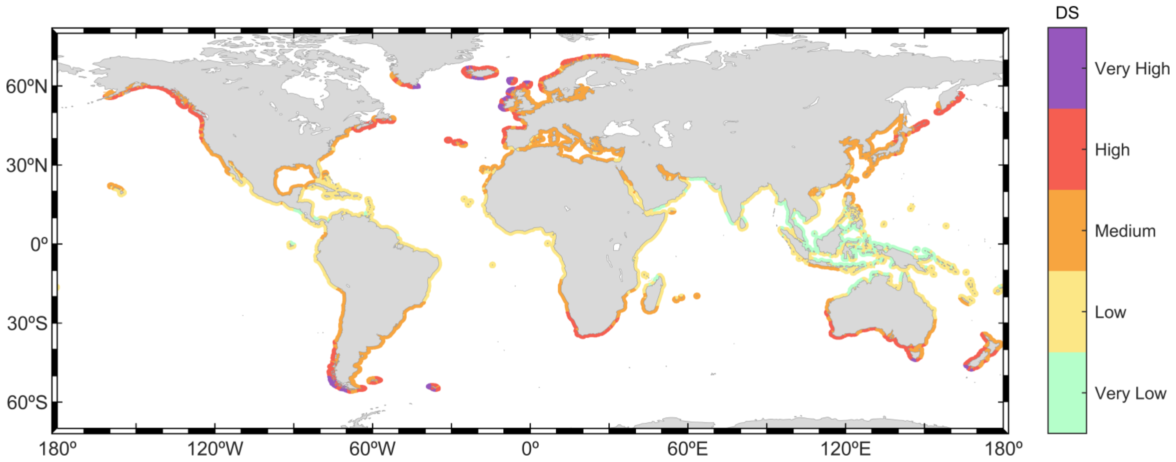

Fig. 3.14 Global coastal degree of storminess.

3.4.4 Storm wave climate classification

A classification of the storm wave climate along the global coastlines in terms of the main characteristics of wave storms is provided in Fig. 3.15. It integrates the annual mean number of events (Eq. 3.1), mean duration (Eq. 3.4), mean H_s (Eq. 3.5), mean Θ_m (Eq. 3.5) and mean wind sea vs. swell dominance of the storms (Eq. 3.6). All the information is summarized in the legend located in the bottom left part of the Fig. 3.15.

As a result, the information in Fig. 3.15 allows to easily identify coastlines, sometimes of hundreds of kilometers, characterized by a similar wave storm climate. For example, the coasts along the Gulf of Guinea, which extends for more than 3000 km, shows a homogenous wave storm climate with mean H_s lower than 2 m and mean duration between 1.5 and 2.5 days. In addition, it makes the comparison between the wave storm conditions in coasts from different regions and continents easier. It is possible to see, for example, that the main characteristics of the wave storms arriving at the southernmost coast of Chile and the west coast of Tasmania (not accounting for the incoming direction of the storms), are quite similar in terms of mean duration, mean H_s and mean frequency. Idem for the Gulf of Alaska and South South-Africa. In this regard, it is noteworthy to point out that all the coasts classified with a very high degree of storminess share relatively high frequency of occurrence of wave storms, more than 10 times per year, as well as very high wave heights (above 6 m), with mean durations of less than 1.5 days. Contrarily, coasts classified with very low storminess are affected by storms of low wave heights, normally below 2 m, with longer durations: more than 1.5 days.

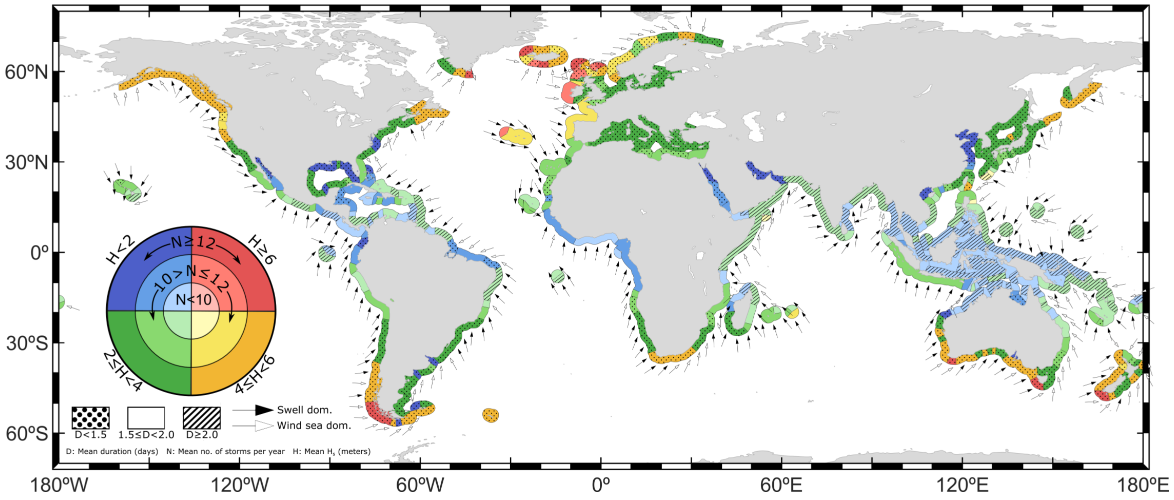

Fig. 3.15 Storm wave climate classification along the global coastlines according to the main characteristics of wave storms: mean H_s (color), mean frequency of occurrence (color scale), mean storm duration (hatching), mean Θ_m (arrow direction) and swell vs. wind sea dominance (arrowhead color).

3.5 Conclusions

The present chapter assesses the wave storminess along the global coastlines. The analysis is performed based on the outputs of a 42-year high-resolution hindcast, produced with close to surface wind fields and sea ice coverage fields from the ECMWF ERA5 reanalysis. Despite multiple storm classification criteria have been used in previous studies, for simplicity and consistency across the global coastlines, a unique criterion widely used in the literature is applied. H_s events are isolated and classified as wave storms by analyzing the exceedances over the H_s95 threshold. In addition, the most energetic wave storms and, hence, those that may cause more damage on the coast, are classified as severe wave storms by assessing the exceedances over the H_s99 percentile threshold.

The main characteristics of the wave storms and severe wave storms are analyzed and depicted based on a set of statistics and indices, some proposed here for the first time, such as inter-arrival time between storm events within storm seasons (Eq. 3.3) and the wave height vs. wave period dominance of wave storms E_f (Eq. 3.8). This study focuses, first, on the key features of wave storms: frequency of occurrence (Fig. 3.2 and Fig. 3.3), duration (Fig. 3.4) and intensity (Fig. 3.13). Additionally, the mean integrated wave parameters H_s (Fig. 3.8), Θ_m (Fig. 3.9), T_m (Fig. 3.11) and E_f (Fig. 3.10) are analyzed. For completeness, qualitative characteristics of wave storms, such as the swell vs. wind sea dominance during the events (Fig. 3.12), as well as the H_s and T_m dominance in the wave storm impairing E_f (wave power) at the coast (Fig. 3.10c), are assessed. The combined analysis of the statistics and indices along the global coastlines offers a wide view of the behavior of the wave storms and severe storms.

The coastal wave storminess classification is conducted based on a new index, the DS (Eq. 3.13; Fig. 3.14). The storminess pattern along global coastlines is characterized by a meridional gradient, with higher DS for higher latitude coastlines in both hemispheres. Coasts in the extra-tropical regions suffer the impact of a high mean number of storms per year (Fig. 3.2a), each of them lasting, on average, less than 1.5 days (Fig. 3.6a; points P1-P2, P10-P12 in Fig. 3.7). These storms are mainly generated in the extra-tropical storm tracks, with a higher frequency in the respective hemisphere winter season (Fig. 3.3) and a strong seasonality (Fig. 3.4b; points P1-P2, P10-P12 in Fig. 3.5). Wave storms arriving at the coast with a certain incoming direction (Fig. 3.9a) can either be generated remotely and propagate as swells, or they can occur under the landfall of a storm, being dominated by wind seas (Fig. 3.12). Coasts at mid to high latitudes, especially those in the western continental coastlines directly facing open ocean, are impacted by highly intense storms (Fig. 3.13a,b) with the highest mean H_s (Fig. 3.8a) along the global coastlines. Poleward of 40° in both hemispheres, the mean H_s during wave storms exceed 6 m in some coastal areas, being the storm wave climate controlled, in most cases, by wind sea waves characterized by a high E_f with a high destructive power (Fig. 3.10a), clearly dominated by H_s over T_m (Fig. 3.10c). At lower latitudes within the extra-tropical meridional band, the wind sea dominance in the western coasts evolves to an almost-full swell dominance (Fig. 3.12a) and lower mean wave storm H_s (Fig. 3.8a). Results for severe storms in the extra-tropical regions show similar patterns to regular wave storms although, as expected, with lower frequency of occurrence (Fig. 3.2b) and more intense characteristics, i.e., longer durations (Fig. 3.6b), higher mean H_s (Fig. 3.8b), higher mean E_f (Fig. 3.10b) and higher intensities (Fig. 3.13c,d), for example.

The analysis of wave storms along the intertropical and subtropical coastlines have shown a more complex wave storm climate due to the convergence of wave storms with different geneses: wave storms generated by extra-tropical storms propagating equatorward, wave storms generated by the trade winds, which have different characteristics and seasonal meridional variabilities in the three main ocean basins, wave storms generated by TCs and local storms affecting regional areas, such as those induced by atmospheric wind features as the Nortes in the Gulf of Mexico or the monsoon in the Arabian Sea. Wave storms generated by extratropical storms mainly affect the intertropical and subtropical western coasts of the continents, but also the eastern coasts in latitudes between 20° and 30°. These wave storms propagate toward the coast as swells (Fig. 3.9a) with very long periods that dominate its energy content (Fig. 3.10c), mostly during the winter months (Fig. 3.3). Trade winds generate low-intensity storms (Fig. 3.13a) that control the storm wave climate in a considerable proportion of the eastern coasts of the continents in low latitudes in both hemispheres. On the other hand, wave storms induced by TCs are characterized by high wave heights (Fig. 3.8a), and, not surprisingly, dominated by wind sea waves (Fig. 3.12a). Such events can be best observed in the NH tropical western Pacific coasts as they are impacted by the highest frequency of TCs in the world, exceeding mean H_s of 4 m (Fig. 3.8a) and, if only considering severe storms, 5 m (Fig. 3.8b). Additionally, the analysis of the mean annual maximum H_s helps to better identify the trace of TCs along the coastline (Fig. 3.8c), exceeding values of 8 m in the NH tropical western Pacific coasts. The main characteristics of wave storms along the global coastlines are summarized in Fig. 3.15.

The results presented here allow an integrated understanding of the main characteristics of coastal wave storms at a global scale, such as frequency of occurrence, duration and intensity, among others. Nevertheless, some intrinsic limitations need to be considered for these results to applied in future studies. In this regard, the selected threshold (i.e., 95th percentile H_s) could be too low in some coastal stretches, classifying as wave storms events not strong enough to cause coastal damage. In addition, this method might have led to integrate wave storms with different origins, thus not clearly reflecting the trace of major events (e.g., wave storms generated by TCs), as occurs, for example, in the NH tropical western Atlantic. The use of these results to develop high-resolution local coastal impact studies should, therefore, be taken with the necessary critical assessment. Such regional scale studies are advised to establish their specific storm definition criterion in terms of a detailed analysis of the local wave climate and the goal of the study. Despite the existing limitations, the use of a unique and ductile criterion that adapts the local climate and a high enough threshold to classify storms, as well as the isolation and independent analysis of severe storms, provide a reliable basis to unravel the global wave storm behavior and depict the differences between regions.

Part II

Climate variability of sea surface dynamics extremes

Chapter 4

Global variability of coastal sea level extremes from altimetry data

Abstract

This chapter presents an assessment of the climate variability of sea level extreme events along the global coastlines based on satellite altimetry data. The non-tidal residual sea level component is the main variable analyzed. An inter-calibrated non-tidal residual sea level component dataset from altimetry data covering the period 1993-2021 is built. The climate variability of sea level return values is modeled through a parametric non-stationary statistical extreme model. Three time scale variations are considered: within the year, inter-annual and long-term trends. Prior to the climate assessment, the skill of altimetry data to reproduce the climate variability of sea level extreme events is validated against a global dataset of TGs. Coasts in extratropical latitudes show a prominent winter-summer seasonality pattern. Variability patterns within the year are however more complex in tropical latitudes, usually showing multiple storm periods. A general increasing long-term trend pattern is observed. A clear relationship between the Arctic Oscillation climate pattern and non-tidal residual extremes are found in northern Europe. El niño-Southern Oscillation phenomenon clearly modulates the occurrence of non-tidal residual extremes along the whole Pacific American coast during el Niño phase, whereas la Niña phase controls the tropical West Pacific Ocean coasts. The relative importance of the astronomical tide with respect to the non-tidal residual sea level component is also assessed. Results show a dominance of the astronomical tide in more than 80% of the global coastlines.

4.1 Introduction

Extreme events of sea level may have a vast destructive power in the coast. Flooding episodes induced by these extreme events cause ocean water to penetrate inland, eroding and destroying on its way and, ultimately, generating important material (e.g., damaged facilities and material goods), economic (e.g., interruption of economic activities), natural (e.g., wetland degradation) and human losses (Losada et al., 2019). Extreme sea levels are mainly generated under stormy conditions at the landfall of low-pressure systems on the coast or as they move close to them, combining the sea level surge induced by low pressures with the surge generated by the wind stress over the sea surface (i.e., the storm surge), the setup of wind waves, any other ocean surface dynamic sea level disruption (e.g., sea level anomalies due to marine currents) and the astronomical tide. The contribution of the latter is critical along coasts with macro- and mesotidal ranges (Rueda et al., 2017), acting as the main contributor to the magnitude of extreme ESLs and modulating the occurrence of maxima values. Under stormy conditions, the sea level induced flooding might also combine with strong winds and heavy rains, as well as with extreme events of other ocean surface dynamics, such as wind waves and currents, hence significantly enhancing the storm destructive power and the derived consequences in the coastal area. For example, the ocean flooding generated by Hurricane Katrina in New Orleans in August 2005 caused monetary losses over $40 million and over 1,500 deaths (Kates et al., 2006).

The assessment of coastal impacts derived from ESLs and, hence, the forthcoming design of coastal protection measures against them, requires, first, knowledge of the maximum sea level magnitudes reaching the coastline. The behavior of extreme events can be statistically modelled by the EVT (Coles, 2001). The fitness of a sea level extreme sample to a long-term extreme distribution allows to estimate the probability of events of a certain magnitude to impact the coast, i.e., their return periods. The magnitude of extreme events with very low frequency of occurrence (e.g., 100-year return period, 500-year return period) can therefore be estimated to model major flooding episodes and assess the associated flood risk (Lewis et al., 2011; Toimil et al., 2017), proposing adequate protection measures (Alves et al., 2020; Toimil et al., 2020b).

Nevertheless, a deep understanding of coastal ESLs impacting the coast should be based not only on the magnitude of the events, but also on their variations through time. Consistently, a broad knowledge of the ESL variability allows to design protection measures adapted to the temporal evolution of the events. Extreme sea levels experience variations characterized by different intrinsic periods, such as seasons or years, all combining to modulate their occurrence. The evidence of nonstationarity in ESLs has already been demonstrated in previous studies at global (Menéndez and Woodworth, 2010), regional (Cid et al., 2016; Marcos and Woodworth, 2017) and local scales (Méndez et al., 2007; Menendez et al., 2009) based on TG records and hindcast products. The climate variability of ESLs can be assessed through approaches based or not based on the EVT. The latter requires, first, establishing a criterion to classify sea level events as storms. The variability of the storms can be assessed by analyzing, for example, the storm frequency of occurrence or the correlation with climate teleconnection patterns (Thompson et al., 2013). The approaches based on the EVT typically address the variability of ESLs by conducting an EVA through parametric statistical models. These models introduce the time dependency through time-varying functions, such as in the μ, σ and ξ parameters of a GEVD model (Méndez et al., 2007). In addition, pseudo-nonstationary extreme models, such as those fitting a GEVD model to moving windows (Wahl and Chambers, 2015), can also be used to assess the ESL variability.

The magnitude of ESLs reaching the coast is not constant throughout the year. The highest events concentrate in one or more storm periods (i.e., consecutive months), alternating with others characterized by lower magnitudes, hence, depicting a monthly variability pattern whose complexity depends on the number of events with different origin involved and their intrinsic variability. The identification of months prone to suffer the impact of higher ESLs is especially important where the destructive power of the highest events within the year may cause very severe consequences on the coast, such as in those affected by TCs, and/or where the differences between the highest and the lowest events within the year are notable. These coasts are susceptible of applying seasonal protection measures against the potential impact of events occurring during storm periods. For example, coasts affected by TCs, fierce events characterized by strong winds and sharp pressure gradients (i.e., very high sea level surges), may adopt measures to reduce their impact, such as the development of seasonal forecasts (Owens and Landsea, 2003), implementation of early alert services (Rogers and Tsirkunov, 2011) and the implementation of evacuation plans in case of major events to occur (Madireddy et al., 2015; Swamy et al., 2017). Coasts affected by highly seasonal extratropical storms (e.g., the Iberian Peninsula) can also adopt protection measures considering the variability within the year, such as defining beach regeneration plans out of the storm periods (Toimil et al., 2021b).

The interannual variability of ESLs can be linked to the intrinsic modulation of atmospheric-ocean circulation patterns. Given the phase and intensity of a certain pattern, greater or lesser probability of occurring ESLs can be derived. These relationships can be estimated through climate teleconnection indices. For example, previous studies have demonstrated that the position of the NH Atlantic extratropical storm track is intimately linked to the phase of NAO teleconnection pattern (Semedo et al. 2015). Depending on its phase, storms are expected to landfall further north or south in the Atlantic European coasts, which consequently affects the magnitude of ESLs at a certain European coastal location. Similarly, the positive phase of the Southern Annular Mode (SAM) is linked to the landfalling of storms along the south Australian coast, whereas during its negative phase storms travel poleward, reducing the storm activity in the mentioned coast (Gillett et al., 2006). Finally, the long-term variability should also be considered, namely what is usually referred as trends. Nowadays, the effect of climate change is assumed to be inavoidable (Masson-Delmotte et al., 2021) and, therefore, the related consequences on ESLs are not trivial issues. The MSLR (Cazenave et al., 2014; Nicholls and Cazenave, 2010), together with the possible changes in climate drivers inducing ESLs, such as in the frequency and intensity of storms, may cause significant increases in extreme events and, therefore, in the severity of the associated impacts (Vousdoukas et al., 2017, 2018).

The study of sea level and, particularly, extreme events has been traditionally addressed from TG data (e.g., Menéndez and Woodworth, 2010; Thompson et al., 2013). This source of information has been used for more than 100 years and is still considered as the most reliable representation of sea level (Adebisi et al., 2021). Nevertheless, TGs have a series of limitations that restrict their use, such as the affection by land movements (Denys et al., 2020), the heterogeneous time sampling, the irregular spatial coverage and the fact that the provide very local information (further details in Section 2.1). Despite these limitations, TG-recorded data provide valuable information to develop climate studies, helping to unravel, for example, MSLR being the main driver of changes in ESLs (Marcos and Woodworth, 2017; Menéndez and Woodworth, 2010; Tebaldi et al., 2012). Numerical models, taking advantage of the technological development, have emerged as an alternative to in situ information to study sea level, allowing to develop EVA at different spatial scales. For example, Muis et al. (2016) provide 100-year return period total water levels based on the global simulations of the hydrodynamic numerical model GTSM. Idem for 10-year return period using model GTSM3.0 (Muis et al., 2020). Besides, Zhang and Sheng (2015) provide 50-year return period total water levels in the northeast Pacific Ocean using the ocean circulation numerical model POM. However, numerical simulations are not yet able to characterize the peak maxima values of ESLs, mainly due to the resolution of the atmospheric forcings.

Satellite altimetry stands as a new sea level data source that provides information since the 90's with global coverage, thus overcoming one of the major limitations of TG data, the irregular spatial coverage. In addition, the current length of this database, approximately 30 years, allows to partly overcome the main intrinsic limitations of this kind of information in terms of irregular spatial and time resolution. In this regard, altimeters sample along their tracks with a characteristic rate (e.g., Altika samples at 1 Hz), so that each altimeter measurement is characterized by specific coordinates and sampling time, causing an irregular spatial and time coverage for satellite products with processing levels below L4. The combination of long records with the continuous accuracy improvement, especially in the coastal area (Cipollini et al., 2017; Valle-Rodríguez and Trasviña-Castro, 2020), favors the use of altimetry data to develop climate studies. The main climate outcome based on altimetry data over the last three decades is the estimation of historical MSL trends (Prandi et al., 2021). Further, despite these trends being normally provided across the deep ocean, the increasing accuracy nearshore offers now the opportunity of estimating coastal MSL trends in the coastal area with notable accuracy (Cazenave et al., 2019). Additionally, other sea level climatic features have been studied, such as the relation between SLAs and climate teleconnection patterns (Lowe et al., 2021) and the analysis of sea level seasonal and mesoscale variability (Korotaev et al., 2001). Nevertheless, the use of altimetry data to develop climate studies on ESLs is still very limited.

In this context, this chapter intends to assess the skill of altimetry data to reproduce the global climate variability of ESLs. Among the different components of ESLs previously mentioned, this research particularly focuses on the NTR component. On this basis, this study aims to provide not only global coastal NTR extreme estimates associated to different return periods, but also to assess the extreme variability at different time scales. Additionally, the relative importance of the NTR sea level component with respect to the astronomical tide in ESLs is analyzed.

4.2 Climate data

4.2.1 Altimetry data

In this study, a global SLA dataset provided by CMEMS is used (Taburet et al., 2021). This dataset collects inter-calibrated along-track altimetry data measured by more than twenty missions from 1992 onward and processed through the DUACS multi-mission processing system (Pujol et al., 2016). In particular, this study focuses on the time slice from January (1993) to August (2021), namely more than 28 years of data. This time span almost meets the minimum climate period of 30 years recommended by the WMO to conduct climate studies. Besides the SLA, this product also provides some of the geophysical corrections applied to the raw altimetry measurements: DAC, TC and long wave correction (LWC; more information on the corrections applied to altimetry measurements can be found in Vignudelli et al. 2011).

In order to assess the variability of coastal NTR extreme events at global scale, a total of 445 coastal units with a length of 500 km and width of 100 km, covering the entire global coastlines, are defined (Fig. 4.1). The size of the coastal units intends to select enough amount of data to conduct the EVA and, at the same time, to correctly capture the climate variability of ESLs.

4.2.2 In situ data for validation

The skill of altimetry data to reproduce the climate variability of NTR extremes is validated using data provided by a global set of 400 TGs. Hourly SWL TG records covering the time slice from January (1993) to December (2018) are downloaded from the legacy data portal at the University of Hawaii Sea Level Data Center (UHSLC) webpage (Data access URL, last time accessed on June 2022).

A tidal analysis is performed at all the available stations using the Utide tool (Codiga, 2011) based on a harmonic fit. The tidal analysis is conducted through a moving two-year time window consisting of a central one-year effective period and two half-year overlapping periods at both ends of the window. Years with less than 60% of hourly data are not considered (further details on the harmonic analysis procedure can be found in Section 2.2). Thus, the NTR sea level signal measured by TG (hereinafter NTR_{TG}) is computed by subtracting the resulting astronomical tide from the SWL time series.

4.2.3 Climate teleconnection indices data

Six teleconnection indices are considered to assess the NTR extreme interannual variability: Arctic Oscillation index (AO), NAO index, the Niño 3.4 index, Dipole Mode index (DMI), SAM index and Anctartic Oscillation index (AAO). These indices relate to the atmospheric circulation of different ocean regions, all together proving a good coverage of the global coastlines. AO and NAO relates to the atmospheric circulation at NH extratropical latitudes. Idem for SAM and AAO but for the SH. ENSO climate pattern, through Niño 3.4 index, reflects the interannual climate variability mainly at Pacific tropical latitudes and West Atlantic tropical latitudes. The Indian Ocean Dipole (IOD) climate pattern, through the DMI index, relates to the atmosphere circulation at Indian Ocean tropical latitudes. Finally, AO, Niño 3.4, SAM and DMI indices are selected to conduct the analysis.

Monthly values for AO, Niño 3.4 and DMI indices are downloaded from the NOAA Physical Sciences Laboratory webpage (Data access URL, last time accessed on April 2022). SAM index is downloaded from the British Antarctic Survey webpage (Data access URL, last time accessed on April 2022).

4.2.4 Astronomical tide data

Astronomical tide is reconstructed from the tidal components provided by TPXO9 database (Egbert and Erofeeva 2002; Data access URL, last time accessed on April 2022). This database provides tidal components at 1/30° global spatial resolution computed from satellite altimetry data. Astronomical tide is reconstructed at the ocean point closest to the midpoint of the coastal stretch covered by each coastal unit (Fig. 4.1).

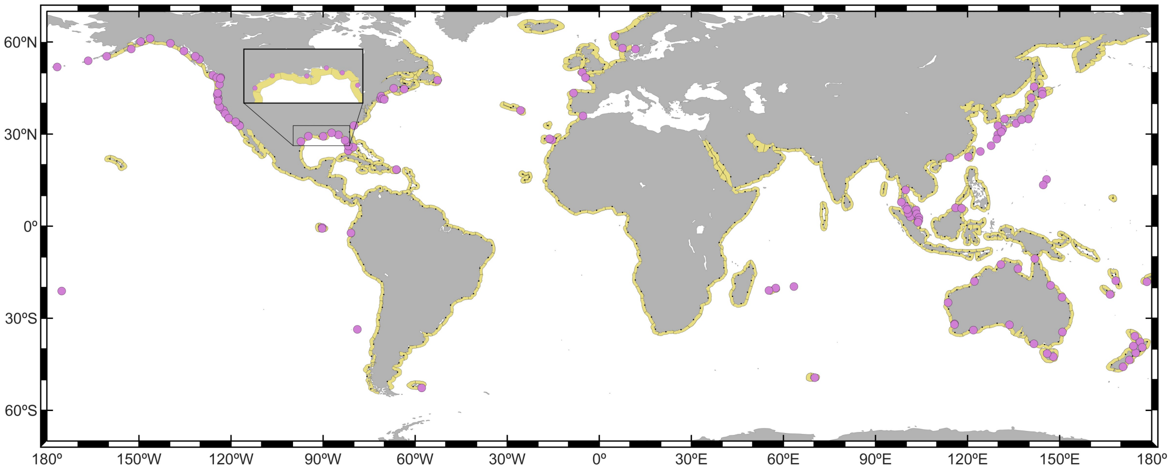

Fig. 4.1 Coastal units defined to conduct the analysis (in yellow). Pink circles represent the location of the TG stations selected for validation. Black dots represent the location where the tidal components from model TPXO9 are extracted.

4.3 Methods

4.3.1 Statistical extreme model

This study makes use of the block maxima approach to model the behavior of NTR maxima through a GEVD statistical model (Eq. 5.2). Contrarily to the standard approach based on the use of AM as block maxima, here MM values are instead used as input (Méndez et al., 2007; Menéndez and Woodworth, 2010), allowing to increase the size of the maxima sample and to capture the variability within the year.

Parametric time-dependent terms are included in the model to introduce the non-stationary behavior of the NTR climate variable. In particular, climate variations are included in the GEVD location parameter $\mu(t)$. The statistical extreme model considers climate variations at three time scales: variations within the year, inter-annual variations and long-term trends. The calculation of NTR values associated to a R-year return period through a non-stationary GEVD ($\overline{z_R}$) can be done according to Eq. 2.9.

The assessment of the variability within the year in EVA of climate variables has been already addressed in previous studies (Méndez et al., 2007). Here, the seasonal variability is modeled by combining two sine functions with periods of one year and half-year, as:

$$\mu_s(t) = \sum_{i=1}^{2} \beta_{2i-1} cos(2^i \pi t) + \beta_{2i} sin(2^i \pi t) \tag{4.1}$$

where β_i (m) is the amplitude of the harmonics and t is given in years.

The long term variability (trend) is included in the model through an exponential function. Therefore, the model is able to simulate the increase or decrease in the magnitude of NTR extreme events, as:

$$\mu_{trend}(t) = \beta_0 \, exp(\beta_{LT} \, t) \tag{4.2}$$

where β_0 (m) determines the initial value of $\mu(t)$ and β_{LT} is the acceleration rate of the trend (m/year). Note that the exponential approach approximates to linear when β_{LT} is very low.

The interannual variability is analyzed by assessing the influence of climate teleconnection patterns on extreme NTR variability. Climate patterns are introduced in the statistical model through monthly values of representative teleconnection indices (see Section 4.2.3) as a covariate, as:

$$\mu_{CI}(t) = \beta_{CI} \, CI(t) \tag{4.3}$$

where β_{CI} is the estimated covariate coefficient (m/IU) and CI(t) is the monthly value of the climate teleconnection index. Hereinafter IU refers to climate index units.

Considering all climate variations, the location parameter can be expressed as:

$$\mu(t) = \mu_{trend}(t) + \mu_s(t) + \mu_{CI}(t) = \beta_0 \, exp(\beta_{LT} \, t) + \sum_{i=1}^{2} \beta_{2i-1} cos(2^i \pi t) + \beta_{2i} sin(2^i \pi t) + \beta_{CI} \, CI(t) \tag{4.4}$$

The definition of the final $\mu(t)$ parametric model for each location follows an orderly and efficient optimization process. Different combinations of the parametric terms considered lead to different $\mu(t)$. The optimal $\mu(t)$ is selected based on the maximum likelihood ratio test and the principle of parsimony, namely minimizing the number of degrees of freedom to avoid over-parameterization of the model (Coles, 2001).

At a first stage, $\mu(t)$ only includes the variability within the year. In order to find the simplest model, a forward algorithm starting from a stationary model (model M_0) is used. Different combinations of sine functions are tested until the optimal is reached (model M_1). Next, the long-term trend is introduced. In case the trend being significant (at 95% confidence level), it is included in model M_2, otherwise, M_2 will be equal to M_1. Finally, based on M_2, the same process is made to define model M_3 but introducing the interannual variability parametric term through each analyzed climate index independently. Thus, M_3 considers the three time scales analyzed if they are relevant to model the climate variability of ESLs.

4.3.2 Non-tidal residual coastal extreme sample

As previously mentioned, this study focuses on the assessment of the extreme climate variability of the NTR component of sea level. Consistently, the analysis requires building a NTR dataset computed from altimetry data. This is done based on the methodology proposed in Section 2.2, so that the altimetry-based NTR dataset, henceforth NTR_{SAT}, is computed by undoing the DAC from the SLA product. In other words, NTR_{SAT} is computed by adding the DAC to the SLA (Eq. 2.7). The final altimetry NTR dataset is an along-track product with irregular time and spatial sampling covering the global ocean.

NTR_{SAT} data are selected for each coastal unit defined along the global coastlines. Next, MM are selected to feed the following EVA. In order to avoid spurious monthly data, months with less than 10 measurements after hourly re-sampling are not considered.

4.3.3 Selection of validation extreme samples

The skill of altimetry data to reproduce the climate variability of ESLs is validated against TG data. For that matter, TG records are filtered, rejecting those precluding fair validations.

From the initial set of 400 TG records, 170 are preliminary selected. This initial selection considers, first, the location of the station, rejecting those in very sheltered and shallow coasts, such as TG stations located inside of atolls and ports, or those located upstream of rivers, as they are likely to be highly affected by local processes not correctly captured by altimetry measurements. Additionally, the amount of data available is analyzed, rejecting TG records with less than 75% of hourly data during the validation period (i.e., 1993-2018).

For each preliminary selected station, NTR_{TG} and NTR_{SAT} comparable extreme samples are needed for validation. These samples are selected following the methodology proposed in Section 2.3.1 based on the correlation between both datasets in the vicinity of TG stations. Accordingly, the correlation between NTR_{TG} and NTR_{SAT} is computed at each node of a 0.25-degree regular grid covering a 7.5-degree circular area centered at the station location. Correlations (r) of contemporaneous pairs NTR_{TG}-NTR_{SAT} within a 0.25-degree circle centered at each ocean grid node are computed (Fig. 2.5). Grid nodes showing r lower than 0.5 are rejected. Next, a correlation cut-off is continuously increased from 0.5 until the mean number of altimetry measurements is approximately 1 measurement per day. Note that in order to avoid selection of very close-in-time measurements, NTR_{SAT} is re-sampled to hourly data at each step of the evolution algorithm. This new filtering criterion leaves a total of 123 TG stations for validation (Fig. 4.1). Finally, MM from NTR_{TG} and NTR_{SAT} for each station are selected to be used as input of the EVA.

4.3.4 Extreme variability assessment

The variability of NTR extremes with very low frequency of occurrence is analyzed. Several metrics to represent the climate variability at different time scales are proposed. All metrics, unless otherwise specified, consider year 2015 as reference to estimate return values.

The extreme variability within the year is represented through two metrics. First, the coefficient of variation of the 20-year return period NTR within the year, computed as:

$$CV^{20} = \frac{std(NTR^{20})}{\overline{NTR^{20}}} \tag{4.5}$$

where NTR^{20} is the 20-year return period NTR and std refers to the standard deviation.

Higher (lower) values of this metric indicate a stronger (weaker) variability within the year.

Additionally, the months with the highest probability of showing higher extreme values are identified. This is done by computing first the number of local maxima of the 20-year return period NTR within the year and, next, identifying the months when these maxima occur.

The interannual variability of NTR extremes is analyzed by assessing the values of the parameter β_{CI} associated to each of the four climate indices considered (Eq. 4.3).

Long-term trends in NTR extremes are assessed through the relative change in the 20-year return period NTR between 1995 and 2020, as:

$$\Delta NTR^{20} = \frac{NTR^{20}_{1995}}{NTR^{20}_{2020}} x100 \tag{4.6}$$

where NTR^{20}_{y} is the 20-year return period NTR in year y.

Finally, the relative dominance of the astronomical tide with respect to the NTR sea level component in ESLs is analyzed. The tidal dominance (TD) is computed as the proportion between the mean annual maximum tide (T_{max}) and NTR return values, as:

$$TD^R = \begin{cases} \frac{T_{max}}{NTR^R}, & if\ T_{max} > NTR^R \\ -\frac{NTR^R}{T_{max}}, & if\ T_{max} < NTR^R \end{cases} \tag{4.7}$$

where NTR^R is the R-year return period NTR.

Therefore, positive TD values indicate a higher contribution of the astronomical tide with respect to NTR extreme events with a return period of R years, whereas negative TD values represent the opposite.

4.4 Results

4.4.1 Validation against in situ data

Fig. 4.2 depicts the validation of altimetry data and the EVA approach to capture the magnitude of NTR extreme events and their variability at different time scales (i.e., within the year, inter-annual and long term trends; Eq. 4.4).

Fig. 4.2a represents the correlation (r) between MM from NTR_{SAT} and NTR_{TG} at each TG station. Results show r values higher than 0.7 for most of the stations (more than 80%). Moreover, more than 50% of the stations show r values higher than 0.8, evidencing a good agreement between both datasets, which is essential for the following EVA. The lowest r values, of between 0.5 and 0.6, are sparsely distributed along the global coastlines and represent less than 5% of the TGs, not reflecting any spatial pattern and likely attributable to local processes not fully captured by altimetry. In general terms, the eastern coast of North America is the region showing the lowest correlation values. Most of these TGs show r values ranging between 0.6 and 0.7. On the other hand, the highest values are observed in stations located in equatorial latitudes in the East Indian Ocean and West Pacific Ocean, showing r values higher than 0.9.

After conducting the EVA with altimetry and in situ extreme samples in all the validation stations, the skill of altimetry data to capture the magnitude of NTR events with a return period of 10 years is depicted in Fig. 4.2b. Results show a general underestimation of altimetry data (bias of -0.10 m), particularly for NTR^{10} magnitudes higher than 60 cm, good correlation (r of 0.74) and moderate errors (RMSE of 0.19 meters). It is noteworthy to point out that the errors enhance in tropical latitudes, mainly due to the poor representation of TC-induced

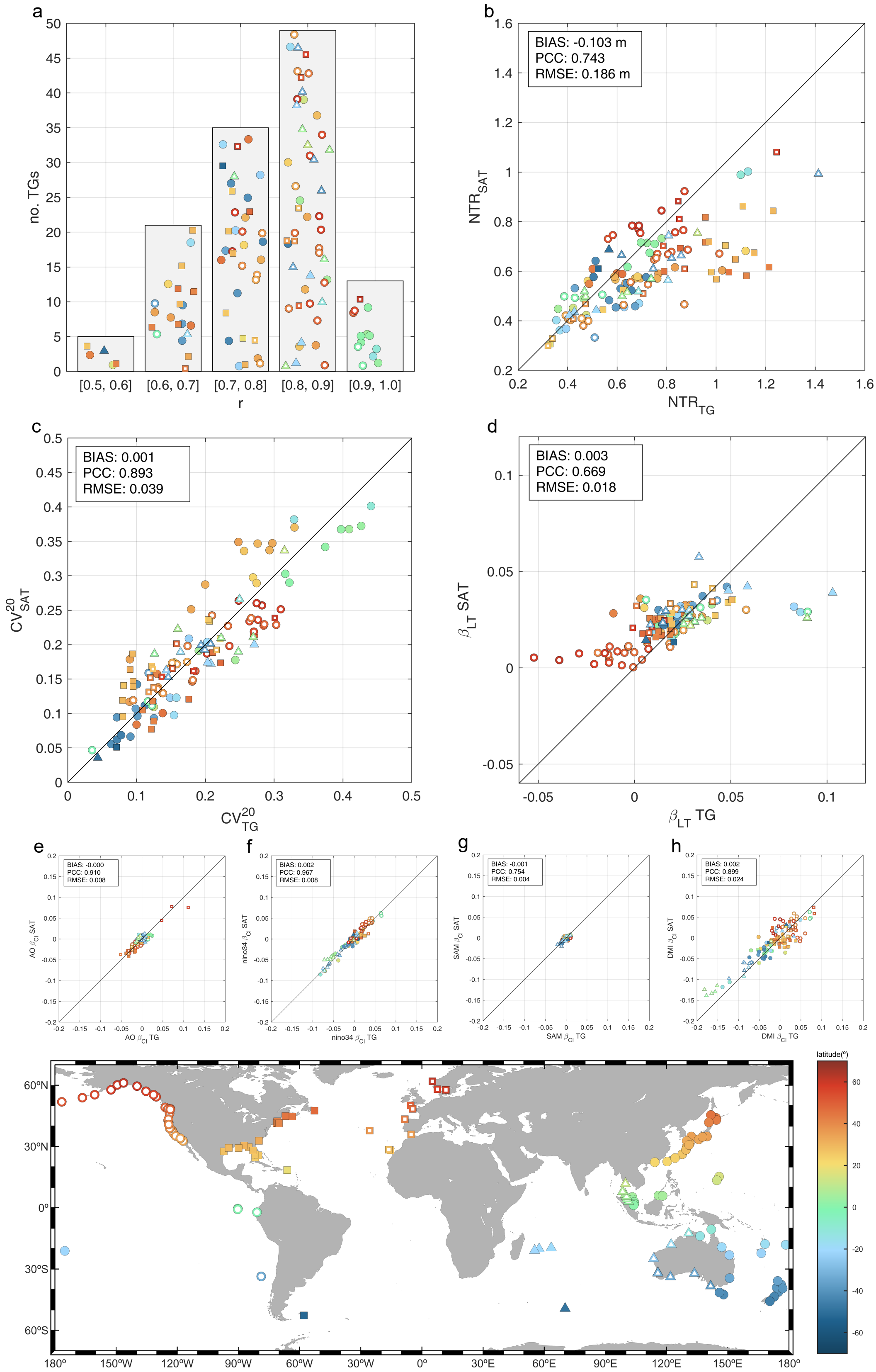

Fig. 4.2 Validation of NTR_{SAT} vs. NTR_{TG} at the 123 selected TG stations. (a) Pearson correlation between MM. (b) 10-year return period NTR (m). (c) Coefficient of variation of the 20-year return period NTR within the year. (d) Extreme model parameter β_{LT} associated to long-term trends (m/year). Extreme model parameter β_{CI} associated to the climate teleconnection index (m/IU) for (e) AO index, (f) Niño 3.4 index, (g) SAM index and (h) DMI index.

ESLs in the altimetry extreme sample. Altimetry data cannot fully capture the magnitude of the NTR extremes caused by TCs within the coastal units due to the combination of the irregular time and spatial data sampling, and the small radius and high moving velocity of these storms. On the other hand, results show good agreements in mid to high latitudes, where extreme events are mainly originated by extra-tropical storms. On top of this, despite the thorough selection of TGs, most of them are still affected by local processes, such as interactions between long waves and the sea floor at low depths, or long wave distortions due to interactions with complex coastal geometries. These issues, combined with the fact that most altimetry measurements are made in the offshore zone, induce discrepancies between extreme estimates from both data sources.

The validation of the climate variability characterization is depicted in Fig. 4.2c-h. Fig. 4.2c shows the validation of the NTR extreme variability within the year through the metric CV^{20} (Eq. 4.5). Results show good agreement between altimetry and TG extreme estimates with an almost null bias, high correlation (r of 0.89) and low errors (RMSE of 0.04).

Long term variations of altimetry extremes are also validated. Results are depicted in Fig. 4.2d by comparing the parameter β_{LT} (Eq. 4.2) estimated from altimetry and TG data. The greatest differences are found, as expected, at TG stations located in the coast of the Gulf of Alaska (dark orange and red empty circles from Fig. 4.2d). The uplift of the continental shelf in this region induces decreasing sea level trends in TG records, which has already been addressed and demonstrated in several studies (e.g., Larsen et al. 2004; Savage and Plafker 1991). Thus, these discrepancies cannot be attributed to a bad skill of altimetry data, but to geodesical processes. Additionally, some sparsely distributed TG stations show important differences in β_{LT}. Nevertheless, since other TG stations located in the same region do not show these inconsistencies and, on top of that, altimetry trends are homogeneous for the rest of stations in these regions, the differences cannot be attributed to the lack of accuracy of altimetry data.

The validation of the interannual variability characterization is depicted in Fig. 4.2e-h by assessing the agreement in the parameter β_{CI} (Eq. 4.3) for the four climate teleconnection patterns considered. A good general agreement between altimetry and TG data can be observed. The weakest consistency can be seen for the SAM index (r of 0.75) due to the low number of TG stations in the SH and, on top of that, the noise induced by the combination of low β_{CI} values in SH stations with those found in NH stations. The rest of climate teleconnection indices show excellent correlations ($r \geq 0.9$), almost null biases ($|\text{bias}| < 0.002$ m/IU) and very low errors (RMSE < 0.025 m/IU).

Validation results presented here provide confidence to the following climate variability analysis developed along the global coastlines. In this regard, despite the general magnitude underestimation found, especially in coastal areas affected by TCs, the magnitude of extremes is reasonably well captured and, above all, the climate variability characterization, the main goal of this study, shows a very good agreement.

4.4.2 Non-tidal residual return values

Fig. 4.3 depicts the 5-, 10- and 20-year return periods NTR (NTR^5, NTR^{10} and NTR^{20}, respectively) along the global coastlines (subpanels a, b c, respectively). Results for all the analyzed return periods show similar patterns, so for the sake of simplicity only results for NTR^{20} are described throughout this section.

Extreme NTR events impacting the eastern coast of America are higher poleward of 40° in both hemispheres, showing NTR^{20} values of between 0.6 m and 0.8 m poleward of 50° and values of between 0.8 m and 1.0 m equatorward of it. Along subtropical and intertropical coasts, NTR^{20} values mostly range between 0.4 m and 0.6 m, with the only exception of the Gulf of California, where values of between 0.6 m and 0.8 m can be seen. The eastern coast of America is reached, in general, by higher NTR extremes than its western homologous, showing NTR^{20} values always higher than 0.6 m north of 30°N, and even exceeding 0.8 m in some coasts north of 45°N. The coast of the Gulf of Mexico shows significant NTR^{20} values despite the likely smoothing of TC-induced NTR extremes. Values above 0.6 m can be seen along all basin's coasts and, particularly, more than 1 m in the east coast of Florida (USA). Coasts south of 30°S generally exceed 0.6 m, especially between 30°S and 45°S, where very intense NTR extreme events are observed, showing NTR^{20} values higher than 1.4 m.

The western coasts of Europe show a strong NTR^{20} gradient. The Atlantic coasts of Spain and Portugal, and the southeast coast of France show NTR^{20} values of between 0.4 m and 0.8 m, whereas the south coasts in the North Sea exceed 1.4 m. Moreover, the Dutch, German and Danish coasts of this basin reach values of more than 1.8 m. African coasts show NTR^{20} values mostly lower than 0.6 m, only exceeding this value in the coast of South Africa, where magnitudes range between 0.6 m and 0.8 m.

Two main coastal areas in the Indian Ocean stand out due to the high magnitudes of NTR extremes. First, the north coast of the Gulf of Bengal, where NTR^{20} values range between 0.8 m and 1.2 m. Second, the Persian Gulf, where values of between 0.8 m and 1.0 can be observed in almost the whole basin. The south coast of Japan and most of the coast of China show NTR^{20} values higher than 0.8 m, exceeding 1.2 m in some stretches in the Yellow Sea. The coast of Australia shows significant NTR^{20} values in excess of 0.6 m in almost the whole coast. Particularly higher are the events impacting the Gulf of Carpentaria and some coastal stretches along the south and east Australian coasts, reaching values of between 1.0 m and 1.2 m. The coasts of Tasmania and South Island in New Zealand also show significant magnitudes of between 0.6 m and 0.8 m.

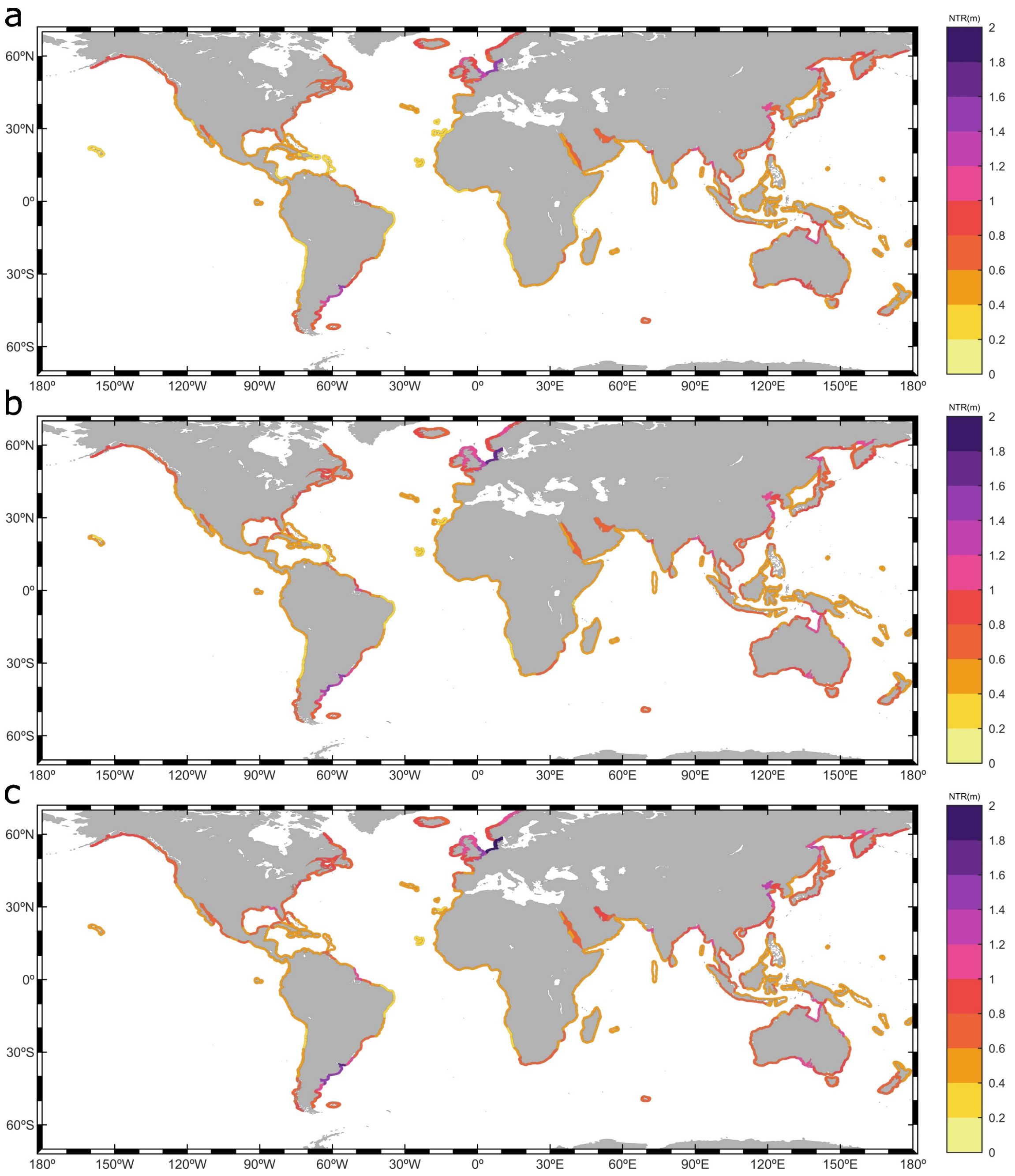

Fig. 4.3 (a) 5-year (a), 10-year (b) and 20-year (c) return period NTR (m).

4.4.3 Variability within the year

The magnitude of NTR extremes reaching the coast varies throughout the year depending on the intrinsic variability of their generating events, as well as their combination. The variability of extreme events within the year is depicted in Fig. 4.4 and Fig. 4.5. Fig. 4.4 shows the month with the highest probability of suffering higher NTR extreme events within the year. It also highlights coastal units in which NTR^{20} shows more than one maximum within the year, likely indicating this coast being reached by extreme events with different origins. Additionally, the month in which the second maximum is located is displayed for the latter cases. For completeness, Fig. 4.4 also depicts the monthly evolution of NTR^{20} at fourteen key points (from P1 to P14) distributed along the global coastlines: five points are in the Pacific Ocean, six points are in the Atlantic Ocean and three points are in the Indian Ocean. Results at these points illustrate the differences between coasts in terms of shape and complexity of the variability pattern within the year. Ocean key points where the extremes have a unique origin show simpler monthly evolution patterns, characterized by a clear annual cycle (e.g., points P1-P4, P11-P14). On the other hand, coasts affected by NTR extreme events with more than one origin, mostly observed in subtropical and intertropical coasts, show more complex patterns (e.g., points P5-P8).

The main driver of NTR extremes impacting coasts in mid to high latitudes are extratropical cyclones (ETCs) reaching the coast while moving west to east along the extratropical storm tracks (Camus et al., 2014b). These events present a strong seasonal variability pattern within the year, showing maximum NTR^{20} magnitudes during the corresponding winter season of each hemisphere and minimum NTR^{20} magnitudes the during the summer. Most coastal units in these latitudes show a single maximum within the year (Poins P1-P4, P11-P14), corroborating the strong winter-summer pattern. Consistently, months from November to February show the highest probability of suffering higher extreme events in coasts north of 40°N (points P1-P4). The pattern in extratropical coasts in the SH is not as clear as in the NH. However, a strong winter dominance (from May to July) in the extreme NTR occurrence can still be seen in the south coast of Chile, the south and west coasts of Australia, the southernmost part of the coast of South Africa and the coast of New Zealand (points P11, P13-P14).

The eastern coastlines of the continents in subtropical and intertropical latitudes are prone to suffer the impact of TCs (Wahl and Chambers, 2015; Zhang et al., 2000). Therefore, months within the TC seasons (i.e., from June to November in the NH and from November to April in the SH) are roughly those showing the highest NTR^{20} values. The coasts in the Gulf of Mexico and the Caribbean Sea suffer the impact of the highest NTR events mainly from September to November (point P6), whereas along open NH tropical West Pacific coasts the highest NTR events are more probable in earlier months, from July to September (point P10). Besides, all mainland coasts in the latter regions show a second maximum from April to May, something that cannot be seen in islands at the same latitudes, such as in the Caribbean islands, Taiwan and Philippines. In the SH, the coasts of Mozambique, Madagascar and Reunion and Mauritius islands show maxima values in January and February (point P9). Additionally, the northeast and southeast coasts of Australia suffer the highest events from January to April.

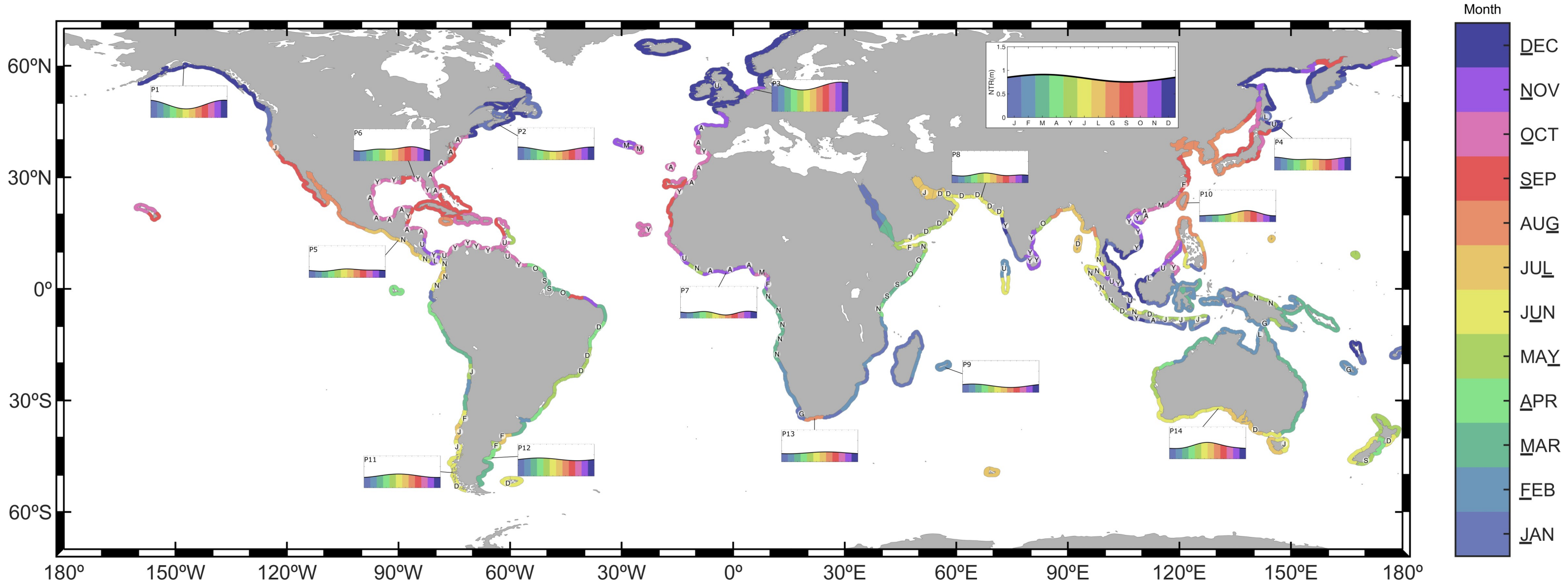

Fig. 4.4 Global coastal month with the highest probability of showing higher NTR extremes. White circles identify coastal units showing two maxima in NTR^{20} within the year. The letter inside the circles indicate the month when the second maximum occurs (letter code is depicted in the colorbar). The time-varying NTR^{20} within the year is displayed for 14 ocean key points.

It is also noteworthy the notable differences found in the month with the highest probability of showing the highest NTR extremes within the same basin mainly depending on the orientation of the coastline. The coasts in the Arabian Sea are a clear example of this issue. While the west coast of India suffers the highest events in December-January, the highest events along the coasts of Pakistan, East Iran and Oman occur in May-June. Nevertheless, the latter coasts seem to still be affected by the same events as the coast of West India, as all of them show a second NTR^{20} maximum in December (point P8). Another clear example is the Gulf of Guinea. While the coasts of Gabon and Angola, orientated to the West, show the highest NTR events in March and a second maximum in November, the coasts of Cameroon, Nigeria, Togo, Ghana and Ivory Coast, orientated to the south, show the highest extremes in October-November and a second maximum in March and April (point P7). This likely reflects all these coasts being affected by the same extreme events, although alternating the dominance in terms of the coastline orientation. Finally, semi enclosed basins, such as the Red Sea, the Persian Gulf and the Japan Sea show patterns in which the highest event occurs in January-March, July and August-October, respectively.

Fig. 4.5 quantifies the strength of the variability within the year through the metric CV^{20} (see Section 4.3.4). Higher CV^{20} values are observed in coasts poleward of 35° in the NH than in the SH. For example, the coast of the Gulf of Alaska, the northernmost part of the northeastern American coast and the northwestern European coast show CV^{20} values of between 0.10 and 0.25, whereas the southernmost part of the Chilean and Argentinean coasts, and the coast of South Africa show CV^{20} values lower than 0.15. This issue reflects a more prominent seasonality in NH extratropical coasts with respect to SH ones. The stronger seasonality in NH extratropical latitudes can also be seen when comparing the evolution of NTR^{20} at ocean points located in the NH (points P1-P3 in Fig. 4.4) and in the SH (points P11-P13 in Fig. 4.4). Additionally, note that the coasts of Uruguay and Argentina, and the south coast of the North Sea, both coastal areas previously highlighted for being impacted by very high NTR extremes (Fig. 4.3), show low NTR^{20} values of between 0.05 and 0.15, thus reflecting that extreme events are intense during the whole year (points P12 and P3, respectively, in Fig. 4.4a).

There is great heterogeneity in the CV^{20} pattern in intertropical and subtropical coasts. This heterogeneity exists even between coasts in the same basin as, for example, in the coasts in the Arabian Sea, which show CV^{20} values ranging between 0.05 and 0.25. The main coasts affected by TC-induced extremes show moderate CV^{20} values roughly ranging between 0.10 and 0.25 at coasts in the Gulf of Mexico and Caribbean Islands (point P6 in Fig. 4.4), and between 0.15 and 0.35 at coasts in the southwestern tropical Pacific (point P10 in Fig. 4.4). The latter evidences the high NTR magnitudes induced by TCs with respect those present the rest of the year.

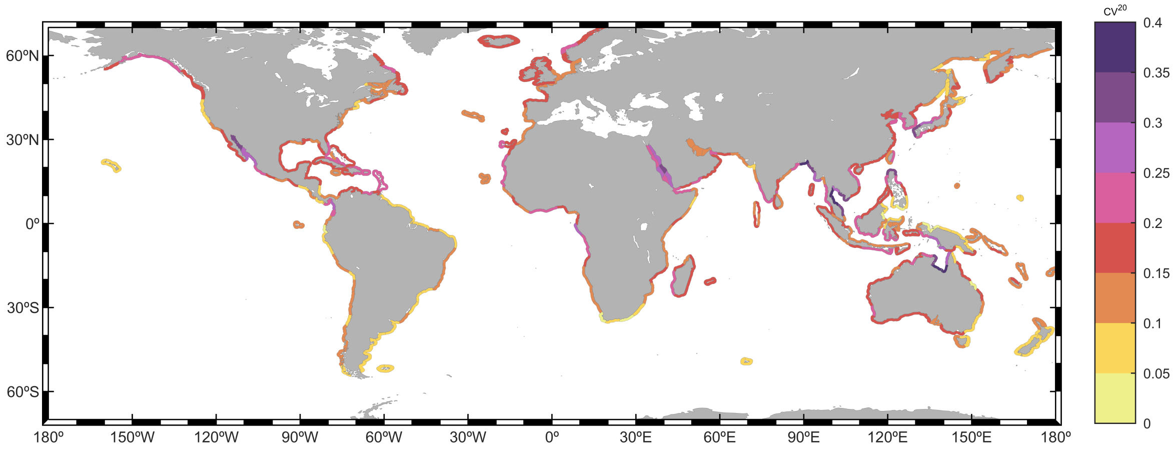

Fig. 4.5 Global coastal CV^{20}.

Finally, it is worth to mention the high CV^{20} values at coasts in semienclosed basins, such as the Gulf of California, the Gulf of Carpentaria and the Red Sea. All these basins show CV^{20} values higher than 0.25, denoting significant differences between storm and calm periods. Among the mentioned coasts, the coast in the Gulf of Carpentaria stands out due to being affected by NTR extremes of great magnitude (Fig. 4.3).

4.4.4 Long-term trends

Fig. 4.6 depicts the long term variations (i.e., long term trends) in NTR^{20} along the global coastlines. Additionally, it shows whether or not the inclusion of the trend to model the behavior of NTR extremes is significant at 95% confidence level. Results show a general robust positive trend in NTR^{20}. All coastal units analyzed show an increasing trend and more than 95% of them show significant trends. Low-robust trends are mainly found in the coast of the Gulf of Alaska. Note that the general positive trend presented in Fig. 4.6 is consistent with the findings from previous studies about MSLR being the main driver of changes in ESLs (Marcos and Woodworth, 2017; Menéndez and Woodworth, 2010).

The strongest trends in NTR^{20} are found in five main coastal regions: the southwestern African coast; the coasts of North Madagascar, North Mozambique and Tanzania; the coasts of Papua New Guinea, Indonesia and Solomon Islands; the coast of West India and the coast of Brazil. All these coasts show increases in NTR^{20} greater than 35%, reaching in some coastal units increases of more than 50%. On the other hand, the lowest increases in NTR^{20}, between 5% and 25%, are expected in the Atlantic European coasts, the southernmost part of the Chilean coast, the Argentinean and Uruguayan coasts, the northwestern coasts of America and the south, west and north coasts of Australia.

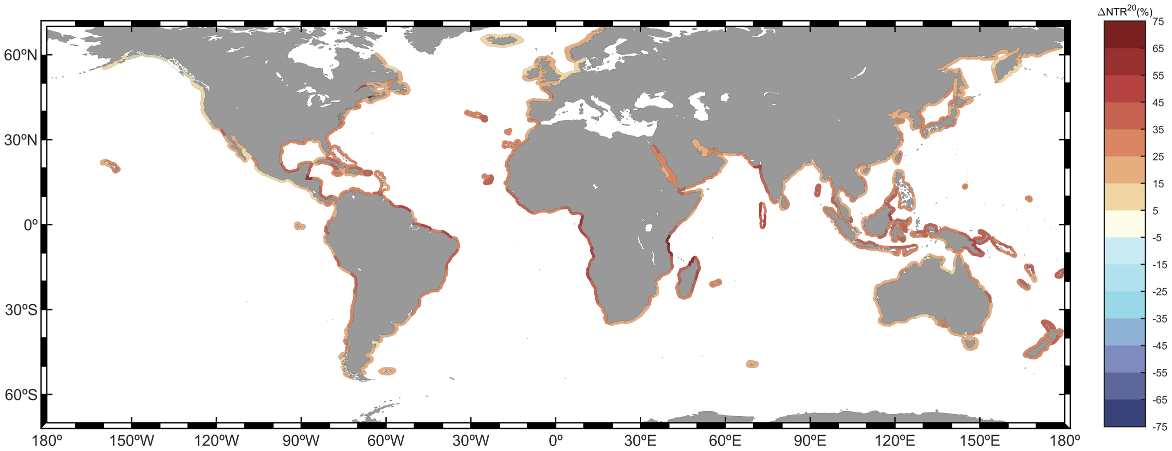

Fig. 4.6 Global coastal relative change in NTR^{20} (%) between 1995 and 2020. Hatching indicates not robust results.

4.4.5 Interannual Variability

Interannual variations are present in NTR extreme events (Menéndez and Woodworth, 2010). Including climate teleconnection indices in the extreme statistical model allows to analyze the individual influence of different climate teleconnection patterns on the intensity of NTR extreme events along the global coastlines. Fig. 4.7 depicts the global values of β_{CI} for the four indices considered (see Section 4.2.3). In addition, the robustness of the relationship between climate patterns and NTR extremes is analyzed by computing the statistical significance of introducing the teleconnection index covariate in the statistical model (see Section 4.3.1). Thus, the influence of the teleconnection pattern is considered as robust when the statistical significance is greater than 95%.

Fig. 4.7a shows a strong correlation between the positive phase of the AO index and NTR extreme events along the northwestern coasts of Europe, especially in the North Sea, where β_{CI} shows values higher than 5 cm/IU. The latter translates in a higher probability of suffering the impact of higher NTR extreme events along these coasts during this phase. The AO index, highly correlated with the NAO index (Ogi et al., 2003), is closely related with the trace of the NH extratropical storm track in the Atlantic Ocean. In this regard, during the AO negative phase, storms reach poleward coastlines, inducing the positive correlation depicted in Fig. 4.7a, whereas during the negative phase storms landfall more to the south. Consistently, the southwestern coasts of Europe, namely those in the Gulf of Biscay and the Atlantic coasts of the Iberian Peninsula, show a negative correlation with the AO index. Same strong correlation can be observed along the northeastern coast of North America, from New Scotland (Canada) to North Carolina (USA), which is consistent with previous studies (Wahl and Chambers, 2015). It is also noteworthy the weak signal observed in the NH extratropical Pacific coasts with respect to the Atlantic, only showing significant positive

β_{CI} values in the westernmost part of the coast of the Gulf of Alaska and the east coast of the Kamchatka Peninsula.

The correlation between the SAM index and NTR extremes is depicted in Fig. 4.7b. Results show weak correlations along the global coastlines and, more importantly, along the SH coastlines too. Only two coastal regions are found to be strongly correlated with this index, although always showing low β_{CI} values (less than 3 cm/IU). First, the southeast coast of Australia, where a strong negative pattern can be observed. During the negative phase of SAM, the SH extra tropical storm track shifts equatorward, hence causing storms to landfall on the Australian coastlines (Gillett et al., 2006). On the other hand, during the positive phase, extra tropical storms move poleward, precluding the impact in South Australia. Additionally, the south coasts of Sumatra and Java also show a strong positive correlation with the SAM index.

The correlation between ENSO teleconnection pattern and NTR extremes is analyzed through the Niño3.4 index and depicted in Fig. 4.7c. The Niño3.4 represents the ENSO phenomenon through the average equatorial sea surface temperature (SST) anomalies in Pacific Ocean between 5°N-5°N and 15°W-15°E. Positive values of this index relate with the Niño phase and negative ones with the Niña phase. A robust influence of ENSO phenomenon can be observed in intertropical and subtropical Pacific coasts with a clear dipole pattern: positive Niño3.4 correlations along eastern Pacific Ocean coasts and negative correlations along western Pacific Ocean coasts. The most robust positive correlations (Niño phase) can be seen along the Pacific coasts of Mexico, Guatemala, El Salvador, Honduras, Nicaragua, Costa Rica and Panama, reaching β_{CI} values of between 6 cm/IU and 8 cm/IU. This positive correlation extends to the entire western coast of America, namely from Alaska (USA) to Chile, although showing lower values in poleward latitudes.

Extreme events of NTR reaching the coasts of Papua New Guinea, Philippines, Indonesia, North Sumatra, North Java, East Vietnam and Northeast Australia show a robust correlation with La Niña phase, which translates in absolute β_{CI} values higher than 5 cm/IU. Further, this negative pattern extends to the Indian ocean along the south coasts of Sumatra and Java, the north, west and south coasts of Australia and the coasts in the Bay of Bengal. Additionally, a robust positive correlation with low β_{CI} values (between 0.5 cm/IU and 1.5 cm/IU) can be seen in the coasts of Tanzania, Kenya and South Somalia.

The most robust correlation between ENSO phenomenon and NTR extremes in the Atlantic Ocean are observed in the coasts of the Caribbean islands and the USA coastline from New York to Georgia (between 1 cm/IU and 3 cm/IU). In addition, the Atlantic coasts of Mexico, Belize, Guatemala, Honduras, Nicaragua, Costa Rica and Panama show a robust positive pattern with low β_{CI} values lower than 1 cm/IU.

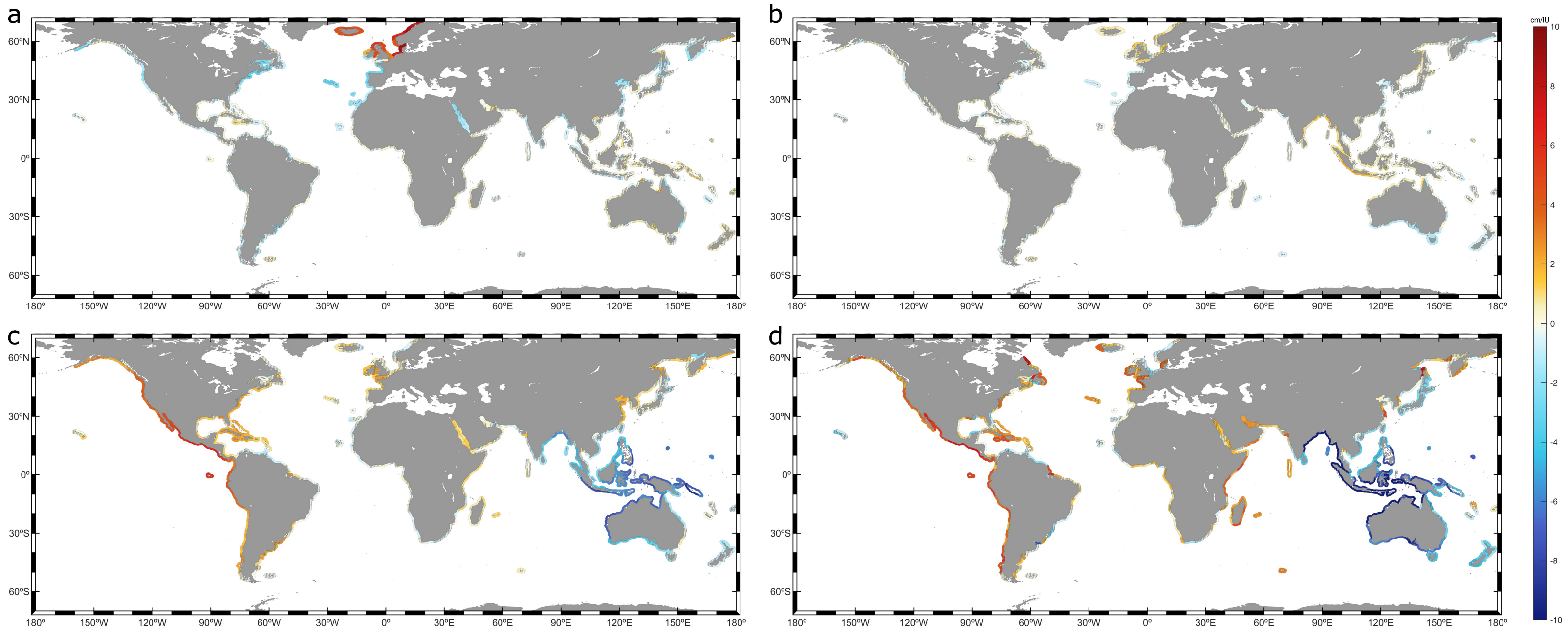

Fig. 4.7 Global coastal β_{CI} for the (a) Arctic Oscillation Index, (b) Southern Annular Mode Index, (c) Niño 3.4 Index and (d) Dipole Mode Index. Hatching indicates not robust results.

The influence of the IOD climate pattern in NTR extremes is depicted in Fig. 4.7d through the DMI index. A robust dipole pattern along Indian coasts can be observed. The coasts of Somalia, Kenya, Tanzania, the south and north coasts of Madagascar, the coasts of Mauritius and Reunion islands, the south coast of Oman, the coasts in the Persian Gulf and the coasts in Maldives show robust positive values of β_{CI} of between 2 cm/IU and 6 cm/IU. On the other hand, the south, east and north Indian Australian coasts, the south coasts of Sumatra and Java, and the coasts in the Bay of Bengal show a robust negative pattern with β_{CI} values of between -4 cm/IU and -10 cm/IU.

Furthermore, the correlation between DMI index and NTR extremes extends to the Pacific and Atlantic oceans. Concerning the former, NTR extremes in the Pacific coasts of Australia, the coasts of New Zealand, Philippines, Papua New Guinea and Indonesia show a robust correlation with the negative phase of DMI index. On the other hand, the western American coast show robust positive β_{CI} values in intertropical and subtropical latitudes. Finally, the coasts of Jamaica, Puerto Rico, Haiti and Dominican Republic also show robust positive values. The great similarities found with the results for the Niño 3.4 index suggest a high correlation between ENSO and IOD climate patterns variability, which is also consistent with findings from previous studies (Stuecker et al., 2017).

4.4.6 Relative contribution of tide

Fig. 4.8 depicts the contribution of the astronomical tide to ESLs with respect to NTR extremes along the global coastlines. Fig. 4.8a and Fig. 4.8b quantify the relative dominance of NTR vs. the astronomical tide in ESLs through the metric TD (see Section 4.3.4) for 5-year return period NTR (TD^5) and 20-year return period NTR (TD^{20}), respectively. In general, ESLs are dominated by the astronomical tide, with 81% of the coastal units showing $TD^5 > 1$ and 77% showing $TD^{20} > 1$. Since results for both return periods show a similar spatial pattern, only results for TD^5 are described.

The dominance of the astronomical tide is not homogeneous along the global coastlines, existing notable differences between regions depending on the amplitude of the tidal range and the magnitude of NTR extremes impacting the coast. To illustrate the former, Fig. 4.8b shows T_{max} along the global coastlines. Coastal units showing T_{max} values higher than 2 m, normally referred as macrotidal coasts (Gerkema, 2019; Short, 1991), are mostly dominated by the astronomical tide -in other words, the astronomical tide is the main driver controlling the magnitude and time occurrence of ESLs. The north coast of Spain, the southwest coast of France, the coast of the Gulf of Alaska, the northwest coast of Australia, the southernmost part of the Argentinean coast and the coasts in the Mozambican Channel are examples of macrotidal coasts in which the astronomical tide dominates over the NTR, all of them showing TD^5 values mostly above 2. Additionally, other coasts such as the coasts of Brazil and Portugal, and the Atlantic coast of Morocco, which show T_{max} values of between 1 m and 2 m, namely mesotidal ranges, also present high TD^5 values of above 3.

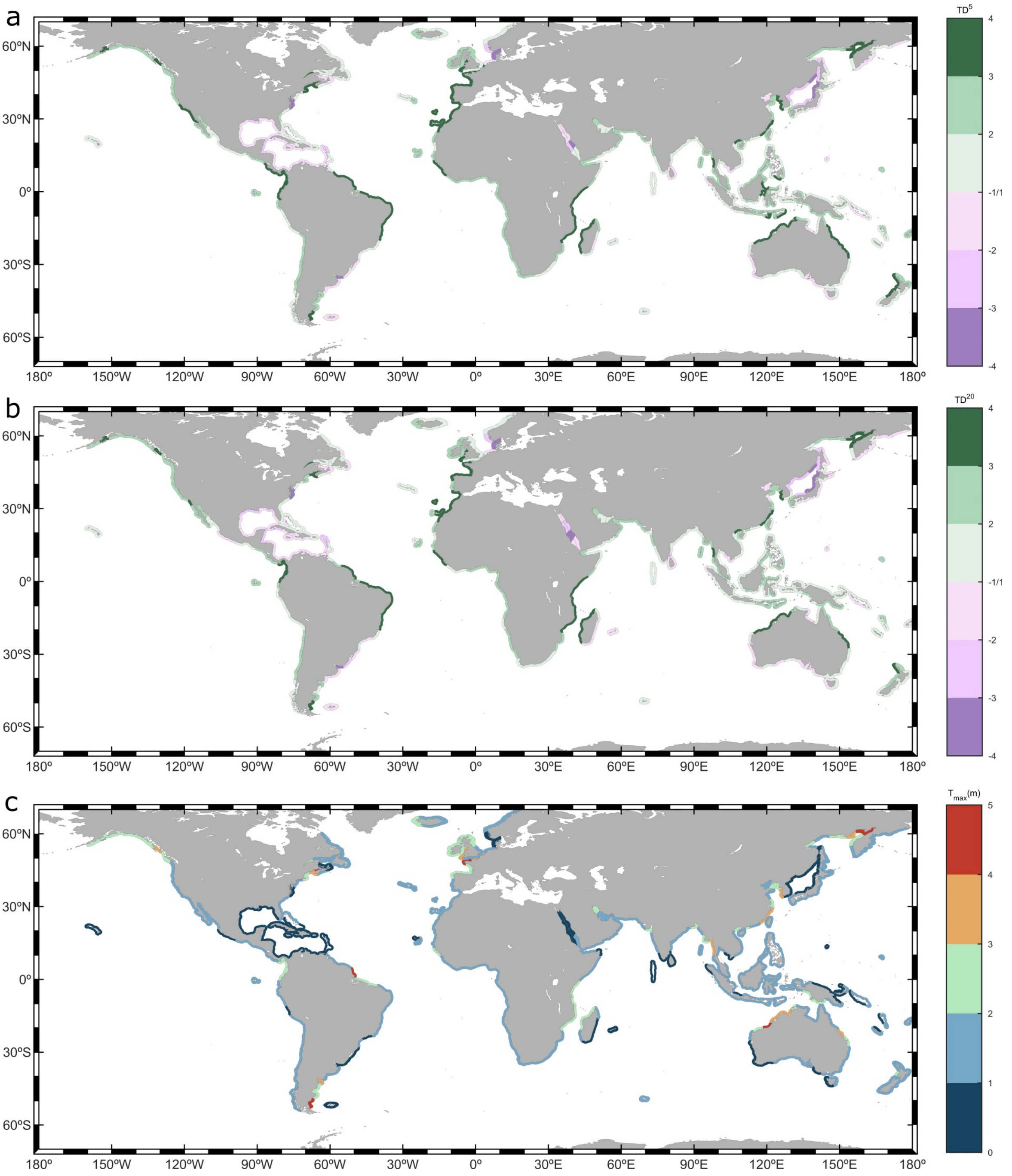

Fig. 4.8 Relative importance of the astronomical tide vs. NTR return values for return periods of (a) 5 years and (b) 20 years through the metrics TD^5 and TD^{20}, respectively. (c) Mean annual maximum tide (m).

According to the results, the dominance of the NTR over the astronomical tide is restricted to three main cases. First, coasts showing T_{max} values lower than 1 m (microtidal ranges), where, despite the NTR extremes not being very high, they still control ESLs. For example, the Red Sea and and the Japan Sea, both semienclosed basins with a microtidal range, show dominance of NTR extremes over the astronomical tide. Second, mesotidal coasts affected by very intense NTR extremes that may overcome the contribution of the astronomical tide. The coasts of Argentina and Uruguay, and the southeast coast of the North Sea, both impacted by very high NTR extremes (Fig. 4.3), illustrate this case. Finally, microtidal coasts affected by intense NTR extremes. The coasts in the Caribbean Sea and Gulf of Mexico are a clear example of this case, showing a plain dominance of NTR extremes in microtidal coasts, resulting in TD^5 of between -1 and -2.

Finally, some coastal regions do not show a clear dominance pattern. The south coast of Australia is a clear example for this issue. The dominance along this coast alternates, being the westernmost and easternmost parts dominated by NTR extremes, and the opposite in the middle part, always showing TD^5 values of between -1.5 to 1.5. Same issue can be seen, for example, in the coast of the Gulf of Carpentaria due to the combination of intense NTR extremes (Fig. 4.3) and a mesotidal range.

4.5 Conclusions

This study assesses the variability of coastal extreme events of the NTR sea level component from altimetry data globally. For that matter, an intercalibrated satellite altimetry NTR dataset, covering the time slice from 1993 to 2021, is built. The analysis is conducted in a set of 445 coastal units homogeneously covering the global coastlines (Fig. 4.1). Altimetry data are selected in each of these coastal units to analyze the NTR extreme variability.

An EVA is conducted at each of the mentioned coastal units. In particular, a time-varying GEVD statistical model from MM is applied. The extreme variability is introduced through the location parameter as a parametric model. Three time scale variations are considered: within the year, through combination of sine functions, inter-annual, through introducing teleconnection indices as covariates and long-term trends, through an exponential function.

The skill of altimetry data to reproduce the variability of NTR extremes is validated against TG data. A quality-filtered global TG dataset of 123 stations is used for validation (Fig. 4.1). Altimetry extreme samples to be compared against in situ records are selected in the vicinity of TG stations based on the correlation between both datasets. Results show good correlation between MM from NTR_{TG} and NTR_{SAT}, exceeding correlations of 70% in more than 80% of the stations (Fig. 4.2a). After applying the EVA to both datasets, the magnitude of NTR^{10} is compared. In general, an underestimation of altimetry data with respect to TG data can be seen (Fig. 4.2b), an issue that enhances at tropical coasts affected by TCs, as these kind of events are not fully captured by altimetry data within the coastal units. Despite the mentioned underestimation, the variability of ESLs is reasonably well captured by altimetry data. First, the variability within the year is validated through the metric CV^{20} (see 4.3.4), showing a correlation of around 90% and a very low bias (Fig. 4.2c). The interannual variability is also well represented in remote data. The statistical model parameter β_{CI} is compared (Fig. 4.2e-h), showing very low biases and correlations higher than 90% for three out of four teleconnection indices considered (the remaining one shows a correlation higher than 75%). Finally, long term trends are compared. Although there are spurious outliers caused by, first, the moving land affecting TGs and, second, local issues disturbing the TG record, a good agreement can also be observed (Fig. 4.2d).

After validation, 5-, 10- and 20-year return period NTR are computed (Fig. 4.3). Results show that the coast of the North Sea and the coasts of Argentina and Uruguay are those suffering the highest NTR events, the former exceeding 1.8 m and the latter 1.4 m for NTR^{20}. Despite TCs not being fully captured, coasts impacted by this type of storms, such as the coasts in the Gulf of Mexico, the coasts of China and South Japan and the coast of the Gulf of Carpentaria, show notably high NTR extremes, all exceeding 1 m for NTR^{20}.

The assessment of the extreme variability within the year shows that coasts in extratropical latitudes are characterized by a clear winter-summer variability pattern, so that they suffer the highest NTR events during the corresponding winter month of each hemisphere (Fig. 4.4). Besides, the metric CV^{20} shows that this seasonality is more prominent in the NH than in the SH (Fig. 4.5). On the other hand, there is great heterogeneity in the most probable month showing the highest extremes in subtropical and intertropical coasts. Further, many of these coasts do not show a simple variability pattern within the year with a periodicity of one year (e.g., winter-summer variability), but show two storm periods (i.e., two local maxima), mainly due to suffering extremes with different origins. For example, the coast in the Gulf of Mexico suffers the impact of the most intense NTR extremes during the TC season, especially in September and October, and shows another maximum between May and April (point P6 in Fig. 4.4). In coasts in the southwestern tropical Pacific affected by TCs, however, the most intense NTR events occur earlier with respect to the Atlantic, mostly in August and September (point P10 in Fig. 4.4).

The main result of the long term variability assessment is a clear increasing pattern along the global coastlines (Fig. 4.6b). Significant trends at 95% confidence level have been found in more than 95% of the coastal units analyzed. Relative changes higher than 50% in NTR^{20} can be seen along some parts of the southwestern African coast and Mozambican channel. On the other hand, the weakest trends are observed in the northwestern coast of America, showing almost null increases and low significance values.

The interannual variability of NTR extremes is analyzed based on the influence of four climate teleconnection patterns (Fig. 4.7): the Arctic Oscillation pattern through the AO index, the Southern Annular Mode pattern through the SAM index, the ENSO phenomenon pattern through the Niño 34 index and the Indian Ocean Dipole pattern through the DMI index. The AO index shows significant correlations in NH extratropical coasts, especially in the Atlantic basin (Fig. 4.7a). Thus, there is a strong negative correlation along the northeastern American coast and the Atlantic southern coast of Europe (β_{CI} values of between -4 cm/IU and -2 cm/IU), whereas there is a strong positive correlation in the Atlantic northern coast of Europe (β_{CI} values of between 6 cm/IU and 8 cm/IU). The SAM index mainly shows significant correlations in two coastal regions: a negative correlation in the south coast of Australia ($|\beta_{CI}| > 2$ cm/IU) and a positive correlation in the south coasts of Sumatra and Java ($|\beta_{CI}| < 2$ cm/IU). The ENSO phenomenon shows a strong correlation with NTR extreme events in the intertropical coasts of the Pacific Ocean. This influence also extends to the extratropical western coasts of America and some intertropical and subtropical coasts in the Indian Ocean and West Atlantic Ocean. In general, a positive correlation (Niño phase) can be observed along coastlines in the tropical East Pacific, reaching absolute β_{CI} values higher than 4 cm/IU, and the opposite (Niña phase) in the tropical West Pacific, where absolute β_{CI} values higher than 5 cm/IU can be seen. The influence pattern found for the DMI index shows significant negative correlations in the eastern coasts of the Indian Ocean ($|\beta_{CI}| < 8$ cm/IU) and the opposite in the western ones ($|\beta_{CI}| > 4$ cm/IU). Additionally, the IOD pattern is found to be highly correlated with ENSO phenomenon.

The relative importance of the astronomical tide vs. NTR extremes in ESLs is assessed through the metric TD (see Section 4.3.4). Results demonstrates that the astronomical tide modulates ESLs in roughly 80% of the global coastlines over NTR events with return periods of between 5 and 20 years. The main coastal regions dominated by the NTR extremes are the coasts in the Gulf of Mexico, the south and east coasts of the North Sea, the coasts of Argentina and Uruguay and coasts in semienclosed seas, such as the Red Sea and the Japan Sea. As expected, the magnitude of ESLs in macrotidal coasts ($T_{max} > 2m$; see Section 4.3.4) are mainly controlled by the astronomical tide, such as in the coasts of the Mozambique Channel, the northwestern coast of Australia or the Atlantic coasts of North Spain and Southwest France.

This study demonstrates the good skill of altimetry data to reproduce the coastal ESL variability. Although there is still room for improvement in terms of accuracy, the results presented here are a reliable prospect of the potential of altimetry data to develop climate studies and, particularly, ESL studies. Despite the time period covered by altimetry being still limited (aprox. 30 years), the promising results presented in this chapter suggest that the extension of this database through time will maximize its main strength, the continuous global coverage, and reduce its mean weakness, the irregular sampling (i.e., along track sampling). In addition, the combination of the accuracy increase nearshore and the increase of data availability, are expected to progressively allow climate studies at lower coastal scales, which is particularly useful where no insitu information and numerical modelling capacity are available.

Chapter 5

Changes in wave climate extremes under future climate change scenarios

Abstract

Extreme waves will undergo changes in the future when exposed to different climate change scenarios. These changes are evaluated through the analysis of significant wave height return values and are also compared with annual mean significant wave height projections. Hourly time series are analyzed through a seven-member ensemble of wave climate simulations and changes are estimated in significant wave height for return periods from 5 to 100 years by the end of the century under RCP4.5 and RCP8.5 scenarios. Despite the underlying uncertainty that characterizes extremes, we obtain robust changes in extreme significant wave height over more than approximately 25% of the ocean surface. The results obtained conclude that increases cover wider areas and are larger in magnitude than decreases for higher return periods. The SO is the region where the most robust increase in extreme significant wave height is projected, showing local increases of over 2 m regardless the analyzed return period under RCP8.5 scenario. On the contrary, the tropical north Pacific shows the most robust decrease in extreme significant wave height, with local decreases of over 1.5 m. Relevant divergences are found in several ocean regions between the projected behavior of mean and extreme wave conditions. For example, an increase in significant wave height return values and a decrease in annual mean H_s is found in the SE Indian, NW Atlantic and NE Pacific. Therefore, an extrapolation of the expected change in mean wave conditions to extremes in regions presenting such divergences should be adopted with caution, since it may lead

to misinterpretation when used for the design of marine structures or in the evaluation of coastal flooding and erosion.

5.1 Introduction

Changes in ocean wave climate, and especially in extremes, can have a significant effect on maritime activities such as seagoing shipping and the offshore industry. These changes combined together with those from other marine dynamics also affected by global warming (e.g., MSLR; Church et al. 2013) may have a sensitive impact on coastal processes such as erosion (Casas-Prat et al., 2016; Toimil et al., 2020a; Zacharioudaki and Reeve, 2011) and flooding (Dodet et al., 2019; Kirezci et al., 2020; Melet et al., 2020; Vousdoukas et al., 2018). Climate change can affect wave climate by the alteration of variables directly linked to its generation and propagation. Future variations in surface wind fields and marine ice coverage may alter wind waves behavior over the oceans, changing the transmitted energy (Reguero et al., 2019) and generation fetch (Lantuit et al., 2012; Thomson and Rogers, 2014).

Several studies have addressed the analysis of future changes in wave climate usually through wave climate projections. Since GCMs do not simulate ocean wind waves, wave climate projections are generated based on physical and atmospheric variable outputs from these general models (e.g., sea level pressure, surface wind fields, ice-coverage). Two are the main approaches used to generate wave climate projections both at regional and global scale: dynamical (Bricheno and Wolf, 2018; Casas-Prat et al., 2018; Dobrynin et al., 2012; Hemer et al., 2013b; Lemos et al., 2019; Mori et al., 2013) and statistical (Camus et al., 2017; Perez et al., 2015; Wang et al., 2014). The COWCLIP community is making remarkable efforts to integrate the existing global studies about future changes in wave climate and asses their robustness and uncertainties (Hemer et al., 2013a; Morim et al., 2018, 2019, 2020). The results obtained in these studies evidence a consensus about the future increase in annual mean H_s in the Southern Ocean and tropical eastern Pacific, and a decrease in the North Atlantic and northwestern Pacific (Oppenheimer et al., 2019).

In spite of its remarked relevance, the analysis of future changes in extreme wave climate under climate change scenarios deserves more attention. To this day, the assessment of the future variations in wave extremes has been carried out mainly through the analysis of high quantiles from wave height time series with a resolution higher than daily (Aarnes et al., 2017; Semedo et al., 2013; Shope et al., 2016; Wang et al., 2004) or AM (Aarnes et al., 2017; Bricheno and Wolf, 2018; Casas-Prat et al., 2018; Wang et al., 2014). An accurate analysis of extreme events with a very low probability of occurrence needs to be grounded on the EVT, which provides asymptotic long-term distributions for extremes and the approaches to estimate return values (Coles, 2001). The limited number of studies on this topic (Aarnes et al., 2017; Caires et al., 2006; Mentaschi et al., 2017; Meucci et al., 2020; Wang et al., 2014), commonly addressed through the assessment of changes in H_s return values, together with the intrinsic complexity of wave extremes, makes it difficult to reach a robust agreement about the regional projected changes by the end of the century. In order to better understand the future behavior of rare wave extremes, this study proposes the assessment of projected changes in H_s for different return periods under climate change scenarios, analyzing their magnitude, uncertainty, geographical distribution and their behavior with respect to mean wave conditions.

5.2 Climate data

Atmosphere–ocean GCMs reproduce the intrinsic behavior of the real global climate, representing the extreme complexity inherent to the interaction between the atmosphere, the land surface, the ocean and the sea ice (Flato et al., 2013). While GCMs faithfully reproduce the past global climate, in the projected period the behavior diverges from the historical trend due to the consideration of different future GHG concentration scenarios. This study makes use of a CMIP5-based multi-model ensemble consistent of seven atmosphere-ocean GCMs (Table 5.1) to develop a seven-member wave climate projection ensemble. The criterion to select the GCMs is defined by the need of producing hourly time series of H_s to better capture the extremes. Therefore, since dynamical wave simulations use sea surface winds and marine ice coverage outputs from GCMs as forcings, we look for GCMs that provide these products with the maximum time resolution as possible. All the GCMs provide 3-hourly winds and daily ice coverage fields (except from HadGEM2-ES that provides monthly ice) for the historical and projected periods. A single run of each GCM is simulated to reduce the storage capacity demanded by the hourly H_s series needed, which is sustained by the low variability between wave projections from runs of the same model (Semedo et al., 2018). In particular, the r1i1p1 member of each realization ensemble is selected.

In addition to the spatial resolution, the independency of the models is analyzed to ensure the reliability of the ensemble mean results. This issue is addressed on the basis of the classification of GCMs proposed by Knutti et al. (2013) in terms of the degree of dissimilarity between pairs of individual models with regard to a multivariate description of the natural variability (Masson and Knutti, 2011). The similarity between models is defined using the Kullback-Leibler divergence distance metric considering the seasonal cycle, interannual variations, annual mean climatology and spatial correlation from temperature and precipitation monthly fields, both for the control state period and for the projected changes by the end of the century. A hierarchical clustering is applied to define the relationship between members, presenting the results as a dendrogram. HadGEM2-ES and ACCESS1.0 are the closest models in the control state, which can be related to sharing the same atmospheric model. Concerning the projected changes, there are no strong enough similarities that may cause a bias in the results, not even for the two models found to be similar in the control period.

Table 5.1 Main characteristics of the selected Atmosphere-Ocean General Circulation Models

GCM	Institution	Country	Atmospheric resolution (latxlon)
MIROC5	MIROC	Japan	1.40°x1.40°
IPSL-CM5A-MR	Institut Pierre-Simon Laplace	France	1.25°x1.25°
GFDL-ESM2G	NOAA Geophysical Fluid Dynamics Laboratory	USA	2.00°x2.50°
CNRM-CM5	Centre National de Recherches Météorologique	France	1.40°x1.40°
CMCC-CM	Centro Euro-Mediterraneo per I Cambiamenti Climatici	Italy	0.75°x0.75°
ACCESS1.0	CSIRO-BOM	Australia	1.25°x1.90°
HadGEM2-ES	Met Office Hadley Centre	UK	1.25°x1.90°

The simulations are run in a regular near-global mesh covering latitudes between 88°N and 85°S with one-degree spatial resolution. The third-generation wave model WaveWatchIII (WW3) version 4.18 (Tolman, 2014) is used to run the simulations. A continuous ice treatment from an ice coverage of 25% (no obstruction) to 75% (complete obstruction) is considered. Below 25% no wave energy dissipation is assumed, whereas a sea ice coverage above 75% is assumed to cause a complete dissipation of energy. In addition, a coastal reflection equal to 0.05 is considered. The main features of the numerical scheme used in this work are summarized below:

- Parametrization TEST45 (Ardhuin et al., 2010).
- Discrete Interaction Approximation (DIA) (Hasselmann et al., 1985).
- Depth-inducing breaking following Battjes and Janssen approach (Battjes and Janssen, 1979).
- SHOWEX bottom friction formulation (Ardhuin et al., 2003).
- Energy flux reduction due to islands or any other coastal obstacles smaller than cell size (Tolman, 2003).
- Third-order ultimate Quickest propagation scheme (Leonard, 1979).

The resulting global wave projections (GWP) allow the study of hourly H_s time series. Grid nodes with less than 60% of the hourly data due to the presence of ice are not selected. We focus on the changes by the end of the century, comparing a climate reference historical period (1986–2005) to the future time slice 2081–2100 under RCP4.5 and RCP8.5 GHG concentration scenarios. RCP4.5 and RCP8.5 are two of the representative concentration pathways (RCPs) covered in Fifth Assessment Report from IPCC (AR5; Cubasch et al. 2013), and represent GHG concentration trajectories with a projected radiative forcing of 4.5 Wm^{-2}

and 8.5 Wm^{-2} by 2100, respectively. The RCP8.5 scenario is representative of scenarios leading to high GHG levels whilst RCP4.5 comprises stabilization scenarios before 2100 by the employment of a range of adaptation technologies and strategies.

5.3 Methods

5.3.1 Bias correction

Although GCMs have the capability to reproduce the climate system and the interconnections between its components, certain issues such as the spatial resolution and the simplifications introduced by the numerical parametrizations of some physical processes cause a systematic bias inherent to each model (Maraun et al., 2017; Rocheta et al., 2017). Theses biases are transmitted to the wave propagations mainly due to the biases in sea surface wind fields (Hemer et al., 2012a). In this context, different bias correction (BC) techniques have been successfully applied in several studies for different climatic variables such as precipitation (Christensen et al., 2008; Piani et al., 2010a,b), temperature (Li et al., 2010; Piani et al., 2010a) and wind (Bao et al., 2010; Hemer et al., 2012a). More recently, BC has as well been applied to ocean wind waves (Lemos et al., 2020a), showing an unaltered change signal (i.e., the climate variability is preserved) and a possible decrease in the uncertainty of the projected changes. These precedents, together with the fact that extreme events are found to present the greatest biases (Lemos et al., 2020a), make BC essential to assess stormy wave conditions. Thus, a correction technique is applied to reduce the biases of the GWP from each GCM ($\mathrm{GWP_{GCM}}$) in the reference period 1986–2005 and then extrapolate the correction to the future time slice. The global wave hindcast GOW2 (Perez et al., 2017) is used as reference historical data to conduct the BC due to its good performance for simulating extremes, especially in the tropical region.

The individual climate of each GCM varies at each run, precluding an hourly comparison between each $\mathrm{GWP_{GCM}}$ and the hindcast data. Hence, a BC method based on the adjustment of empirical quantiles is applied (Déqué, 2007; Lemos et al., 2020a). The assessment of the 99^{th} percentile bias indicates important differences between GCMs when compared with the reference historical data (Fig. 5.1). Thus, while $\mathrm{GWP_{CMCC-CM}}$ and $\mathrm{GWP_{MIROC5}}$ present the smallest discrepancies with GOW2 wave hindcast, $\mathrm{GWP_{IPSL-CM5A-MR}}$ and $\mathrm{GWP_{CNRM-CM5}}$ show the largest. In general, the differences are higher at latitudes poleward of 35° and lower in the tropical region.

The empirical quantile mapping technique (EQM; Déqué 2007), slightly modified to better correct the upper-tail of the distribution, is the method selected to correct biases from GWP_{GCM}. EQM consists in adjusting the empirical CDF from each GWP_{GCM} to the empirical CDF from the reference historical data (Eq. 5.1). Thus, a correcting increment

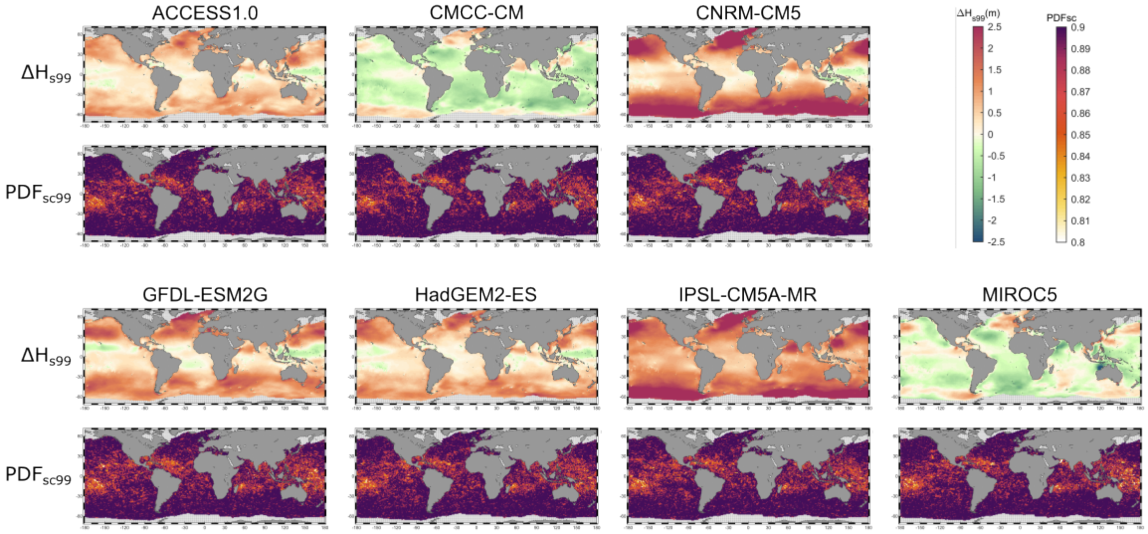

Fig. 5.1 Upper panels: 99th percentile bias of H_s for each member of the ensemble (GOW2-GWP$_{\text{GCM}}$). Lower panels: PDF-based skill score of the upper tail of the distribution over the 99th percentile after applying the BC under RCP8.5 scenario.

(X_{corr}) is obtained for each selected quantile and then a linear interpolation is applied between them. The correction outside the range defined by the selected quantiles is the same as the applied to the first or the last quantiles.

$$X_{corr} = CDF_{Ref}^{-1}[CDF_{GCM}(X)] \tag{5.1}$$

where CDF_{Ref} is the cumulative distribution function of the reference data and CDF_{GCM} is the cumulative distribution function of each GWP_{GCM}.

The quantile selection plays an important role in the adequate performance of the method. The selected quantile probabilities (q_i) are defined as follows:

- Quantile 0.01 (q01) followed by linearly distributed quantiles from 0.05 (q_{05}) to 0.90 (q_{90}) each 0.05.
- Twelve Gumbel scaled quantiles (Eq. 5.2) from q_{90} for a better representation of the upper tail of the distribution.

$$q_i = exp[-exp(-x_{qi})] \tag{5.2}$$

The same correction is applied to the 20-year time slice at the end of the century (2081–2100).

The performance of the BC is measured by comparing the probability density function (PDF) of H_s in the present time slice through the PDF-based skill score (PDF_{sc}; Perkins et al. 2007):

$$PDF_{sc} = \sum_{i=1}^{n} min\left(f\left(H_{s,i}^{Ref}\right), f\left(H_{s,i}^{GCM}\right)\right) \Delta H_s \tag{5.3}$$

where n is the number of elements in which the sample of H_s is discretized; ΔH_s is the width of each element.

In this study a non-parametric empirical PDF from a H_s sample over the q_{99} for both data sets is calculated using the Kernel density estimation. Bias correction allows to improve the agreement between the GWP_{GCM} and the reference data, reducing the variability between members.

Results show a global effectiveness of the correction (Fig. 5.1) for every member of the ensemble, presenting values above 0.8 in almost all the global ocean. The lowest performance (i.e., white and yellow areas from PDFsc maps in Fig. 5.1) is found in areas directly influenced by TC activity, which evidence the difficulty of the BC to correct TC-induced wave extremes.

5.3.2 Statistical extreme model

In order to provide coherent results globally, a common method is applied in all regions notwithstanding the complexity involved in the different geneses of wave extremes. Considering this issue, we apply the GEVD parametric model (Eq. 5.2) based on the fit of AM from hourly time series. This is a widely used method in engineering together with exceedances over a threshold, although more mathematically stable for global studies and to analyze different climate simulations. Since the objective is to study the effect of climate change on extreme wave conditions using future time slices of 20 years, we consider a stationary statistical model assuming an unchanged behavior of the block maxima within these periods (Vanem, 2015). In particular, we apply the simplified extreme value distribution family of the GEVD: type I Extreme value distribution (type I EVD) or Gumbel distribuition ($\xi = 0$ in Eq. 5.2).

5.3.3 Goodness of fit of the extreme model

The goodness of fit (GoF) of the Gumbel distribution is assessed with the Anderson–Darling test (AD; Anderson and Darling 1954), a method proven to be optimal to analyze the performance of this distribution (Abidin et al., 2012; Shimokawa and Min Liao, 1999) and widely applied in engineering studies to evaluate the fit of climatic extremes to extreme distributions (Caires and Sterl, 2005; Dong et al., 2015; Ferreira and Guedes Soares, 2000; Masina et al., 2015; Najid et al., 2009). This test statistic (Eq. 5.4; Stephens 1974) measures the distance between the proposed distribution with the estimated parameters and the empirical distribution, introducing as well a weight function that gives heavier weights in both tails to improve the performance. AD test is applied to evaluate whether the null hypothesis (H_0) is rejected or not at the 95% confidence level ($\alpha = 0.05$). H_0 states that the data follows a Gumbel distribution and H_1, the alternative hypothesis, the contrary. The null hypothesis is rejected or not depending on the comparison between the p-value and the considered significance level.

$$A_n^2 = -n - \sum_{i=1}^{n} \frac{2i-1}{n} \left[log\left(F\left(X_i\right)\right) + log\left(1 - F\left(X_{n+1-i}\right)\right)\right] \tag{5.4}$$

where $X_1 < \cdots < X_n$ are the ordered sample data points and n is the size of the sample.

5.3.4 Validation with buoy data

The H_s return values are validated against buoy data. The buoy data set used to conduct the validation is obtained from the Global Ocean Delayed Mode Wave Product from CMEMS (In Situ Thematic Centre, 2021). All the selected buoys meet a number of quality requirements to ensure a proper performance of the EVA and an adequate comparison with the outcomes of the numerical projections, resulting in a final set of fifty-two buoys. These requirements are listed below:

- The buoy should be moored at a water depth higher than 50 m to ensure that waves do not propagate in shallow waters and avoid non-linear processes.
- The buoy should be moored at a distance to the coast higher than 20 km to take into account the spatial resolution of the global wave climate simulations (i.e., one-degree). Nevertheless, the limited number of buoys in the SH makes us to relax this requirement to ensure a validation of southern extreme waves, setting the distance limit at 5 km for buoys located in the SH.
- AM are selected differently depending on the latitude of the buoy. For buoys located above 40°N, AM are selected from years presenting more than a 60% of the hourly data in the boreal winter months (i.e., January, February and December). For buoys located below 40°S, AM are selected in years presenting more than a 60% of the hourly data in the austral winter months (i.e., June, July and August). For the rest of buoys, AM are selected in years presenting more than 60% of the hourly data.

- The resulting AM sample should have at least twenty values to carry out the EVA.

5.3.5 Robustness of the projected change

The uncertainty assessment of the projected changes is based on a method proposed in the AR5 report (Collins et al., 2013). In particular, the robustness of the change is addressed considering, first, its significance and, second, the agreement in the sign of change between the members of the ensemble. Grid nodes in which the change is statistically significant at 95% confidence level ($\alpha = 0.05$; Eq. 5.5) in more than 50% of the ensemble members and at least 80% of the them agree in the sign of change are stippled and the change is considered as robust. If both conditions are not met, grid nodes are not stippled.

$$(1-\alpha)\ confidence\ intervals : \overline{X} \pm t_{\frac{\alpha}{2},n-1}\frac{s}{\sqrt{n}} \tag{5.5}$$

where α is the significance level, n is the sample size and s is the standard deviation normalized by $n-1$.

5.4 Results

5.4.1 Extreme value analysis

The behavior of wave extremes is studied through an EVA of bias-corrected H_s. The regional distribution of the estimated μ, σ and ξ GEVD parameters for the present-day wave climate and their future projected changes by the end of the century under RCP8.5 scenario are shown in Fig. 5.2. The location parameter, an indicator of the central values of the extreme distribution, increases with latitude until reaching its highest values in the extratropical region and, in particular, in the North Atlantic Ocean, where μ shows values close to 14m (Fig. 5.2a). There is a robust agreement concerning the future decrease in μ in the NH, showing local decreases close to 1m in the North Atlantic Ocean and around the Japanese Archipelago. The northernmost Pacific Ocean and the northwestern Atlantic are the most remarkable exceptions found within this decreasing pattern (Fig. 5.2d). A robust projected change is also obtained in the Southern Ocean although with the opposite sign (i.e., increase in μ).

The spatial distribution of σ is quite similar to the one for μ (i.e., higher values at higher latitudes) although showing some relevant differences such as the very high σ values found around Japan (Fig. 5.2b). Concerning future changes (Fig. 5.2e), a higher noise in the sign of change with respect to μ can be observed, making it difficult to find other consistent general conclusions beyond an increase in the Southern Ocean. In spite of this, some relevant aspects

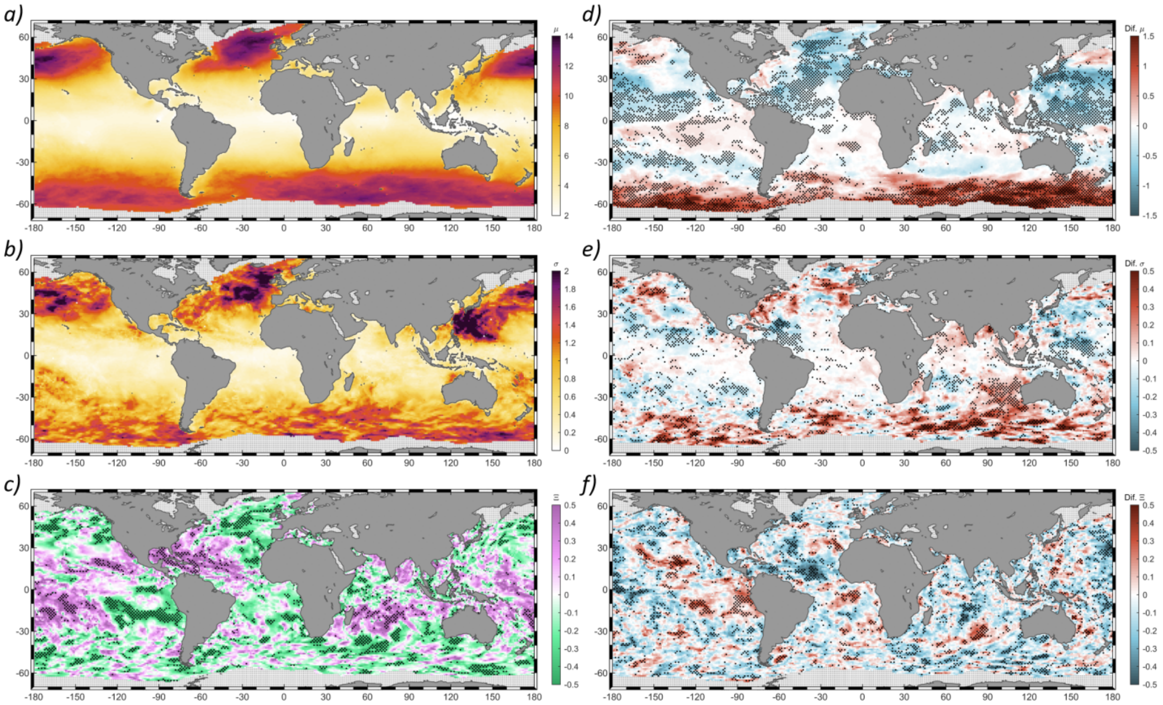

Fig. 5.2 (a) Location, (b) scale and (c) shape GEVD parameters from GOW2 hindcast. Multi-model ensemble mean change in the (d) location, (e) scale and (f) shape parameters by the end of the century (2081-2100 relative to 1986-2005) under RCP8.5 scenario. Stippling in (c) denotes significant fit of the shape parameter at 95% confidence level. Stippling in right panels denotes changes statistically significant at 95% confidence level in at least 50% of the members and an agreement in the sign of change in more than 80% of the members.

such as the robust decrease found in the tropical southeastern Indian Ocean and the loss of a clear decreasing change pattern in the North Atlantic Ocean can be pointed out.

The shape parameter presents positive values (i.e., heavy-tailed distribution) in TC activity regions and TC-induced swell affecting zones (Caribbean Sea, West Pacific, South-West Indian Ocean; Fig. 5.2c). Negative values (i.e., bounded upper tail distribution) can be observed throughout the global ocean, being the northeastern Atlantic, southeastern Pacific and south Indian the regions which present the clearest negative patterns.

The low proportion of the global ocean showing both a statistically significant fit and a robust future change in ξ (14% and 16%, respectively) indicates an underlying instability when adding this degree of freedom in the extreme model to estimate return values, leading us to fit the AM to a type I EVD (i.e., Gumbel distribution). The use of a simpler bi-parametric extreme model offers an overall greater robustness although it may lead to an underestimation of heavy-tailed distributions in TC activity areas (Fig. 5.2c). The GoF of the type I EVD through the AD test statistic, shows an overall good fit of the model except for some areas where the suitability of the Gumbel distribution is compromised (Fig. 5.3), mostly matching, as expected, the areas where the fit of ξ is found to be significant.

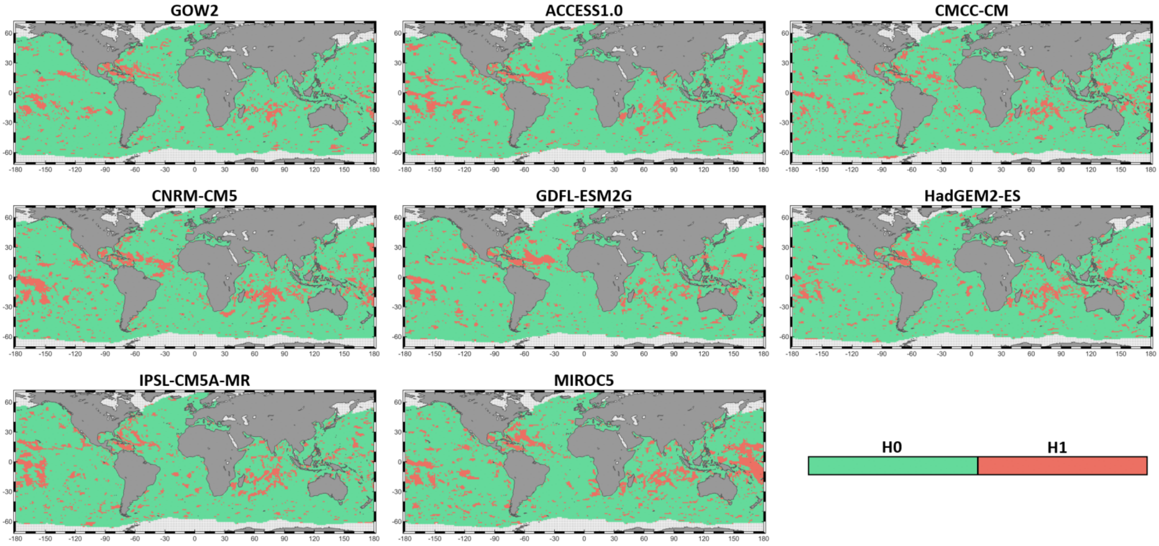

Fig. 5.3 Anderson-Darling test statistic at 95% confidence level (α =0.05) for GOW2 and every ensemble member. Orange grid points indicate where the null hypothesis (H0) is rejected at 95% confidence level (α =0.05) for each GCM.

5.4.2 Validation of extreme H_s return values

To provide confidence in the estimated H_s return values from model runs, a validation against return values estimated from buoy records is carried out. A mean relative error of 13%, 18% and 20% and a mean squared error of 2 m^2, 7 m^2 and 12 m^2 are obtained after applying the BC for H_s^5, H_s^{20} and H_s^{50}, respectively (Fig. 5.4).

5.4.3 Extreme wave climate future changes

Present-day wave climate estimates for very low probabilities of occurrence studied through the H_s parameter (5-, 20-, 50- and 100-year return periods, i.e. H_s^5, H_s^{20}, H_s^{50} and H_s^{100}, respectively), evidence a very similar spatial pattern regardless the analyzed return level (Fig. 5.5c; Fig. 5.6a-c). The increasing H_s gradient from the equator to higher latitudes (Semedo et al., 2011; Young, 1999) reaches its maximum in the northernmost regions of the Atlantic and Pacific oceans, showing magnitudes above 19 m and 22 m for H_s^{20} and H_s^{100}, respectively. Similarly, the Southern Ocean is a highly energetic region that presents values up to 17 m and 20 m for H_s^{20} and H_s^{100} in the southern Indian Ocean. Note that the high magnitudes observed in the extratropical region extend to TC activity areas (e.g., tropical northeastern Atlantic, tropical northeastern Pacific or tropical southeastern

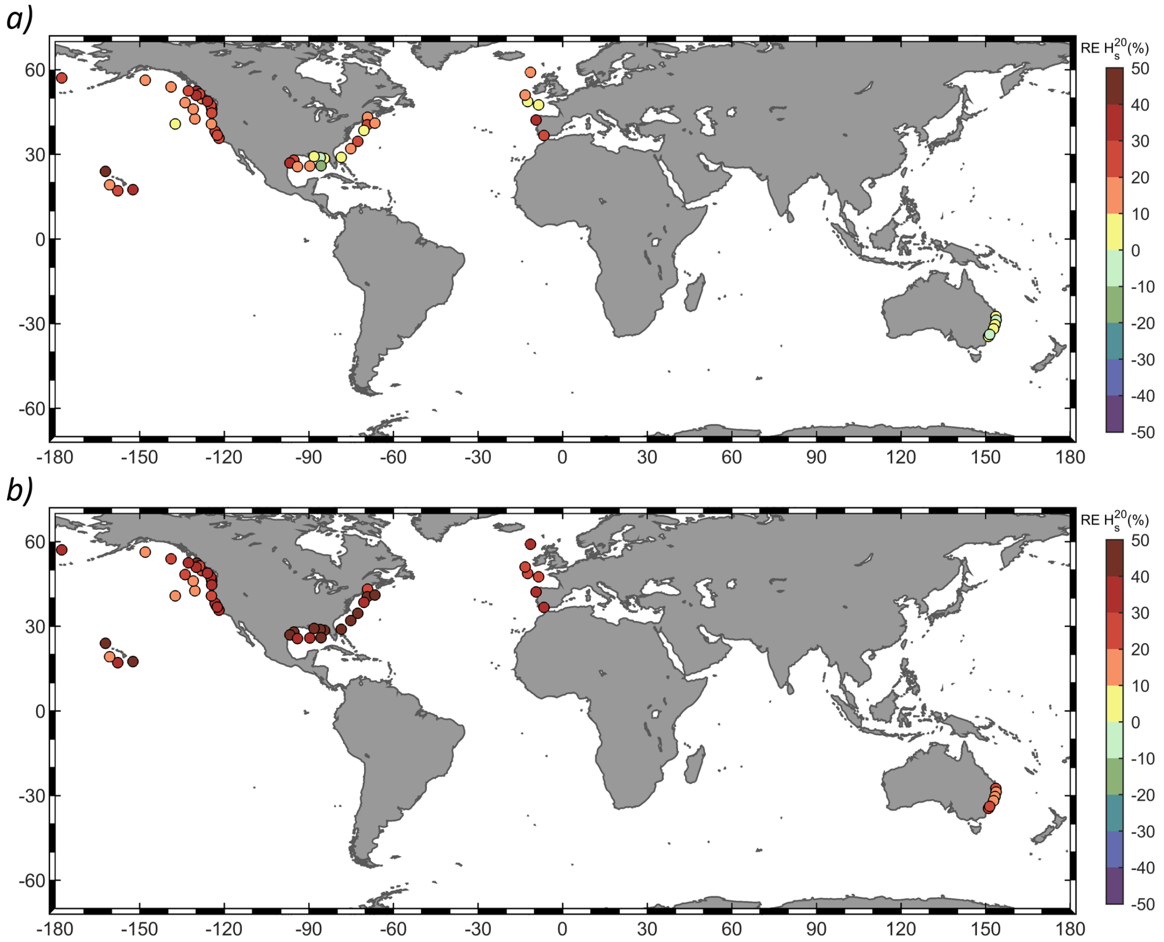

Fig. 5.4 Relative error (%) in H_s 20-year return values calculated from the dynamical projections with (a) and without (b) BC with respect to return values from buoy records.

Pacific), inducing a very strong gradient toward the low values found around the equator (i.e., magnitudes lower than 2.0 m for H_s^{100}).

The spatial distribution of the projected changes is also similar for different return periods although showing an increasing uncertainty for higher extreme estimates. A clear geographical pattern characterized by an overall expected increase in wave extremes in the Southern Ocean and a decrease in the NH can be distinguished, presenting as well minor exceptions such as the northernmost Pacific and northwestern Atlantic. The tropical south region, however, shows a heterogeneous change pattern in which both negative and positive trends can be observed. Hence, a regionalization of the global ocean is proposed to better understand the future changes under climate change scenarios and their uncertainty (Fig. 5.5a). Table 5.2 summarizes the proportion of area in which changes are found to be robust and the average projected change for all the analyzed return periods in each region under RCP4.5 and RCP8.5 scenarios.

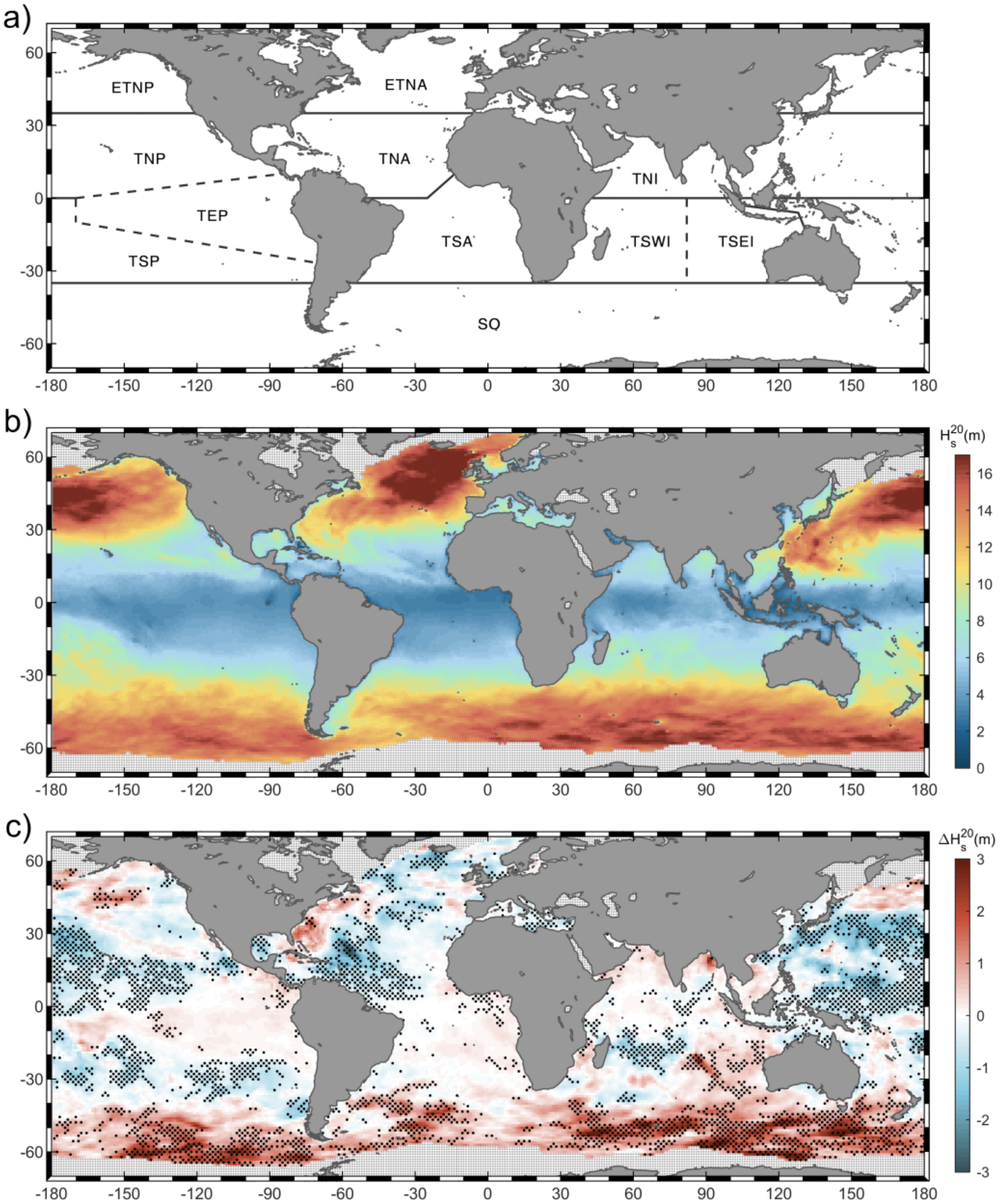

Fig. 5.5 (a) Proposed global ocean regionalization. ETNP (extratropical north Pacific), ETNA (extratropical north Atlantic), TNP (tropical north Pacific), TNA (tropical north Atlantic), TNI (tropical north Indian), TEP (tropical eastern Pacific), TSP (tropical south Pacific), TSA (tropical south Atlantic), TSWI (tropical southwestern Indian), TSEI (tropical southeastern Indian), SO (Southern Ocean). (b) Present-day H_s^{20} climate (m) from GOW2 hindcast. (c) Multi-model ensemble mean change in H_s^{20} (m) under RCP8.5 by the end of the century (2081–2100 relative to 1986–2005). Stippling denotes changes statistically significant at 95% confidence level in at least 50% of the members and an agreement in the sign of change in more than 80% of the members.

To facilitate the understanding of the results, in the following we will use the projected changes in H_s^{20} as the baseline of the exposition throughout the text. The estimated future changes in H_s^{20} under RCP8.5 scenario (Fig. 5.5c) exhibits a robust increase in a 34% of SO with a higher uncertainty in the Atlantic region (from 60°W to 30°E). The agreement between this increasing pattern and the projected changes found in previous studies (Caires et al., 2006; Mentaschi et al., 2017; Meucci et al., 2020; Wang et al., 2014) based on different scenarios, models and EVA approaches, provide confidence to the expected behavior of wave extremes in SO. The proportion of robust changes increases with latitude, reaching 29% in the roaring forties (between 40°S and 50°S) and 45% in the furious fifties (between 50°S and 60°S) regions. The average expected change of +0.8 m, with local increases of over 3.5 m, makes SO the region where the greatest change in extreme H_s is expected. Furthermore, this projected increase can also be interpreted as an increase by 2100 in the frequency of occurrence of waves associated at present to a 20-year return period, i.e. present-day H_s^{20} would have associated by 2100 a return period lower than 20 years. In this regard, almost half SO region (42%) shows a return period of present-day H_s^{20} lower than 10 years by the end of the century, with local areas presenting return periods lower than 5 years (Fig. 5.7b). The effect of the intensification and poleward shift of the southern extratropical storm track (Chang et al., 2012; Yin, 2005) has been already discussed in previous wave climate studies (Hemer et al., 2013a; Mentaschi et al., 2017) as a plausible cause of the expected increase in H_s. In addition, the projected increase in the frequency of extreme ETCs in the SH found from the analysis of CMIP5 ensembles (Chang, 2017; Chang et al., 2012), might as well be related to the obtained change. In particular, the latter is especially significant between 45°S and 60°S and in the Southern Indian Ocean, which is consistent with the spatial pattern found.

Regarding the extratropical north region, the Pacific (13%) and Atlantic (18%) basins show a spatial change pattern characterized by the presence of small robust areas dispersedly distributed that induce an average change with opposite sign (+0.0 m and 0.3 m, respectively). These results could be explained by the great uncertainty associated to the effect of global warming on northern extratropical storm tracks (Oppenheimer et al., 2019), the main forcing of these events, due to great discrepancies between models (Priestley et al., 2020). In addition, the good fit of the extreme model above 35°N shown by AD test statistic (Fig. 5.3), supports the model definition of storm tracks as the main source of uncertainty of the estimated changes. Notwithstanding these limitations, the poleward shift in the Pacific storm track shown in previous studies (Catto et al., 2011; Shaw, 2019) and the ice cover reduction are the most likely causes of the positive average change found in ETNP.

The assessment of tropical projected changes needs to be done cautiously. Results in regions affected by TC activity are directly conditioned by the skill of the models to reproduce these storms and the capability of the extreme distribution to model their behavior. The former is surely influenced by the spatial resolution of the models (in this case from 0.75°

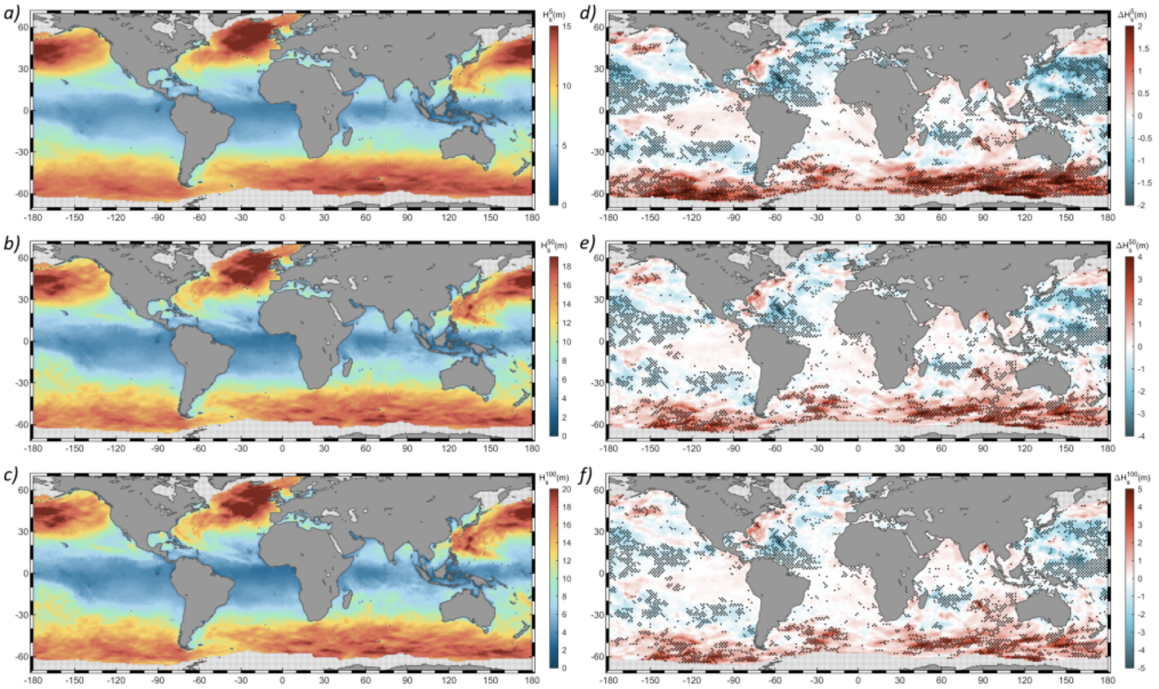

Fig. 5.6 (a) H_s^5, (b) H_s^{50} and (c) H_s^{100} from GOW2 hindcast. Multi-model ensemble mean change in (d) H_s^5, (e) H_s^{50} and (f) H_s^{100} under RCP8.5 scenario by the end of the century. Stippling denotes the same as in Figure 5.5.

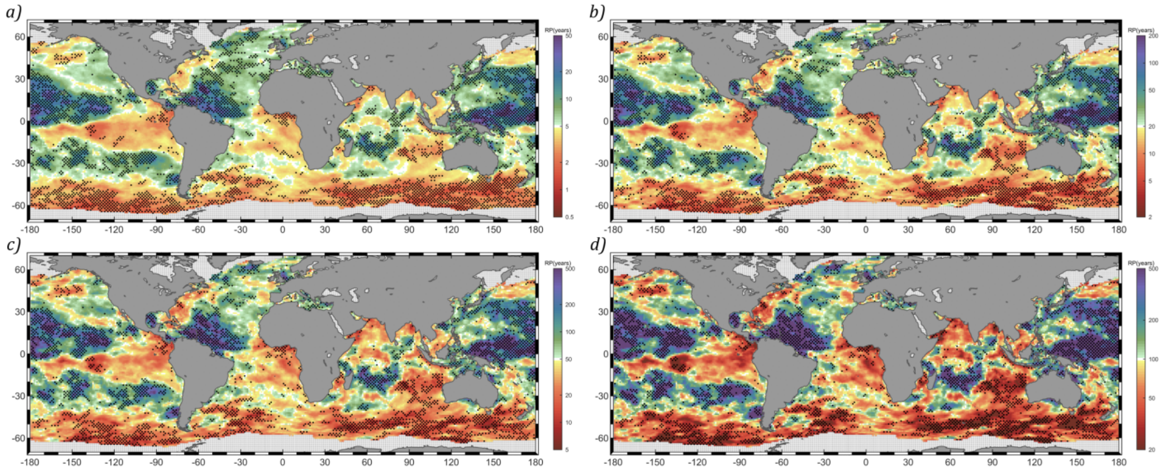

Fig. 5.7 Projected return period (years) under RCP8.5 scenario by the end of the century of present-day (a) H_s^5, (b) H_s^{20}, (c) H_s^{50} and (d) H_s^{100}. Stippling indicates the same as in Figure 5.5.

to 2.5°), although other features such as the physical parametrizations and dynamical cores should also be considered (Camargo, 2013; Shimura et al., 2017). The skill of the models is analyzed by comparing the maximum wave height registered by the ensemble members and the reference hindcast as it has been similarly done in previous studies (Shimura et al., 2017, 2015). Results show that although all models simulate TCs, there is a general underestimation of the

Table 5.2 For each analyzed ocean region, upper row: proportion of the region showing robust changes and (between brackets) proportion of the region showing a robust increase. Lower row: average magnitude of the projected changes and (between brackets) 5th and 95th percentiles of the projected changes with the same sign as the estimated average in the region. Results are displayed for 5-, 20-, 50- and 100-year return periods under RCP4.5 and RCP8.5 scenarios. All results are rounded to one decimal place.

	RCP4.5				**RCP8.5**			
	H_s^5	H_s^{20}	H_s^{50}	H_s^{100}	H_s^5	H_s^{20}	H_s^{50}	H_s^{100}
Global								
Robustness(%)	$22.4_{(10.5)}$	$18.2_{(8.7)}$	$16.8_{(8.1)}$	$16.2_{(7.7)}$	$31.6_{(14.2)}$	$27.6_{(12.3)}$	$25.4_{(11.3)}$	$24.3_{(10.8)}$
Avg. change (m)	$+0.0_{(+0.0;+0.8)}$	$+0.1_{(+0.0;+1.1)}$	$+0.1_{(+0.0;+1.3)}$	$+0.1_{(+0.0;+1.5)}$	$+0.1_{(+0.0;+1.5)}$	$+0.1_{(+0.0;+1.8)}$	$+0.1_{(+0.0;+2.0)}$	$+0.1_{(+0.0;+2.2)}$
ETNP								
Robustness(%)	$16.3_{(8.5)}$	$12.4_{(4.8)}$	$12.2_{(4.9)}$	$11.9_{(4.5)}$	$15.6_{(5.9)}$	$12.6_{(5.5)}$	$11.4_{(5.2)}$	$11.6_{(5.1)}$
Avg. change (m)	$+0.1_{(+0.0;+0.7)}$	$+0.1_{(+0.0;+1.1)}$	$+0.1_{(+0.0;+1.3)}$	$+0.2_{(+0.0;+1.5)}$	$+0.0_{(+0.0;+0.8)}$	$+0.0_{(+0.0;+1.2)}$	$+0.0_{(+0.0;+1.5)}$	$+0.0_{(+0.0;+1.7)}$
TNP								
Robustness(%)	$31.1_{(0.7)}$	$22.2_{(1.1)}$	$19.9_{(1.5)}$	$18.6_{(1.9)}$	$44.6_{(0.1)}$	$42.4_{(0.3)}$	$39.6_{(0.3)}$	$38.1_{(0.4)}$
Avg. change (m)	$-0.2_{(-0.0;-0.9)}$	$-0.2_{(-0.0;-1.3)}$	$-0.2_{(-0.0;-1.5)}$	$-0.2_{(-0.0;-1.7)}$	$-0.5_{(-0.1;-1.2)}$	$-0.5_{(-0.1;-1.5)}$	$-0.6_{(-0.1;-1.7)}$	$-0.6_{(-0.1;-1.9)}$
TEP								
Robustness(%)	$11.1_{(9.2)}$	$8.3_{(6.8)}$	$7.3_{(5.7)}$	$7.1_{(5.3)}$	$9.4_{(8.1)}$	$9.1_{(6.1)}$	$8.7_{(5.3)}$	$8.6_{(5.2)}$
Avg. change (m)	$+0.0_{(+0.0;+0.1)}$	$+0.0_{(+0.0;+0.2)}$	$+0.0_{(+0.0;+0.3)}$	$+0.0_{(+0.0;+0.3)}$	$+0.1_{(+0.0;+0.3)}$	$+0.1_{(+0.0;+0.4)}$	$+0.1_{(+0.0;+0.4)}$	$+0.1_{(+0.0;+0.5)}$
TSP								
Robustness(%)	$24.0_{(1.0)}$	$20.7_{(1.0)}$	$19.8_{(1.3)}$	$19.5_{(1.6)}$	$30.6_{(0.2)}$	$27.2_{(0.5)}$	$25.9_{(0.8)}$	$25.5_{(0.7)}$
Avg. change (m)	$-0.2_{(-0.0;-0.6)}$	$-0.2_{(-0.0;-0.9)}$	$-0.2_{(-0.0;-1.1)}$	$-0.2_{(-0.0;-1.2)}$	$-0.2_{(-0.0;-0.6)}$	$-0.3_{(-0.0;-0.9)}$	$-0.3_{(-0.0;-1.1)}$	$-0.4_{(-0.1;-1.2)}$
ETNA								
Robustness(%)	$18.4_{(1.7)}$	$13.4_{(2.2)}$	$11.7_{(2.1)}$	$10.7_{(1.9)}$	$25.3_{(1.6)}$	$17.6_{(2.1)}$	$14.7_{(2.4)}$	$12.8_{(2.2)}$
Avg. change (m)	$-0.3_{(-0.0;-0.9)}$	$-0.2_{(-0.0;-1.1)}$	$-0.2_{(-0.0;-1.2)}$	$-0.2_{(-0.1;-1.4)}$	$-0.3_{(-0.1;-1.0)}$	$-0.3_{(-0.0;-1.2)}$	$-0.3_{(-0.1;-1.4)}$	$-0.2_{(-0.0;-1.5)}$
TNA								
Robustness(%)	$25.0_{(2.5)}$	$22.2_{(2.9)}$	$20.7_{(3.0)}$	$21.0_{(2.9)}$	$37.7_{(0.6)}$	$31.4_{(1.0)}$	$29.3_{(0.9)}$	$28.5_{(0.8)}$
Avg. change (m)	$-0.1_{(-0.0;-0.4)}$	$-0.0_{(-0.0;-0.6)}$	$-0.0_{(-0.0;-0.8)}$	$-0.0_{(-0.0;-0.8)}$	$-0.3_{(-0.0;-1.0)}$	$-0.4_{(-0.0;-1.4)}$	$-0.4_{(-0.0;-1.7)}$	$-0.4_{(-0.0;-2.0)}$
TSA								
Robustness(%)	$15.4_{(13.2)}$	$15.5_{(12.4)}$	$15.2_{(11.7)}$	$14.6_{(11.2)}$	$10.2_{(8.3)}$	$10.4_{(8.1)}$	$10.2_{(8.1)}$	$10.1_{(8.1)}$
Avg. change (m)	$+0.0_{(+0.0;+0.2)}$	$+0.1_{(+0.0;+0.4)}$	$+0.1_{(+0.0;+0.5)}$	$+0.1_{(+0.0;+0.5)}$	$+0.0_{(+0.0;+0.2)}$	$+0.1_{(+0.0;+0.3)}$	$+0.1_{(+0.0;+0.4)}$	$+0.1_{(+0.0;+0.4)}$
TNI								
Robustness(%)	$12.5_{(3.4)}$	$11.3_{(5.8)}$	$10.6_{(5.9)}$	$11.3_{(6.9)}$	$15.8_{(3.4)}$	$10.7_{(4.2)}$	$8.8_{(4.1)}$	$8.5_{(4.6)}$
Avg. change (m)	$+0.0_{(+0.0;+0.3)}$	$+0.0_{(+0.0;+0.4)}$	$+0.1_{(+0.0;+0.5)}$	$+0.1_{(+0.0;+0.6)}$	$+0.0_{(+0.0;+0.5)}$	$+0.1_{(+0.0;+0.7)}$	$+0.2_{(+0.0;+0.8)}$	$+0.2_{(+0.0;+0.9)}$
TSWI								
Robustness(%)	$15.1_{(4.8)}$	$16.3_{(7.2)}$	$15.8_{(6.8)}$	$15.9_{(6.9)}$	$24.3_{(2.0)}$	$21.9_{(2.5)}$	$20.5_{(2.7)}$	$20.1_{(3.2)}$
Avg. change (m)	$-0.0_{(-0.0;-0.5)}$	$-0.0_{(-0.0;-0.8)}$	$-0.0_{(-0.0;-0.9)}$	$-0.1_{(-0.0;-1.1)}$	$-0.1_{(-0.0;-0.6)}$	$-0.1_{(-0.0;-1.0)}$	$-0.2_{(-0.0;-1.2)}$	$-0.2_{(-0.0;-1.3)}$
TSEI								
Robustness(%)	$19.7_{(15.4)}$	$18.8_{(14.0)}$	$19.2_{(14.3)}$	$19.1_{(14.0)}$	$20.6_{(14.6)}$	$27.3_{(21.0)}$	$27.6_{(22.0)}$	$28.4_{(22.9)}$
Avg. change (m)	$+0.1_{(+0.0;+0.6)}$	$+0.2_{(+0.0;+0.9)}$	$+0.3_{(+0.0;+1.2)}$	$+0.3_{(+0.0;+1.3)}$	$+0.1_{(+0.0;+0.5)}$	$+0.2_{(+0.0;+0.9)}$	$+0.3_{(+0.1;+1.1)}$	$+0.4_{(+0.1;+1.3)}$
SO								
Robustness(%)	$25.3_{(23.6)}$	$20.2_{(18.2)}$	$18.2_{(16.2)}$	$17.1_{(15.0)}$	$41.4_{(39.7)}$	$34.3_{(32.5)}$	$30.9_{(29.2)}$	$28.8_{(27.0)}$
Avg. change (m)	$+0.3_{(+0.0;+1.0)}$	$+0.4_{(+0.1;+1.3)}$	$+0.5_{(+0.1;+1.5)}$	$+0.5_{(+0.1;+1.7)}$	$+0.6_{(+0.1;+1.7)}$	$+0.8_{(+0.1;+2.2)}$	$+0.9_{(+0.1;+2.5)}$	$+0.9_{(+0.1;+2.8)}$

maximum wave height and sensitive differences between members (Fig. 5.8). Nevertheless, the applied BC helps to correct the magnitude in these areas, providing more accurate results. Concerning the model performance, the AD test statistic evidences a poor fit of TC-induced extremes to the Gumbel distribution in these regions as expected from the analysis of the GEVD shape parameter (Fig. 5.2).

In spite of these issues, the Pacific Ocean shows a consistent tropical decrease except for the eastern part, where a highly uncertain increase can be observed (<10% of TEP show robust changes). TNP shows a negative change (42%; 0.5 m) consistent with the projected decrease in low-to-mid latitude winds (Casas-Prat et al., 2018) in the Pacific most likely caused by the poleward shift expected for the northern storm track (Lemos et al., 2019), becoming the region with the highest robustness among the eleven analyzed. This projected decrease implies a correlative increase in the return period of present-day H_s^{20} by the end of the century, which exceeds 50 years in a notable proportion of the region (45%) (Fig. 5.7b). Similarly, the strong decrease found in TSP (27%; 0.3 m) may be as well explained by the poleward displacement of the southern storm track. Nevertheless, note that the westernmost part of both regions, the areas most affected by intense TCs in the models (Fig. 5.8), show great uncertainty and a heterogeneous change pattern, precluding a consistent conclusion about the projected changes. TNA (31%) is mostly characterized by a decreasing pattern with an average change of 0.4 m, which agrees with the robust decrease found by Meucci et al. (2020) for 100-yr return period H_s. The low ability of the models to reproduce the TC activity areas makes it very difficult to reach a consistent conclusion about the cause of the obtained projected changes. For example, the projected decrease found in the tropical northwestern Atlantic may be caused by the decrease in low-intense TCs or, more likely, by a westward extension of the negative change induced by the projected decrease in northern mid to low latitude winds (Casas-Prat et al., 2018; Lemos et al., 2019) observed between 30°W and 50°W. Consistently with the Pacific basin, the westernmost part of the region affected by intense TCs shows great uncertainty in the projected changes. However, a homogenous increase can be observed around Florida that agrees with the expected increase in wind speed of major TCs in the Atlantic Ocean (Patricola and Wehner, 2018). In the tropical south region, however, a weak increase in extreme waves is obtained (10%; +0.1 m). The change pattern in the tropical Indian Ocean is characterized by a dipole behavior in the southern region so that while a decrease is expected on the west (22%; 0.1 m), the sign of change on the east turns out to be the opposite (27%; +0.2 m). The latter implies that the extreme waves that at present reach the western coast of Australia on average once every 20 years, by 2100 would do it with a return period lower than 15 years (Fig. 5.7b). Contrarily to the Pacific and Atlantic basins, the tropical north Indian Ocean shows great uncertainty (11%).

Projected changes in H_s^{20} under RCP4.5 scenario (Fig. 5.9 b) show an overall great similarity in the spatial change pattern (same sign of change in every region) and higher uncertainty (proportion of the global ocean with a robust projected change reduces from 28% to 18%) with respect to RCP8.5. The most notable variations in the magnitude of the average change are observed in SO (from +0.8 to +0.4 m), TNP (from 0.5 to 0.2 m) and TNA (from 0.4 to 0.0 m) regions. Note that the latter case is caused by the projected increase found around Florida, which far from reducing the robustness and magnitude of the changes found for RCP8.5 scenario, show an increase in both features regardless the analyzed return level.

Despite the future changes in mean wave height have been assessed in several studies (Hemer et al., 2013a; Mori et al., 2013; Morim et al., 2018), the differences between the expected behavior of mean and extreme wave conditions with a low occurrence rate under

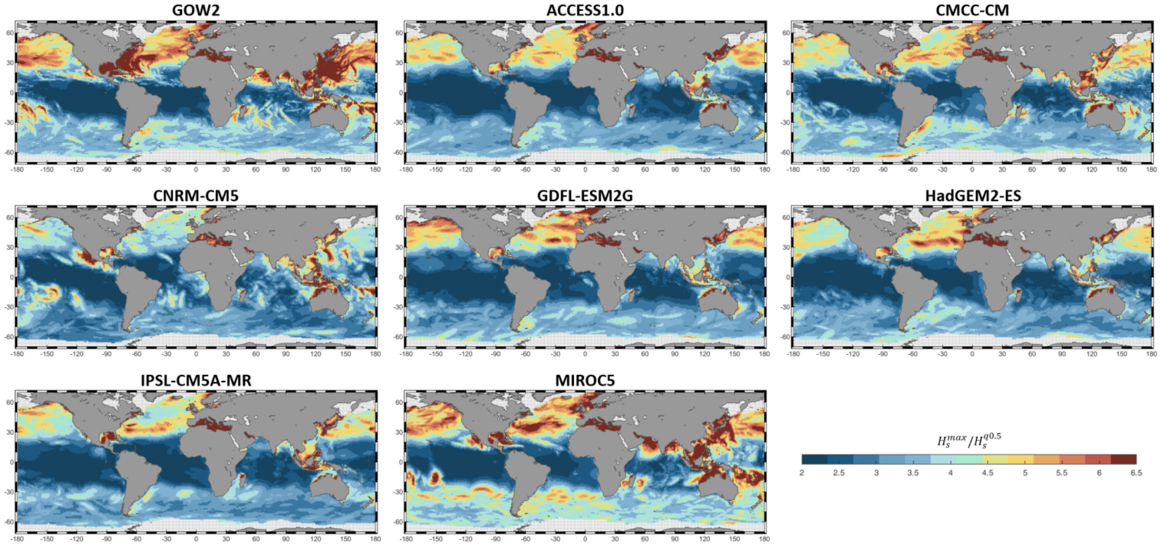

Fig. 5.8 Relation between the maximum H_s (H_s^{max}) and the median H_s ($H_s^{q0.5}$) before correcting the bias for GOW2 and each GCM.

climate change scenarios is still unclear. In this regard, it is essential to determine whether future changes in wave extremes have the same spatial pattern as those from mean conditions, likely indicating a shift of the probability distribution that is affecting the tails in a similar way, or if there exist other causes that may be the source of the discrepancies between both behaviors (e.g., specific changes in intense circulation patterns where internal feedbacks of the climate system are the main drivers). Therefore, in order to evaluate the similarities and differences between the future behavior of mean and extreme wave conditions, we compare the projected relative changes in annual mean (H_s^m) and H_s^{20} under RCP8.5 (Fig. 5.10) and RCP4.5 (Fig. 5.11) scenarios. We assess the agreement in the sign of change between changes in mean and extreme H_s (blue, green, yellow and red colors of Fig. 5.10), ranking variations as low or large by comparison with the global median (one or two arrows in Fig. 5.10). The combined uncertainty of the changes is also analyzed (stippling denotes robust changes in both H_s^m and H_s^{20}).

Although an overall agreement in the sign of change under RCP8.5 scenario is found (blue and red in Fig. 5.10), relevant differences in the spatial change pattern (yellow and green in Fig. 5.10) and in the uncertainty assessment can also be observed. There is a general expected decrease in H_s^m in the whole NH (Fig. 5.12), being the North Atlantic and northwestern Pacific the regions that, in line with the existent consensus (Hemer et al., 2013a; Morim et al., 2018; Oppenheimer et al., 2019), present the most robust projected changes. This robust decreasing uniformity found for mean conditions is not met for extremes since certain areas located in the Atlantic (e.g., east coast of North America), Pacific (e.g., northeastern region) and Indian oceans show the opposite sign of change (i.e., increase), accompanied, in many

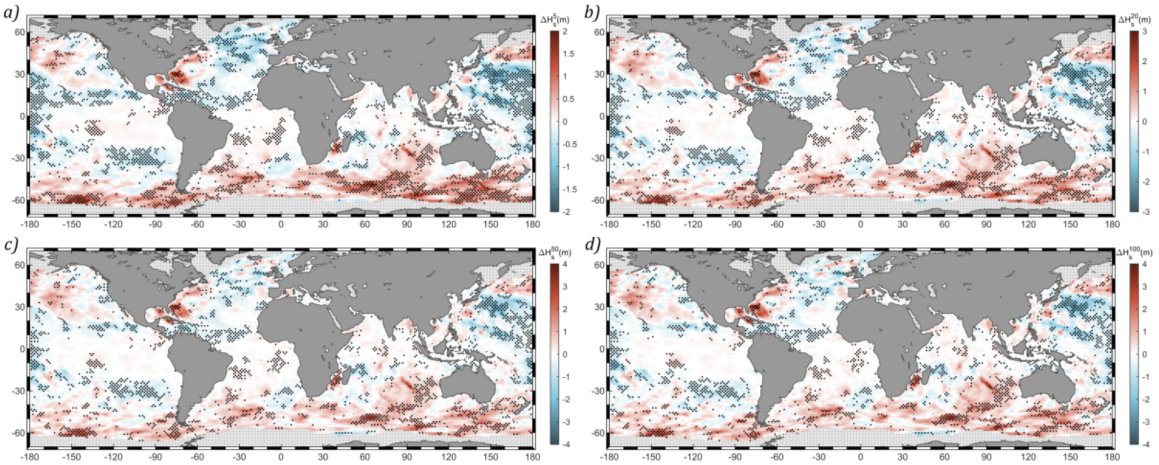

Fig. 5.9 Multi-model ensemble mean change (m) in (a) H_s^5, (b) H_s^{20}, (c) H_s^{50} and (d) H_s^{100} under RCP4.5 scenario by the end of the century. Stippling denotes the same as in Figure 5.5.

cases, by a remarkable increase in the uncertainty. Among all these areas of disagreement in the sign of change, the northeastern Pacific stands out due to the robustness and the high magnitude of the obtained changes (darkest yellow colors in Fig. 5.10). In addition, it is especially noteworthy the great uncertainty and heterogeneous pattern found in the northernmost Atlantic for extremes, likely corroborating a different cause for the expected changes than only a direct shift of the distribution.

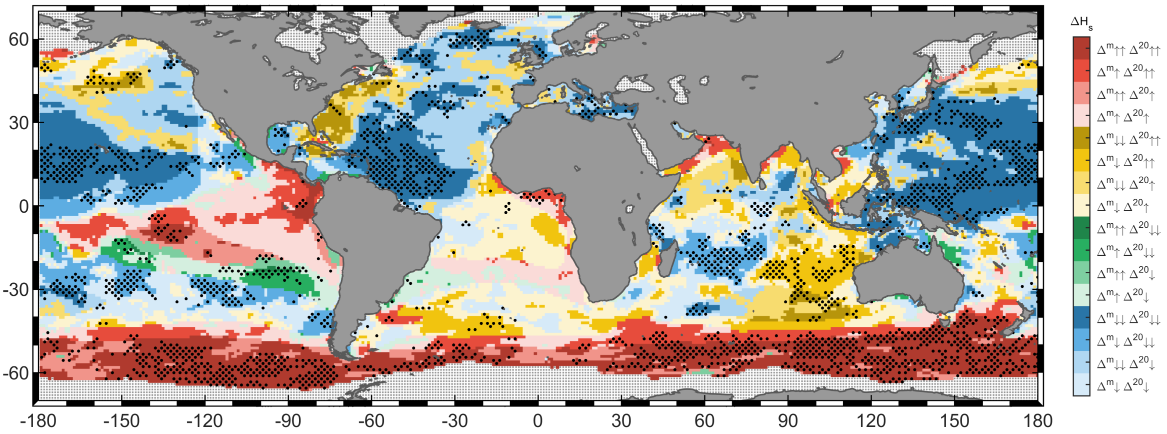

Fig. 5.10 Comparison between projected changes in mean (Δ^m) and extreme (Δ^{20}) H_s under RCP8.5 scenario by the end of the century (2081–2100 relative to 1986–2005). Colors represent the combinations of sign of change between mean and extreme wave conditions: red indicates an increase in both conditions, blue represent a decrease in both conditions, yellow represent a decrease in mean and an increase in extreme conditions and green represents an increase in mean and a decrease in extreme conditions. For each combination, one arrow indicates a relative change lower than the global median and two arrows indicate relative changes higher than the global median. The global median is obtained as the median of the relative changes with the same sign as the analyzed variation. Stippling denotes changes statistically significant at 95% confidence level in at least 50% of the members and an agreement in the sign of change in more than 80% of the members for both mean and extreme H_s.

Concerning the SH, projected changes in H_s^m are robust in a high percentage of the region (Fig. 5.12a), which is consistent with previous studies about the expected increase in the Southern Ocean and tropical eastern Pacific (Hemer et al., 2013a; Morim et al., 2018; Oppenheimer et al., 2019). Changes in H_s^{20} are also robust in a great percentage of the Southern Ocean, therefore leading to a strong agreement between extreme and mean conditions. Although a high percentage of the south tropical region shows robust projected changes in H_s^m (60% from 35°S to the equator), the great uncertainty related to extremes causes that only around 13% of the whole region shows robust changes in both conditions. In spite of this, regions such as the tropical south Indian Ocean presents robust future changes in mean and extreme wave height, projecting a decrease in the whole region in H_s^m and a dipole change in H_s^{20} characterized by an increase in the eastern part consistent with previous studies (Meucci et al., 2020). Note that this strong disagreement is observed in the very same area where a robust increase in the GEVD scale parameter is found (Fig. 5.2e). Finally, it is also remarkable how the same wedge-shaped increasing pattern likely caused by the expected intensification of southeasterly trades (Hemer et al., 2013a), appears in the tropical eastern Pacific Ocean for mean and extreme conditions. Nevertheless, a severe increase in the uncertainty for extremes and an amplification for mean waves denoted by the presence of green areas in the southern part can be observed.

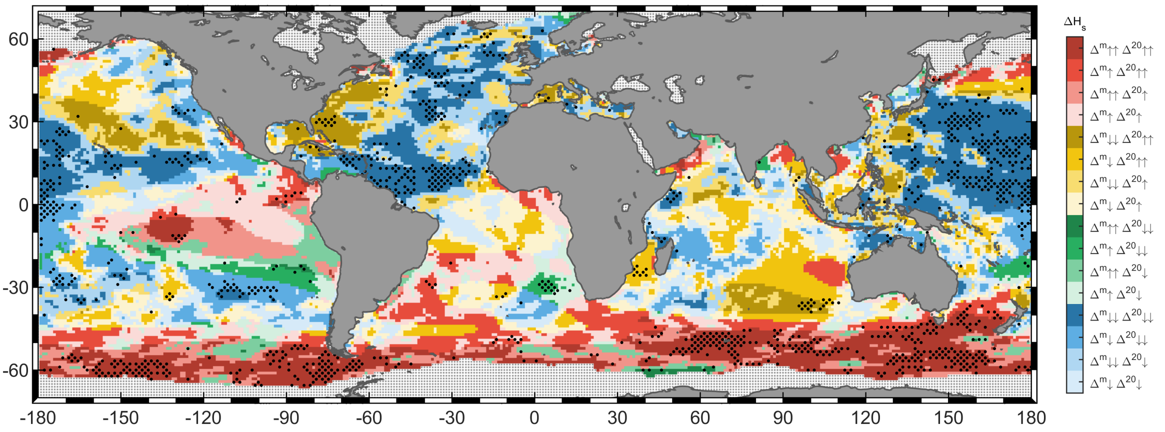

Fig. 5.11 Same as in Figure 5.10 but for RCP4.5 scenario.

The increase in the uncertainty previously seen for changes in H_s return values under RCP4.5 scenario with respect to RCP8.5 also exists for future variations in H_s^m (Fig. 5.12b), reducing the proportion of the global ocean that shows robust changes from 63% to 46%. Hence, this inevitably involves a decrease in the proportion of area in which changes are consistent for H_s^m and H_s^{20} (from 19% to 9%; Fig. 5.11). Nonetheless, the agreement in the sign of change between mean and extreme H_s show a pretty similar spatial pattern as for the RCP8.5 scenario. Most remarkable differences are found in the northeastern Pacific and

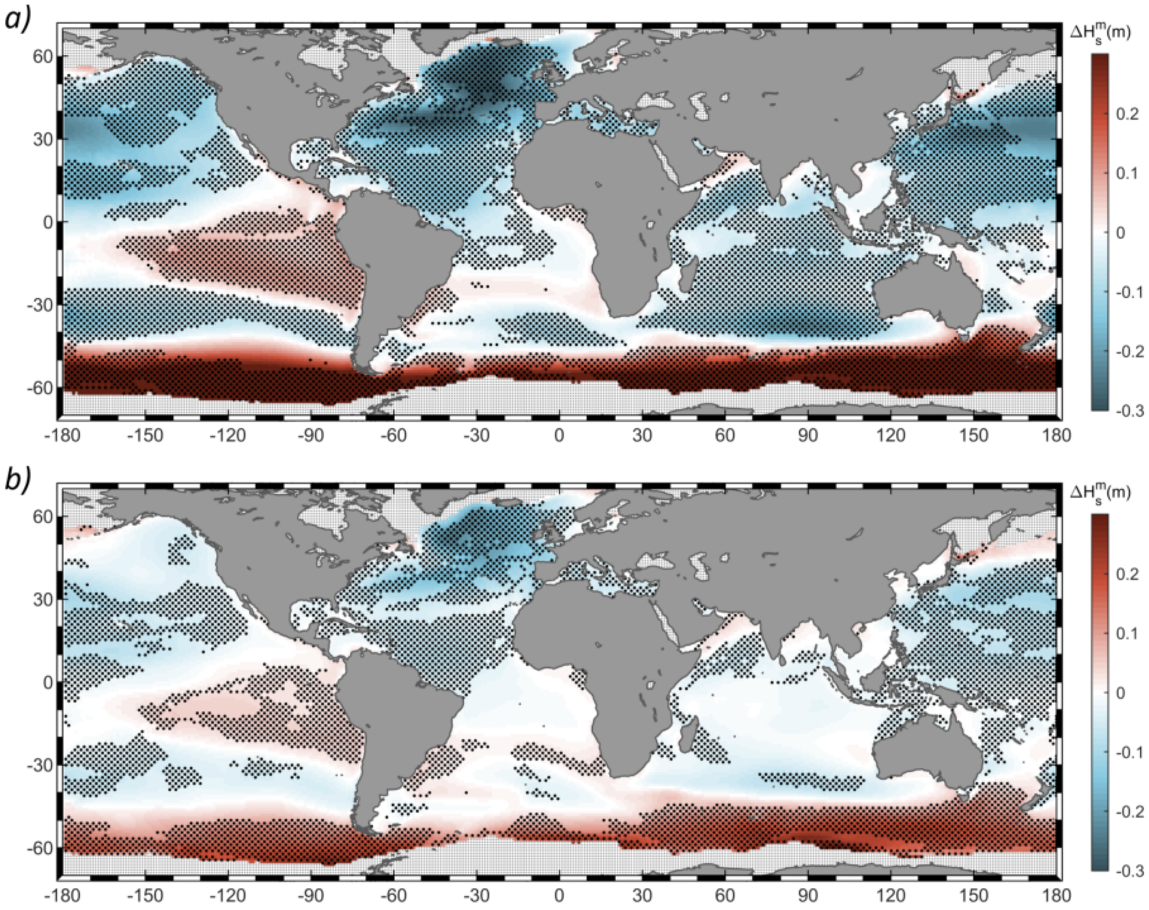

Fig. 5.12 (a) Multi-model ensemble mean change in H_s^m (m) under (a) RCP8.5 scenario and (b) RCP4.5 scenario by the end of the century. Stippling denotes changes statistically significant at 95% confidence level in at least 50% of the members and an agreement in the sign of change in more than 80% of the members.

westernmost north Atlantic, where an amplification of the area showing a projected increase in H_s^{20} and a decrease in H_s^m can be observed.

5.5 Conclusions

There is a consensus among the climate community about the future changes in annual mean H_s due to climate change by the end of the century in several regions around the global ocean (Hemer et al., 2013a; Morim et al., 2018; Oppenheimer et al., 2019). Nonetheless, the future behavior of extreme events with a very low probability of occurrence (i.e., return values) and the similarities and differences with respect to the expected for mean wave conditions are yet to be fully explored. In order to assess projected changes in wind wave extremes, we apply a statistical extreme analysis commonly used in engineering to calculate design return periods. The outcomes evidence that the type I EVD can be used from hourly time series to obtain robust statistics in almost all the global ocean. Only areas directly influenced by TC activity may underestimate extreme wave heights (Fig. 5.2c) as they are characterized by heavy-tailed distributions.

In this study, we assess the projected changes in H_s extreme events for 5-, 20-, 50- and 100-year return periods. The obtained changes and the proposed regionalization (Fig. 5.5a) open the possibility of reaching consistent conclusions on the future regional variability of wave extremes and comparing them with the projected changes in mean wave heights. In this regard, although an overall spatial concordance in the sign of change is observed (approximately two-thirds of the global ocean; Fig. 5.10 and Fig. 5.11), robust discrepancies also emerge in some areas by the end of the century concerning not only this feature, but also the magnitude and uncertainty. Hence, inferring the behavior of wave extremes from projected changes in mean conditions may lead to misinterpretation when used for the assessment of coastal processes or in the design of maritime infrastructures in these areas (e.g., sediment transport depends on $(H_s)^2$; breakwater armor unit weight depends on $(H_s)^3$, design loads of offshore structures depend on H_s^{100}). The possible origin of the projected changes in return values is as well discussed throughout the text, although specific regional analyses are recommended to discern the actual causes and their different contribution.

In addition to the increasing uncertainty found for changes in less frequent extremes (e.g., robustness of changes at global scale reduces from 32% for H_s^5 to 24% for H_s^{100} under RCP8.5 scenario), two general conclusions can be drawn as return periods are higher. First, the proportion of positive changes increases, leading to an increase in the global average change (from 0.5% for H_s^5 to +0.3% for H_s^{100} and from 0.0% to +0.6% for RCP8.5 and RCP4.5, respectively). Second, the magnitude of the observed changes is higher for regions with positive changes.

The Southern Ocean exhibits a consistent increase in H_s return values characterized by an average change up to +0.5 m for RCP4.5 and +0.9 m for RCP8.5 scenarios, showing for the latter local increases larger than 3.5 m for 20-year return period and higher. In the North Atlantic Ocean, although a robust homogeneous decrease can be observed for H_s^m, changes for extremes are characterized by great uncertainty with the sole exception of the decrease found in the tropical northwestern Atlantic. In addition, a low-robust increase is obtained in the westernmost part of the basin (USA and Canadian coasts) and some other European areas. The Pacific Ocean shows a robust general decrease in extreme events in the tropical region. This decreasing signal, however, is not found in the tropical eastern Pacific (the genesis area of the ENSO phenomenon), where projections provide a robust increase in mean conditions and an uncertain rise for extremes. The Indian Ocean shows remarkable differences between projected changes in mean and extreme H_s. These discrepancies are especially relevant in the tropical southeastern region along the west Australian and Indonesian coasts, where the results indicate a robust increase in H_s return values and a decrease in H_s^m.

Changes in extreme events are smaller and less robust for lower concentration scenarios. The robustness of the projected changes reduces from RCP8.5 to RCP4.5 globally around 10% for any of the estimated return periods (e.g., from 25% to 17% for 50-year return period). This fact indicates that future impacts due to both extreme and mean wave height will be conditioned by the strategies taken for reducing GHG emissions.

Projected changes in areas affected by TC activity should be considered carefully as different issues preclude consistent conclusions. First, to this day and in spite of the important efforts done to elucidate the effect of global warming on TCs, there is still no consensus about the expected changes in frequency, intensity and tracks (Patricola and Wehner, 2018). Second, the global resolution of the selected models (Camargo 2013; Table 5.1), among other factors, induce their limited skill in reproducing these storms, which leads to a general underestimation of extreme waves generated by TCs. Finally, the goodness-of-fit analysis show a low-robust fit of the type I EVD in TC activity areas (Fig. 5.3) as they are mostly characterized by heavy-tailed distributions. The above mentioned limitations in addressing this issue have also been observed in previous studies at global scale (Meucci et al., 2020; Wang et al., 2014), evidencing the need for progress in the field of climate projections on TCs, as well as the development of a specific approach to assess the future changes in TC-induced wave climate to obtain more accurate results (Shimura et al., 2017, 2015). For the latter, a regional approach based on synthetic TCs may be a suitable option. In fact, it has already been done for other sea surface dynamics (storm surge) for the present climate around the coastline of Australia (Haigh et al., 2014) or, more recently, for climate change scenarios along US Atlantic and Gulf Coasts (Marsooli et al., 2019).

Future changes in the behavior of wave extremes may have severe implications on maritime shipping and the offshore industry (e.g., gas and oil fields). Although this analysis is out of the scope of the present study, the projected changes obtained here could help to unravel the impact that these variations may have on the said economic activities. Similarly, the changes in extreme wave heights due to climate change may have an important impact in coastal processes due for instance to its direct implication in composing ESLs or in sediment transport. Nevertheless, it is important to highlight that the main goal of this study is to describe how the behavior of events with a very low probability of occurrence will change across the ocean basins, not addressing how to transfer those changes to the coast. Therefore, a downscaling procedure would be required to develop an accurate analysis on the projected changes in wave extremes nearshore.

Part III

The use of directional spectra to assess the climate change effect on wave climate

Chapter 6

Added value of directional spectra to assess the future behavior of wave climate

Abstract

Based on a novel approach, present-day and future spectral wind wave conditions in a high-emission scenario from a seven-member wave climate projection ensemble are compared. The spectral analysis at the selected locations aids in understanding the propagation of swell projected changes from the generation areas across the ocean basins. For example, a projected increase in the energy from Southern Ocean swells can be observed in all ocean basins and both hemispheres, which is especially relevant in the west coast of North America due to the penetration of these swells beyond 30°N. Similarly, a consistent decrease in the energy of large northern Atlantic swells is noted close to the equator. This work provides evidence that assessments based on only integrated wave parameters (e.g., H_s and T_m) can mask information about the sign, magnitude, and robustness of the actual wave climate changes due to the offset of positive and negative variations within the spectrum, leading to a significant underestimation of the change associated with certain wave systems.

6.1 Introduction

The sea surface elevation spectrum constitutes the most complete way to describe wind waves as a stochastic process. This spectrum represents the distribution of energy resulting from the contributions of several superimposed waves with different periods and directions that reach a particular location (Holthuijsen, 2007), and it is essential for assessing coastal processes and engineering designs. The distribution and magnitude of the energy within the spectrum provide information about the number of wave systems it contains, as well as their degree of development. Two are the main ways to represent the spectral energy: in terms of the wave frequency (hereinafter known as frequency spectrum) and in terms of wave frequency and wave propagation direction (directional spectrum). The frequency spectrum has been used extensively by fitting observations to parametric spectral forms (e.g., JONSWAP and Pierson-Moskowitz). Directional spectra provide additional information by characterizing how wave energy is spread along directional sectors, enabling us to undertake a more detailed analysis of the wave climatology in a particular location (Espejo et al., 2014; Shimura and Mori, 2019) and to identify the different wave systems reaching it (Portilla-Yandún et al., 2015). More recently, directional spectra have been utilized to develop studies at global scale, assessing the wave climate seasonality through the identification of wave modes and their variations throughout the year (Echevarria et al., 2019), as well as their relation with climate teleconnection patterns (Echevarria et al., 2020).

The prominent role of wind-generated waves in ocean sea surface dynamics (Cavaleri et al., 2012) implies that changes in magnitude, direction, and frequency may have a notable impact on offshore related economic activities (e.g., offshore industry and shipping routes) and in coastal areas, affecting processes such as shoreline erosion (Toimil et al., 2020a) and flooding (Hemer et al., 2012a; Kirezci et al., 2020; Melet et al., 2018). Projected changes in wind-generated waves induced by climate change have thus been widely studied, especially during the last decade (Hemer et al., 2013a; Mori et al., 2013), to assess both the magnitude of future variations and associated uncertainty (Morim et al., 2019). The numerous studies that have been conducted are usually developed on the outputs of GCM-based wave climate projection ensembles, covering different GHG concentrations scenarios and temporal horizons. General circulation models are characterized by systematic biases caused by factors such as the spatial resolution or the simplifications introduced by the parametrization of physical processes (Maraun et al., 2017), hence also inducing biases in projections of wind waves (Hemer et al., 2012b). Despite BC being usual practice in climatic variables such as precipitation or temperature, its application in wave climate ensembles is relatively recent. In this regard, since its need was demonstrated (Lemos et al., 2020a), BC has been applied in various wave climate studies (Lemos et al., 2020b; Meucci et al., 2020). All these researches apply BC to ensembles of integrated wave parameters, not existing, to the best of our knowledge, any study applying BC to wave spectra.

Despite the wave spectrum fully describes the wind wave climate, almost all the studies on changes in wave climate due to climate change assess the projected variations in representative integrated wave parameters. The reasons behind this simplification lie in the huge storage capacity demanded by directional spectra and the extended use of integrated parameters in multiple formulations related to the design of marine structures and coastal processes.

In particular, the usual approach relates the expected changes in wave climate with future changes in H_s (Fan et al., 2013; Wang et al., 2014), which have led to a consensus about the expected changes in annual and seasonal mean H_s in some regions along the global ocean. In this regard, there exist agreement on an increase in H_s in the Southern Ocean and tropical eastern Pacific and a decrease in the North Atlantic Ocean, northwestern Pacific, and Mediterranean Sea (Morim et al., 2018; Oppenheimer et al., 2019). Nonetheless, a deeper understanding of these future variations needs the study of a wider number of variables, such as period and direction, especially considering the notable role their changes may have in coastal impacts (Harley et al., 2017; van Gent et al., 2008). The assessment of changes in period and direction through parameters such as T_m and Θ_m, is now common practice (Casas-Prat et al., 2018), which offers a closer vision to the expected change in the full wave spectrum. In the same vein, there is an increasing interest in evaluating the effect of climate change in variables that integrate different parameters and provide more complete information about wave climate. For example, E_f (Mentaschi et al., 2017), a variable that integrates wave height and wave period, has been proven to be a valid indicator of global warming (Reguero et al., 2019) and provided robust changes in areas where H_s changes alone have great uncertainty (Lemos et al., 2019). However, none of the described studies provide any information about the projected changes in the different wave systems reaching a certain location.

Based on the above information and to gain a broader understanding of how the global wave climate will be affected by climate change, as well as its consequences for impact assessments, this study attempts to explore the future changes in directional spectra under a high-emission scenario across all ocean regions. We aim to show the added value offered by a novel approach that explore simultaneously the effect of climate change on the energy, period, and direction of the waves, unraveling as well the differences with respect to the standard use of projected integrated wave parameters.

6.2 Climate data

This study makes use of the same seven-member GWP ensemble previously described in Section 5.2. Present-day and future wave conditions are characterized through 20-year time slices (1986–2005 and 2081–2100, respectively). The RCP8.5 GHG concentration scenario is selected to conduct the research. In addition, GOW2 wave hindcast (Perez et al., 2017) is used as reference data for the present-day wave climate, both to analyze the mean wave climatology and to assess the magnitude of the systematic biases in the projections by comparing the annual mean wave spectrum.

The projected changes in directional spectra are analyzed at 14 selected locations according to geographical and physical criteria (Fig. 6.1). Concerning the former, we choose a representative sample of regional wave conditions along the global coast. Thus, six points are selected in the Pacific basin, three along the east coast (P2, P11, and P12) and another three along the west coast (P1, P9, and P10). Six points are also analyzed in the Atlantic basin, three in the west coast (P3, P4, and P13) and three more along the east coast (P5, P6, and P7). Finally, two more points are selected in the Indian basin (P8 and P14). Physical criteria account, first, for a multimodal wave climate at the target locations (Echevarria et al., 2019), i.e., reached by multiple wave systems. Second, the selected locations should be at a distance to the coast higher than 30 km to avoid local diffraction and/or non-linear processes due to propagation in shallow waters.

As a result of the simulations, hourly time series of directional spectra are stored at the target locations (Fig. 6.1), discretized in 32 frequency bins, exponentially distributed from 0.0373 to 0.7159 Hz (i.e., from 1.4 to 26.8 s) and 24 directional sectors of 15° each, i.e., each spectrum is divided into 768 frequency-direction spectral bins (hereinafter spectral bins). Additionally, hourly temporal series of H_s, T_m y Θ_m are stored.

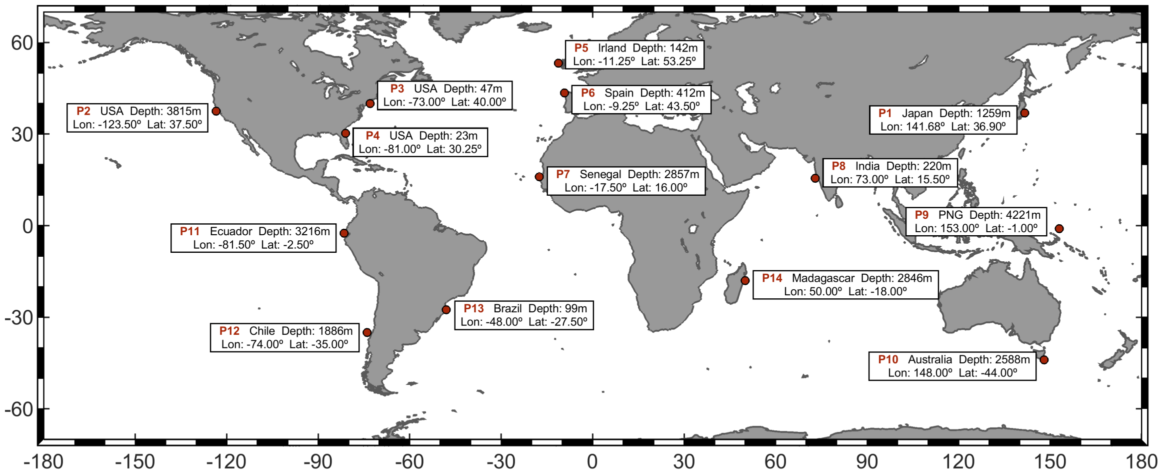

Fig. 6.1 Fourteen target points selected to develop the analysis. For each location, the closest country, coordinates, and depth are displayed.

6.3 Methods

6.3.1 Estimation of Projected Changes

The spectral approach enables the detailed study of future changes in wave energy, providing the variations at each spectral bin. Similarly, it is possible to assess how the bulk of the energy moves along the frequency axis. Nevertheless, an accurate analysis of wave climate spectral changes at each of these locations also requires specific study of local wind conditions and the geometry of the coast to account for reflections. Considering the main purpose of this work, we focus on only the main wave systems that reach the target points, neglecting the small changes related to local wind seas, which represent a very small percentage of the total energy in the spectrum.

The projected change for each GCM is obtained as the difference between the annual mean spectrum of future and present-day wave climate. The ensemble mean change is then calculated as the average of the individual changes for each GCM (Eq. 6.1), i.e., we assume equal contributions from all the ensemble members.

$$\Delta E_{ens} = \frac{\sum\limits_{i=1}^{i=N} E_{fc}^{i} - E_{pc}^{i}}{N_{md}} \tag{6.1}$$

where N_{md} is the number of models, ΔE_{ens} is the projected ensemble mean change, E_{pc}^{i} is the mean wave spectrum for the present climate (1986–2005), and E_{fc}^{i} is the mean wave spectrum for the future climate (2081–2100).

To compute the shift of the mean wave energy along the frequency axis (i.e., to lower or higher periods) for each direction, we calculate the range of periods within which the energy interquartile range is concentrated at present and in the future, and then we determine its shift.

6.3.2 Uncertainty Assessment

The uncertainty of the projected change is assessed based on a method proposed in the AR5 report (Collins et al., 2013; Tebaldi et al., 2011), which consists in the analysis of its significance first and then considering the agreement in the sign of change between the members of the wave climate projection ensemble. Nevertheless, as the number of selected models is notably smaller than in the study defining the method (21 vs. 7), we require a stricter agreement between members to consider the changes to be robust. Namely, more than 80% of the models (6) must present a statistically significant change, and at least 80% of them must agree on the sign of change. The statistical significance is calculated by applying a Welch's t-test to the mean of the reference and future periods at the 95% confidence level. The consideration of an unequal variance t-test lies in the possible shift of the energy along the frequency and direction axes in the future, hence causing a change in the energy variance at each spectral bin with respect to the present-day climate. Spectral bins in which the change is found to be robust are highlighted. Only changes above 1% of the maximum change within the spectrum are highlighted to ease the understanding of the results.

6.4 Results

Prior to the assessment of the projected changes in wind wave directional spectra, we analyze the biases in the developed wave climate projections. As an example, Fig. 6.2 depicts the biases at P7 for all the models considered. Results show that bias increases with latitude, which is consistent with the higher wave energy in the extratropical region. In addition, a heterogeneous pattern can be observed within the spectra, i.e., there coexist positive and negative biases. The reasons behind this behavior can be, first, biases with different sign associated to different wave systems (e.g., see biases for ACCESS1.0 model in Fig. 6.2). Second, biases in the location of the generation areas that induce a frequency-direction mismatch between wave systems from GCMs and the reference hindcast. Ensemble members also show sensitive differences between them. CMCC-CM and MIROC5 are clearly the models that show the lowest biases. On the contrary, IPSL-CM5A-MR and CNRM-CM5 are the models that worst represent present-day climate (i.e., greatest biases). Despite the lack of BC, the low biases found, the fact that not applying BC do not alter the sign of the projected changes (Lemos et al., 2020a) and the comparison of consistent ensemble changes of integrated parameters and wave directional spectra (i.e., from the same models and affected by the same GCM biases), make the obtained results a reliable evidence of the added value offered by the spectral approach.

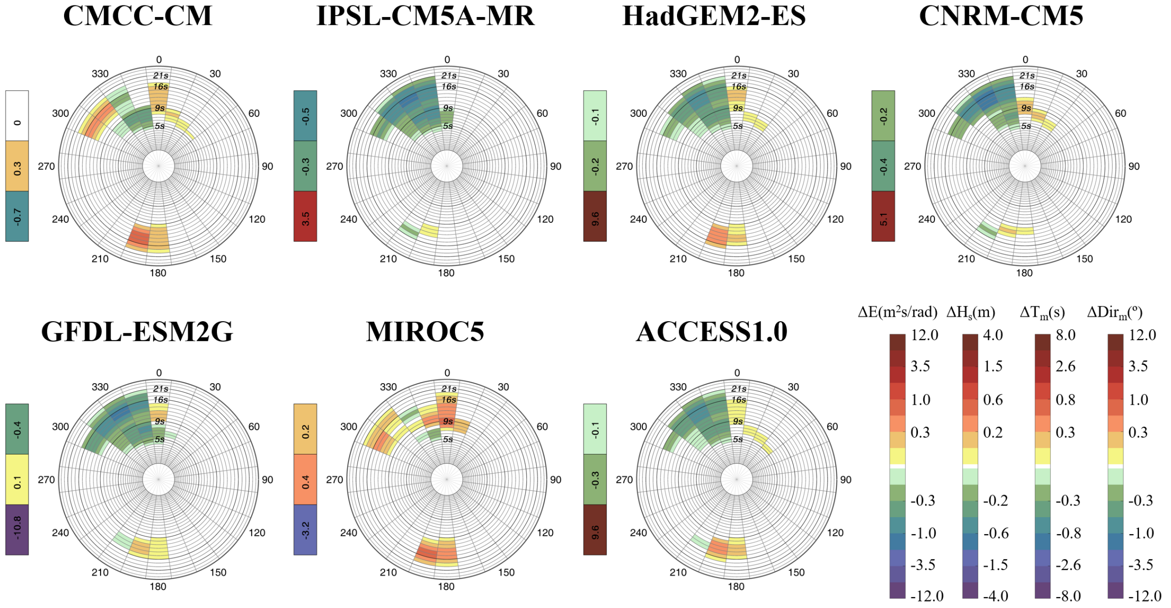

Fig. 6.2 Bias in present-day (1986–2005) annual mean wave climate at P7 using GOW2 hindcast as a reference (GCM-GOW2). Polar plots: bias in annual mean spectral energy. Left boxes (from top to bottom): bias in annual mean H_s, T_m and Θ_m. The color bars used to represent each variable are displayed in the bottom-right part of the panel. From left to right: energy (m^2 s/rad), H_s (m), T_m (s), and Θ_m (°).

Below, we provide a brief description of the present-day wave climate at each location (Fig. 6.3, Fig. 6.4) and the main projected changes by the end of the century under the RCP8.5 scenario (Fig. 6.5). For completeness, the shift in the energy interquartile range for each direction is shown (Fig. 6.6). The information provided by the assessment of the directional spectra that cannot be obtained from integrated wave parameters is highlighted.

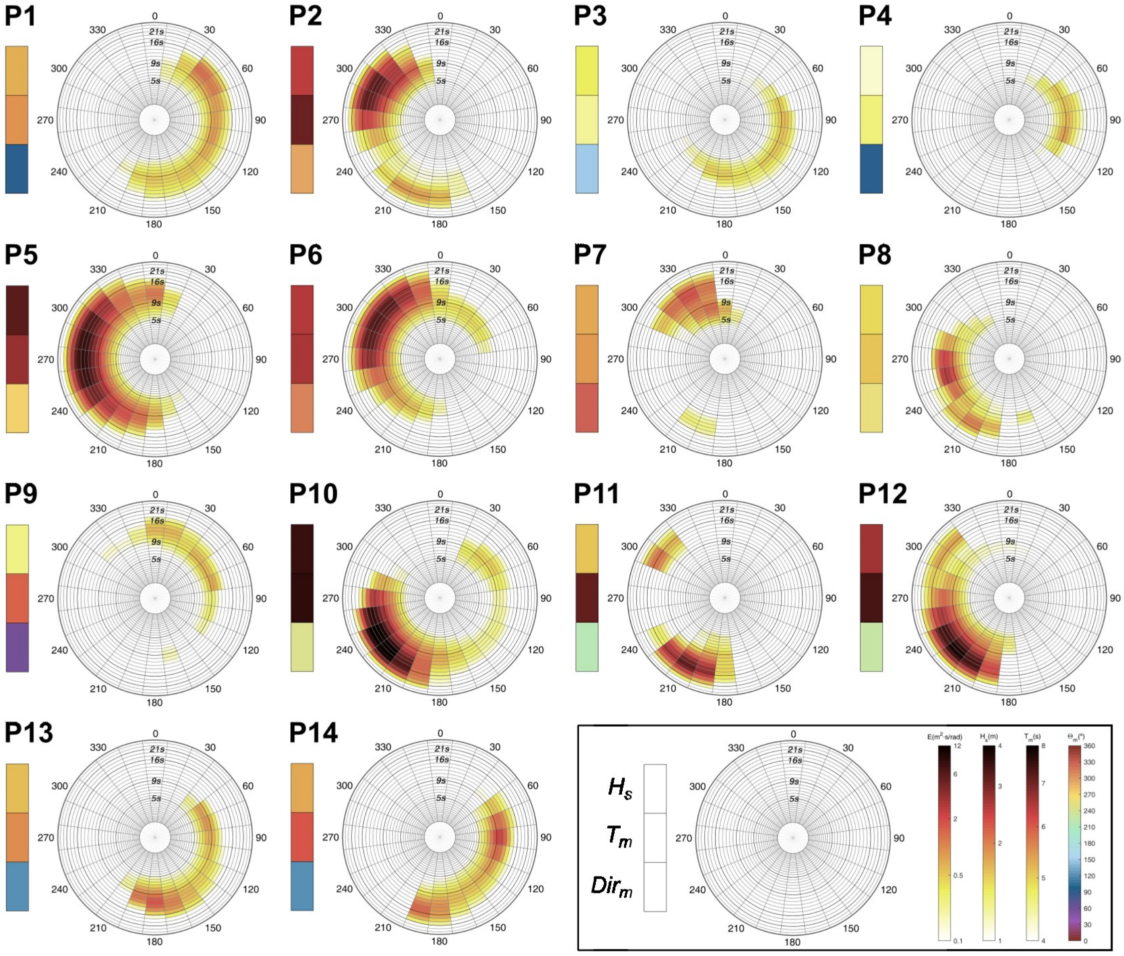

Fig. 6.3 Present-day (1986–2005) mean wave climate at the fourteen analyzed locations from GOW2 hindcast. Polar plots: annual mean spectral energy. Left boxes (from top to bottom): annual mean H_s, T_m and Θ_m. The color bars used to represent each variable are displayed in the bottom-right part of the panel. From left to right: energy (m^2 s/rad), H_s (m), T_m (s), and Θ_m (°).

P5 and P6 are in the northeastern Atlantic on the European coast. Most of the wave energy at these points is carried by swells propagating from the west at P5 and northwest at P6, which are generated under ETCs crossing the northernmost Atlantic Ocean (Camus et al., 2014b; Pérez et al., 2014). These points show the greatest decrease in energy among all the locations analyzed (Fig. 6.5), as well as a shift to lower periods (Fig. 6.6). A closer look at P5 also highlights an expected robust negative change in the low-energetic swells coming from the north and the wind seas from the south. Analogously, the results at P6 also show a future decrease in the wind seas coming from the northeast and southwest. This negative pattern at both points agrees with the expected decrease in H_s and with the results obtained in previous studies regarding projected changes in wave height along the European Atlantic coast (Bricheno and Wolf, 2018). Although P7 is also located in the northeastern Atlantic, its lower latitude (16° north) causes it to not only be affected by swells generated in the NH but also by swells that travel from the SH that cross the equator, especially during austral winter (Semedo et al., 2011) (Fig. 6.4). This point is also reached by wind seas coming from the northeast and northwest with a T_m of approximately 8 s (Fig. 6.3). Therefore, the robust decreases in H_s and T_m integrate the variations in these four wave systems, concealing the nonuniform behavior of the spectral projected changes (i.e., there are spectral bins with both signs of change). Thus, while an increase and displacement to higher periods are expected for swells generated in the SH, a decrease is projected in the energy carried by swells and wind seas from the North Atlantic Ocean, which agrees with the results at P5 and P6.

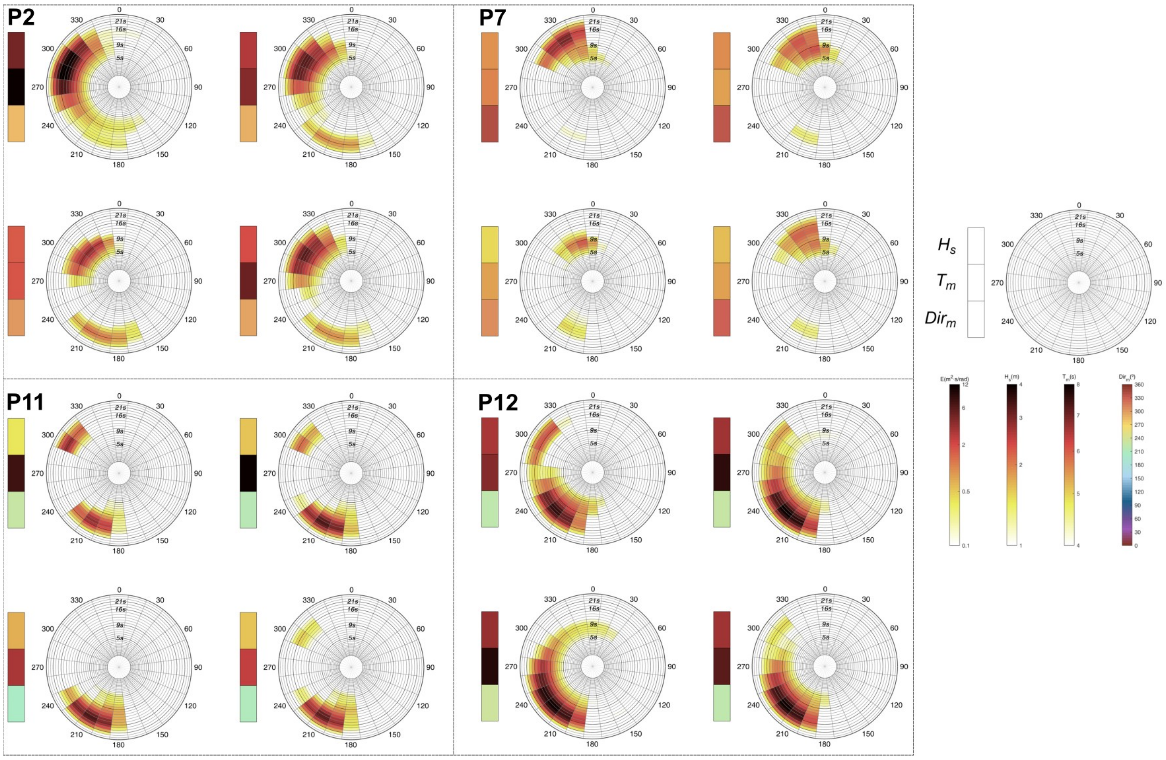

Fig. 6.4 Present-day (1986–2005) seasonal mean wave climate from GOW2 hindcast at P2, P7, P11 and P12: Dec-Jan-Feb (upper left subpannel corner), Mar-Apr-May (upper right subpannel corner), Jun-Jul-Aug (bottom left subpannel corner) and Sep-Oct-Nov (bottom right subpannel corner). Polar plots: annual mean spectral energy. Left boxes (from top to bottom): annual mean H_s, T_m and Θ_m. The color bars used to represent each variable are displayed in the right part of the Figure. From left to right: energy (m^2 s/rad), H_s (m), T_m (s), and Θ_m (°).

The North Atlantic west coast is represented by P3 and P4, which are low energy locations affected by low-period waves. Most of the energy that reaches P4 comes from waves generated by trade winds in the tropical North Atlantic that propagate from the east with a T_m of approximately 9 s. Results show a robust decrease in this energy and a shift to lower periods, agreeing with the projected decreases in H_s and T_m. P3 is mainly affected by swells generated in the tropical-north trade wind region coming from the southeast and two local wind wave systems that propagate from the south and east. Spectral results show a generalized projected decrease and a negligible shift in the energy that is consistent with the decrease expected in H_s and the almost null decrease in T_m. P13 is located on the coast of Brazil in the tropical southwestern Atlantic. The mean wave climate indicates that it is mainly affected by swells generated in the Southern Ocean that propagate from the south, swells generated in the tropical south Atlantic coming from the east and wind waves propagating from a direction of approximately 200°. The projected increase in H_s agrees with the change expected for the energy carried by southern and eastern swells. However, while a displacement of the energy to higher periods is expected for the swells from the Southern Ocean, the opposite is obtained for eastern waves, which likely causes the very low projected change found in T_m.

P2 is located on the west coast of North America, so it is mainly affected by the swells generated by ETCs in the North Pacific. This point is also affected by wind seas coming from the northwest and by mature energetic swells generated in the Southern Ocean that penetrate the NH mostly during austral winter (Semedo et al. 2011; Young 1999; Fig. 6.3). The results show a robust projected increase in southern swells with periods between 14 and 22 s. Nevertheless, a consistent change is not found for the largest swells generated in the northernmost Pacific, as has been found in the Atlantic (i.e., periods above 14 s). Fig. 6.6 displays a notable shift in the southern energy to higher periods and an almost null shift in the north Pacific energy. The integration of all these spectral changes leads to an uncertain decrease in H_s and a very small increase in T_m that mask the important increase expected for long southern swells.

The southeastern Pacific wave climate is studied at locations P11 and P12. The main energy contributors to the total energy at these points are swells generated in the Southern Ocean. Despite their southern latitude, both points still receive a low amount of energy during boreal winter carried by very long swells from the NH (Fig. 6.4); together with P2, this provides evidence of the seasonal displacement of the swell front in the eastern Pacific (Young, 1999). Regarding P11, a dipole change pattern in the energy coming from southern mid-latitudes can be observed, showing a robust increase in the swells generated below approximately 40°S and a consistent decrease in waves from higher latitudes. The shift to higher periods and the large changes expected for the energy carried by the southernmost swells induce a projected increase in H_s and T_m. The results at P12 exhibit the same robust dipole pattern as at P11 and an increase in wind seas propagating from the south. The balance between spectral energy variations with different signs is clearly the cause of the low negative change expected in H_s, which is not reflecting, as it occurs at P2, the notable increase expected for very energetic Southern Ocean swells. Finally, a robust decreasing signal is not found for long swells coming from the NH at P11 and P12, corroborating the results at P2.

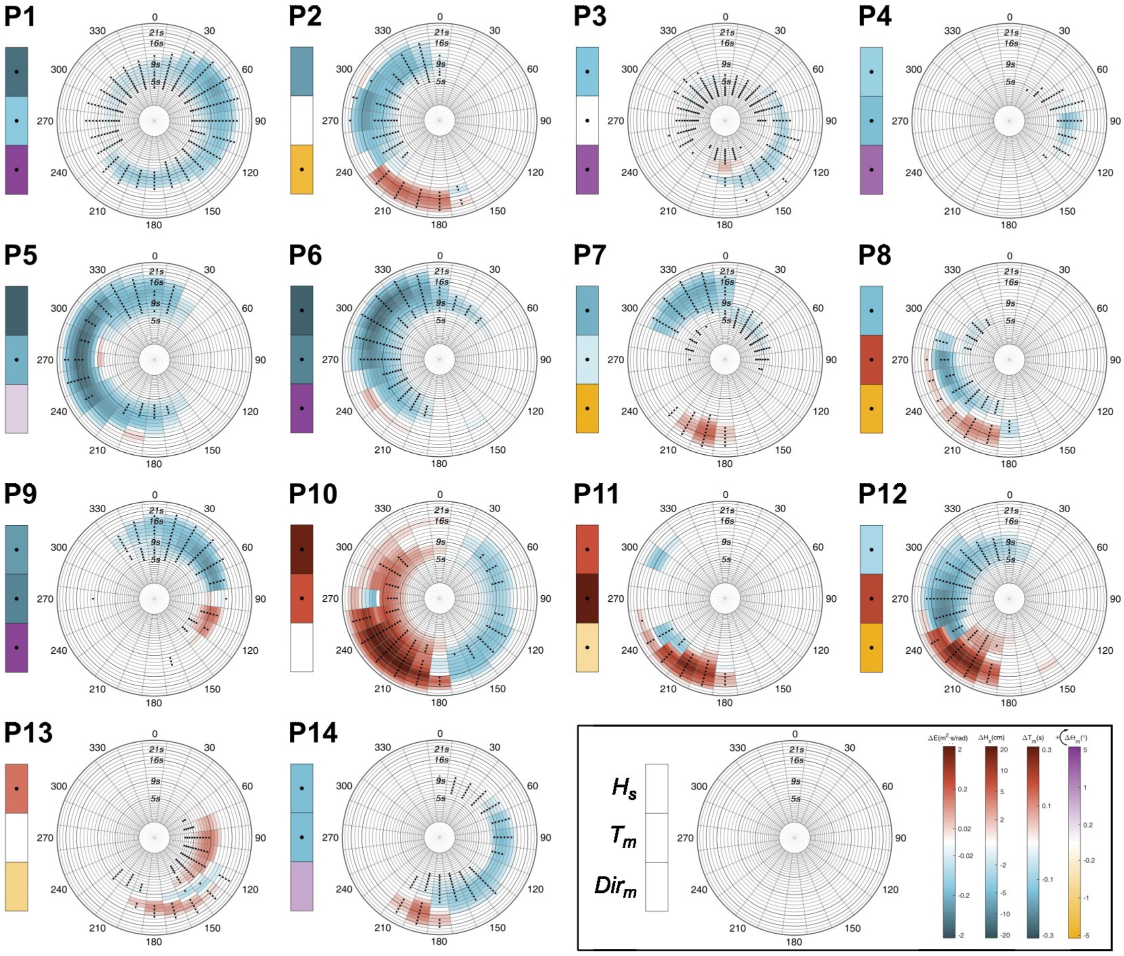

Fig. 6.5 Projected changes at the analyzed locations by the end of the century (2081–2100) under the RCP8.5 scenario with respect to present-day wave climate (1986–2005). Polar plots: multimodel ensemble mean change in annual mean spectral energy. Left boxes (from top to bottom): multimodel ensemble mean changes in annual mean H_s, T_m and Θ_m. Stippling denotes statistically significant change and agreement in the sign of change in at least 80% of the models. The color bars used to represent the change in each variable are displayed in the bottom-right part of the panel. From left to right: energy (m^2 s/rad), H_s (cm), T_m (s) and Θ_m (°).

The northwestern Pacific coast is represented by a point located on the east coast of Japan (P1). This point is affected by the energetic swells generated in the northernmost Pacific, swells coming from the east and swells from the south. The projected spectral changes highlight a robust decrease in energy and a remarkable shift to lower periods that is consistent with the projected negative changes in H_s and T_m. P9 is close to the equator (latitude 1°S) and is sheltered from the Southern Ocean swells due to the presence of Australia and multiple islands. Therefore, most of the energy arriving at this point is carried by the waves originating in the NH, namely swells coming from the north and northeast. However, a swell system generated in the tropical south Pacific propagating from the southeast is still discernible. Regarding the projected changes, an energy increase with a slight shift to higher periods, likely related to the found intensification of southeasterly trades (Timmermann et al., 2010), is expected for southern waves, and in line with the results at P1, a robust decrease with a shift to lower periods can be observed in the wave systems generated in the NH. The preponderant role of northern wave systems induces negative projected changes in H_s and T_m, precluding the possibility of reaching any conclusion about future variations in energy from SH waves. Finally, the southwestern Pacific wave climate is studied at P10, a point located in the Southern Ocean and affected by highly energetic swells generated by southern westerly winds. In addition, it is also reached by swells coming from the southeast and northeast and wind seas coming from the west. Projected spectral changes show a robust dipole pattern characterized by an increase in wave systems with a western component and a decrease in wave systems coming from the eastern directional sectors. Therefore, the consistent increase obtained in H_s involves a great loss of information since it cannot account for the important projected decrease in waves coming from the east. Moreover, Fig. 6.6 shows a shift in energy to higher periods for swells propagating from the southwest and the opposite for waves coming from the east, resulting in a robust projected increase in T_m that masks the existent energy shift to lower periods.

Changes in the wave conditions in the Indian basin are studied at P14 and P8. The mean wave climate shows that P14 is mainly reached by three wave systems: the Southern Ocean swells from the south and the southeast and the tropical-north swells from the northeast. While a robust increase is obtained in swells from the south, a consistent decrease is seen for the other two wave systems. In addition, a shift to lower periods is observed for waves coming from the east, and in agreement with previous locations, a shift to higher periods is observed for the Southern Ocean energy. Although robust decreases in H_s and T_m are obtained, the consideration of changes from integrated parameters prevents the derivation of the clear increase found for southern swells. Regarding P8, although it is located in tropical northern Indian, it is still affected by swells generated in the Southern Ocean that travel beyond the equator. This point also receives waves generated in the tropical Indian Ocean propagating from the west that are especially strong during the summer monsoon season (Portilla-Yandún, 2018) and wind waves from the northwest. A projected uncertain decrease is observed for tropical swells with no clear energy shift. By contrast, a robust increase in the energy carried by swells generated in the Southern Ocean with a shift to higher periods is found. Integrated wave parameters indicate a consistent decrease in H_s, which conceals the change in southern swells, as seen at P14.

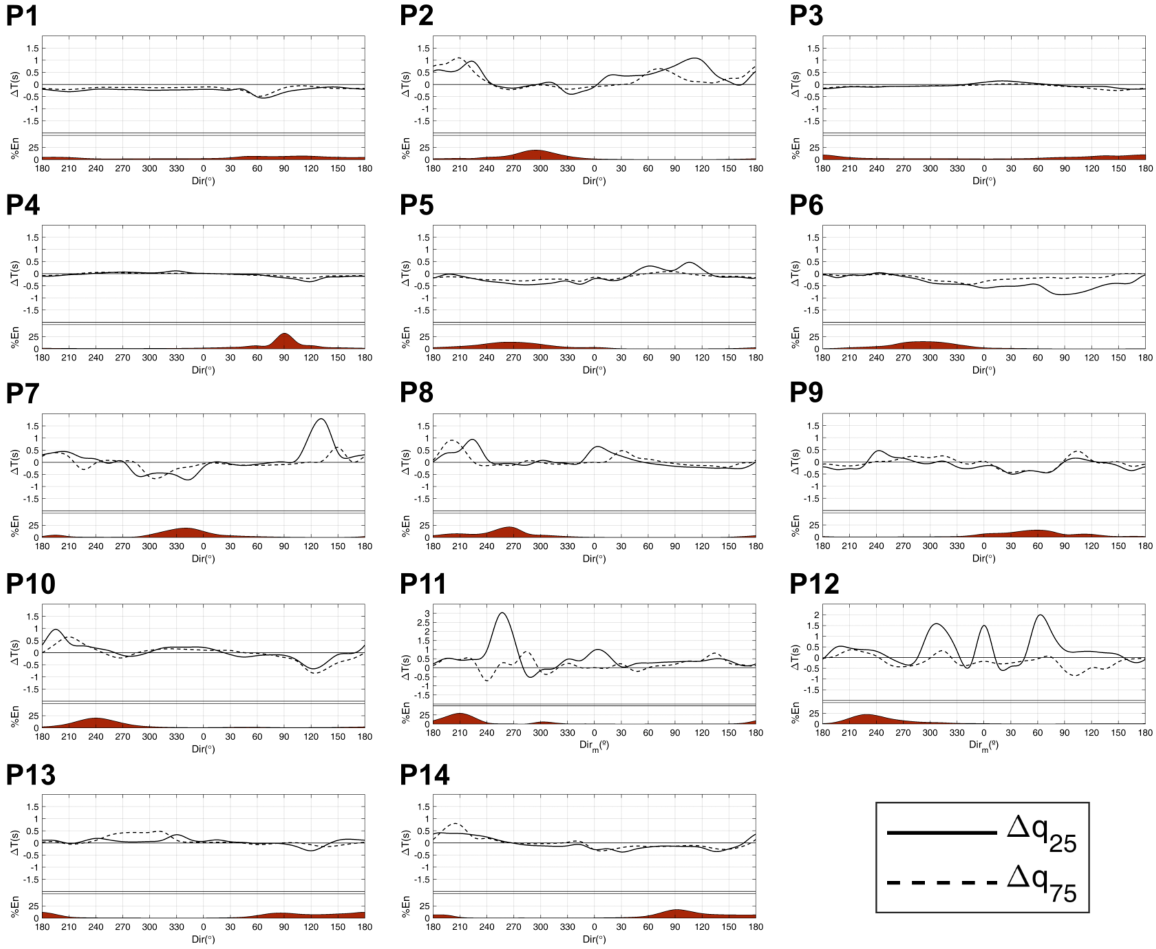

Fig. 6.6 Shift in the energy interquartile range between the present (1986–2005) and the end of the century (2086–2100) under RCP8.5 scenario. For each panel: shift in seconds of the quantile 0.25 (solid line) and the quantile 0.75 (dashed line) of the energy for each direction. Percentage of energy coming from each direction (in red).

The assessment of the projected changes at each location independently provides us a global overview of the spectral changes and allows us to draw some conclusions about the future behavior of energetic swells (large-period swells) along the global coastlines. Results evidence a robust increase in the energy carried by swells generated by ETC activity in the Southern Ocean below approximately 40°S that can be observed at points located in the Southern Pacific (e.g., P11 and P12), Atlantic (P13), and Indian basins (P14). Similarly, the propagation of these swells beyond the equator makes it feasible to note this consistent increase in northern locations, such as on the west coast of North America, Senegal, and India (P2, P7, and P8, respectively). This positive change may be related to the increase in energy transferred to the ocean surface due to the expected intensification of surface westerly winds in the roaring forties and furious fifties regions (Swart and Fyfe, 2012) and could also be favored by the fetch increase caused by the expected reduction in ice coverage in high latitudes (Thomson and Rogers, 2014). Regarding changes in northern energetic swells, a clear decrease in the energy carried by swells generated by ETCs in the northernmost Atlantic can be observed at points located in Europe (P5 and P6) and with a lower magnitude along the tropical coast of Africa (P7). Nonetheless, a robust change cannot be found in the energetic swells (periods above 14 s) coming from the northernmost Pacific on the coast of North America (P2) or at points located in the SH that still receive northern mature swells during boreal winter (P11 and P12).

6.5 Conclusions

The assessment of projected wave climate changes from directional spectra provides information that cannot be obtained from the commonly used method based on integrated wave parameters. While the spectral approach allows us to separately analyze the sign and magnitude of change from different swells and seas that reach a certain location, the consideration of changes from integrated wave parameters necessarily overlooks the existence of positive and negative variations within the spectrum. Similarly, the analysis of wave climate changes following the standard approach may entail an underestimation of the actual changes due to the integration of variations with opposite sign from different wave systems. The results on the coast of Chile (P12; Fig. 6.5) are clear evidence for this statement. Notwithstanding that the projected change from integrated parameters indicates a low decrease in H_s, future changes from directional spectra show a clear dipole change pattern characterized by positive and negative variations with a high magnitude (increase for southwestern swells and decrease for western swells). This issue can also be seen in other locations, such as the west coast of North America (P2) and southwestern Indian (P14).

Moreover, the uncertainty assessment of the projected changes denotes that the spectral analysis can provide consistent results for some of the wave systems that integrate the spectrum, even when the projected changes from integrated wave parameters exhibit a lack of robustness. This can be observed at points in both the Pacific (P2) and Atlantic (P5) basins. In this regard, although changes in H_s are not robust in the northwestern Pacific coast, spectral changes indicate that the future variations in large swells propagating from the Southern Ocean at P2 are still robust. Similarly, a strong conclusion about the future behavior of northern swells and southern seas can be derived at P5 on the British coast from the spectral approach despite the great uncertainty associated with the change in H_s.

The spectral analysis also shows a misleading climate change signal from T_m. Again, there can be an offset of variations with opposite sign that can drive a deceptive change, making it unfeasible to observe the existence of negative and positive variations and more importantly, to see the actual magnitude of the projected change associated to each wave system. From the number of locations analyzed, a clear increase in periods in the Southern Ocean energetic swells can be seen. Nevertheless, the assessment from integrated parameters masks this projected increase when these swells are not the main energy contributor at the location of analysis. The points located in the tropical eastern Atlantic (P7) and southeastern Pacific (P12) are two examples of this issue.

The use of integrated wave parameters can have severe implications in locations where an increase and shift in the energy carried by recurrent wave systems to higher periods are masked. In other words, although a decrease can be projected for integrated parameters, such as T_m or H_s, the spectral approach can show a notable increase in wave systems periodically reaching a certain location. Separately assessing the projected changes in the most severe wave systems that reach the coast, especially at coastal stretches affected by a multimodal wave climate, can help to more accurately determine the impacts derived from changes in wave conditions in view of the significant influence that wave period and direction have on coastal processes.

The present study is developed without correcting the existing systematic bias of the wave climate projections (Fig. 6.2). In this regard, despite BC has recently been shown to be optimal to obtain more accurate projected changes in integrated wave parameters (Lemos et al., 2020a), its application to directional spectra is yet to be addressed. Furthermore, the way of application of BC to integrated wave parameters (e.g., quantile mapping) cannot be directly extrapolated to directional spectra. As previously seen, future changes do not only apply to the energy magnitude within the spectrum, since shifts along the frequency and direction axes may also occur. The energy in a certain spectral bin at present could move to another one in the future, therefore, introducing an important error if we correct the bias equally in both time periods. In addition, the bias assessment indicates a heterogeneous bias pattern within the spectrum for some locations (e.g., P7 and P10), precluding a proportional correction based on the comparison of an integrated parameter such as the total energy. Therefore, further research is needed to raise a BC technique applicable to spectra that accounts for the described issues and helps to provide more accurate changes.

We consider that the results presented in this study offer a clear vision of the potential contribution of directional spectra within the understanding of wave climate projected changes and their implications, which is evidence of a misleading climate change signal in some cases according to the standard approach based on integrated wave parameters. These insights, together with the technological progress that boosts storage in larger databases, encourage the development of deeper studies that are not constrained to a limited number of locations and the annual mean climate, opening the door to a much more advanced comprehension of the future behavior of wind waves in entire regions.

Chapter 7

Climate change effect on wave climate from directional spectra

Abstract

Through assessment of wind wave directional spectra, we provide a comprehensive explanation of the projected 21st Century changes in the global wind wave climatology under a high green-house emissions scenario. Using a seven-member wave climate projection ensemble, we estimate wave climate changes by comparing present and projected climatologies. Clustering techniques are applied to define regional patterns of change with homogeneous behavior. The underlying mechanisms behind the changes are also explored by exploiting the relationship between the wave generation area and the effective energy flux propagating toward a target location. A robust transition from positive to negative trends in Southern Ocean westerly swells is observed around 45°S. The increasing signal found in the southernmost swells propagates north beyond 30°N, contributing significantly to the projected changes in tropical regions such as the tropical southern Atlantic and tropical southeastern Pacific. Results highlight the great complexity of the Pacific Ocean due to the convergence of multiple wave systems with different geneses. In the northern basins, the combined effect of the ice melting and a poleward shift of the storm track drives an increase of the northernmost westerly swells. This is countered by a decreasing trend projected in the main wave systems propagating in the North Atlantic Ocean. A poleward shift of trade-induced waves due to the Hadley cell expansion can also be observed globally, causing a clear dipole change pattern in the tropical South Atlantic and tropical Indian oceans.

7.1 Introduction

Wind waves are a key feature of the sea surface, with several co-existing wave trains of differing characteristics superimposed. At any point on the ocean surface, the wave climate is fully described as a stochastic process by the sea surface elevation spectrum. The spectral density variance captures contributions of superimposed wave fields characterized by different wave heights, periods and direction, depending on their relative point of origin. The variance spectrum, usually referred to as the energy spectrum as both variables are directly related (Holthuijsen, 2007), integrates the information about the genesis of the waves arriving at a specific location. In this regard, the shape, size and location of the peak from each local energy maximum within the spectrum relate to the geographical wave origin, maturity and amount of transported energy (Jiang and Mu, 2019). Despite the directional spectrum being the most comprehensive way to describe the wave climate, it is common practice to use integrated wave parameters instead (e.g., H_s, T_m). The integrated wave parameters are defined from the sea surface elevation spectrum to provide an average representation of the wave conditions. Therefore, its definition implies the loss of information about the multimodality of the sea state (i.e., number of wave systems propagating at the same time) and the actual relation between the different variables included in the spectrum (i.e., energy, period and direction). The inclusion of wave climate information in coastal engineering formulations such as in coastal structure design or in coastal processes modeling (e.g., Usace, 1984) is typically captured through integrated parameters, but this can lead to an over-simplification of the wave field as it was explained in Chapter 6.

The use of directional spectra to develop climate studies is still limited. The availability of full spectra from real measurements is both recent and scarce. There is a growing but still low number of spectral buoys available with a heterogeneous spatial coverage, precluding development of large-scale studies. In the same vein, satellite altimetry is yet progressing on providing a global database of wave spectra. Therefore, the use of directional spectra is mainly limited to the products of numerical simulations and conditioned by the relatively high data storage requirements for high frequency (e.g., hourly) spectra. Typically, discrete wave-model spectra store of order 500–1000 values per archived time-step, which is a significant cost relative to storing several integrated parameters at the same temporal frequency. The great complexity inherent to its multidimensionality is a further reason behind the low usage of full spectral information. However, the analysis of directional spectra has already led to a very detailed description of the wave climate in some regions, such as the North Sea (Boukhanovsky et al., 2007), the coast of Spain (Espejo et al., 2014) or the coast of Japan (Shimura and Mori, 2019). More recently, the wave spectral modality has been assessed at global scale, also determining its seasonality (Echevarria et al., 2019). Furthermore, the relation between these wave modes and different teleconnection patterns can also be analyzed, shedding light on the drivers of the inter-annual wave variability (Echevarria et al., 2020). In addition, as the directional spectrum contains information about the convergent wave systems, different methods have been proposed to isolate each of them (Portilla et al., 2009). Then, the derived product can be statistically analyzed (Portilla-Yandún et al., 2019, 2015) to determine the frequency, age and wave height associated to each wave system as has been done globally in the GLOSWAC database (Portilla-Yandún, 2018).

The effect of climate change on surface wind waves has been a recurrent subject of study during the last two decades. In this regard, the COWCLIP community integrates efforts to reunite the existent studies on the matter and to offer an estimation of the uncertainty associated with observed historical and projected future changes (Morim et al., 2018, 2019, 2020). The development of atmosphere-ocean GCMs has provided the resources to build wave climate projections and to study the future wave conditions under different GHG concentration scenarios and time horizons. General climate models reproduce the real global climate, representing the physical processes in the atmosphere, ocean, cryosphere and land, as well as their complex interactions (Flato et al., 2013). Nevertheless, certain issues such as the parametrizations included in the models to reproduce some physical processes or the spatial resolution cause intrinsic biases (Maraun et al., 2017). These biases are inevitably transferred to the wave model forcings (i.e., marine surface wind fields) and therefore to the wave climate (Hemer et al., 2012a). A reliable study of the future behavior of wind waves necessarily needs to be held by a realistic representation of the wave climate, although always being aware of the limitations of the data used to develop the analysis. Concerning the latter, despite BC allowing more accurate results in the simulated wave climate to be obtained, and assumed to carry to the projected changes in integrated parameters (Lemos et al., 2020a), a direct extrapolation of the commonly used correcting methods to directional spectra cannot be done.

Two are the main approaches used to generate wave climate projections from GCMs forcings: statistical and dynamical. Although statistical projections have been a helpful way to obtain future wave series without a massive computational demand (e.g., Camus et al., 2017; Perez et al., 2015; Wang et al., 2014), many studies now use dynamical simulations to investigate potential changes (e.g., Fan et al., 2013; Hemer et al., 2013a; Mori et al., 2013; Semedo et al., 2013). The projected changes are commonly estimated from the outputs of wave climate projection ensembles. Thus, the uncertainty associated with the change signal of each GCM is partly overcome through the assessment of the ensemble mean change, which normally implies the evaluation of the agreement between members and/or the statistical significance of the estimated variation (Collins et al., 2013).

The standard approach to assess the future behavior of wave conditions consists in analyzing the projected changes in integrated wave parameters (e.g., H_s, T_m or Θ_m). In particular, the H_s has been the most studied parameter as its changes are considered a representation of the expected variations in the energy captured in the full spectrum. The assessment of changes in T_m (e.g., Casas-Prat et al. 2018) or in variables that integrate both the wave height and period, such as E_f, is gaining popularity (Lemos et al., 2019; Mentaschi et al., 2017; Reguero et al., 2019). This fact demonstrates the advances of the climate community in having a broader understanding of the effect of climate change on ocean wind waves, not being constrained to the limitations offered by the analysis of only H_s. For completeness, the proven influence of the wave characteristics in future projected coastal processes like shoreline evolution (Alvarez-Cuesta et al., 2021a,b; Toimil et al., 2021a), provides a compelling reason to expand the assessment to less analyzed wave parameters (e.g., period, direction), yet acknowledging there is higher uncertainty in these (Morim et al., 2019). More recently, new studies based on the analysis of each independent wave system through its associated H_s have been developed (Amores and Marcos, 2020; Fan et al., 2014; Lemos et al., 2021b). Although these analyses are not based on spectral data but derived from integrated parameters using swell-tracking formulation, they have demonstrated the existence of different climate change signals for different systems and the importance of directionality.

The present study intends to go further, contributing to the understanding of the future behavior of wind waves globally through the assessment of the projected changes in wave energy from directional spectra. The scope is not only limited to provide a global overview of the projected changes, but also to identify regional patterns of change to describe the future behavior of the main wave systems propagating across the oceans.

7.2 Climate data

The effect of climate change on wave climate is studied through the outputs of the same seven-member GWP ensemble previously described in Section 5.2. Present-day and future wind wave climate are simulated through the twenty-year time slices 1986–2005 and 2081–2100, respectively. The projected wave conditions are modeled under the RCP8.5 GHG concentration scenario. In addition, a simulation for the historical period with forcings from ERA5 and the very same numerical model configuration as for the GCM-driven wave simulations is developed to be used as reference data.

In this study we make use of hourly time series of H_s and spectral data. The storage of full directional spectra at hourly resolution requires large capacity resources, even more considering the number of GCMs used and the global perspective of the study. Hence, we implement an alternative approach to reconstruct the directional spectra based on the use of spectral partitions. A spectral partition (SP) represents each of the wave systems reaching a certain location at any time and can be identified as each of the spectral peaks within the full spectrum (Portilla-Yandún et al., 2015). The isolation of each SP and its treatment as an independent spectrum enables to calculate their associated integrated wave parameters (hereinafter SP parameters, SPP). The number of SP varies in time and space, influenced by the climate variability at different scales (e.g., seasonal, interannual) and the exposure of the target location to the open ocean (i.e., the possibility of being reached by multiple wave systems propagating from different directions), among other factors. In general, the wave climate is dominated by one or two swell systems, although additional secondary systems can also exist. For example, according to the study of Echevarria et al. (2019), while a location in the northeastern Atlantic is mostly affected by one swell system, locations in the tropical Pacific can be affected by five different swell systems. Considering so, the number of SP stored is a compromise between an accurate reconstruction of full spectra from hourly time series of SPP and a reasonable amount of data to be stored. Here, three SP are used, two of them corresponding to swell systems and the remaining related to wind sea waves. The spectral partitioning scheme used in the propagation numerical model is based on an analogy between the surface-elevation spectrum and a topographic surface (Hanson and Phillips, 2001). In this context, the sub-peaks and associated surface are identified by applying a digital image watershed partitioning algorithm, implemented as described in Tracy et al. (2007). For each SP the parameters H_s, T_p, Θ_m and directional spread (Spr_Θ) are stored.

7.3 Methods

7.3.1 Methodology overview

Fig. 7.1 shows a flowchart summarizing the approach followed in this study. The methodology is based on a seven-member wave climate projection ensemble. As a result of the simulations, a global spectral dataset of three SPs is produced. Next, spectra are reconstructed from the partitional information globally at 8-degree spatial resolution. Projected changes in wave climate are then estimated by comparing present and future mean climatologies. Resulting annual mean changes are geographically classified into sixteen ocean regions with a similar pattern of spectral change using a k-means algorithm. Finally, the underlying mechanisms behind the changes found in the wave systems are explored using the ESTELA method (Pérez et al., 2014).

7.3.2 Spectral reconstruction

The reconstruction of directional spectra from SPP (i.e., H_s, T_p, Θ_m, Spr_Θ) needs to be grounded on a theoretical basis to define the SP shape. We consider the JONSWAP (Joint North Sea Wave Project) spectrum (Hasselmann et al., 1973) due to its extended use in multiple studies related to coastal and ocean engineering (Benoit, 1992; Onorato et al., 2001;

Rueda-Bayona et al., 2020; Wang, 2014; Whittaker et al., 2016). The generation conditions of the observed waves used to define the formulation initially restrict its validity for developing seas with a limited generation fetch. However, over the years the JONSWAP spectrum has been proven to be valid for a wider range of wave generation conditions, including storms and hurricanes, making it the most extended design spectrum for coastal engineers (Holthuijsen, 2007).

Among the multiple formulas derived from the original JONSWAP research (e.g., Donelan et al. 1985; Goda 2010), we use the one proposed by Goda. This expression considers the spectral shape in terms of the H_s and T_p of the sea state and three calibration parameters: the energy scale parameter, the peak-width parameters (σ_a and σ_b) and the peak-enhancement parameter (γ). The peak enhancement parameter varies through time depending on the transported energy and degree of development of the sea state, i.e. it takes higher values for mature frequency-filtered swells and energetic sea states. Here, we use an average γ of 3.3, which is the standard approach among the coastal engineering community (Holthuijsen, 2007). Similarly, we consider the average values $\sigma_a = 0.07$ and $\sigma_b = 0.09$ for the peak-width parameters (Hasselmann et al., 1973).

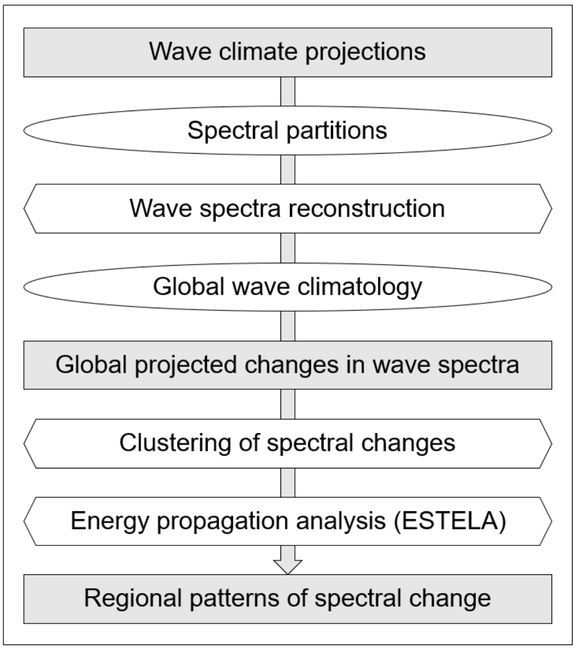

Fig. 7.1 Scheme overview of the methodology. Rectangles represent main results, ellipses intermediate results and hexagons methods.

Since we are reconstructing directional spectra, a correct representation of the real spectrum entails defining as accurately as possible the energy spreading across directional sectors. Among the different directional spreading functions proposed in the literature (e.g., Longuet-Higgins et al. 1963; Pierson, Jr. et al. 1952), the Mitsuyasu et al. (1975) formulation is selected to this purpose. This function assumes a decay in the energy from its maximum at the principal wave direction until zero for an azimuth equal or greater than 180°.

The reconstruction scheme of the full directional spectrum defines the spectral shape for each SP as a JONSWAP spectrum. Then, the directional spreading coefficient is calculated for each direction to scale the SP shape. Finally, the full directional spectrum is obtained as the sum of all the reconstructed SPs. In this study, the spectral wave energy is discretized in 32 frequency bins, exponentially distributed from 0.0373 to 0.7159 Hz (i.e., from 1.4 to 26.8 s) and 24 directional sectors of 15° each, i.e., each spectrum is divided into 768 frequency-direction spectral bins (hereinafter spectral bins). We analyze spectral conditions globally at 8-degree spatial resolution, resulting in a total of 491 spectra.

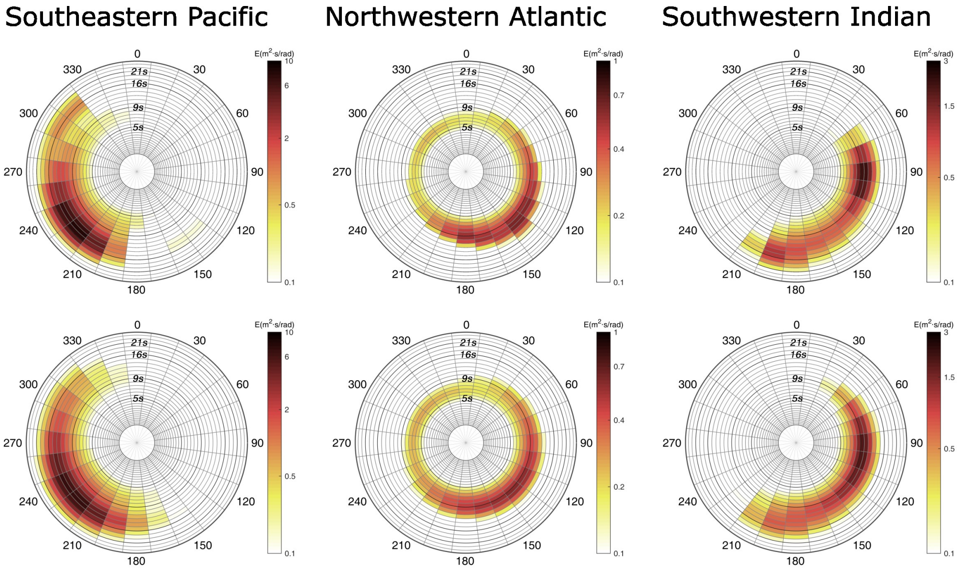

Fig. 7.2 Annual mean wave energy for the period 1986–2005 and CMCC-CM model from full directional spectra (upper panels) and reconstructed directional spectra (lower panels) at three locations from different ocean basins.

The reconstruction is validated by comparison with full directional spectra equally discretized (i.e., 24 directions, 32 frequencies). Fig. 7.2 shows the result of the reconstruction in three locations from different basins and for the CMCC-CM climate member. The first one is located in the southeastern Pacific (37°S, 74°E), the second one in the northwestern Atlantic (40°N, 73°W) and the third one is located in the southwestern Indian (18°S, 50°E). The validation evidences a good representation of the annual mean climatology by the reconstructed spectra. A slight overestimation of the total energy in the reconstructed spectra is however observed. This overestimation is 4%, 7% and 3% for the SE Pacific, NW Atlantic and SW Indian spectra, respectively. The energy spread across directional sectors and frequencies is also well captured. For each of the three spectra showed in Fig. 7.2, the mean relative error in the energy proportion at each 15-degree directional sector is 12%, 8% and 16%, and at each of the 32 frequency bins is 7%, 5% and 13%, respectively. For a given set of bins, the mean relative errors are calculated as the mean of the absolute normalized differences in the proportion of energy between the full and the reconstructed spectra.

7.3.3 ESTELA method

The ESTELA method (Pérez et al., 2014) allows to study the propagation of the wave energy from the generation area to any ocean location assuming that it travels along great circle paths (Young, 1999). It provides valuable information about the genesis of the waves, unraveling where they were generated and the different energy contribution among ocean regions. Furthermore, the analysis of the E_f and its variations along the great circle paths determines not only the travelling time of the waves to reach the analyzed point, but also the main areas of energy gain and dissipation. Here, the ESTELA method complements the analysis of directional spectra, helping to define the generation area of the different wave systems discernible within the spectrum and their projected changes under climate change scenarios.

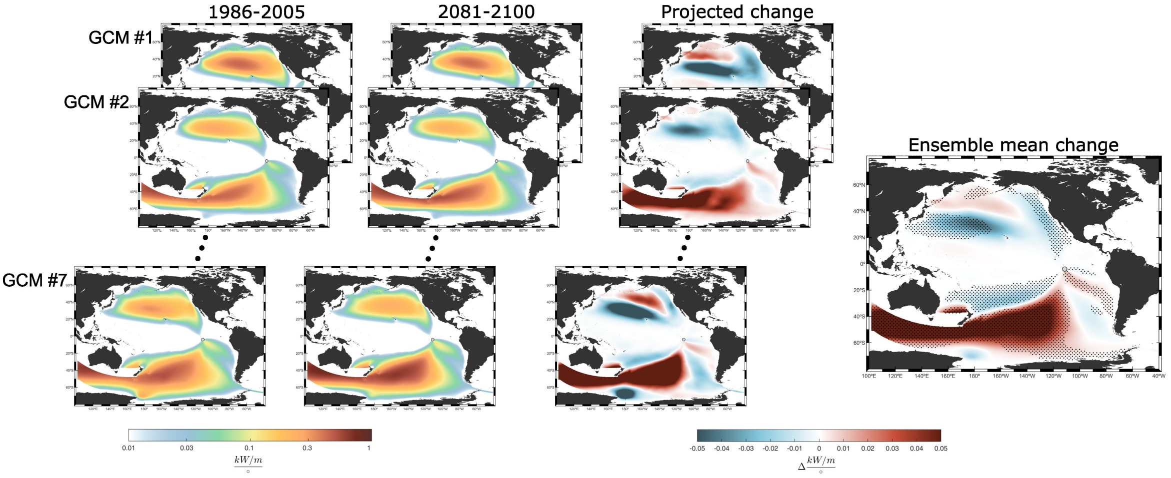

Fig. 7.3 Assessment scheme of the projected changes in EF_w propagating toward a target location. Left panels: Present-day and projected mean EF_w. Central panels: Projected change in mean EF_w. Right panel: Ensemble mean projected change in mean EF_w. Stippling indicates robust projected changes.

The effective energy flux (EF_w) propagating toward a target location from any ocean point is calculated based on geographical and physical criteria. The obstacles encountered by the wave trajectory, such as islands or mainland, determines firstly whether the energy can travel from a point to another. Then, the EF_w at each ocean point is obtained as the portion of energy heading the target location along the circle path. The total energy is calculated following the same spectral reconstruction method previously explained. Thus, the spreading function determines the fraction of the total that propagates toward the direction of analysis.

The annual mean EF_w is calculated for the present-day and future time slices at the points of interest for all the ensemble members. Then, the ensemble mean projected change in annual mean EF_w is estimated and the associated uncertainty is assessed. Fig. 7.3 shows an example for a point located in the tropical eastern Pacific Ocean.

7.3.4 Projected changes and uncertainty assessment

We assess the differences between the present-day and projected end of the century wave climate under the high concentration scenario RCP8.5. The projected change is estimated as the unweighted ensemble mean change, i.e. it is calculated as the average of the individual changes from each member assuming a homogeneous contribution from all of them.

The proposed method to assess the uncertainty of the projected changes is based on one of the techniques proposed in AR5 (Collins et al., 2013). The robustness of the future variations at each frequency-direction bin is evaluated in terms of the individual statistical significance of the change for each model and the homogeneity of the sign of change between the members of the ensemble. Therefore, the change is considered robust when more than 80% of the members present a statistically significant change at 95% confidence level and at least 80% of those agree in sign of change. The statistical significance is calculated by applying a Welch's t-test to the mean of the historical and future periods at 95% confidence level (Tebaldi et al., 2011). The implementation of a heteroscedastic t-test is based on the possible shift of the energy from present-day to future periods, thus precluding to assume an equal variance at each spectral bin. Spectral bins showing robust changes are stippled. We do not consider changes lower than a 1% the maximum variation within the spectrum, to avoid noise in the representation of the results. The projected changes in H_s are also assessed as described above. The projected changes in EF_w are considered as robust when the absolute value of the change is higher than the inter-model standard deviation.

7.3.5 Clustering

The projected changes in annual mean spectral energy are clustered to identify ocean regions with a similar change pattern. Numerous unsupervised machine learning techniques to perform data clustering can be found in the literature (e.g., k-means, DBSCAN, spectral clustering). The main feature of these algorithms is that they are able to group the observations without being trained before with labeled data. They are classified in terms of the set of rules they follow to assess the similarity between observations. An intuitive classification is to divide the algorithms between partitioning and hierarchical methods (Kaufman and Rousseeuw, 2009). After testing several clustering techniques, we select k-means (Camus et al., 2014a, 2011; Lucio et al., 2020).

K-means is based on the minimization of the distance between the center of mass of each cluster and its members. Thus, from a given k number of clusters and n observations $x_1, x_2, \ldots, x_n$, the algorithm finds the centers c so as to minimize a potential function. The potential function varies depending on the distance metric considered (e.g., Euclidean, cosine). In this particular case, we use the squared-Euclidean distance. The initialization plays a key role in the performance of the algorithm in terms of speed and accuracy (Arthur and Vassilvitskii, 2007). In this regard, Lloyd's algorithm proposes a random selection of the initial centroids, which implies that results could be different on each realization. To avoid this source of uncertainty, the initial centers are selected using the maximum dissimilarity algorithm (Snarey et al., 1997).

K-means is applied to the spectral changes considering the spectral bins as variables and the spectra as observations, i.e. 768 variables with 491 observations each. The high number of variables and analyzed locations requires a preprocessing to assist the clustering algorithm and remove noisy signals. First, the input dimensionality is reduced by aggregating the spectral bins, changing from the initial discretization of 24 directions and 32 frequencies to 12 and 5, respectively. The aggregation is done so that each new spectral bin represents a directional sector of 30° and the following period ranges: <5 s; 5 s – 10s; 10s – 15 s; 15 s – 20s; >20s. Then, the variable of analysis is transformed by applying the function $Y = X^{1/3}$ to reduce the variance between spectral bins. Finally, we apply principal component analysis in the sample of variables and observations, considering only the principal components that explain 99% of the variance. We apply the clustering to the Atlantic, Pacific and Indian oceans independently. The final number of clusters for each basin is selected iteratively, on the basis of the minimum number that can represent the spatial change variability pattern.

7.4 Results

Prior to the assessment of projected changes, the biases in spectral energy and H_s relative to the reference hindcast are analyzed to evaluate the skill of the ensemble members to reproduce the wind wave climatology. Results show that, in agreement with the findings from Chapter 6, the bias of the spectral energy can vary not only from one member to another, but also within the spectrum, i.e. wave systems can show biases with different magnitude and sign. While CMCC-CM and MIROC5 mostly overestimate the present-day H_s climate, the rest of the models show a general underestimation. ACCESS1.0 and GFDL-ESM2G are the models that show the lowest biases, presenting a global mean bias in H_s of 0.07 m and 0.14 m, respectively. CNRM-CM5 and IPSL-CM5A-MR show the greatest discrepancies (0.29 m and 0.48 m, respectively). These results, although taken with caution, provide confidence in the wave climatology representation and the estimated projected changes from the GCM-based wave spectral data.

In view of the above, the annual (Fig. 7.4) and seasonal (Fig. 7.5 for DJF and JJA; Fig. 7.6 for MAM and SON) mean wave climatology for the historical period is analyzed from the ensemble mean. There is high dominance of extra-tropical swells across the global ocean as they transport most of the wave energy. These swells mainly propagate from the

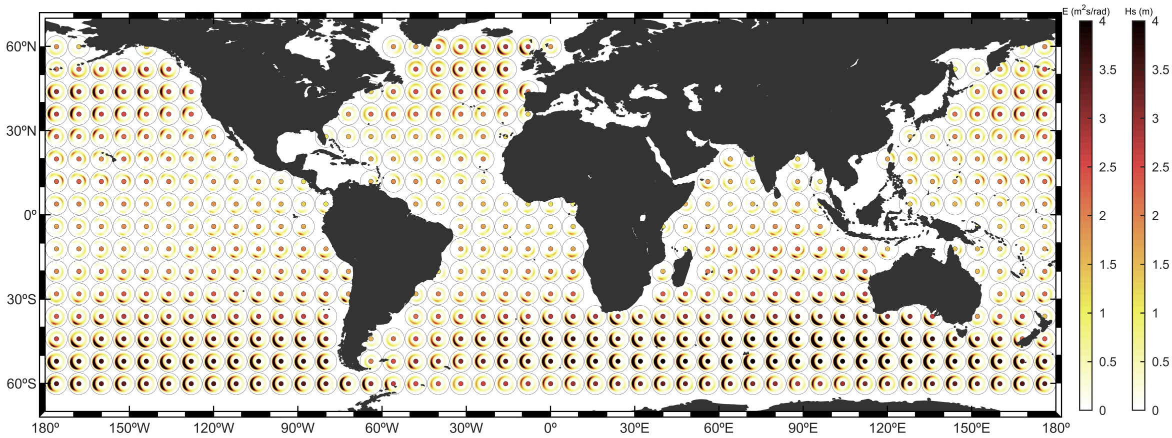

Fig. 7.4 Annual mean wave climate estimated for the period 1986–2005 and the ensemble mean. The map displays the annual mean wave spectral energy (polar plot) and the annual mean H_s (dots in the center of the polar plots).

west across the extra-tropical regions (Odériz et al., 2021), showing a clear seasonal change pattern characterized by more energetic swells during the winter season. The Southern Ocean is the most energetic ocean basin, favored by the long continuous fetch south of 40°S, only partially interrupted by the southernmost part of America (Semedo et al., 2011; Young, 1999). Seasonal mean climatology shows very energetic westerly swells in the Southern Ocean regardless the season analyzed, which are notably strong in the Indian region during the austral winter. The seasonality is more prominent in the NH, showing big differences between the energy transported by westerly swells during winter and summer seasons.

The extra-tropical swell systems also propagate toward the equator, converging with less-energetic easterly wave systems generated in the tropical region by the trade winds. Thus, tropical and extra-tropical wave systems coexist in all ocean basins between 30°S and 30°N and especially in the Pacific, which agrees with the results shown by Echevarria et al. (2019). As a result, the dominant system in the north tropical region varies seasonally depending on the extra-tropical swell contribution. Although weak seasonal patterns can also be observed in swells induced by trade winds, except for the Monsoon areas where it is more prominent (Dima and Wallace, 2003), there is a change from an almost even contribution from extra-tropical and tropical swells during the winter season to a clear dominance of the latter during the summer. The areas affected by the Monsoon phenomenon in the northwestern Indian Ocean show remarkable seasonal differences. In this regard and consistent with previous studies (Portilla-Yandún, 2018), the Monsoon-induced winds generate waves that propagate from the northeast during the boreal winter and from the southwest during summer.

We compare the mean wave climatology for the historical and future periods and every ensemble member, subsequently estimating the ensemble mean projected changes in both the

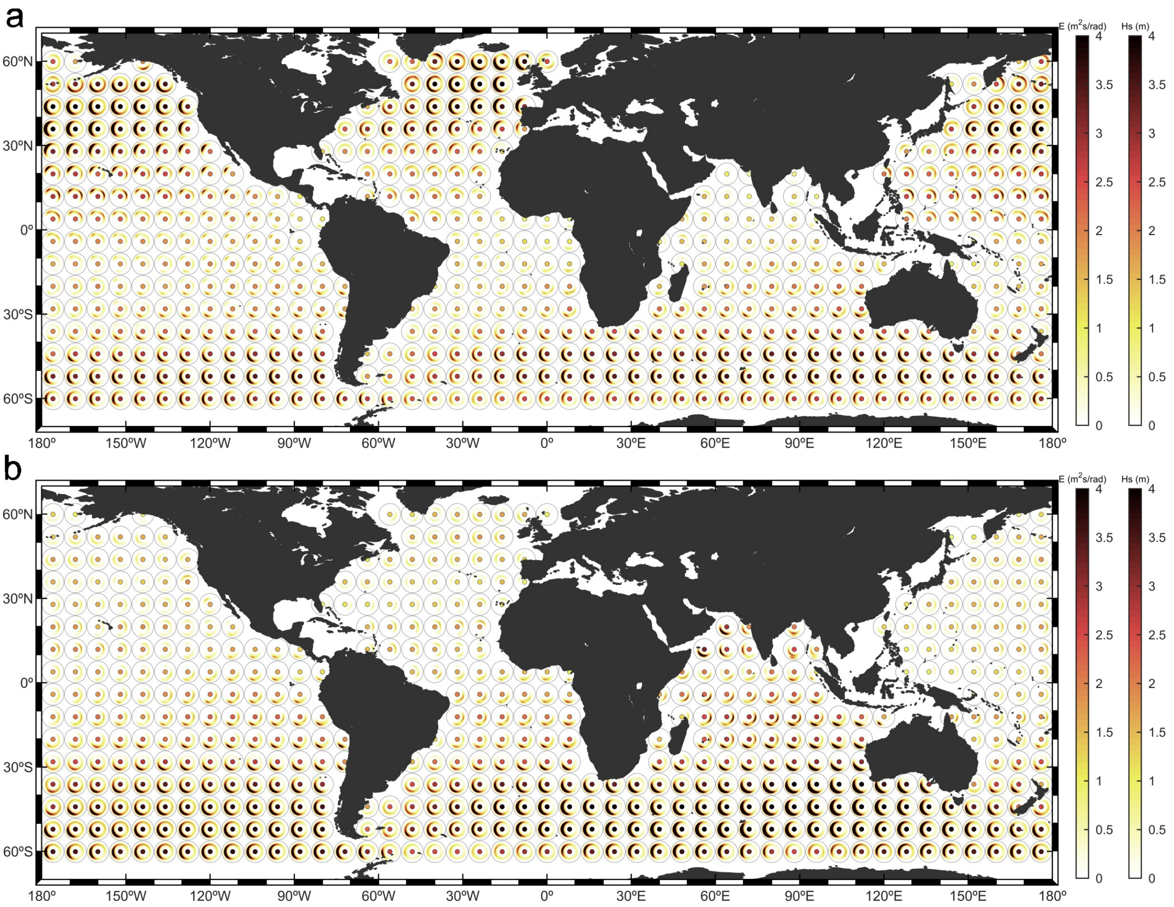

Fig. 7.5 (a) Boreal winter (DJF) and (b) boreal summer (JJA) mean wave climate estimated for the period 1986–2005 and the ensemble mean. The maps display the seasonal mean wave spectral energy (m^2s/rad; polar plots) and the seasonal mean H_s (m; dots in the center of the polar plots).

spectral energy and H_s parameter. The changes in annual mean wave energy are shown in Fig. 7.7. Seasonal changes are depicted in Fig. 7.8 for DFJ and JJA and in Fig. 7.9 for MAM and SON. The projected changes in annual mean spectral energy show a robust projected increase in westerly swells generated in the Southern Ocean, which is consistent with the community consensus about the projected increase in H_s in this region (e.g., Morim et al. 2018; Oppenheimer et al. 2019). The increasing change signal propagates north across all ocean basins, reaching latitudes beyond 30°N in the Pacific and Atlantic oceans, mainly during the austral winter season. The projected increase in Southern Ocean swells dominates not only the projected changes in H_s in the Southern Ocean, but also significantly contributes to the change expected in tropical areas. For example, there exists agreement on a projected increase in H_s in the tropical southeastern Pacific that is mainly attributed to the expected increase in the intensity of southeasterly Pacific trades (e.g., Hemer et al. 2013a). However, the spectral analysis indicates that the energy increase in this region is also affected by the increase in swell energy from the Southern Ocean, especially in the easternmost area.

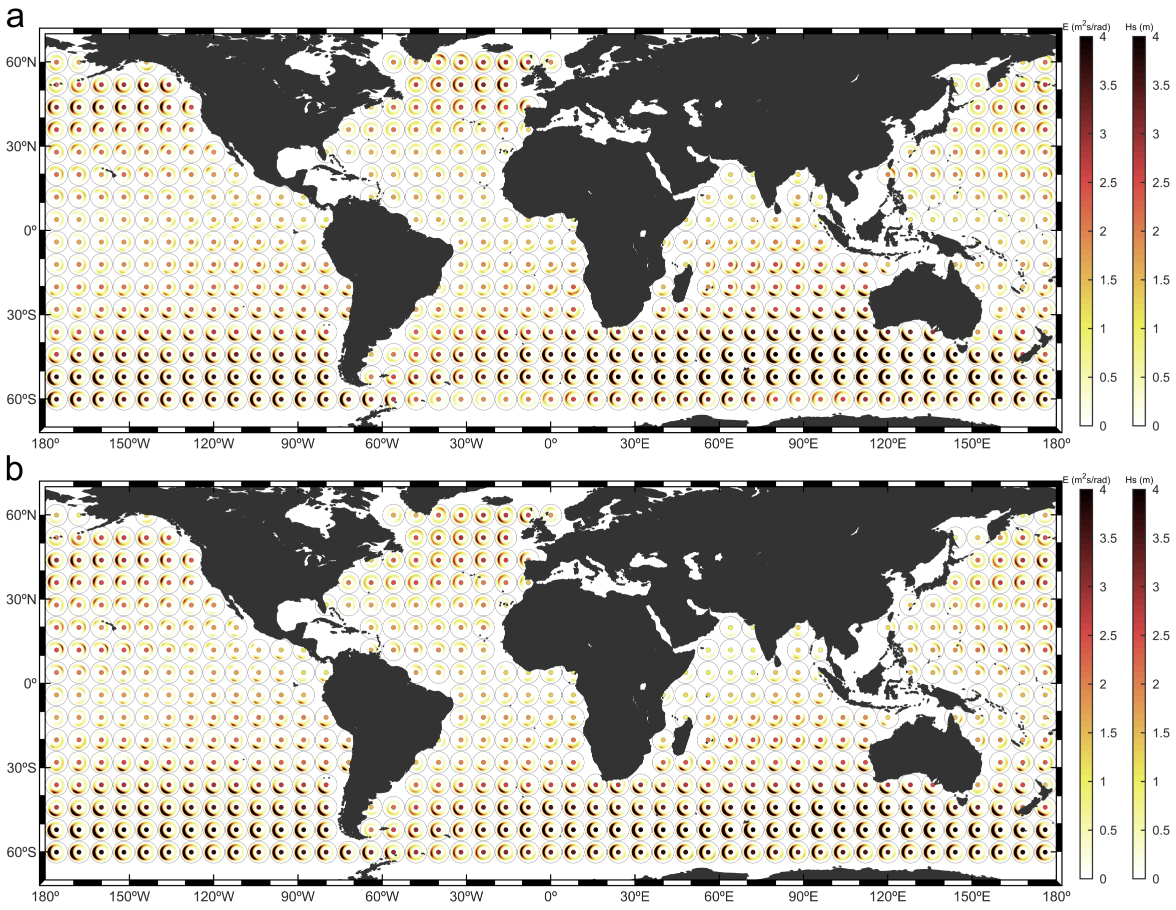

Fig. 7.6 (a) Boreal fall (MAM) and (b) boreal spring (SON) mean wave climate estimated for the period 1986–2005 and the ensemble mean. The maps display the seasonal mean wave spectral energy (m^2s/rad; polar plots) and the seasonal mean H_s (m; dots in the center of the polar plots).

Results also show a northward transition from positive to negative changes in Southern Ocean westerly wave energy in every basin, which agrees with previous studies (Fan et al., 2014). Moreover, this boundary seasonally shifts, moving north during the austral winter and the opposite during the summer.

Results show a robust projected decrease in swells generated in the extra-tropical North Atlantic Ocean. The decreasing signal propagates south, combining in the tropical region with the decreases expected in waves generated by northeasterly trade winds. Thus, there is a projected decrease in the whole North Atlantic basin consistent with the community agreement (Morim et al., 2018; Oppenheimer et al., 2019). Further south, the extra-tropical North Atlantic decreasing signal converges around the equator with the projected changes in extra-tropical southern swells and the projected changes in tropical waves. As a result, the projected changes in H_s in this region show a small projected decrease that mask the increases in swells propagating from the Southern Ocean. This behavior enhances during the boreal winter, maximizing the decreases in H_s in the North Atlantic and hence also their

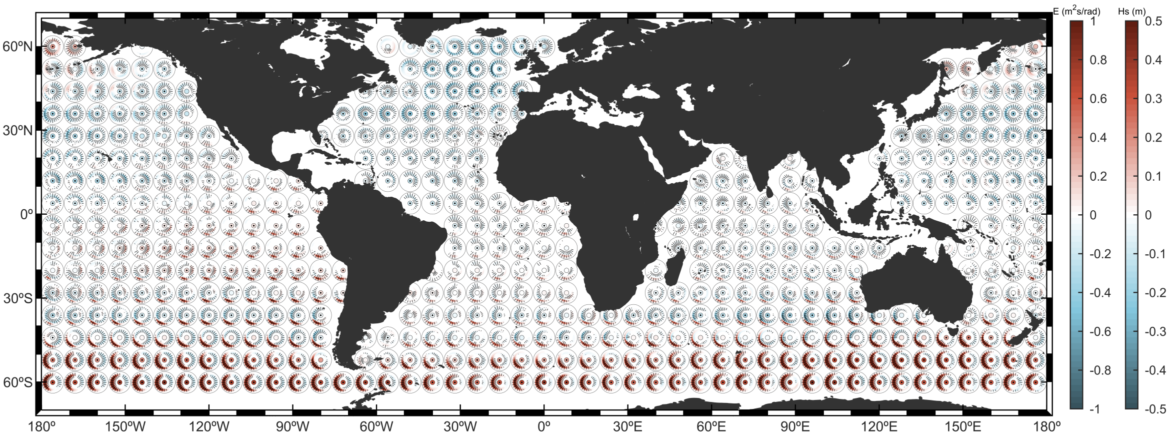

Fig. 7.7 Ensemble mean projected changes in annual mean wave spectral energy (m^2s/rad; polar plots) and H_s (m; dots in the center of the polar plots) under RCP.8.5 scenario by the end of the century. Stippling indicates robust projected changes.

contribution beyond the equator, inducing a projected decrease in almost the whole tropical South Atlantic region.

Future changes in the extra-tropical North Pacific Ocean do not present a homogeneous pattern as in the North Atlantic. First, the spectra at highest latitudes show a general increase in the energy. As we move south, an energy increase associated to westerly swells can be easily identified. This positive change signal evolves to a negative change as we continue moving further from the pole, similarly as it happens in the SH. During the boreal winter this behavior is maximized, which translates in greater changes in wave energy. These high change magnitudes, however, do not appear in H_s since the offset between positive and negative variations within the spectra induces small changes in this parameter. The propagation of these swells to the tropical region causes their change signal to combine with the decrease in tropical waves induced by northeasterly trades and with the projected increase in Southern Ocean swells. Moreover, during the boreal winter the extra-tropical change signal can travel beyond the equator, also combining with the increases in the waves generated by southeasterly trades. Therefore, the changes in H_s are the result of the integration of those associated to the multiple wave systems propagating in the low Pacific latitudes. For completeness, the contributions from each wave system seasonally vary due to changes in the amount of transported energy. The spectral change pattern in the Indian Ocean is mainly characterized by the combination of the increases expected in Southern Ocean swells and the changes associated to tropical waves induced by trade winds. Concerning northwestern region, the Indian Ocean area strongly affected by the Monsoon phenomenon, a robust decrease is expected in the wave systems generated by Monsoon-induced winds regardless the season.

In order to better understand the estimated spectral changes, we develop an additional analysis which consists in identifying geographic regions with similar spectral change patterns.

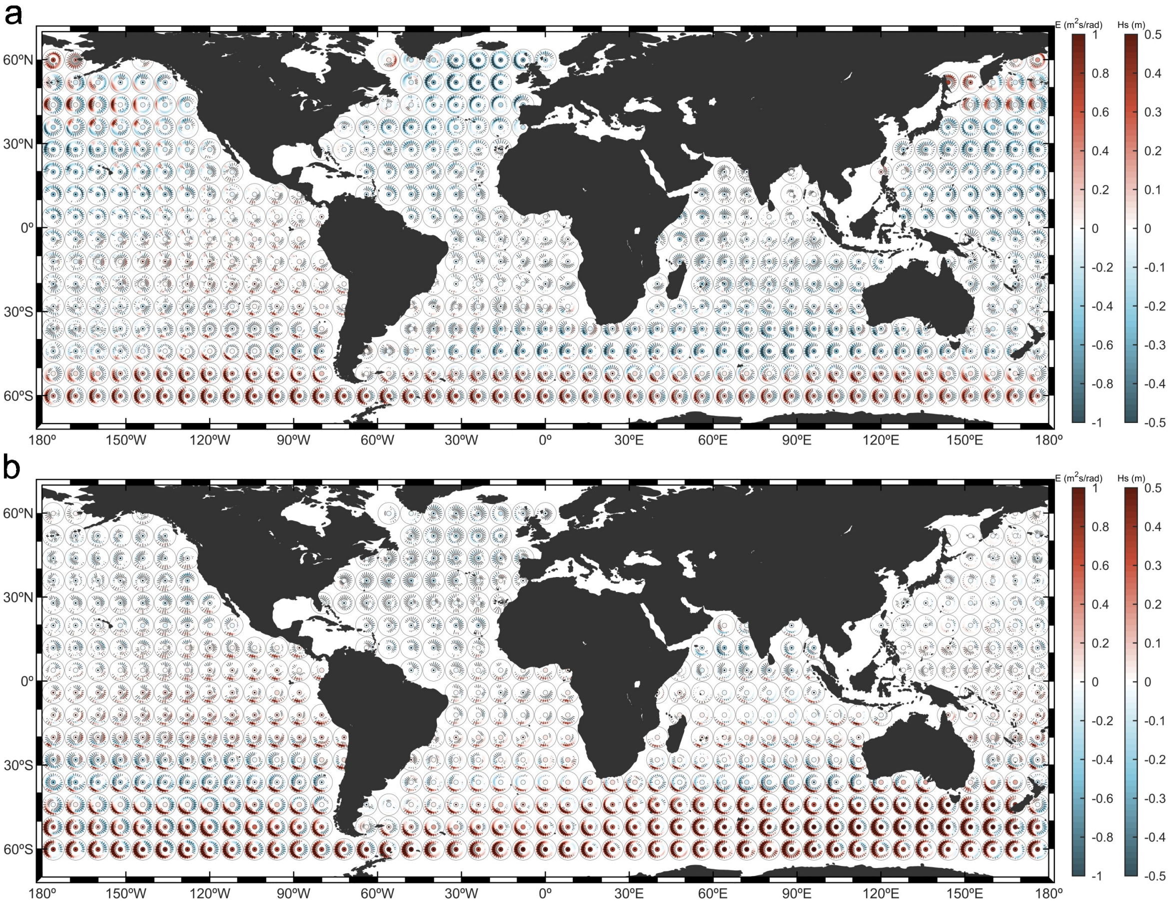

Fig. 7.8 (a) Ensemble mean projected changes in boreal winter (DJF) and (b) boreal summer (JJA) mean wave spectral energy (m^2s/rad; polar plots) and H_s (m; dots in the center of the polar plots) under RCP8.5 scenario by the end of the century. Stippling indicates robust projected changes.

Then, each region is individually analyzed regarding the propagation behavior of the swells. For example, the sign-of-change boundaries found in the Southern Ocean and North Pacific require a deeper analysis to be explained, as well as the future behavior of swells generated in the tropical regions by trade winds. The detailed description of the change pattern within these clusters, supported by the ESTELA method, provide a physical basis not only to the spectral changes, but also to the agreed changes in integrated parameters in different ocean regions.

The resulting classification provides sixteen regional patterns of spectral changes, named from C-01 to C-16 (Fig. 7.10). The Atlantic, Pacific and Indian oceans are represented by five, seven and three groups, respectively. A unique cluster representing the Southern Ocean is defined from the merging of the southernmost region of each basin. The final classification separates the spectra characterized by swell increases in the Southern Ocean from those located further from the pole clearly dominated by a decrease in westerly wave energy. Similarly, other issues such as the high number of clusters in the Pacific, coherent with

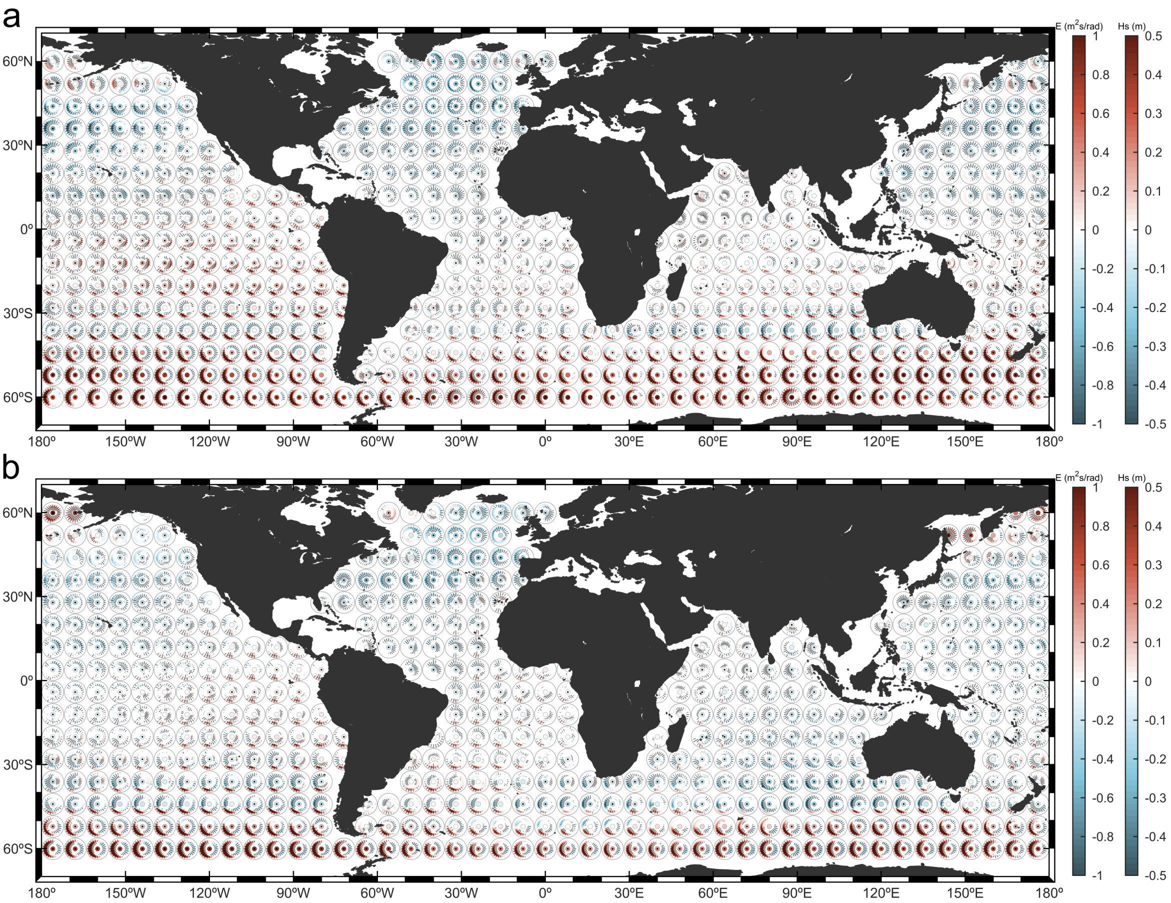

Fig. 7.9 (a) Ensemble mean projected changes in boreal fall (MAM) and (b) boreal spring (SON) mean wave spectral energy (m^2s/rad; polar plots) and H_s (m; dots in the center of the polar plots) under RCP8.5 scenario by the end of the century. Stippling indicates robust projected changes.

its multi-modal wave climate, the isolation of the northernmost Atlantic spectra characterized by westerly swell decreases and the transition between the tropical northern and southern Atlantic basins are also distinguished in the obtained groups. Fig. 7.10 also displays a reference location for each analyzed cluster. The locations are selected as points with a similar spectral change to each cluster centroid given by the k-means algorithm.

We assess the climate change fingerprint on the Southern Ocean (C-01) by analyzing the spectral changes in each ocean basin (i.e., Atlantic, Pacific and Indian; Fig. 7.11). The wave climate in this region is characterized by swells propagating eastward all year round (Young, 1999) mostly generated south of 35°S along the roaring forties and furious fifties regions. A robust and clear projected increase is expected in these swells, which agrees with the results found in many studies concerning the future behavior of H_s (e.g., Morim et al. 2018; Oppenheimer et al. 2019). Nevertheless, a clear boundary at approximately 45°S can be observed in every basin, showing a decrease north of that latitude and an increase south of it. This dipole pattern may be related to the expected poleward shift of the southern

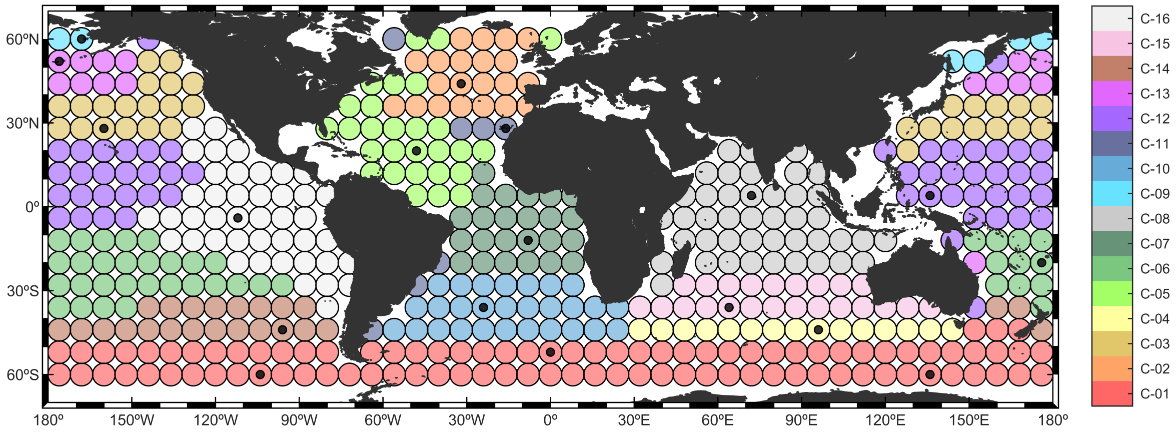

Fig. 7.10 Sixteen regional patterns of spectral change. Black dots indicate the reference location used to analyze each cluster.

extra-tropical storm track (Tamarin-Brodsky and Kaspi, 2017; Yin, 2005) and also favored by the continuous shift of the SAM climate pattern toward its positive phase, which induces a southward shift of subtropical ridge (Fan et al., 2014). In addition, the southern storm track is projected to intensify in a changing climate (Chang et al., 2012; O'Gorman, 2010), which enhances the increasing signal in the southernmost part of the region. These results are consistent and provide an explanation for the projected decrease in H_s north of 35°S found in numerous studies (e.g., Casas-Prat et al. 2018; Hemer et al. 2013a; Mori et al. 2013).

Fig. 7.12 displays the analysis of the clusters from the Atlantic Ocean. C-02 mainly receives energy transported by waves generated by ETCs crossing the northernmost Atlantic Ocean (Camus et al., 2014b; Pérez et al., 2014). Depending on the position of the storm track and the marine ice coverage, waves can be generated in different areas such as the south of Newfoundland, the Labrador Sea and between Iceland and Greenland. These swell systems are characterized by a robust projected decrease regardless of their geographical origin, which is explained by the projected displacement of the storm tracks to higher latitudes and the more frequent atmospheric blocking systems (Lemos et al., 2021a). In addition, results agree and provide confidence in the expected decrease in H_s found by numerous studies in this particular region (e.g., Aarnes et al. 2017; Lemos et al. 2021a). C-05 represents the tropical-north Atlantic region. The energy in this cluster is mainly transported by two systems, waves generated by northeasterly trades and extra-tropical northern swells coming from higher latitudes. Results show a robust decrease in the energy, consistent with the projected decrease expected in H_s. This cluster can also receive energy from waves generated by southeasterly trades and Southern Ocean swells, although their projected change is negligible in most of the studied region. C-07 pattern shows the future behavior of wind waves in the tropical-south Atlantic Ocean. Projected changes in EF_w show a heterogeneous change pattern in trade-induced waves propagating from the southeast. The changes in this

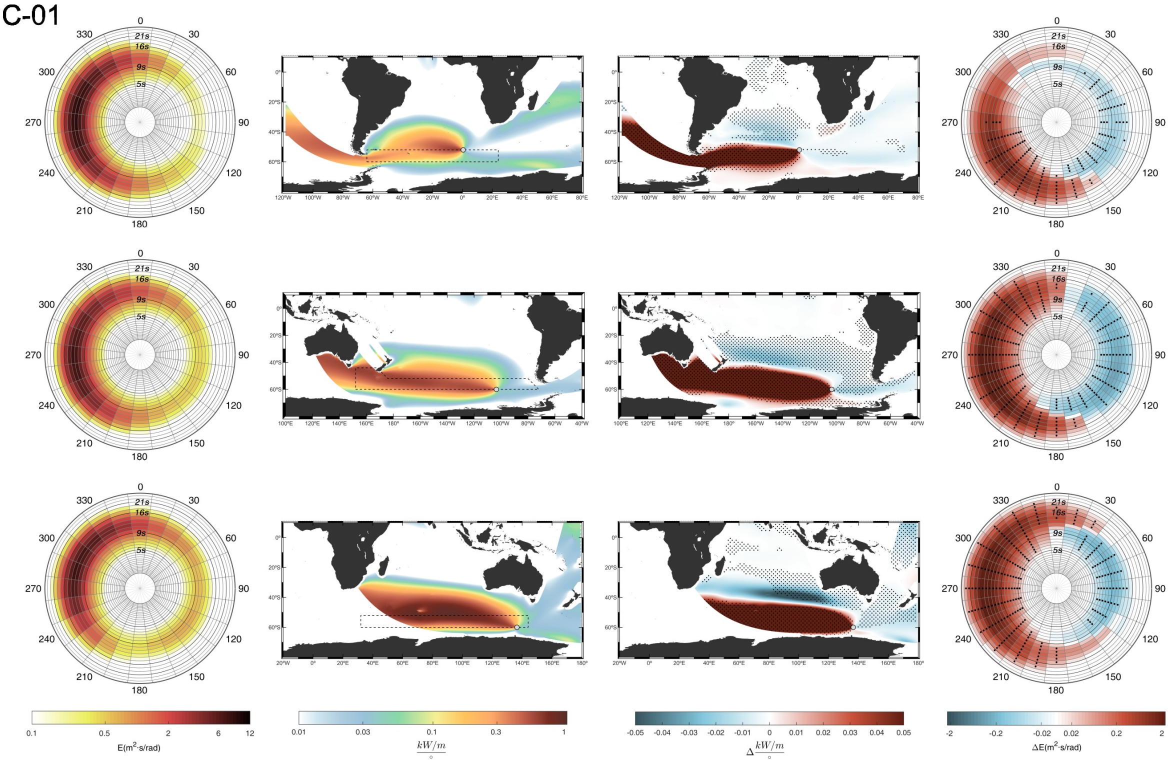

Fig. 7.11 Analysis of the regional patterns of spectral change in the Southern Ocean. First column: Annual mean wave energy spectrum (m^2s/rad). Second column: Annual mean EF_w (kW/m/°) propagating toward the target point. The dashed line represents the contour of the cluster. Third column: Ensemble mean change in annual mean EF_w propagating toward the target point (kW/m/°). Fourth column: Ensemble mean change in the annual mean wave energy spectrum (m^2s/rad). Stippling indicates robust projected changes.

swell system and, in general, in waves generated by trade winds are directly linked to the changes in the Hadley Cell (Odériz et al., 2021). In this regard, the expected expansion of this cell globally (Grise and Davis, 2020) affects surface winds fields (Casas-Prat et al., 2018) and provides an explanation to the heterogeneous change pattern found in wave energy. Moreover, this cell expansion is also visible in C-05 and C-10 for northern and southern tropical waves, respectively. The south-tropical Atlantic is highly conditioned by the increase expected in Southern Ocean swells. Therefore, the uncertain increase found in previous studies in this ocean region (e.g., Hemer et al. 2013a; Morim et al. 2019) can be explained by the combination of the increase signal from the Southern Ocean and the uncertain dipole change in tropical waves likely caused by the disagreement of the models in representing the future behavior of the Hadley cell. Most of the energy propagating toward the southernmost cluster of the Atlantic Ocean (C-10) are waves generated by westerly winds south of 40°S within the analyzed cluster and further south in the Southern Ocean region. The same change signal boundary described in the analysis of the Southern Ocean that induces positive and

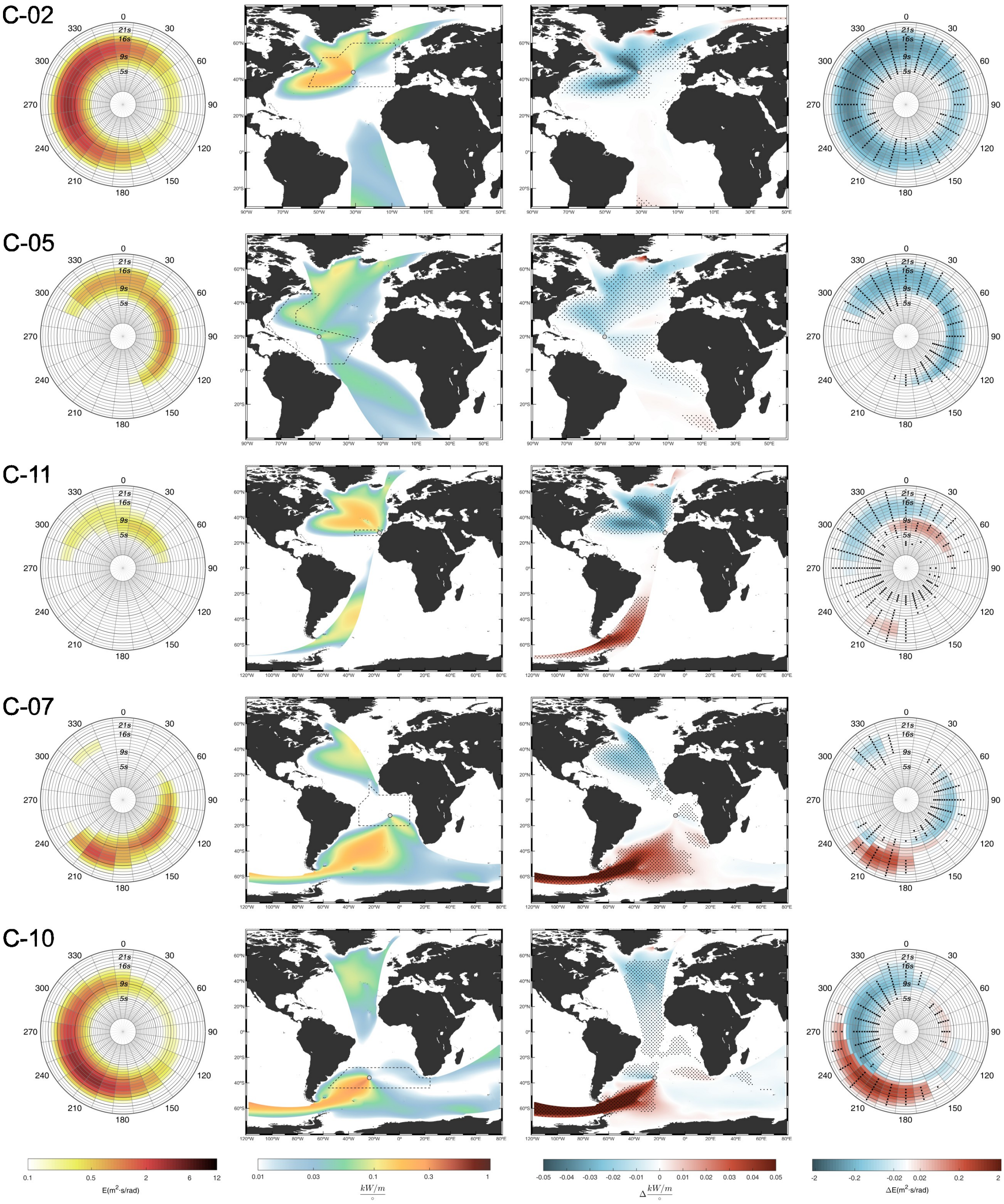

Fig. 7.12 Same as in Figure 7.11 but for the Atlantic Ocean.

negative variations within the spectra can be observed here, providing confidence to the small projected changes in H_s.

The clustering of the Pacific Ocean (Fig. 7.13) divides the extra-tropical north region in three different clusters. C-09 is located at a very high latitude (60°N) so that the effect

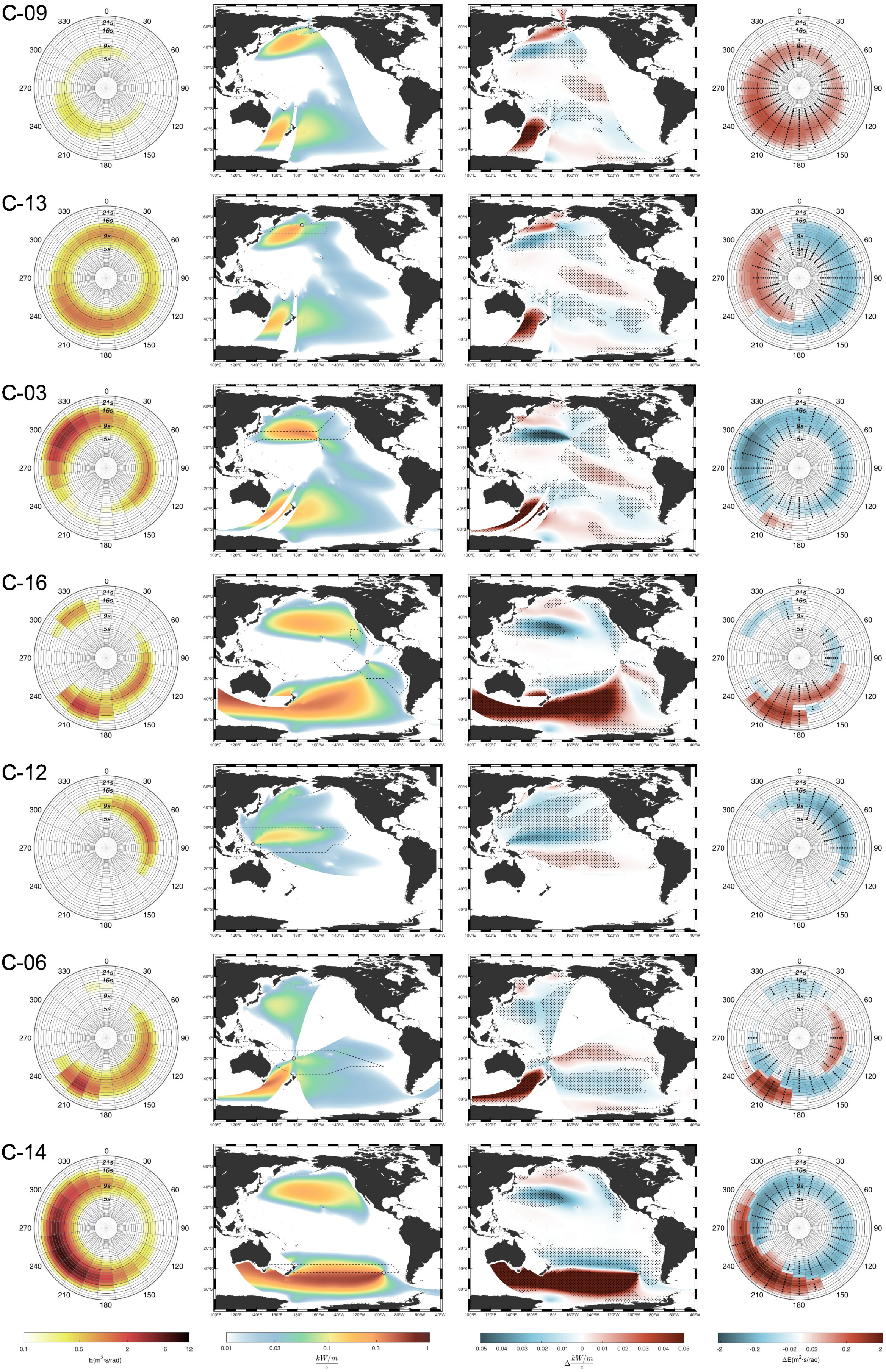

Fig. 7.13 Same as in Figure 7.11 but for the Pacific Ocean.

of global warming on ice melting has a preponderant role on the homogeneous increase found in wave energy due to the significant extension of the generation fetch (Lantuit et al., 2012; Thomson and Rogers, 2014). These changes are remarkably robust in waves from the arctic ocean according to the projected changes in EF_w. In the same vein, C-13, which covers latitudes between 45°N and 55°N, also displays an increase in westerly waves. In addition to the ice melting, the change pattern found can be likely favored by the expected poleward shift of the Pacific storm track (Harvey et al., 2020; Tamarin-Brodsky and Kaspi, 2017). Two main reasons support this statement. First, the analysis of the ensemble mean projected change in ice coverage during boreal winter season (Fig. 7.14) does not sustain the significant increase in waves propagating from the southwest during winter around 180°, nor that the maximum increases are found in those longitudes (Fig. 7.8). Second, the changes in EF_w show an increase in a proportion of the main generation area that is not affected by a major decrease in ice coverage. Nevertheless, results should be taken with caution as there exists great uncertainty in the projected changes in EF_w in this region, likely indicating discrepancies between models concerning the definition of the storm tracks and their future behavior (Priestley et al., 2020), as well as on the ice melting projection (Fig. 7.14).

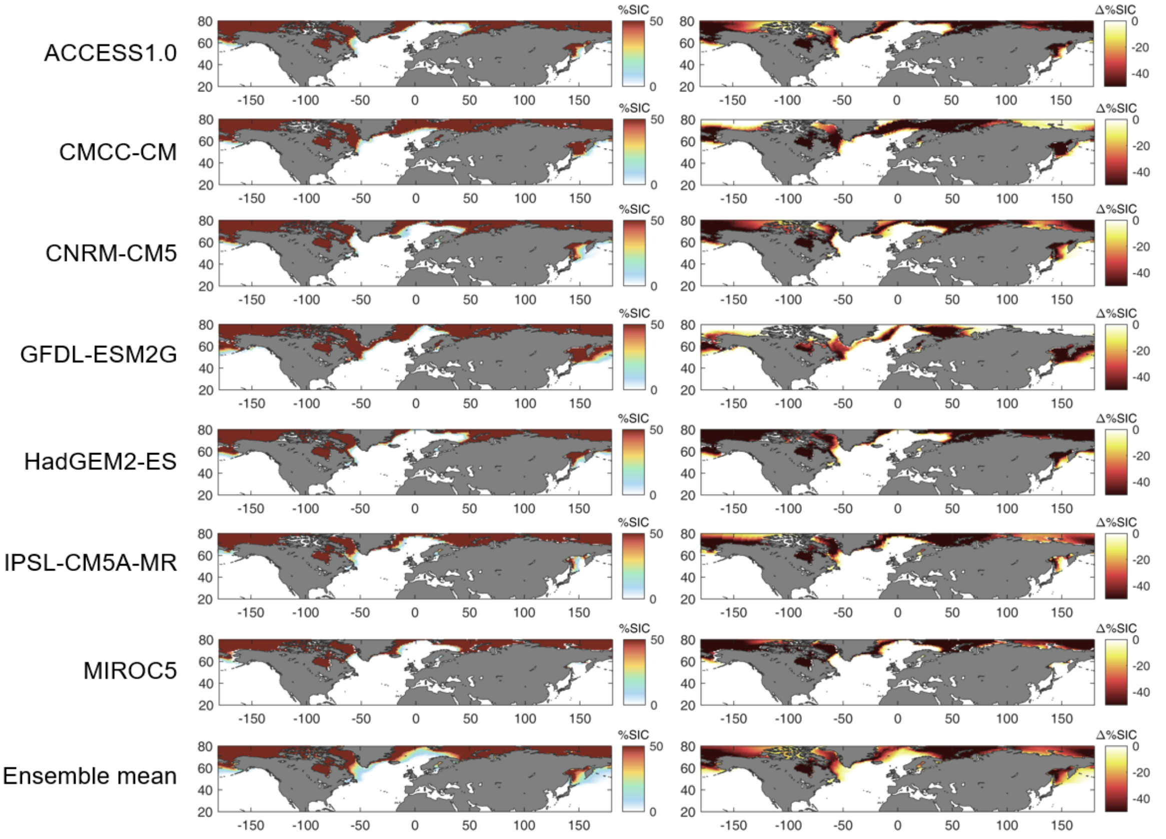

Fig. 7.14 Left panels: Sea ice concentration during boreal winter months (DJF) in the 20-year period 1986- 2005, in percentage of time. Right panels: Increment of sea ice concentration during boreal winter months (DJF) between the 20-year period 1986-2005 and 2081-2100.

As we move south, the decrease in wave energy dominates the region north of 30°N. This issue is represented by C-03, whose change pattern shows a homogeneous decrease both in extra-tropical waves and in tropical waves generated by northeasterly trades; the latter being consistent with previous studies that analyzed the future behavior of surface winds (Casas-Prat et al., 2018). As previously explained, wave climate in C-06, C-12 and C-16 is characterized by multiple wave systems whose different contribution is highly seasonal (Fig. 7.5, Fig. 7.6). Concerning C-16, it is mainly reached by five wave systems: southern waves generated south of 30°S, waves induced by southeasterly trades, waves generated by northeasterly trades, waves generated by the Californian low level coastal jet and northern extra-tropical waves (Jiang and Mu, 2019). The change in wave energy from the first two systems evidence a robust increasing signal. Note that the latter is consistent with the expected intensification in southeasterly trades found in previous studies (Timmermann et al., 2010). The combination of both change signals results in a projected increase in H_s consistent with the community agreement (Oppenheimer et al., 2019). Moreover, a poleward shift can still be discerned from the spectrum and EF_w changes for both wave systems. The decreasing signal associated with the other three described systems slightly contributes to reduce the projected change in H_s. In C-12 the contribution of the increasing signal from the extra-tropical southern swells reduces due to the presence of Australia and the importance of trade-induced waves enhances. Thus, the most important wave system are swells generated by northeasterly trades. In addition, this cluster receives energy from southeasterly tropical swells and extra-tropical waves form both hemispheres. Consistently with previous clusters, changes in EF_w show a robust decrease in northeasterly and northern extra-tropical waves and an increase in southeasterly swells. Similarly, C-06 is also highly affected by southeasterly swells although its southern latitude makes it also reached by a high amount of energy from the Southern Ocean. The change signals agree with those already discussed for previous clusters. Finally, C-14 is located south of 40°S so that it mainly receives energy transported by waves generated by southern westerly winds. As it was observed in the Southern Ocean (Fig. 7.11) and in the southernmost cluster of the Atlantic Ocean (Fig. 7.12), a robust transition from positive to negative changes appears around 45°S.

Fig. 7.15 shows the analysis of the three clusters in the Indian Ocean. Wave climate in C-08 is mainly represented by three wave systems: waves generated by southeasterly trade winds, waves generated in the extra-tropical southern region and waves generated by monsoon-induced winds. Concerning the first system, the projected changes in EF_w show a dipole pattern likely indicating a poleward shift. This issue can also be observed in C-15, both cases characterized by a significant uncertainty. In addition, the expected increase in energy from Southern Ocean swells and the projected decrease in monsoon waves also reach the analyzed cluster. Apart from trade-induced waves, C-15 is affected by westerly swells generated south of 35°S. In this regard, as this cluster extends between 25°S and 35°S, the decreases expected in westerly waves north of 45°S dominate the change signal within the cluster, causing an expected decrease in H_s. Projected changes in C-04 are already described as it is mostly affected by southern westerly swells.

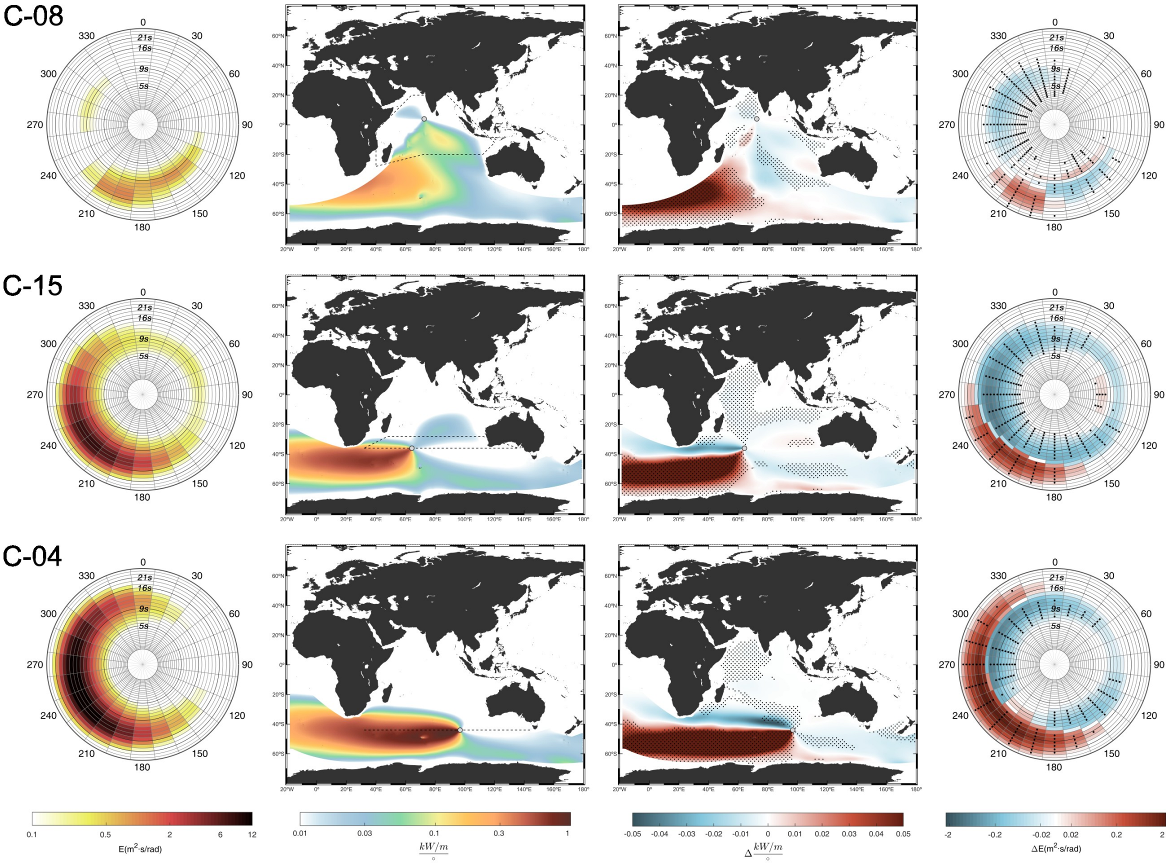

Fig. 7.15 Same as in Figure 7.11 but for the Indian Ocean.

7.5 Conclusions

The present study assesses the projected changes in wave climate globally from a novel perspective based on the use of directional spectra. Seven GCM-based wave climate members (Table 5.1) are analyzed to estimate mean ensemble changes and related uncertainty by the end of the century under the RCP8.5 concentration scenario. The skill of the models to reproduce the historical wave climatology is assessed by comparison against a reference hindcast. We find low-magnitude biases, which provides confidence in the representation of the wave climatology. However, further research is needed to develop a methodology to correct the intrinsic bias of directional spectra and provide more accurate results.

The projected changes in directional spectra provide much more information about the future change in wave climate than an analysis approached by assessing the variations in integrated parameters only, such as H_s. The spectral changes evidence the propagation of the change signal associated with each wave system from the generation area. Hence, the assessment of the spectral change at a certain location offers a clear view of the combination of all the signals, each of them characterized by a magnitude and sign of change. On this basis, the use of integrated parameters disguises most of this information as it cannot discern the different contributing change signals, nor their individual characteristics.

To complete the spectral analysis, we cluster the annual mean spectral changes. Sixteen groups distributed through ocean basins with a similar spectral change pattern are found (Fig. 7.10). Then, we explore the propagation scheme of the main wave systems arriving at the representing point from each group to assess the changes in the transported energy and their influence in the change patterns found. The individual analysis of each cluster (Fig. 7.11, Fig. 7.12, Fig. 7.13, Fig. 7.15) together with the overview provided by the annual (Fig. 7.7) and seasonal (Fig. 7.8) global changes, makes us reach solid conclusions about the expected change in the main swell systems propagating across the oceans.

Results show a robust increase in the energy transported by westerly swells generated south of 45°S. This change signal propagates and is noticeable in both hemispheres, reaching latitudes higher than 30°N in the Pacific and Atlantic oceans, mainly during the austral winter. Around 45°S, a clear transition to a decreasing change signal in westerly swells likely caused by a poleward shift of the southern storm track can be observed, inducing a projected decrease in H_s north of the mentioned latitude. The projected behavior in the northern storm track is significantly different between the Atlantic and the Pacific oceans. While the Atlantic Ocean shows a homogeneous decrease regardless of the generation area, the Pacific Ocean shows three different spectral change patterns. In the Pacific, the combined effect of the ice melting in high latitudes and the expected change in the storm track causes a transition from a projected increase to a decrease in northern westerly waves, similarly to the SH extra-tropical region.

The complex interaction between different wave systems in the tropical latitudes can only be assessed from a spectral perspective. The change pattern can also vary within the year mainly depending on the contribution of the change signal associated with extra-tropical wave systems (Fig. 7.8). The projected change in the energy transported by waves generated by trade winds varies depending on the ocean basin. The Pacific and North Atlantic basins show the clearest change pattern in trade waves, projecting a decrease in northeasterly waves in both basins and an increase in southeasterly waves in the Pacific. The poleward shift expected in trade winds due to the expansion of the Hadley cell dominates the trade wave systems in the South Atlantic and Indian basins, therefore inducing a dipole change pattern and precluding determination of a clear change signal associated with the wave energy.

The assessment of projected changes in directional spectra provides a solid basis to the future variations in integrated wave parameters. For example, results show that the decreases in H_s projected in the North Atlantic Ocean are mainly caused by a projected decrease in both extra-tropical waves and in northeasterly trade waves. Also, the agreed increase in H_s in the tropical eastern Pacific is significantly influenced by the increase in Southern Ocean swells together with the increases in southeasterly trade waves. Further research on physical processes such as the ice melting in high latitudes, changes in storm tracks and shifts in the main wind systems may elucidate the causes of the found projected changes in wave spectra. In addition, the skill of the climate models to reproduce these physical processes should also be analyzed as it might be a major source of uncertainty. It is relevant to point out that the number of SPs and the reconstruction scheme used in this study imply some limitations that should also be considered when interpreting the results. The use of three SPs to reconstruct the directional spectrum may smooth the energy content of secondary wave systems in ocean areas recurrently reached by more than two swells simultaneously, mainly in the tropical region. Consistently, the projected change in the energy carried by these wave systems is also expected to be smoothed, although not varying the sign of change. In addition, the reconstructed spectrum is an approximation of the full spectrum based on a theoretical shape. Although the validation shows a good representation of the full spectrum using a JONSWAP shape with a standard γ value of 3.3 (Fig. 7.2), further research is needed on the evaluation of the most accurate spectral shape to reconstruct each wave system.

The information provided by the spectral approach can be relevant in coastal impact assessment (i.e., flooding and erosion). Identifying changes in different wave systems and including them in impact studies, rather than integrated parameters only, could provide different results. A detail individual analysis of the projected changes in each wave system may give a more realistic prospect of the impacts the wave climate changes would have in a target coastal stretch, not masking, as it happens with integrated parameters, relevant changes in key variables such as period and direction.

To conclude, this study aims to entail a solid argument to assess the projected changes in wave climate through a novel perspective based on spectral information, opening the door to the next logical step along this new approach, namely developing studies based on full directional spectra and not restricted to the limitations inherent to reconstructed spectra.

Chapter 8

Conclusions, scientific contributions and future research

8.1 Conclusions

This section summarizes the main contributions made and conclusions reached throughout this dissertation.

- After completing the thesis research and recapitulating the studies developed based on the three pivotal elements (Fig. 1.1) described at the beginning of this dissertation (i.e., wind waves and sea level sea surface dynamics, extreme events, and climate variability and climate change), it can be concluded that the results obtained are state of the art and that all general objectives raised have been met. Specific methods for a better characterization of sea level and wind waves sea surface dynamics have been proposed, allowing to better understand of the behaviour of extreme conditions at global scale.
- This dissertation demonstrates that satellite altimetry data can be used to characterize coastal extreme sea levels with significant accuracy, which accomplishes *S.Obj. 1* (see Section 1.2). Therefore, these kind of data could be a valid alternative to tide gauge and numerical model data, especially in coastal areas when these data sources are not available.
- A novel methodology to study the behavior of sea level extremes based on altimetry data has been proposed. The methodology uses an inter-calibrated along-track altimetry product as input. Focusing on the climate component of the still water level (i.e. the non-tidal residual), the method has been calibrated and validated using the information provided by tide gauges. The analysis has been conducted regionally along the East coast of North America and for the global coastlines.

- In general, altimetry data moderately underestimate the information provided by tide gauges, a behavior that enhances in tropical areas affected by tropical cyclones. A method to correct the differences between altimetry and tide gauge data has been proposed based on different physical and geographical features.

- This dissertation provides a global assessment of the wave storminess along the global coastlines. The analysis has been conducted using a unique global criterion, which allows comparison between different coastal regions (*S.Obj. 2*).

- The most relevant characteristics of wave storms, such as the frequency of occurrence, the duration and the intensity have been analyzed. In addition, the mean integrated wave parameters during storms significant wave height, mean wave direction, mean wave period and energy flux have been assessed. To complete the analysis, other secondary wave storm characteristics like the wind sea vs. swell energy dominance or the wave period vs. wave height energy flux dominance are examined.

- Consistently with *S.Obj. 3*, the global coastlines have been classified in terms of their wave storminess based on a novel metric that integrates the frequency of occurrence of storms and their intensity, namely the degree of storminess. Results have shown a general meridional storminess gradient in which extratropical coasts show higher degree of storminess than tropical coasts, with the main exception of those affected by tropical cyclones.

- The variability of non-tidal residual extremes has been assessed using altimetry data along the global coastlines, thus meeting *S.Obj. 4*. Three time scale variations have been analyzed: within the year, long-term trends and interannual. For the latter, the correlation between the occurrence of non-tidal residual extremes and four climate teleconnection patterns has been assessed: Arctic Oscillation, Enso, Southern Annular Mode and Indian Ocean Dipole.

- Satellite altimetry has shown a good skill to reproduce the variability of extreme sea levels by validation against a global set of 123 tide gauge records. Results have shown good correlations and low errors for climate variations within the year and between years (interannual). In addition, acceptable results have been found on the estimation of long term trends.

- Astronomical tide modulates sea level extremes over more than 80% of the global coastlines. The main areas dominated by the non-tidal residual sea level component are the coasts in the Gulf of Mexico, the south and east coasts of the North Sea, the coasts of Argentina and Uruguay and coasts in semienclosed seas, such as the Red Sea and the Japan Sea.

- Robust projected changes have been obtained over more than 25% of the ocean surface in significant wave height for return periods from 5 to 100 years by the end of the century under the RCP4.5 and RCP8.5 concentration scenarios (*S.Obj. 5*). The Southern Ocean is the region where the most robust increase in extreme significant wave height has been projected, whereas the tropical north Pacific has shown the most robust decrease in extreme significant wave height.

- Changes in extreme events are smaller and less robust for RCP4.5 than for RCP8.5. The robustness of the projected changes reduces from the latter to the former globally around 10% for all the estimated return periods. Therefore, future impacts caused by extreme wave heights will be conditioned by the strategies taken for reducing greenhouse gas emissions.

- Robust discrepancies have been found after comparing the future behavior of mean and extreme wind wave conditions (*S.Obj 6*). The main ocean regions showing divergent behaviors are the southeast Indian Ocean, northwest Atlantic Ocean and northeast Pacific Ocean, all of them projecting an increase in significant wave height return values and a decrease in annual mean significant wave height. Therefore, this dissertation demonstrates that the extrapolation of the projected behavior of mean wave conditions to extremes could lead to severe misleading results.

- The analysis of the future changes in wave climate from directional spectra has demonstrated that the standard approach based on integrated parameters can mask relevant information about the projected changes (*S.Obj 7*). Each wave system within the spectrum has shown projected changes characterized by a specific sign and magnitude. Mean integrated parameters, by its own nature, integrate all these changes, masking the individual system information. In addition, they integrate the information about the robustness of the projected changes, which sometimes could lead to low robust changes in significant wave height while changes for certain individual systems are instead robust, for example.

- The use of integrated wave parameters may lead to misleading results on impact assessment studies as they could mask important increases in wave height or wave period for certain wave systems, as well as significant direction shifts. In this regard, a detail analysis of the projected changes in individual wave systems reaching a coastal stretch may give a more realistic view of the impacts that wave climate changes due to climate change could generate.

- The global assessment of the future behavior of wind waves based on wave directional spectra (*S.Obj 8*) significantly increases understanding of the projected changes in wave climate due to climate change. Projected changes in directional spectra have been assessed by the end of the century and for the RCP8.5 concentration scenario.

- The individual change signal of each wave system propagates across the oceans, so that the projected change at each ocean location may integrate changes in wave systems generated locally or remotely. In this regard, the increasing projected change in Southern Ocean swells propagates north beyond 30°N, significantly contributing to the projected changes in tropical regions such as the tropical South Atlantic and tropical Southeast Pacific. The convergence of multiple wave systems in tropical Pacific latitudes induces highly complex spectral change patterns.
- In order to assess the changes in the main wave systems propagating across the oceans (*S.Obj 9*), projected changes in directional spectra have been geographically clusterized. The resulting sixteen spectral patterns of change have been individually analyzed by assessing the changes in the effective flux propagating toward a representative point of each group.

8.2 Thesis derived scientific references

This work yielded several scientific contributions in the form of papers and conference presentations.

Research articles

- **Lobeto, H.**, Menendez, M., Losada, I. J., Hemer, M. (2022). The effect of climate change on wind wave directional spectra. Global and Planetary Change, 103820. DOI.
- **Lobeto, H.**, Menendez, M., Losada, I. J. (2021). Projections of directional spectra help to unravel the future behavior of wind waves. Frontiers in Marine Science. DOI.
- **Lobeto, H.**, Menendez, M., Losada, I.J. (2021) Future behavior of wind wave extremes due to climate change. Sci Rep 11, 7869. DOI.
- **Lobeto, H.**, Menendez, M., Losada, I. J. (2018). Toward a methodology for estimating coastal extreme sea levels from satellite altimetry. JGR: Oceans. DOI.

Conference presentations

- **Lobeto, H.**, Menendez, M., Toimil, A. Evaluación de los cambios proyectados en el clima extremo del oleaje e implicaciones en impactos costeros. November, 2022. Uhinak 2022.

- **Lobeto, H.**, Semedo, A., Menendez, M., Lemos, G., Ranasinghe, R., Dastgheib, A. On the global assessment of the coastal wave storminess. EGU General Assembly 2022. May, 2022. Vienna, Austria.
- **Lobeto, H.**, Menendez, M. A global study of coastal extreme sea level climate variations from satellite altimetry data. Ocean Science Meeting 2022. March, 2022. Online.
- **Lobeto, H.**, Menendez, M., Losada I.J. Projected changes in wind wave directional spectra and their impact on coastal processes. EGU General Assembly 2021. April, 2021. Online.
- **Lobeto, H.**, Menendez, M., Losada I.J, Hemer, M. Exploring directional spectra data to assess future changes in wind wave climate. COWCLIP meeting 2021. May, 2021. Online.
- **Lobeto, H.**, Menendez, M. Coastal extreme sea levels from satellite altimetry: a global study. 12th Coastal Altimetry Workshop. February, 2020. Frascati, Italia.
- **Lobeto, H.**, Menendez, M. Towards a Methodology for Estimating Extreme Return Levels and Its Climate Variability of Coastal Sea Level from Satellite Altimetry. 25 Years of Progress in Radar Altimetry Symposium. September, 2018. Azores, Portugal.

8.3 Future Research

This section summarizes the ongoing work and potential future lines of research derived from the analyses conducted throughout this thesis.

- New coastal altimetry retrackers are continuously improving the accuracy of altimetry measurements nearshore and reducing the distances to the coast where altimetry data are reliable. Incorporate altimetry new products with better accuracy into the methodology proposed in Chapter 2 could improve the characterization of sea level extreme events and reduce the differences found with respect to tide gauge data.
- Chapter 2 proposes several correction constituents to reduce the differences between altimetry and tide gauge return values of the non-tidal residual sea level component. Nevertheless, as can be seen in Fig. 2.8 and Fig. 2.10, there is still room for improvement. Therefore, new correction constituents need to be explored, as well as possible improvements on those proposed above.
- According to the method proposed in Chapter 2 to define the altimetry maxima sample at each tide gauge station location, the final correlation cut-off defines an area to select

altimetry data of different shape and extension for each location analyzed. To improve the application of the methodology where no in situ information is available for a target coastal location, a method to select the regional maxima values from the altimetry data is needed.

- The proposed methodology to assess sea level extremes from altimetry data could be applied to characterize extreme events of other sea surface dynamics, such as wind waves, using buoys as calibration reference instead of tide gauges.
- Chapter 3 comprises an analysis of the coastal wave storminess along the global coastlines based on a unique criterion. This approach is very useful as it allows to compare the results from different geographic regions. However, since waves storms may have different origins, the methodology could be improved by individually selecting the thresholds and/or independence times required to classify storm events at each coastal location. The time evolution of the wave storms behaviour, in addition to the duration, is also a required input for related erosion and flooding coastal impacts.
- Chapter 3 classifies the global coastlines in terms of their degree of wave storminess. Nevertheless, coastal storms involve other sea surface dynamics beyond wind waves such as sea level. In this context, a similar approach to the one proposed in Chapter 3 could be followed to assess the coastal storminess, but instead considering different sea level components in the storm definition criteria and subsequent coastal classification, such as the storm surge or the astronomical tide.
- Chapter 4 analyzes the long-term variability of non-tidal residual extreme events. Results depict a general increasing pattern likely induced by the mean sea level rise. Further analyses are needed to derive the causes of these increasing trends, as well as the individual trends associated to each sea level component involved.
- Chapter 5 assesses the projected changes in wind waves with very low probability of occurrence and discusses about the plausible causes of the changes found. Deeper studies are required to identify the underlying causes of the projected changes, as well as the reasons for the great uncertainty found in some ocean regions.
- The assessment of projected changes in wind wave extremes due to climate change is characterized by great uncertainty. Further research to better understand the contribution of different uncertainty sources are needed, especially for the future behavior of wave heights with very low probability of occurrence. For example, the uncertainty associated to the wave modelling may be assessed by analyzing the differences in projected changes estimated from runs developed with different numerical propagation models.

- The estimated future behavior of mean and extreme wave climate conditions diverges in some ocean regions. Research is needed to identify the causes of these divergences.

- Standard bias correction techniques applied to meteorological variables are now common practice to estimate wave climate projected changes. However, further studies are needed to develop bias correction approaches focused on the multi-dimensional characterization of extreme sea states.

- Despite several methods could be applied for correcting the bias of integrated wave parameters from wave climate projections, a direct application of these methods to directional spectra has not been achieved. Therefore, the development of new methodologies for bias correction in directional spectra is required to avoid biasing of ensemble mean projected changes.

- Chapter 7 shows a clear sign-of-change boundary at 45°S in westerly energy propagating in the Southern Ocean. While south of that latitude an increase is projected, a decrease is projected north of it. This dissertation proposes the poleward shift of the extratropical south storm track as one of the main causes. More detailed analyses are needed to unravel the causes and implications of this dipole behavior.

- The availability of spectral partitions from wind wave hindcasts or reanalyses is increasing. Since spectral partitions inform about the individual characteristics of the wave systems converging at each time step in a certain ocean location, they could be classified to identify the main wave systems reaching that location. Therefore, new methodologies are needed to develop this spectral partition classification from a climate point of view.

- Despite the information provided by wind wave spectra being very useful to understand the future behavior of wind waves, its applicability on coastal impact assessment is very complex. The isolation of wave systems and posterior analysis of the projected changes in their characteristics and climate variability could allow to more easily identify which systems are expected to induce more severe impacts in the future.

- This research provides insights on sea level components and waves. The total water level results as a combination of both sea surface dynamics. Future climate analyses may focus on the combined contribution to high water levels. The hazardous characterization of extreme total water levels combined with other risk components, such as exposure, may be useful to identify higher vulnerability areas.

References

Aarnes, O. J., Reistad, M., Breivik, Ø., Bitner-Gregersen, E., Ingolf Eide, L., Gramstad, O., Magnusson, A. K., Natvig, B., and Vanem, E. (2017). Projected changes in significant wave height toward the end of the 21st century: Northeast Atlantic. *Journal of Geophysical Research: Oceans*, 122(4):3394–3403.

Abdalla, S., Abdeh Kolahchi, A., Ablain, M., Adusumilli, S., Aich Bhowmick, S., Alou-Font, E., Amarouche, L., Andersen, O. B., Antich, H., Aouf, L., Arbic, B., Armitage, T., Arnault, S., Artana, C., Aulicino, G., Ayoub, N., Badulin, S., Baker, S., Banks, C., Bao, L., Barbetta, S., Barceló-Llull, B., Barlier, F., Basu, S., Bauer-Gottwein, P., Becker, M., Beckley, B., Bellefond, N., Belonenko, T., Benkiran, M., Benkouider, T., Bennartz, R., Benveniste, J., Bercher, N., Berge-Nguyen, M., Bettencourt, J., Blarel, F., Blazquez, A., Blumstein, D., Bonnefond, P., Borde, F., Bouffard, J., Boy, F., Boy, J. P., Brachet, C., Brasseur, P., Braun, A., Brocca, L., Brockley, D., Brodeau, L., Brown, S., Bruinsma, S., Bulczak, A., Buzzard, S., Cahill, M., Calmant, S., Calzas, M., Camici, S., Cancet, M., Capdeville, H., Carabajal, C. C., Carrere, L., Cazenave, A., Chassignet, E. P., Chauhan, P., Cherchali, S., Chereskin, T., Cheymol, C., Ciani, D., Cipollini, P., Cirillo, F., Cosme, E., Coss, S., Cotroneo, Y., Cotton, D., Couhert, A., Coutin-Faye, S., Crétaux, J. F., Cyr, F., D'Ovidio, F., Darrozes, J., David, C., Dayoub, N., De Staerke, D., Deng, X., Desai, S., Desjonqueres, J. D., Dettmering, D., Di Bella, A., Díaz-Barroso, L., Dibarboure, G., Dieng, H. B., Dinardo, S., Dobslaw, H., Dodet, G., Doglioli, A., Domeneghetti, A., Donahue, D., Dong, S., Donlon, C., Dorandeu, J., Drezen, C., Drinkwater, M., Du Penhoat, Y., Dushaw, B., Egido, A., Erofeeva, S., Escudier, P., Esselborn, S., Exertier, P., Fablet, R., Falco, C., Farrell, S. L., Faugere, Y., Femenias, P., Fenoglio, L., Fernandes, J., Fernández, J. G., Ferrage, P., Ferrari, R., Fichen, L., Filippucci, P., Flampouris, S., Fleury, S., Fornari, M., Forsberg, R., Frappart, F., laure Frery, M., Garcia, P., Garcia-Mondejar, A., Gaudelli, J., Gaultier, L., Getirana, A., Gibert, F., Gil, A., Gilbert, L., Gille, S., Giulicchi, L., Gómez-Enri, J., Gómez-Navarro, L., Gommenginger, C., Gourdeau, L., Griffin, D., Groh, A., Guerin, A., Guerrero, R., Guinle, T., Gupta, P., Gutknecht, B. D., Hamon, M., Han, G., Hauser, D., Helm, V., Hendricks, S., Hernandez, F., Hogg, A., Horwath, M., Idžanović, M., Janssen, P., Jeansou, E., Jia, Y., Jia, Y., Jiang, L., Johannessen, J. A., Kamachi, M., Karimova, S., Kelly, K., Kim, S. Y., King, R., Kittel, C. M., Klein, P., Klos, A., Knudsen, P., Koenig, R., Kostianoy, A., Kouraev, A., Kumar, R., Labroue, S., Lago, L. S., Lambin, J., Lasson, L., Laurain, O., Laxenaire, R., Lázaro, C., Le Gac, S., Le Sommer, J., Le Traon, P. Y., Lebedev, S., Léger, F., Legresy, B., Lemoine, F., Lenain, L., Leuliette, E., Levy, M., Lillibridge, J., Liu, J., Llovel, W., Lyard, F., Macintosh, C., Makhoul Varona, E., Manfredi, C., Marin, F., Mason, E., Massari, C., Mavrocordatos, C., Maximenko, N., McMillan, M., Medina, T., Melet, A., Meloni, M., Mertikas, S., Metref, S., Meyssignac, B., Minster, J. F., Moreau, T., Moreira, D., Morel, Y., Morrow, R., Moyard, J., Mulet, S., Naeije, M., Nerem, R. S., Ngodock, H., Nielsen, K., Nilsen, J. E. Ø., Niño, F., Nogueira Loddo, C., Noûs, C., Obligis, E., Otosaka, I., Otten, M., Oztunali Ozbahceci, B., P. Raj, R., Paiva, R., Paniagua, G., Paolo, F., Paris, A., Pascual, A., Passaro, M., Paul, S., Pavelsky, T., Pearson, C., Penduff, T., Peng, F., Perosanz, F., Picot, N., Piras, F., Poggiali, V., Poirier, É., Ponce de León, S., Prants, S., Prigent, C., Provost, C., Pujol, M. I., Qiu, B., Quilfen, Y., Rami, A., Raney, R. K., Raynal, M., Remy, E., Rémy, F., Restano, M., Richardson, A., Richardson, D., Ricker, R., Ricko, M., Rinne, E., Rose, S. K., Rosmorduc, V., Rudenko, S., Ruiz, S., Ryan, B. J., Salaün, C., Sanchez-Roman, A., Sandberg Sørensen, L., Sandwell, D., Saraceno, M., Scagliola, M., Schaeffer, P., Scharffenberg, M. G., Scharroo, R., Schiller, A., Schneider, R., Schwatke, C., Scozzari, A., Ser-giacomi, E., Seyler, F., Shah, R., Sharma, R., Shaw, A., Shepherd, A., Shriver, J., Shum, C. K., Simons, W., Simonsen, S. B., Slater, T., Smith, W., Soares, S., Sokolovskiy, M., Soudarin, L., Spatar, C., Speich, S., Srinivasan, M., Srokosz, M., Stanev, E., Staneva, J., Steunou, N., Stroeve, J., Su, B., Sulistioadi, Y. B., Swain, D., Sylvestre-baron, A., Taburet, N., Tailleux, R., Takayama, K., Tapley, B., Tarpanelli, A., Tavernier, G., Testut, L., Thakur, P. K., Thibaut, P., Thompson, L. A., Tintoré, J., Tison, C., Tourain, C., Tournadre, J., Townsend, B., Tran, N., Trilles, S., Tsamados, M., Tseng, K. H., Ubelmann, C., Uebbing, B., Vergara, O., Verron, J., Vieira, T., Vignudelli, S., Vinogradova Shiffer, N., Visser, P., Vivier, F., Volkov, D., von Schuckmann, K., Vuglinskii, V., Vuilleumier, P., Walter, B., Wang, J., Wang, C., Watson, C., Wilkin, J., Willis, J., Wilson, H., Woodworth, P., Yang, K., Yao, F., Zaharia, R., Zakharova, E., Zaron, E. D., Zhang, Y., Zhao, Z., Zinchenko, V., and Zlotnicki, V. (2021). Altimetry for the future: Building on 25 years of progress. *Advances in Space Research*, 68(2):319–363.

Abidin, N. Z., Adam, M. B., and Midi, H. (2012). The Goodness-of-fit Test for Gumbel Distribution: A Comparative Study. *Matematika*, 28(1):35–48.

Adebisi, N., Balogun, A. L., Min, T. H., and Tella, A. (2021). Advances in estimating Sea Level Rise: A review of tide gauge, satellite altimetry and spatial data science approaches. *Ocean and Coastal Management*, 208(April).

Alvarez-Cuesta, M., Toimil, A., and Losada, I. J. (2021a). Modelling long-term shoreline evolution in highly anthropized coastal areas. Part 1: Model description and validation.

Coastal Engineering, 169(July):103960.

Alvarez-Cuesta, M., Toimil, A., and Losada, I. J. (2021b). Modelling long-term shoreline evolution in highly anthropized coastal areas. Part 2: Assessing the response to climate change. *Coastal Engineering*, 168(July):103961.

Alves, B., Angnuureng, D. B., Morand, P., and Almar, R. (2020). A review on coastal erosion and flooding risks and best management practices in West Africa: what has been done and should be done. *Journal of Coastal Conservation*, 24(3).

Amarouche, K., Akpınar, A., Çakmak, R. E., Houma, F., and Bachari, N. E. I. (2020). Assessment of storm events along the Algiers coast and their potential impacts. *Ocean Engineering*, 210.

Amarouche, K., Akpınar, A., and Semedo, A. (2022). Wave storm events in the Western Mediterranean Sea over four decades. *Ocean Modelling*, 170.

Amores, A. and Marcos, M. (2020). Ocean swells along the global coastlines and their climate projections for the twenty-first century. *Journal of Climate*, 33(1):185–199.

Anderson, T. W. and Darling, D. A. (1954). A Test of Goodness of Fit. *Journal of the American Statistical Association*, 49(268):765–769.

Anfuso, G., Rangel-Buitrago, N., Cortés-Useche, C., Iglesias Castillo, B., and Gracia, F. J. (2016). Characterization of storm events along the Gulf of Cadiz (eastern central Atlantic Ocean). *International Journal of Climatology*, 36(11):3690–3707.

Ardhuin, F., Chapron, B., and Collard, F. (2009). Observation of swell dissipation across oceans. *Geophysical Research Letters*, 36(6).

Ardhuin, F., O'Reilly, W. C., Herbers, T. H., and Jessen, P. F. (2003). Swell transformation across the continental shelf. Part I: Attenuation and directional broadening. *Journal of Physical Oceanography*, 33(9):1921–1939.

Ardhuin, F., Rogers, E., Babanin, A. V., Filipot, J. F., Magne, R., Roland, A., van der Westhuysen, A., Queffeulou, P., Lefevre, J. M., Aouf, L., and Collard, F. (2010). Semiempirical dissipation source functions for ocean waves. Part I: Definition, calibration, and validation. *Journal of Physical Oceanography*, 40(9):1917–1941.

Armaroli, C., Ciavola, P., Perini, L., Calabrese, L., Lorito, S., Valentini, A., and Masina, M. (2012). Critical storm thresholds for significant morphological changes and damage along the Emilia-Romagna coastline, Italy. *Geomorphology*, 143-144:34–51.

Arthur, D. and Vassilvitskii, S. (2007). K-means++: The advantages of careful seeding. *Proceedings of the Annual ACM-SIAM Symposium on Discrete Algorithms*, 07-09-Janu:1027–1035.

Athanasiou, P., van Dongeren, A., Giardino, A., Vousdoukas, M., Antolinez, J. A., and Ranasinghe, R. (2021). A Clustering Approach for Predicting Dune Morphodynamic Response to Storms Using Typological Coastal Profiles: A Case Study at the Dutch Coast. *Frontiers in Marine Science*, 8.

Aucan, J., Hoeke, R., and Merrifield, M. A. (2012). Wave-driven sea level anomalies at the Midway tide gauge as an index of North Pacific storminess over the past 60 years. *Geophysical Research Letters*, 39(17):1–6.

Bader, J., Mesquita, M. D., Hodges, K. I., Keenlyside, N., Østerhus, S., and Miles, M. (2011). A review on Northern Hemisphere sea-ice, storminess and the North Atlantic Oscillation: Observations and projected changes.

Bao, L., Gneiting, T., Grimit, E. P., Guttorp, P., and Raftery, A. E. (2010). Bias correction and bayesian model averaging for ensemble forecasts of surface wind direction. *Monthly Weather Review*, 138(5):1811–1821.

Battjes, J. A. and Janssen, J. P. (1979). ENERGY LOSS AND SET-UP DUE TO BREAKING OF RANDOM WAVES. In *Proceedings of the Coastal Engineering Conference*, volume 1, pages 569–587.

Benoit, M. (1992). Practical comparative performance survey of methods used for estimating directional wave spectra from heave-pitch-roll data. *Coastal Engineering*, pages 62–75.

Bernardara, P., Mazas, F., Kergadallan, X., and Hamm, L. (2014). A two-step framework for over-threshold modelling of environmental extremes. *Natural Hazards and Earth System Sciences*, 14(3):635–647.

Bidlot, J.-r. (2001). ECMWF wave model product. *ECMWF Newsletters*, 91:9–15.

Birol, F., Léger, F., Passaro, M., Cazenave, A., Niño, F., Calafat, F. M., Shaw, A., Legeais, J. F., Gouzenes, Y., Schwatke, C., and Benveniste, J. (2021). The X-TRACK/ALES multi-mission processing system: New advances in altimetry towards the coast. *Advances in Space Research*, 67(8):2398–2415.

Boukhanovsky, A. V., Lopatoukhin, L. J., and Guedes Soares, C. (2007). Spectral wave climate of the North Sea. *Applied Ocean Research*, 29(3):146–154.

Bradbury, D. L. (1958). On the Behavior Patterns of Cyclones and Anticyclones as Related to Zonal Index. *Bulletin of the American Meteorological Society*, 39(3):149–151.

Bricheno, L. M. and Wolf, J. (2018). Future Wave Conditions of Europe, in Response to High-End Climate Change Scenarios. *Journal of Geophysical Research: Oceans*, 123(12):8762–8791.

Caires, S. and Sterl, A. (2005). 100-year return value estimates for ocean wind speed and significant wave height from the ERA-40 data. *Journal of Climate*, 18(7):1032–1048.

Caires, S., Swail, V. R., and Wang, X. L. (2006). Projection and analysis of extreme wave climate. *Journal of Climate*, 19(21):5581–5605.

Camargo, S. J. (2013). Global and regional aspects of tropical cyclone activity in the CMIP5 models. *Journal of Climate*, 26(24):9880–9902.

Camus, P., Losada, I., Izaguirre, C., Espejo, A., Menendez, M., and Perez, J. (2017). Statistical wave climate projections for coastal impact Earth ' s Future. *Earth ' s Future*.

Camus, P., Méndez, F. J., Losada, I. J., Menéndez, M., Espejo, A., Pérez, J., Rueda, A., and Guanche, Y. (2014a). A method for finding the optimal predictor indices for local wave climate conditions. *Ocean Dynamics*, 64(7):1025–1038.

Camus, P., Mendez, F. J., Medina, R., and Cofiño, A. S. (2011). Analysis of clustering and selection algorithms for the study of multivariate wave climate. *Coastal Engineering*, 58(6):453–462.

Camus, P., Menéndez, M., Méndez, F. J., Izaguirre, C., Espejo, A., Cánovas, V., Pérez, J., Rueda, A., Losada, I. J., and Medina, R. (2014b). A weather-type statistical downscaling framework for ocean wave climate. *Journal of Geophysical Research: Oceans*, 119(11):7389–7405.

Carrère, L. and Lyard, F. (2003). Modeling the barotropic response of the global ocean to atmospheric wind and pressure forcing - comparisons with observations. *Geophysical Research Letters*, 30(6):1997–2000.

Casas-Prat, M., McInnes, K. L., Hemer, M. A., and Sierra, J. P. (2016). Future wave-driven coastal sediment transport along the Catalan coast (NW Mediterranean). *Regional Environmental Change*, 16(6):1739–1750.

Casas-Prat, M., Wang, X. L., and Swart, N. (2018). CMIP5-based global wave climate projections including the entire Arctic Ocean. *Ocean Modelling*, 123(April 2017):66–85.

Castelle, B., Marieu, V., Bujan, S., Splinter, K. D., Robinet, A., Sénéchal, N., and Ferreira, S. (2015). Impact of the winter 2013-2014 series of severe Western Europe storms on a double-barred sandy coast: Beach and dune erosion and megacusp embayments. *Geomorphology*, 238:135–148.

Catto, J. L., Shaffrey, L. C., and Hodges, K. I. (2011). Northern hemisphere extratropical cyclones in a warming climate in the higem high-resolution climate model. *Journal of Climate*, 24(20):5336–5352.

Cavaleri, L., Fox-Kemper, B., and Hemer, M. (2012). Wind waves in the coupled climate system. *Bulletin of the American Meteorological Society*, 93(11):1651–1661.

Cazenave, A., Dieng, H. B., Meyssignac, B., Von Schuckmann, K., Decharme, B., and Berthier, E. (2014). The rate of sea-level rise. *Nature Climate Change*, 4(5):358–361.

Cazenave, A., Gouzenes, Y., Birol, F., Leger, F., Passaro, M., Calafat, F. M., Shaw, A., Nino, F., Legeais, J. F., Oelsmann, J., Restano, M., and Benveniste, J. (2019). measured by a network of virtual altimetry stations. (2022):1–9.

Chang, E. K. (2017). Projected Significant Increase in the Number of Extreme Extratropical Cyclones in the Southern Hemisphere. *Journal of Climate*, 30(13):4915–4935.

Chang, E. K., Guo, Y., and Xia, X. (2012). CMIP5 multimodel ensemble projection of storm track change under global warming. *Journal of Geophysical Research Atmospheres*, 117(23):1–19.

Christensen, J. H., Boberg, F., Christensen, O. B., and Lucas-Picher, P. (2008). On the need for bias correction of regional climate change projections of temperature and precipitation. *Geophysical Research Letters*, 35(20).

Christie, E. K., Spencer, T., Owen, D., McIvor, A. L., Möller, I., and Viavattene, C. (2018). Regional coastal flood risk assessment for a tidally dominant, natural coastal setting: North Norfolk, southern North Sea. *Coastal Engineering*, 134:177–190.

Church, J. A., Clark, P. U., Cazenave, A., Gregory, J. M., Jevrejeva, S., Levermann, A., Merrifield, M. A., Milne, G. A., Nerem, R. S., Nunn, P. D., Payne, A. J., Pfeffer, W. T., Stammer, D., and Unnikrishnan, A. S. (2013). Chapter 13: Sea level change. In Stocker, T., Qin, D., Plattner, G.-K., Tignor, M., Allen, S., Boschung, J., Nauels, A., Xia, Y., Bex, V., and Midgley, P., editors, *Climate Change 2013: The Physical Science Basis. Contribution of Working Group I to the Fifth Assessment Report of the Intergovernmental Panel on Climate Change*, chapter 13, pages 1137–1216. Cambridge University Press, New York.

Cid, A., Castanedo, S., Abascal, A. J., Menéndez, M., and Medina, R. (2014). A high resolution hindcast of the meteorological sea level component for Southern Europe: the GOS dataset. *Climate Dynamics*, 43(7-8):2167–2184.

Cid, A., Menéndez, M., Castanedo, S., Abascal, A. J., Méndez, F. J., and Medina, R. (2016). Long-term changes in the frequency, intensity and duration of extreme storm surge events in southern Europe. *Climate Dynamics*, 46(5-6):1503–1516.

Cipollini, P., Calafat, F. M., Jevrejeva, S., Melet, A., and Prandi, P. (2017). Monitoring Sea Level in the Coastal Zone with Satellite Altimetry and Tide Gauges. *Surveys in Geophysics*, 38(1):33–57.

Codiga, D. L. (2011). Unified Tidal Analysis and Prediction Using the UTide Matlab Functions. Technical Report 2011.01. Technical report, Graduate School of Oceanography, University of Rhose Island, Narragansett, RI. 59pp.

Coles, S. (2001). *An introduction to statistical modeling of extreme values.*

Collins, M., Knutti, R., Arblaster, J., Dufresne, J.-L., Fichefet, T., Friedlingstein, P., Gao, X., Gutowski, W. J., Johns, T., Krinner, G., Shongwe, M., Tebaldi, C., Weaver, A. J., and Wehner, M. (2013). Long-term climate change: Projections, commitments and irreversibility. In *Climate Change 2013: the Physical Science Basis: Working Group I Contribution to the Fifth Assessment Report of the Intergovernmental Panel on Climate Change.*

Corbella, S. and Stretch, D. D. (2012). Predicting coastal erosion trends using non-stationary statistics and process-based models. *Coastal Engineering*, 70:40–49.

Cubasch, U., Wuebbles, D., Chen, D., Facchini, M., Frame, D., Mahowald, N., and Winther, J.-G. (2013). Introduction. In Stocker, T. F., Quin, D., Plattner, G.-K., Tignor, M., Allen, S. K., Boschung, J., Nauels, A., Xia, Y., Bex, V., and Midgley, P. M., editors, *Climate Change 2013: The Physical Science Basis. Contribution of Working Group I to the Fifth Assessment Report of the Intergovenermnetal Panel on Climate Change.*

Davies, G., Callaghan, D. P., Gravios, U., Jiang, W., Hanslow, D., Nichol, S., and Baldock, T. (2017). Improved treatment of non-stationary conditions and uncertainties in probabilistic models of storm wave climate. *Coastal Engineering*, 127:1–19.

Del Río, L., Plomaritis, T. A., Benavente, J., Valladares, M., and Ribera, P. (2012). Establishing storm thresholds for the Spanish Gulf of Cádiz coast. *Geomorphology*, 143-144:13–23.

Denys, P. H., Beavan, R. J., Hannah, J., Pearson, C. F., Palmer, N., Denham, M., and Hreinsdottir, S. (2020). Sea Level Rise in New Zealand: The Effect of Vertical Land Motion on Century-Long Tide Gauge Records in a Tectonically Active Region. *Journal of Geophysical Research: Solid Earth*, 125(1):1–19.

Déqué, M. (2007). Frequency of precipitation and temperature extremes over France in an anthropogenic scenario: Model results and statistical correction according to observed values. *Global and Planetary Change*, 57(1-2):16–26.

Dietrich, J. C., Bunya, S., Westerink, J. J., Ebersole, B. A., Smith, J. M., Atkinson, J. H., Jensen, R., Resio, D. T., Luettich, R. A., Dawson, C., Cardone, V. J., Cox, A. T., Powell, M. D., Westerink, H. J., and Roberts, H. J. (2010). A High-Resolution coupled riverine flow, tide, wind, wind wave, and storm surge model for southern louisiana and mississippi. Part II: Synoptic description and analysis of hurricanes katrina and rita. *Monthly Weather Review*, 138(2):378–404.

Dima, I. M. and Wallace, J. M. (2003). On the seasonality of the Hadley Cell. *Journal of the Atmospheric Sciences*, 60(12):1522–1527.

Dobrynin, M., Murawsky, J., and Yang, S. (2012). Evolution of the global wind wave climate in CMIP5 experiments. *Geophysical Research Letters*, 39(17):2–7.

Dodet, G., Melet, A., Ardhuin, F., Bertin, X., Idier, D., and Almar, R. (2019). The Contribution of Wind-Generated Waves to Coastal Sea-Level Changes.

Dodet, G., Piolle, J. F., Quilfen, Y., Abdalla, S., Accensi, M., Ardhuin, F., Ash, E., Bidlot, J. R., Gommenginger, C., Marechal, G., Passaro, M., Quartly, G., Stopa, J., Timmermans, B., Young, I., Cipollini, P., and Donlon, C. (2020). The Sea State CCI dataset v1: Towards a sea state climate data record based on satellite observations. *Earth System Science Data*, 12(3):1929–1951.

Dolan, R. and Davis, R. (1994). Coastal Storm Hazards. *Journal of Coastal Research*, (Special Issue No. 12):103–114.

Dolan, R. and Davis, R. E. (1992). An intensity scale for Atlantic Coast Northeast Storms. *Journal of Coastal Research*, 8(4):840–853.

Donelan, M. A., Hamilton, J., and Hui, W. H. (1985). Directional spectra of wind-generated ocean waves. *Philosophical Transactions of the Royal Society of London. Series A, Mathematical and Physical Sciences*, 315:509–562.

Dong, S., Wang, N., Lu, H., and Tang, L. (2015). Bivariate distributions of group height and length for ocean waves using Copula methods. *Coastal Engineering*, 96:49–61.

Echevarria, E. R., Hemer, M. A., and Holbrook, N. J. (2019). Seasonal Variability of the Global Spectral Wind Wave Climate. *Journal of Geophysical Research: Oceans*, 124(4):2924–2939.

Echevarria, E. R., Hemer, M. A., Holbrook, N. J., and Marshall, A. G. (2020). Influence of the Pacific-South American Modes on the Global Spectral Wind-Wave Climate. *Journal of Geophysical Research: Oceans*, 125(8):1–16.

Egbert, G. D. and Erofeeva, S. Y. (2002). Efficient inverse modeling of barotropic ocean tides. *Journal of Atmospheric and Oceanic Technology*, 19(2):183–204.

Espejo, A., Camus, P., Losada, I. J., and Méndez, F. J. (2014). Spectral Ocean Wave Climate Variability Based on Atmospheric Circulation Patterns. *Journal of Physical Oceanography*, 44(8):2139–2152.

Fan, Y., Held, I. M., Lin, S. J., and Wang, X. L. (2013). Ocean warming effect on surface gravity wave climate change for the end of the twenty-first century. *Journal of Climate*, 26(16):6046–6066.

Fan, Y., Lin, S. J., Griffies, S. M., and Hemer, M. A. (2014). Simulated global swell and wind-sea climate and their responses to anthropogenic climate change at the end of the twenty-first century. *Journal of Climate*, 27(10):3516–3536.

Ferreira, J. A. and Guedes Soares, C. (2000). Modelling distributions of significant wave height. *Coastal Engineering*, 40(4):361–374.

Fisher, R. A. and Tippett, L. H. C. (1928). Limiting forms of the frequency distribution of the largest or smallest member of a sample. *Mathematical Proceedings of the Cambridge Philosophical Society*, 24(2):180–190.

Flato, G., Marotzke, J., Abiodun, B., Braconnot, P., Chou, S., Collins, W., Cox, P., Driouech, F., Emori, S., Eyring, V., Forest, C., Gleckler, P., Guilyardi, E., Jakob, C., Kattsov, V., Reason, C., and Rummukainen, M. (2013). Evaluation of Climate Models. In Stocker, T. F., Quin, D., Plattner, G.-K., Tignor, M., Allen, S. K., Boschung, J., Nauels, A., Xia, Y., Bex, V., and Midgley, P. M., editors, *Climate Change 2013: The Physical Science Basis. Contribution of Working Group I to the Fifth Assessment Report of the Intergovenermnetal Panel on Climate Change.*

Gerkema, T. (2019). *An introduction to tides.* Cambridge University Press.

Gillett, N. P., Kell, T. D., and Jones, P. D. (2006). Regional climate impacts of the Southern Annular Mode. *Geophysical Research Letters*, 33(23):1–4.

Goda, Y. (2010). *Random seas and design of maritime structures (3rd Edition)*, volume 33.

Goswami, B. N., Wu, G., and Yasunari, T. (2006). The annual cycle, intraseasonal oscillations, and roadblock to seasonal predictability of the Asian summer monsoon. *Journal of Climate*, 19(20):5078–5099.

Grise, K. M. and Davis, S. M. (2020). Hadley cell expansion in CMIP6 models. *Atmospheric Chemistry and Physics*, 20(9):5249–5268.

Haigh, I. D., Eliot, M., and Pattiaratchi, C. (2011). Global influences of the 18.61 year nodal cycle and 8.85 year cycle of lunar perigee on high tidal levels. *Journal of Geophysical Research: Oceans*, 116(6):1–16.

Haigh, I. D., MacPherson, L. R., Mason, M. S., Wijeratne, E. M., Pattiaratchi, C. B., Crompton, R. P., and George, S. (2014). Estimating present day extreme water level exceedance probabilities around the coastline of Australia: Tropical cyclone-induced storm surges. *Climate Dynamics*, 42(1-2):139–157.

Hanson, J. L. and Phillips, O. M. (2001). Automated analysis of ocean surface directional wave spectra. *Journal of Atmospheric and Oceanic Technology*, 18(2):277–293.

Haritos, N. (2007). Introduction to the analysis and design of offshore structures–an overview. *Electronic Journal of Structural Engineering*, (1):55–65.

Harley, M. D., Turner, I. L., Kinsela, M. A., Middleton, J. H., Mumford, P. J., Splinter, K. D., Phillips, M. S., Simmons, J. A., Hanslow, D. J., and Short, A. D. (2017). Extreme coastal erosion enhanced by anomalous extratropical storm wave direction. *Scientific Reports*, 7(1):1–9.

Harvey, B., Cook, P., Shaffrey, L. C., and Schiemann, R. (2020). The response of the Northern Hemisphere storm tracks and jetstreams to climate change in the CMIP3, CMIP5, and CMIP6 climate models. *Journal of Geophysical Research (Atmospheres)*, pages 0–3.

Hasselmann, K., Barnett, T. P., Bouws, E., Carlson, H., Cartwright, D. E., Eake, K., Euring, J. A., Gicnapp, A., Hasselmann, D. E., Kruseman, P., Meerburg, A., Mullen, P., Olbers, D. J., Richren, K., Sell, W., and Walden, H. (1973). Measurements of wind-wave growth and swell decay during the joint North Sea wave project (JONSWAP). (January).

Hasselmann, S., Hasselmann, K., Allender, J. H., and Barnett, T. P. (1985). Computations and parameterizations of the nonlinear energy transfer in a gravity-wave spectrum. Part II: parameterizations of the nonlinear energy transfer for application in wave models. *J. PHYS. OCEANOGR.*, 15(11 , Nov. 1985):1378–1391.

Hatzikyriakou, A. and Lin, N. (2018). Assessing the vulnerability of structures and residential communities to storm surge: An analysis of flood impact during hurricane sandy. *Frontiers in Built Environment*, 4.

Hemer, M. A., Fan, Y., Mori, N., Semedo, A., and Wang, X. L. (2013a). Projected changes in wave climate from a multi-model ensemble. *Nature Climate Change*, 3(5):471–476.

Hemer, M. A., Katzfey, J., and Trenham, C. E. (2013b). Global dynamical projections of surface ocean wave climate for a future high greenhouse gas emission scenario. *Ocean Modelling*, 70:221–245.

Hemer, M. A., McInnes, K. L., and Ranasinghe, R. (2012a). Climate and variability bias adjustment of climate model-derived winds for a southeast Australian dynamical wave model. *Ocean Dynamics*, 62(1):87–104.

Hemer, M. A., Wang, X. L., Weisssse, R., and Swail, V. R. (2012b). Advancing wind-waves climate science: The COWCLIP project. *Bulletin of the American Meteorological Society*, 93(6):791–796.

Hersbach, H., Bell, B., Berrisford, P., Hirahara, S., Horányi, A., Muñoz-Sabater, J., Nicolas, J., Peubey, C., Radu, R., Schepers, D., Simmons, A., Soci, C., Abdalla, S., Abellan, X., Balsamo, G., Bechtold, P., Biavati, G., Bidlot, J., Bonavita, M., De Chiara, G., Dahlgren, P., Dee, D., Diamantakis, M., Dragani, R., Flemming, J., Forbes, R., Fuentes, M., Geer, A., Haimberger, L., Healy, S., Hogan, R. J., Hólm, E., Janisková, M., Keeley, S., Laloyaux, P., Lopez, P., Lupu, C., Radnoti, G., de Rosnay, P., Rozum, I., Vamborg, F., Villaume, S., and Thépaut, J. N. (2020). The ERA5 global reanalysis. *Quarterly Journal of the Royal Meteorological Society*, 146(730):1999–2049.

Hoeke, R. K., McInnes, K. L., Kruger, J. C., McNaught, R. J., Hunter, J. R., and Smithers, S. G. (2013). Widespread inundation of Pacific islands triggered by distant-source wind-waves. *Global and Planetary Change*, 108:128–138.

Holthuijsen, L. H. (2007). *Waves in oceanic and coastal waters*, volume 9780521860.

Hoskins, B. J. and Hodges, K. I. (2005). A new perspective on Southern Hemisphere storm tracks. *Journal of Climate*, 18(20):4108–4129.

Hossain, M. N. (2015). Analysis of human vulnerability to cyclones and storm surges based on influencing physical and socioeconomic factors: Evidences from coastal Bangladesh. *International Journal of Disaster Risk Reduction*, 13:66–75.

In Situ Thematic Centre (2021). Global Ocean - Delayed Mode Wave Product, E.U. Copernicus Marine Service Information [Data set].

IPCC (2019). IPCC Special Report on the Ocean and Cryosphere in a Changing Climate. *Intergovernmental Panel on Climate Change*, pages –undefined.

Izaguirre, C., Méndez, F. J., Menéndez, M., and Losada, I. J. (2011). Global extreme wave height variability based on satellite data. *Geophysical Research Letters*, 38(10):1–6.

Jiang, H. and Mu, L. (2019). Wave climate from spectra and its connections with local and remote wind climate. *Journal of Physical Oceanography*, 49(2):543–559.

Jiang, H., Stopa, J. E., Wang, H., Husson, R., Mouche, A., Chapron, B., and Chen, G. (2016). Tracking the attenuation and nonbreaking dissipation of swells using altimeters. *Journal of Geophysical Research: Oceans*, 121(2):1445–1458.

Jiménez, J. A., Sancho-García, A., Bosom, E., Valdemoro, H. I., and Guillén, J. (2012). Storm-induced damages along the Catalan coast (NW Mediterranean) during the period 1958-2008. *Geomorphology*, 143-144:24–33.

Kates, R. W., Colten, C. E., Laska, S., and Leatherman, S. P. (2006). Reconstruction of New Orleans after Hurricane Katrina: A research perspective. *Proceedings of the National Academy of Sciences of the United States of America*, 103(40):14653–14660.

Kaufman, L. and Rousseeuw, P. J. (2009). *Finding groups in data: an introduction to cluster analysis*, volume 344. John Wiley & Sons.

Kirezci, E., Young, I. R., Ranasinghe, R., Muis, S., Nicholls, R. J., Lincke, D., and Hinkel, J. (2020). Projections of global-scale extreme sea levels and resulting episodic coastal flooding over the 21st Century. *Scientific Reports*, 10(1):1–12.

Knutti, R., Masson, D., and Gettelman, A. (2013). Climate model genealogy: Generation CMIP5 and how we got there. *Geophysical Research Letters*, 40(6):1194–1199.

Kopp, R. E., Horton, R. M., Little, C. M., Mitrovica, J. X., Oppenheimer, M., Rasmussen, D. J., Strauss, B. H., and Tebaldi, C. (2014). Probabilistic 21st and 22nd century sea-level projections at a global network of tide-gauge sites. *Earth's Future*, 2(8):383–406.

Korotaev, G. K., Saenko, O. A., and Koblinsky, C. J. (2001). Satellite altimetry observations of the Black Sea level. *Journal of Geophysical Research: Oceans*, 106(C1):917–933.

Lantuit, H., Overduin, P. P., Couture, N., Wetterich, S., Aré, F., Atkinson, D., Brown, J., Cherkashov, G., Drozdov, D., Donald Forbes, L., Graves-Gaylord, A., Grigoriev, M., Hubberten, H. W., Jordan, J., Jorgenson, T., Ødegård, R. S., Ogorodov, S., Pollard, W. H., Rachold, V., Sedenko, S., Solomon, S., Steenhuisen, F., Streletskaya, I., and Vasiliev, A. (2012). The Arctic Coastal Dynamics Database: A New Classification Scheme and Statistics on Arctic Permafrost Coastlines. *Estuaries and Coasts*, 35(2):383–400.

Larsen, C. F., Motyka, R. J., Freymueller, J. T., Echelmeyer, K. A., and Ivins, E. R. (2004). Rapid uplift of southern Alaska caused by recent ice loss. *Geophysical Journal International*, 158(3):1118–1133.

Legeais, J.-F., Ablain, M., Zawadzki, L., Zuo, H., Johannessen, J. A., Scharffenberg, M. G., Fenoglio-Marc, L., Fernandes, M. J., Andersen, O. B., Rudenko, S., Cipollini, P., Quartly, G. D., Passaro, M., Cazenave, A., and Benveniste, J. (2017). An Improved and Homogeneous Altimeter Sea Level Record from the ESA Climate Change Initiative. *Earth System Science Data Discussions*, pages 1–35.

Lemos, G., Menendez, M., Semedo, A., Camus, P., Hemer, M., Dobrynin, M., and Miranda, P. M. (2020a). On the need of bias correction methods for wave climate projections. *Global and Planetary Change*, 186(August 2019):103109.

Lemos, G., Menendez, M., Semedo, A., Miranda, P. M. A., and Hemer, M. (2021a). On the decreases in North Atlantic significant wave heights from climate projections. *Climate Dynamics*, (0123456789).

Lemos, G., Semedo, A., Dobrynin, M., Behrens, A., Staneva, J., Bidlot, J. R., and Miranda, P. M. (2019). Mid-twenty-first century global wave climate projections: Results from a dynamic CMIP5 based ensemble. *Global and Planetary Change*, 172(July 2018):69–87.

Lemos, G., Semedo, A., Dobrynin, M., Menendez, M., and Miranda, P. M. (2020b). Bias-corrected cmip5-derived single-forcing future wind-wave climate projections toward the end of the twenty-first century. *Journal of Applied Meteorology and Climatology*, 59(9):1393–1414.

Lemos, G., Semedo, A., Hemer, M., Menendez, M., and Miranda, P. M. A. (2021b). Remote climate change propagation across the oceans – the directional swell signature. *Environmental Research Letters*.

Leonard, B. P. (1979). A stable and accurate convective modelling procedure based on quadratic upstream interpolation. *Computer Methods in Applied Mechanics and Engineering*, 19(1):59–98.

Lewis, M., Horsburgh, K., Bates, P., and Smith, R. (2011). Quantifying the uncertainty in future coastal flood risk estimates for the U.K. *Journal of Coastal Research*, 27(5):870–881.

Li, F., van Gelder, P. H., Ranasinghe, R., Callaghan, D. P., and Jongejan, R. B. (2014). Probabilistic modelling of extreme storms along the Dutch coast. *Coastal Engineering*, 86:1–13.

Li, H., Sheffield, J., and Wood, E. F. (2010). Bias correction of monthly precipitation and temperature fields from Intergovernmental Panel on Climate Change AR4 models using equidistant quantile matching. *Journal of Geophysical Research Atmospheres*, 115(10).

Lin-Ye, J., Garcia-Leon, M., Gracia, V., and Sanchez-Arcilla, A. (2016). A multivariate statistical model of extreme events: An application to the Catalan coast. *Coastal Engineering*, 117:138–156.

Link, L. E. (2010). The anatomy of a disaster, an overview of Hurricane Katrina and New Orleans. *Ocean Engineering*, 37(1):4–12.

Lira-Loarca, A., Cobos, M., Losada, M. Á., and Baquerizo, A. (2020). Storm characterization and simulation for damage evolution models of maritime structures. *Coastal Engineering*, 156.

Liu, Y., Li, J., Fasullo, J., and Galloway, D. L. (2020). Land subsidence contributions to relative sea level rise at tide gauge Galveston Pier 21, Texas. *Scientific Reports*, 10(1).

Longuet-Higgins, M. S., Cartwright, D. E., and Smith, N. D. (1963). Observations of the directional spectrum of sea waves using the motions of a floating buoy. *Ocean Wave Spectra*, pages 111–136.

Losada, I. J., Toimil, A., Muñoz, A., Garcia-Fletcher, A. P., and Diaz-Simal, P. (2019). A planning strategy for the adaptation of coastal areas to climate change: The Spanish case. *Ocean and Coastal Management*, 182(April).

Lowe, R. J., Cuttler, M. V., and Hansen, J. E. (2021). Climatic Drivers of Extreme Sea Level Events Along the Coastline of Western Australia. *Earth's Future*, 9(4).

Lucio, D., Tomás, A., Lara, J. L., Camus, P., and Losada, I. J. (2020). Stochastic modeling of long-term wave climate based on weather patterns for coastal structures applications. *Coastal Engineering*, 161(July):103771.

Madireddy, M., Kumara, S., Medeiros, D. J., and Shankar, V. N. (2015). Leveraging social networks for efficient hurricane evacuation. *Transportation Research Part B: Methodological*, 77:199–212.

Madsen, K. S., Hoyer, J., Weiwei, F., and Donlon, C. (2015). Blending of satellite and tide gauge sea level observations and its assimilation in a storm surgemodel of the North Sea and Baltic Sea. *Journal of Geophysical Research : Oceans*, 120:1–14.

Maraun, D., Shepherd, T. G., Widmann, M., Zappa, G., Walton, D., Gutiérrez, J. M., Hagemann, S., Richter, I., Soares, P. M., Hall, A., and Mearns, L. O. (2017). Towards process-informed bias correction of climate change simulations. *Nature Climate Change*, 7(11):764–773.

Marcos, M. and Woodworth, P. L. (2017). Journal of Geophysical Research : Oceans of the North Atlantic and the Gulf of Mexico. *Journal of Geophysical Research : Oceans*, pages 7031–7048.

Marsooli, R., Lin, N., Emanuel, K., and Feng, K. (2019). Climate change exacerbates hurricane flood hazards along US Atlantic and Gulf Coasts in spatially varying patterns. *Nature Communications*, 10(1):1–9.

Martzikos, N., Afentoulis, V., Tsoukala, V. K., Martzikos, N., Afentoulis, V., and Tsoukala, V. (2018). Storm clustering and classification for the port of Rethymno in Greece. Technical report.

Martzikos, N. T., Prinos, P. E., Memos, C. D., and Tsoukala, V. K. (2021a). Key research issues of coastal storm analysis.

Martzikos, N. T., Prinos, P. E., Memos, C. D., and Tsoukala, V. K. (2021b). Statistical analysis of Mediterranean coastal storms. *Oceanologia*, 63(1):133–148.

Masina, M., Lamberti, A., and Archetti, R. (2015). Coastal flooding: A copula based approach for estimating the joint probability of water levels and waves. *Coastal Engineering*, 97:37–52.

Masselink, G., Austin, M., Scott, T., Poate, T., and Russell, P. (2014). Role of wave forcing, storms and NAO in outer bar dynamics on a high-energy, macro-tidal beach. *Geomorphology*, 226:76–93.

Masselink, G., Castelle, B., Scott, T., Dodet, G., Suanez, S., Jackson, D., and Floc'H, F. (2016). Extreme wave activity during 2013/2014 winter and morphological impacts along the Atlantic coast of Europe. *Geophysical Research Letters*, 43(5):2135–2143.

Masson, D. and Knutti, R. (2011). Climate model genealogy. *Geophysical Research Letters*, 38(8):1–4.

Masson-Delmotte, V., Zhai, P., Pirani, A., Connors, S. L., Péan, C., Berger, S., Caud, N., Chen, Y., Goldfarb, L., Gomis, M. I., Huang, M., Leitzell, K., Lonnoy, E., Matthews, J., Maycock, T. K., Waterfield, T., Yelekçi, O., Yu, R., Zhou, B., and (eds.) (2021). IPCC, 2021: Climate Change 2021: The Physical Science Basis. Technical report.

Melet, A., Almar, R., Hemer, M., Le Cozannet, G., Meyssignac, B., and Ruggiero, P. (2020). Contribution of Wave Setup to Projected Coastal Sea Level Changes. *Journal of Geophysical Research: Oceans*, 125(8).

Melet, A., Meyssignac, B., Almar, R., and Le Cozannet, G. (2018). Under-estimated wave contribution to coastal sea-level rise. *Nature Climate Change*, 8(3):234–239.

Méndez, F. J., Menéndez, M., Luceño, A., and Losada, I. J. (2007). Analyzing monthly extreme sea levels with a time-dependent GEV model. *Journal of Atmospheric and Oceanic Technology*.

Mendoza, E. T., Jimenez, J. A., and Mateo, J. (2011). A coastal storms intensity scale for the Catalan sea (NW Mediterranean). *Natural Hazards and Earth System Science*, 11(9):2453–2462.

Mendoza, E. T., Jiménez, J. A., and Mendoza, E. T. (2006). Storm-Induced Beach Erosion Potential on the Catalonian Coast The National Coastal Resilience Laboratory View project Storm-Induced Beach Erosion Potential on the Catalonian Coast. *Proceedings) Spain Journal of Coastal Research*, 48:81–88.

Mendoza, E. T., Trejo-Rangel, M. A., Salles, P., Appendini, C. M., Lopez-Gonzalez, J., and Torres-Freyermuth, A. (2013). Storm characterization and coastal hazards in the Yucatan Peninsula. *Journal of Coastal Research*, 65:790–795.

Menendez, M., Mendez, F. J., and Losada, I. J. (2009). Forecasting seasonal to interannual variability in extreme sea levels. *ICES Journal of Marine Science*, 66(7):1490–1496.

Menéndez, M. and Woodworth, P. L. (2010). Changes in extreme high water levels based on a quasi-global tide-gauge data set. *Journal of Geophysical Research: Oceans*, 115(10):1–15.

Mentaschi, L., Vousdoukas, M. I., Voukouvalas, E., Dosio, A., and Feyen, L. (2017). Global changes of extreme coastal wave energy fluxes triggered by intensified teleconnection patterns. pages 2416–2426.

Meucci, A., Young, I. R., Hemer, M., Kirezci, E., and Ranasinghe, R. (2020). Projected 21st century changes in extreme wind-wave events. *Sci. Adv*, 6(June):7295–7305.

Mitsuyasu, H., Tasai, F., Suhara, T., Mizuno, S., Ohkusu, M., Honda, T., and Rikiishi, K. (1975). Observation of the directional spectrum of ocean waves using a cloverleaf buoy. *Physical Oceanography*, 5:750–760.

Molina, R., Manno, G., Re, C. L., Anfuso, G., and Ciraolo, G. (2019). Storm energy flux characterization along the mediterranean coast of Andalusia (Spain). *Water (Switzerland)*, 11(3).

Mori, N., Shimura, T., Yasuda, T., and Mase, H. (2013). Multi-model climate projections of ocean surface variables under different climate scenarios-Future change of waves, sea level and wind. *Ocean Engineering*, 71:122–129.

Morim, J., Hemer, M., Cartwright, N., Strauss, D., and Andutta, F. (2018). On the concordance of 21st century wind-wave climate projections. *Global and Planetary Change*, 167(May):160–171.

Morim, J., Hemer, M., Wang, X. L., Cartwright, N., Trenham, C., Semedo, A., Young, I., Bricheno, L., Camus, P., Casas-Prat, M., Erikson, L., Mentaschi, L., Mori, N., Shimura, T., Timmermans, B., Aarnes, O., Breivik, Ø., Behrens, A., Dobrynin, M., Menendez, M., Staneva, J., Wehner, M., Wolf, J., Kamranzad, B., Webb, A., Stopa, J., and Andutta, F. (2019). Robustness and uncertainties in global multivariate wind-wave climate projections. *Nature Climate Change*, 9(9):711–718.

Morim, J., Trenham, C., Hemer, M., Wang, X. L., Mori, N., Casas-Prat, M., Semedo, A., Shimura, T., Timmermans, B., Camus, P., Bricheno, L., Mentaschi, L., Dobrynin, M., Feng, Y., and Erikson, L. (2020). A global ensemble of ocean wave climate projections from CMIP5-driven models. *Scientific Data*, 7(1):1–10.

Muis, S., Apecechea, M. I., Dullaart, J., de Lima Rego, J., Madsen, K. S., Su, J., Yan, K., and Verlaan, M. (2020). A High-Resolution Global Dataset of Extreme Sea Levels, Tides, and Storm Surges, Including Future Projections. *Frontiers in Marine Science*, 7(April):1–15.

Muis, S., Verlaan, M., Winsemius, H. C., Aerts, J. C., and Ward, P. J. (2016). A global reanalysis of storm surges and extreme sea levels. *Nature Communications*, 7(May).

Najid, S. K., Zaharim, A., Razali, A. M., Zainol, M. S., Ibrahim, K., and Sopian, K. (2009). Analyzing the East Coast Malaysia Wind Speed Data. *International Journal of Energy and Environment*, 3(2):8.

Nicholls, R. J. and Cazenave, A. (2010). Sea-Level Rise and Its Impact on Coastal Zones. *Science*, 328(5985):1517–1520.

Notteboom, T. E. (2006). The Time factor in liner shipping services. *Maritime Economics and Logistics*, 8(1):19–39.

Odériz, I., Silva, R., Mortlock, T., Mori, N., Shimura, T., Webb, A., Padilla-Hernandez, R., and Villers, S. (2021). Natural Variability and Warming Signals in Global Ocean Wave Climates. *Geophysical Research Letters*, pages 1–12.

Ogi, M., Tachibana, Y., and Yamazaki, K. (2003). Impact of the wintertime North Atlantic Oscillation (NAO) on the summertime atmospheric circulation. *Geophysical Research Letters*, 30(13):2–5.

O'Gorman, P. A. (2010). Understanding the varied response of the extratropical storm tracks to climate change. *Proceedings of the National Academy of Sciences of the United States of America*, 107(45):19176–19180.

Ojeda, E., Appendini, C. M., and Mendoza, E. T. (2017). Storm-wave trends in Mexican waters of the Gulf of Mexico and Caribbean Sea. *Natural Hazards and Earth System Sciences*, 17(8):1305–1317.

Onorato, M., Osborne, A. R., Serio, M., and Bertone, S. (2001). Freak waves in random oceanic sea states. *Physical Review Letters*, 86(25):5831–5834.

Oppenheimer, M., Glavovic, B., Hinkel, J., van de Wal, R., Magnan, A. K., Abd-Elgawad, A., Cai, R., Cifuentes-Jara, M., DeConto, R. M., Ghosh, T., Hay, J., Isla, F., Marzeion, B., Meyssignac, B., and Sebesvari, Z. (2019). Sea Level Rise and Implications for Low Lying Islands, Coasts and Communities. *IPCC Special Report on the Ocean and Cryosphere in a Changing Climate*, 355(6321).

Ortego, M. I., Tolosana-Delgado, R., Gibergans-Báguena, J., Egozcue, J. J., and Sánchez-Arcilla, A. (2012). Assessing wavestorm hazard evolution in the NW Mediterranean with hindcast and buoy data. *Climatic Change*, 113(3-4):713–731.

Owens, B. F. and Landsea, C. W. (2003). Assessing the Skill of Operational Atlantic Seasonal Tropical Cyclone Forecasts. *Weather and Forecasting*, 18(1):45–54.

Pandey, S., Rao, A. D., and Haldar, R. (2021). Modeling of Coastal Inundation in Response to a Tropical Cyclone Using a Coupled Hydraulic HEC-RAS and ADCIRC Model. *Journal of Geophysical Research: Oceans*, 126(7).

Paprotny, D., Terefenko, P., Giza, A., Czapliński, P., and Vousdoukas, M. I. (2021). Future losses of ecosystem services due to coastal erosion in Europe. *Science of the Total Environment*, 760.

Passaro, M., Cipollini, P., Vignudelli, S., Quartly, G. D., and Snaith, H. M. (2014). ALES: A multi-mission adaptive subwaveform retracker for coastal and open ocean altimetry. *Remote Sensing of Environment*, 145:173–189.

Patricola, C. M. and Wehner, M. F. (2018). Anthropogenic influences on major tropical cyclone events. *Nature*, 563(7731):339–346.

Peltier, W. R. (2001). Chapter 4 Global glacial isostatic adjustment and modern instrumental records of relative sea level history. *International Geophysics*, 75(C):65–95.

Pérez, J., Méndez, F. J., Menéndez, M., and Losada, I. J. (2014). ESTELA: A method for evaluating the source and travel time of the wave energy reaching a local area. *Ocean Dynamics*, 64(8):1181–1191.

Perez, J., Menendez, M., Camus, P., Mendez, F. J., and Losada, I. J. (2015). Statistical multi-model climate projections of surface ocean waves in Europe. *Ocean Modelling*, 96:161–170.

Perez, J., Menendez, M., and Losada, I. J. (2017). GOW2: A global wave hindcast for coastal applications. *Coastal Engineering*, 124(March):1–11.

Perkins, S. E., Pitman, A. J., Holbrook, N. J., and McAneney, J. (2007). Evaluation of the AR4 climate models' simulated daily maximum temperature, minimum temperature, and precipitation over Australia using probability density functions. *Journal of Climate*, 20(17):4356–4376.

Piani, C., Haerter, J. O., and Coppola, E. (2010a). Statistical bias correction for daily precipitation in regional climate models over Europe. *Theoretical and Applied Climatology*, 99(1-2):187–192.

Piani, C., Weedon, G. P., Best, M., Gomes, S. M., Viterbo, P., Hagemann, S., and Haerter, J. O. (2010b). Statistical bias correction of global simulated daily precipitation and temperature for the application of hydrological models. *Journal of Hydrology*, 395(3-4):199–215.

Pierson, Jr., W. J., Tuttell, J. J., and Woolley, J. A. (1952). The theory of the refraction of a short crested gaussian sea surface with application to the northern New Jersey Coast. *3rd Conf. Coastal Engineering*, pages 86–108.

Portilla, J., Ocampo-Torres, F. J., and Monbaliu, J. (2009). Spectral partitioning and identification of wind sea and swell. *Journal of Atmospheric and Oceanic Technology*, 26(1):107–122.

Portilla-Yandún, J. (2018). The Global Signature of Ocean Wave Spectra. *Geophysical Research Letters*, 45(1):267–276.

Portilla-Yandún, J., Barbariol, F., Benetazzo, A., and Cavaleri, L. (2019). On the statistical analysis of ocean wave directional spectra. *Ocean Engineering*, 189(August):106361.

Portilla-Yandún, J., Cavaleri, L., and Van Vledder, G. P. (2015). Wave spectra partitioning and long term statistical distribution. *Ocean Modelling*, 96:148–160.

Prandi, P., Meyssignac, B., Ablain, M., Spada, G., Ribes, A., and Benveniste, J. (2021). Local sea level trends, accelerations and uncertainties over 1993–2019. *Scientific Data*, 8(1):1–12.

Priestley, M. D., Ackerley, D., Catto, J. L., Hodges, K. I., McDonald, R. E., and Lee, R. W. (2020). An Overview of the Extratropical Storm Tracks in CMIP6 Historical Simulations. *Journal of Climate*, 33(15):6315–6343.

Pugh, D. T. (1987). Tides, surges and mean sea level.

Pujol, M. I., Faugère, Y., Taburet, G., Dupuy, S., Pelloquin, C., Ablain, M., and Picot, N. (2016). DUACS DT2014: The new multi-mission altimeter data set reprocessed over 20 years. *Ocean Science*, 12(5):1067–1090.

Quartly, G. D., Legeais, J. F., Ablain, M., Zawadzki, L., Joana Fernandes, M., Rudenko, S., Carrère, L., Nilo Garciá, P., Cipollini, P., Andersen, O. B., Poisson, J. C., Mbajon Njiche, S., Cazenave, A., and Benveniste, J. (2017). A new phase in the production of quality-controlled sea level data. *Earth System Science Data*, 9(2):557–572.

Ranasinghe, R. (2016). Assessing climate change impacts on open sandy coasts: A review.

Rangel-Buitrago, N. and Anfuso, G. (2011). Coastal storm characterization and morphological impacts on sandy coasts. *Earth Surface Processes and Landforms*, 36(15):1997–2010.

Ranjha, R., Tjernström, M., Semedo, A., Svensson, G., and Cardoso, R. M. (2015). Structure and variability of the Oman coastal low-level jet. *Tellus, Series A: Dynamic Meteorology and Oceanography*, 67(1).

Rawson, A., Brito, M., Sabeur, Z., and Tran-Thanh, L. (2021). A machine learning approach for monitoring ship safety in extreme weather events. *Safety Science*, 141(March):105336.

Reguero, B. G., Losada, I. J., and Méndez, F. J. (2019). A recent increase in global wave power as a consequence of oceanic warming. *Nature Communications*, 10(1).

Rocheta, E., Evans, J. P., and Sharma, A. (2017). Can Bias correction of regional climate model lateral boundary conditions improve low-frequency rainfall variability? *Journal of Climate*, 30(24):9785–9806.

Roebeling, P. C., Costa, L., Magalhães-Filho, L., and Tekken, V. (2013). Ecosystem service value losses from coastal erosion in Europe: Historical trends and future projections. *Journal of Coastal Conservation*, 17(3):389–395.

Rogers, D. and Tsirkunov, V. (2011). Costs and benefits of early warning systems. *Global assessment rep.*

Rueda, A., Vitousek, S., Camus, P., Tomás, A., Espejo, A., Losada, I. J., Barnard, P. L., Erikson, L. H., Ruggiero, P., Reguero, B. G., and Mendez, F. J. (2017). A global classification of coastal flood hazard climates associated with large-scale oceanographic forcing /704/106/829/2737 /704/4111 /141 /129 article. *Scientific Reports*, 7(1):1–8.

Rueda-Bayona, J. G., Guzmán, A., and Cabello Eras, J. J. (2020). Selection of JONSWAP Spectra Parameters during Water-Depth and Sea-State Transitions. *Journal of Waterway, Port, Coastal, and Ocean Engineering*, 146(6):04020038.

Savage, J. C. and Plafker, G. (1991). Tide gage measurements of uplift along the south coast of Alaska. *Journal of Geophysical Research*, 96(B3):4325–4335.

Semedo, A., Dobrynin, M., Lemos, G., Behrens, A., Staneva, J., de Vries, H., Sterl, A., Bidlot, J. R., Miranda, P. M., and Murawski, J. (2018). CMIP5-derived single-forcing, single-model, and single-scenario wind-wave climate ensemble: Configuration and performance evaluation. *Journal of Marine Science and Engineering*, 6(3).

Semedo, A., Rutgersson, A., Sterl, A., and Sušelj, K. (2012). The global wave age climate. In *Maritime Engineering and Technology - Proceedings of 1st International Conference on Maritime Technology and Engineering, MARTECH 2011*, pages 539–543.

Semedo, A., SušElj, K., Rutgersson, A., and Sterl, A. (2011). A global view on the wind sea and swell climate and variability from ERA-40. *Journal of Climate*, 24(5):1461–1479.

Semedo, A., Vettor, R., Breivik, Sterl, A., Reistad, M., Soares, C. G., and Lima, D. (2015). The wind sea and swell waves climate in the Nordic seas. *Ocean Dynamics*, 65(2):223–240.

Semedo, A., Weisse, R., Behrens, A., Sterl, A., Bengtsson, L., and Günther, H. (2013). Projection of global wave climate change toward the end of the twenty-first century. *Journal of Climate*, 26(21):8269–8288.

Senechal, N., Coco, G., Castelle, B., and Marieu, V. (2015). Storm impact on the seasonal shoreline dynamics of a meso- to macrotidal open sandy beach (Biscarrosse, France). *Geomorphology*, 228:448–461.

Shaw, T. A. (2019). Mechanisms of Future Predicted Changes in the Zonal Mean Mid-Latitude Circulation. *Current Climate Change Reports*, 5(4):345–357.

Shaw, T. A., Baldwin, M., Barnes, E. A., Caballero, R., Garfinkel, C. I., Hwang, Y. T., Li, C., O'Gorman, P. A., Rivière, G., Simpson, I. R., and Voigt, A. (2016). Storm track processes and the opposing influences of climate change.

Shimokawa, T. and Min Liao (1999). Goodness-of-fit tests for type-I extreme-value and 2-parameter Weibull distributions. *IEEE Transactions on Reliability*, 48(1):79–86.

Shimura, T. and Mori, N. (2019). High-resolution wave climate hindcast around Japan and its spectral representation. *Coastal Engineering*, 151(May):1–9.

Shimura, T., Mori, N., and Hemer, M. A. (2017). Projection of tropical cyclone-generated extreme wave climate based on CMIP5 multi-model ensemble in the Western North Pacific. *Climate Dynamics*, 49(4):1449–1462.

Shimura, T., Mori, N., and Mase, H. (2015). Future projections of extreme ocean wave climates and the relation to tropical cyclones: Ensemble experiments of MRI-AGCM3.2H. *Journal of Climate*, 28(24):9838–9856.

Shope, J. B., Storlazzi, C. D., Erikson, L. H., and Hegermiller, C. A. (2016). Changes to extreme wave climates of islands within the Western Tropical Pacific throughout the 21st century under RCP 4.5 and RCP 8.5, with implications for island vulnerability and sustainability. *Global and Planetary Change*, 141:25–38.

Short, A. D. (1991). Macro-meso tidal beach morphodynamics - an overview. *Journal of Coastal Research*, 7(2):417–436.

Silva-Araya, W. F., Santiago-Collazo, F. L., Gonzalez-Lopez, J., and Maldonado-Maldonado, J. (2018). Dynamic modeling of surface runoff and storm surge during hurricane and tropical storm events. *Hydrology*, 5(1):1–28.

Smithers, S. G. and Hoeke, R. K. (2014). Geomorphological impacts of high-latitude storm waves on low-latitude reef islands - Observations of the December 2008 event on Nukutoa, Takuu, Papua New Guinea. *Geomorphology*, 222:106–121.

Snarey, M., Terrett, N. K., Willett, P., and Wilton, D. J. (1997). Comparison of algorithms for dissimilarity-based compound selection. *Journal of Molecular Graphics and Modelling*, 15(6):372–385.

Splinter, K. D., Turner, I. L., Reinhardt, M., and Ruessink, G. (2017). Rapid adjustment of shoreline behavior to changing seasonality of storms: observations and modelling at an open-coast beach. *Earth Surface Processes and Landforms*, 42(8):1186–1194.

Stephens, M. A. (1974). EDF statistics for goodness of fit and some comparisons. *Journal of the American Statistical Association*, 69(347):730–737.

Stockdon, H. F., Holman, R. A., Howd, P. A., and Sallenger, A. H. (2006). Empirical parameterization of setup, swash, and runup. *Coastal Engineering*, 53(7):573–588.

Stuecker, M. F., Timmermann, A., Jin, F. F., Chikamoto, Y., Zhang, W., Wittenberg, A. T., Widiasih, E., and Zhao, S. (2017). Revisiting ENSO/Indian Ocean Dipole phase relationships. *Geophysical Research Letters*, 44(5):2481–2492.

Sutton-Grier, A. E., Wowk, K., and Bamford, H. (2015). Future of our coasts: The potential for natural and hybrid infrastructure to enhance the resilience of our coastal communities, economies and ecosystems.

Swamy, R., Kang, J. E., Batta, R., and Chung, Y. (2017). Hurricane evacuation planning using public transportation. *Socio-Economic Planning Sciences*, 59:43–55.

Swart, N. C. and Fyfe, J. C. (2012). Observed and simulated changes in the Southern Hemisphere surface westerly wind-stress. *Geophysical Research Letters*, 39(16):6–11.

Tamarin-Brodsky, T. and Kaspi, Y. (2017). Enhanced poleward propagation of storms under climate change. *Nature Geoscience*, 10(12):908–913.

Tebaldi, C., Arblaster, J. M., and Knutti, R. (2011). Mapping model agreement on future climate projections. *Geophysical Research Letters*, 38(23):1–5.

Tebaldi, C., Ranasinghe, R., Vousdoukas, M., Rasmussen, D. J., Vega-Westhoff, B., Kirezci, E., Kopp, R. E., Sriver, R., and Mentaschi, L. (2021). Extreme sea levels at different global warming levels. *Nature Climate Change*, 11(9):746–751.

Tebaldi, C., Strauss, B. H., and Zervas, C. E. (2012). Modelling sea level rise impacts on storm surges along US coasts. *Environmental Research Letters*, 7(1).

Thompson, P. R., Mitchum, G. T., Vonesch, C., and Li, J. (2013). Variability of winter storminess in the Eastern United States during the Twentieth Century from tide gauges. *Journal of Climate*, 26(23):9713–9726.

Thomson, J. and Rogers, W. E. (2014). Swell and sea in the emerging Arctic Ocean. *Geophysical Research Letters*, 41(9):3136–3140.

Timmermann, A., McGregor, S., and Jin, F. F. (2010). Wind effects on past and future regional sea level trends in the southern Indo-Pacific. *Journal of Climate*, 23(16):4429–4437.

Toimil, A., Camus, P., Losada, I. J., and Alvarez-Cuesta, M. (2021a). Visualising the Uncertainty Cascade in Multi-Ensemble Probabilistic Coastal Erosion Projections. *Frontiers in Marine Science*, 8(June):1–19.

Toimil, A., Camus, P., Losada, I. J., Le Cozannet, G., Nicholls, R. J., Idier, D., and Maspataud, A. (2020a). Climate change-driven coastal erosion modelling in temperate sandy beaches: Methods and uncertainty treatment. *Earth-Science Reviews*, 202(January):103110.

Toimil, A., Díaz-Simal, P., Losada, I. J., and Camus, P. (2018). Estimating the risk of loss of beach recreation value under climate change. *Tourism Management*, 68:387–400.

Toimil, A., Losada, I. J., Díaz-Simal, P., Izaguirre, C., and Camus, P. (2017). Multi-sectoral, high-resolution assessment of climate change consequences of coastal flooding. *Climatic Change*, 145(3-4):431–444.

Toimil, A., Losada, I. J., Hinkel, J., and Nicholls, R. J. (2021b). Using quantitative dynamic adaptive policy pathways to manage climate change-induced coastal erosion. *Climate Risk Management*, 33(July):100342.

Toimil, A., Losada, I. J., Nicholls, R. J., Dalrymple, R. A., and Stive, M. J. (2020b). Addressing the challenges of climate change risks and adaptation in coastal areas: A review. *Coastal Engineering*, 156(December 2018).

Tolman, H. L. (2003). Treatment of unresolved islands and ice in wind wave models. *Ocean Modelling*, 5(3):219–231.

Tolman, H. L. (2014). User manual and system documentation of WAVEWATCH III.

Tracy, B., Devaliere, E., Hanson, J., Nicolini, T., and Tolman, H. (2007). Wind sea and swell delineation for numerical wave modeling. In *10th International Workshop on Wave Hindcasting and Forecasting Coastal Hazard Symposium.*

Trifonova, E. V., Valchev, N. N., Andreeva, N. K., and Eftimova, P. T. (2012). Critical storm thresholds for morphological changes in the western Black Sea coastal zone. *Geomorphology*, 143-144:81–94.

Tuomi, L., Kahma, K. K., and Pettersson, H. (2011). Wave hindcast statistics in the seasonally ice-covered Baltic Sea. *Boreal Environment Research*, 16(6):451–472.

Ulbrich, U., Leckebusch, G. C., and Pinto, J. G. (2009). Extra-tropical cyclones in the present and future climate: A review. In *Theoretical and Applied Climatology*, volume 96, pages 117–131. Springer Wien.

Valle-Rodríguez, J. and Trasviña-Castro, A. (2020). Sea level anomaly measurements from satellite coastal altimetry and tide gauges at the entrance of the Gulf of California. *Advances in Space Research*, 66(7):1593–1608.

van Gent, M. R., van Thiel de Vries, J. S., Coeveld, E. M., de Vroeg, J. H., and van de Graaff, J. (2008). Large-scale dune erosion tests to study the influence of wave periods. *Coastal Engineering*, 55(12):1041–1051.

van Gent, M. R. and Wolters, G. (2018). Effects of storm duration and oblique wave attack on open filters underneath rock armoured slopes. *Coastal Engineering*, 135:55–65.

Vanem, E. (2015). Uncertainties in extreme value modelling of wave data in a climate change perspective. *Journal of Ocean Engineering and Marine Energy*, 1(4):339–359.

Vignudelli, S., Kostianoy, A. G., Cipollini, P., and Benveniste, J., editors (2011). *Coastal Altimetry*. Springer Berlin Heidelberg, Berlin, Heidelberg.

Vinogradov, S. V. and Ponte, R. M. (2011). Low-frequency variability in coastal sea level from tide gauges and altimetry. *Journal of Geophysical Research: Oceans*, 116(7):1–11.

Volkov, D. L., Larnicol, G., and Dorandeu, J. (2007). Improving the quality of satellite altimetry data over continental shelves. *Journal of Geophysical Research: Oceans*, 112(6):1–20.

Vousdoukas, M. I., Almeida, L. P. M., and Ferreira, Ó. (2012). Beach erosion and recovery during consecutive storms at a steep-sloping, meso-tidal beach. *Earth Surface Processes and Landforms*, 37(6):583–593.

Vousdoukas, M. I., Mentaschi, L., Feyen, L., and Voukouvalas, E. (2017). Earth ' s Future Extreme sea levels on the rise along Europe ' s coasts Earth ' s Future. *Earth's Future*, 5(3):1–20.

Vousdoukas, M. I., Mentaschi, L., Hinkel, J., Ward, P. J., Mongelli, I., Ciscar, J. C., and Feyen, L. (2020a). Economic motivation for raising coastal flood defenses in Europe. *Nature Communications*, 11(1).

Vousdoukas, M. I., Mentaschi, L., Voukouvalas, E., Verlaan, M., Jevrejeva, S., Jackson, L. P., and Feyen, L. (2018). Global probabilistic projections of extreme sea levels show intensification of coastal flood hazard. *Nature Communications*, 9(1).

Vousdoukas, M. I., Ranasinghe, R., Mentaschi, L., Plomaritis, T. A., Athanasiou, P., Luijendijk, A., and Feyen, L. (2020b). Sandy coastlines under threat of erosion. *Nature Climate Change*, 10(3):260–263.

Wahl, T. and Chambers, D. P. (2015). Evidence for multidecadal varibility in US extreme sea level records. *Journal of Geophysical Research: Oceans*, 120:5342–5357.

Wahl, T., Plant, N. G., and Long, J. W. (2016). Probabilistic assessment of erosion and flooding risk in the northern Gulf of Mexico. *Journal of Geophysical Research: Oceans*, 121(5):3029–3043.

Wang, X. L., Feng, Y., and Swail, V. R. (2014). Changes in global ocean wave heights as projected using multimodel CMIP5 simulations. *Geophysical Research Letters*, 41(3):1026–1034.

Wang, X. L., Zwiers, F. W., and Swail, V. R. (2004). North Atlantic ocean wave climate change scenarios for the twenty-first century. *Journal of Climate*, 17(12):2368–2383.

Wang, Y. (2014). Calculating crest statistics of shallow water nonlinear waves based on standard spectra and measured data at the Poseidon platform. *Ocean Engineering*, 87:16–24.

Whittaker, C. N., Raby, A. C., Fitzgerald, C. J., and Taylor, P. H. (2016). The average shape of large waves in the coastal zone. *Coastal Engineering*, 114:253–264.

Woodruff, J. D., Irish, J. L., and Camargo, S. J. (2013). Coastal flooding by tropical cyclones and sea-level rise.

Woolf, D. K., Shaw, A. G., and Tsimplis, M. N. (2003). The influence of the North Atlantic Oscillation on sea-level variability in the North Atlantic region. *Global Atmosphere and Ocean System*, 9(4):145–167.

Wöppelmann, G. and Marcos, M. (2016). Vertical land motion as a key to understanding sea level change and variability.

Yin, J. H. (2005). A consistent poleward shift of the storm tracks in simulations of 21st century climate. *Geophysical Research Letters*, 32(18):1–4.

Young, I. R. (1999). Seasonal variability of the global ocean wind and wave climate. *International Journal of Climatology*, 19(9):931–950.

Zacharioudaki, A. and Reeve, D. E. (2011). Shoreline evolution under climate change wave scenarios. *Climatic Change*, 108(1):73–105.

Zhang, H. and Sheng, J. (2015). Examination of extreme sea levels due to storm surges and tides over the northwest Pacific Ocean. *Continental Shelf Research*, 93:81–97.

Zhang, K., Douglas, B. C., and Leatherman, S. P. (2000). Twentieth-century storm activity along the U.S. East Coast. *Journal of Climate*, 13(10):1748–1761.